Title
CELL-INTRINSIC AND CELL-EXTRINSIC BIOPHYSICAL FORCES IN CANCER AGGRESSION

Author
Miroshnikova, Yekaterina Andreevna

Publication Date
2015

Peer reviewed|Thesis/dissertation

Cell-Intrinsic and Cell-Extrinsic Biophysical Forces in Cancer Aggression

by

Yekaterina A. Miroshnikova

DISSERTATION

Submitted in partial satisfaction of the requirements for the degree of

DOCTOR OF PHILOSOPHY

in

Bioengineering

in the

GRADUATE DIVISION

of the

UNIVERSITY OF CALIFORNIA, SAN FRANCISCO

AND

UNIVERSITY OF CALIFORNIA, BERKELEY

DEDICATION

Dedicated to my mom, Yelena Lydia Miroshnikova, who has been my inspiration and the driving force behind all of my accomplishments. Thank you for your everlasting and unwavering love, support, and encouragement.

ACKNOWLEDGEMENTS

My six-year-long journey to a PhD has been has been a tremendous experience that I will treasure forever. A number of individuals have been with me throughout this endeavor and I am grateful to each and every one of you – you have supported me beyond belief.

Professional Context

My PhD mentor (Valerie) - thank you so incredibly much for taking me under your wing for these past six years and providing me with critical guidance, yet allowing me to be independent with my work. Your passion for science that you infused into me and your support for my scientific and professional aspirations will never be forgotten. I greatly value and treasure both our professional and personal relationships and am looking forward to staying in touch with you throughout life.

My dissertation committee & my graduate advisor (Valerie, Joanna, David, and Jeff) – thank you all for your support and mentorship throughout the dissertation process and helping me to grow professionally in this PhD Program.

Scientific Collaborators at UCSF (Joanna, Tracy, Cynthia, Anders, Shirin, Hanane, Christian) – thank you so very much for being incredible colleagues and kind, wonderful people throughout my PhD – you have made a tremendously positive impact on my professional development and personal experience at UCSF – thank you for being amazing individuals.

Professors/Advisors/Colleagues at Olin (Alisha, Debbie, Zhenya) – my years at Olin have not only been the best of my life but also the most transformative and impactful with respect to my

professional and personal development – thank you not only for the endless recommendation letters but for helping me discover my passion for bioengineering and desire to make a positive contribution to humanity with whatever career choice that I make – you made me a better human being.

Professors at UC Berkeley (Fyodor, Terry, Hayley) – your dedication and passion for education have profoundly impacted my PhD experience and have made me a lifelong advocate of STEM education. Thank you also for all your mentorship, advice, and support over the last six years.

Teachers at Southern Regional (Susan Miller, Margaret MacPhee, Carol Giblin, Ruth Tummey) – thank you for giving me an incredible academic foundation within a fantastic environment during my formative years. Your love and passion for teaching and science has inspired me more than you can imagine.

Weaver Lab members, especially Jon, Matt Paszek, and Janna– thank you for your advice and technical support with my research throughout the PhD. I have learned a tremendous amount from you and for that I will always be grateful.

Graduate Funding Sources: I would like to thank the National Science Foundation Graduate Research Fellowship (NSF GRFP) and the National Cancer Institute Ruth L. Kirschstein National Research Service Award for Individual Predoctoral Fellows (NCI NRSA F31) grants for providing financial support in the form of course fees and annual stipend to support my PhD

work. In addition, I am incredibly grateful for the UCSF Discovery Fellowship which has allowed me meet and interact with an incredible number of inspiring UCSF supporters and alumni.

Personal Context

Mom – you have always been my number one fan in life and it is your love and support that propels me forward every day, especially in the most difficult of times. Words cannot describe what you mean to me but as long as you are with me, there is nothing I cannot achieve. You are the most amazing human being and I am so incredibly proud to call you mom – you are simply the best.

To my grandma/dad – thank you for your lifelong support and for providing me with the happiest childhood that one can have. I can feel your love and belief in me across the tremendous distance that exists between us. **Баба и папа -** благодарю вас за поддержку на протяжении всей моей жизни и за предоставление наисчастливейшего детства для меня. Я чувствую вашу любовь и веру в меня через огромные расстояния которое существует между нами.

American mom (Nancy) – thank you for teaching me the American way of life and guiding me in the choice of all my academic institutions from Southern Regional and Olin to Berkeley/UCSF – you were there every step of the way from applications to college visits with your support, love, and advice and I will always treasure and love all of our times together. I am writing my thesis today, in large part, because of your presence in my life. I am proud to call you family.

My best friend and life companion (Heather) – you have been there for me from day one of the PhD journey and have helped me to get through the toughest of times and shared the best of them. You are one of the most amazing human beings that I have ever met and I feel incredibly fortunate to have you in my life. I am forever grateful for all your support and all the incredible times/places that we shared together.

Olin SF Crew (William, Russell, David, Molly): – thank you for your extraordinary friendships throughout both the undergraduate and graduate years – you have been a huge part of my life for the last ten years and I love and cherish each and every one of you. Thank you for the many wonderful memories from Boston to San Francisco and beyond. Friends for life.

UCB/UCSF PhD Crew (Dawn, Phil, Sophie, Wiktor, Sean, Arunan, Giulia) – thank you for your friendship and companionship throughout the PhD experience – together we survived – I am ecstatic to have gotten to know you and proud to leave the PhD phase of life with your friendships. I will cherish all our laughs and brunches together and will look forward to more in the future.

ABSTRACT

CELL-INTRINSIC AND CELL-EXTRINSIC BIOPHYSICAL FORCES IN CANCER AGGRESSION

Yekaterina A. Miroshnikova

Supervisor: Dr. Valerie M. Weaver, PhD.

Tumors are mechanically-corrupted tissues. Although a role for tissue force in malignancy is slowly becoming appreciated, the molecular mechanisms underlying this phenotype remain poorly understood. Moreover whether similar relationships exist across distinct tumor types is not known. This motivated me to conduct a number of mechanobiological studies in breast, pancreatic, and brain cancers. To begin with I first developed the necessary tools with which to quantitatively assess tumor biology. This involved the development of a highly-controlled *in vitro* 3-dimensional hydrogel system that recapitulates biophysical stiffening of epithelial cancers and a bioreactor system that is able to model the compressive forces observed in intracranial cancers.

Epithelial malignancies contain abundant cross-linked collagen that increases tissue tension to promote malignant transformation by inducing focal adhesions and potentiating PI3 kinase signaling. In a context of breast cancer collagen cross-linking requires fibronectin and tumors contain abundant fibronectin and frequently express high levels of its ligand α5β1 integrin. I

detected that fibronectin-bound α5β1 integrin is essential for collagen-dependent, stiffness-driven malignant transformation and explained why α5β1 integrin and fibronectin are consistently up-regulated in tumors and correlated their expression with breast cancer aggression. In a context of pancreatic ductal carcinoma I undertook collaborative studies which revealed that the cellular genotype tuned the tension of the malignant epithelium to mechanically prime the stroma and promote tumor progression through epithelial pSTAT3 and YAP. Highly aggressive pancreatic phenotypes developed within a highly stiff, matricellular-enriched and fibrotic tissue, and exhibited increased epithelial myosin activity with elevated cytokine, JAK, ROCK, FAK and Yap signaling, as well as STAT3-dependent inflammation. My work in these tumor tissues illustrated how tissue tension can force malignancy, drive tumor aggression, and compromise patient survival in the context of a collagen-rich microenvironments.

To detect whether these same principles apply to tissues lacking collagen-induced fibrosis, I extended my studies to glioblastoma multiforme (GBM). GBM brain tumors develop within a mechanically-challenged microenvironment that is characterized by high intracranial pressure, elevated solid stress and a dense hyaluronic acid (HA)-rich extracellular matrix that compromise vascular integrity to induce hypoxia and activate HIF1α. Interestingly, the presence of an R132H mutation in the metabolic regulator isocitrate dehydrogenous 1 (IDH1) improves patient prognosis in aggressive GBMs brain tumors and I hypothesized that IDH1 mutant GBM tumors would be less mechanically active than the more aggressive IDH WT tumors and that elevation of matrix mechanics could induce HIF1α and HIF1α-dependent gene expression in IDH1 mutant context to bypass the protective activity of the mutation and foster tumor aggression. Indeed, my

studies showed that a stiff HA-rich ECM enhanced the aggressiveness of IDH1 mutant GBMs by inducing HIF1α-dependent tenascin C expression.

Taken together with the currently available data, my findings point to new possibilities for cancer intervention by normalizing tumor mechanobiology as they highlight the existence of a conserved mechanosignaling mechanism across the different tumor tissues towards which therapies might be developed.

TABLE OF CONTENTS

LIST OF TABLES

LIST OF FIGURES

CHAPTER 1: INTRODUCTION TO THE WORK

Tumors are characterized by profound alterations in mechanical properties and a number of studies have demonstrated that biophysical alterations actively modulate various aspects of cellular behavior in healthy and diseased tissues through a process known as mechanotransduction which transforms mechanical cues into biochemical cues [1–4]. Yet, much of the underlying molecular signaling mechanisms modifying cellular fate are still poorly understood. This has motivated me to conduct a comprehensive analysis of a number of mechanical features of breast, pancreatic, and brain cancers with the immediate goal of defining the underlying biophysically active molecular mechanisms contributing to cancer aggression and progression and a long term goal of enhancing patient diagnosis and contributing to the development of novel treatment strategies with which to target these pathologies and improve patient survival.

Until recently the vast majority of cancer research has been single molecule- or pathway-centric with particular focus on tumor-promoting or tumor-suppressing genetic alterations. The field now recognizes the fact that tumor cells do not exist in a vacuum but instead synergize not only with their surrounding cellular neighbors but also the tissue stroma and that these interactions are required for the establishment of the altered tissue environment which supports tumor development, progression, and aggression. In that respect, a number of biochemical differences between normal and tumor microenvironments have been characterized, yet the study of the biophysical changes has only been appreciated recently despite the fact that, clinically, differential biophysical properties of cancerous tissues as compared to healthy tissues, have been

exploited for decades to diagnose a number of tumor types, such as breast, pancreatic, liver, and brain cancers [5–10]. Taken together with clinical utilization, new scientific realizations led to the development of the field of epigenetics which definitely established that alterations in genetic cellular programs do not necessarily arise from direct changes in DNA sequence but instead can be driven by cell-extrinsic factors. Biophysical force was found to be one such external environmental factor [11–13] which provided evidence for an instructional role of tissue mechanics to cancer initiation and promotion. As a matter of fact, we now understand that non-malignant cells containing normal genetic information can be driven to malignant-like state simply by altering their local extracellular matrix stiffness[12]. Similarly, the lineage of naïve multipotent mesenchymal stem cells can be specified by extracellular matrix elasticity such that soft matrices that mimic brain mechanics are neurogenic and stiff matrices that match muscle and bone mechanics are myogenic and osteogenic, respectively[14]. These examples illustrate the fact that tissue mechanics and mechanotransduction are intrinsically implicated in modifying cellular fate in both health and disease. Nevertheless there are many outstanding issues that remain unanswered and the work presented in this thesis addresses a few of such issues. First, there is the need for easily manipulatable culture model systems with which to test the sole impact of force (stiffness and compression) on cell behavior in order to carefully and specifically identify and interrogate the downstream effectors that are modified by biophysical forces. Secondly, it is necessary to clarify whether disease-altered tissue mechanics in different tissues manifests in similar phenotypes and whether it activates similar or distinct set(s) of downstream effectors. Lastly, there is an emerging need for the integration of findings regarding biophysically-driven means of disease aggression across the different tissue types in order to find common nodes or pathways and aid in the development of therapeutic modalities targeting tissue mechanics.

CHAPTER 2: *IN VITRO* TOOL DEVELOPMENT WITH WHICH TO STUDY BIOENGINEERING ASPECTS OF TUMOR BIOLOGY

Engineering strategies to recapitulate epithelial morphogenesis within synthetic 3 dimensional extracellular matrix with tunable mechanical properties

Summary: The mechanical properties (e.g. stiffness) of the extracellular matrix (ECM) influence cell fate and tissue morphogenesis and contribute to disease progression. Nevertheless, our understanding of the mechanisms by which ECM rigidity modulates cell behavior and fate remains rudimentary. To address this issue, a number of two and three dimensional (3D) hydrogel systems have been used to explore the effects of mechanical properties of the ECM on cell behavior. Unfortunately, many of these systems have limited application because fiber architecture, adhesiveness and/or pore size often change in parallel when gel elasticity is varied. Here we describe the use of ECM-adsorbed, synthetic, self-assembling peptide gels (SAPs) that are able to recapitulate normal epithelial acini morphogenesis and gene expression in a 3D context. By exploiting the range of visco-elasticity attainable with these SAP gels, and their ability to recreate native-like ECM fibril topology with minimal variability in ligand density or pore size, we were able to reconstitute normal and tumor-like phenotypes and gene expression patterns in nonmalignant mammary epithelial cells (MECs). Accordingly, this SAP hydrogel system presents the first tunable system capable of independently assessing the interplay between ECM stiffness and multi-cellular epithelial phenotype in a 3D context.

Introduction

Cells *in vivo* are constantly exposed to an array of biophysical forces such as hydrostatic pressure, shear stress, compression loading, and tensional forces. Cells rely on these physical cues to maintain homeostasis and adapt to them by altering cell signaling and gene expression and by remodeling their local microenvironment[15,16]. From an organismal point of view, ECM compliance directs the development of tissues[14,15] and influences the onset of many pathological conditions, including cardiovascular disease[17], arthritis[18], and neural degenerative diseases[19]. The ECM also progressively stiffens in tumors and recent work suggests this phenotype has functional significance because increasing ECM rigidity promotes malignant transformation, while inhibiting ECM stiffening reduces tumor incidence[12,20,21]. Accordingly, clarifying the role by which ECM compliance influences diverse cellular and tissue level functions is central to understanding the molecular basis for development and organ homeostasis. Nevertheless, the molecular mechanisms whereby ECM compliance regulates cellular behavior and tissue phenotype remain poorly understood.

One frequently employed simplified model system used to study the effect of ECM stiffness on cell behavior is protein-conjugated polyacrylamide (PA gels) gels[22–26]. These nearly elastic 2D gels permit the systematic and predictable modulation of ECM compliance by changing cross-linker concentration while maintaining ligand density and growth factor milieu constant. PA gels have proved quite useful in exploring fundamental links between ECM stiffness and cell behavior, and when used in conjunction with a matrix overlay assay, they have illustrated a role for ECM tension in epithelial morphogenesis [12,14,19,27–31]. These PA gels have also been used to identify molecular mechanisms by which ECM stiffness modulates cell phenotype, including

highlighting how ECM compliance can regulate cell behavior by influencing integrin adhesions and growth factor receptor signaling[12,32–35]. Indeed, studies using PA gels have proved instrumental in illustrating how physical cues from the ECM are sensed and propagated and how ECM tension can alter membrane receptor function and nuclear morphology to modify gene expression[36–38]. Yet, most cells exist within the context of a three dimensional (3D) tissue and it is now recognized that dimensionality per se is a profound regulator of cell and tissue phenotype[13,39–46]. In this regard, PA gels represent a pseudo 3D rigidity assay system because only the basal domain of the cell remains in contact with, and therefore responds to, the elasticity of the protein-laminated PA gel. Moreover, while animal studies have yielded important insight regarding the interplay between ECM topology and rigidity within a 3D context[12,45,47,48], *in vivo* tissues are inherently complex and hence do not lend themselves as readily to rigorous mechanistic manipulations and quantitative analysis. Accordingly, tractable *in vitro* systems are needed with which to study the molecular basis by which ECM stiffness influences cellular fate in the context of a 3D ECM.

A variety of natural matrices, such as Matrigel (rBM), collagen I (col I), and fibrin gels have been exploited with varying degrees of success to explore the effect of ECM stiffness and topology *in vitro* on cellular behavior and fate in a 3D context[49–53]. Using these hydrogel systems gel stiffness has been routinely modulated by altering the concentration or composition of the gel constituents or by varying cross-link density. However, approaches such as these simultaneously alter gel pore size, fiber architecture, and/or the number or availability of adhesion sites[54,55]. Further, these natural ECM systems frequently display inconsistencies and batch to batch variation. By contrast, synthetic biomaterials promise greater control of

mechanical and adhesive properties. In this regard, a variety of approaches have been undertaken to design 3D scaffolds that combine biological functionality and the architecture of natural ECM materials with the robust controllability of synthetic materials. These scaffolds include agarose-stiffened collagen I gels[56], polyethylene glycol (PEG) gels with tethered adhesion and degradation sites[57–60], as well as a variety of systems with dynamic biophysical and biochemical properties[61,62]. Unfortunately however, many of these gel systems lack the appropriate ECM-like fiber architecture and display limited pore size with increased ECM stiffness.

Self-assembling peptides (SAPs) are a family of 8-32 amino acid peptides that, when exposed to physiological salt solutions, self-assemble into fibrils[63,64]. SAPs are chemically defined and biologically compatible biomaterials that mimic the architectural features observed in some natural matrices such as type I collagen gels[65]. Moreover, SAP family members support cell adhesion and can direct the differentiated behavior of neural stem cells[66], osteoblasts[67], hepatocytes[68,69], and endothelial cells[65]. Motivated by these results I decided to explore the applicability of PuraMatrix, one type of commercially available SAP, to study the interplay between ECM stiffness and MEC morphogenesis in 3D. I determined that laminin-adsorbed (ligation of laminin receptors promotes MEC tissue polarity and differentiation) PuraMatrix SAPs not only support MEC acinar morphogenesis but that stiff SAPs promote an invasive epithelial tumor-like phenotype and do so without significantly changing pore size or gel architecture. Accordingly, I contend that these studies represent the first demonstration of a tractable, well defined hydrogel system that is able to recapitulate the biochemical and micro architectural features of the native normal tissue ECM so that the interplay between ECM compliance and multi-cellular tissue behavior can be studied in a 3D “tissue-like” context.

Increasing Collagen Concentration and Rigidity Stimulate Epithelial Growth and Survival and Compromise Tissue Morphogenesis and Integrity

Primary and immortalized MECs have been used to study the role of the ECM and its receptors in tissue morphogenesis and differentiation. When incorporated into a 3D rBM (Matrigel) human and murine MECs assemble into growth-arrested, polarized multi-cellular structures that resemble terminal ductal lobular units of the in vivo mammary gland[41,49]. MECs will also assemble into non-polarized 3D organoids when grown within type I collagen gels and can be induced to polarize if either purified laminin or rBM (2 mg/ml) is added[70].

The viscoelasticity of collagen I gels is proportional to their concentration. As such collagen gels provide an attractive system with which to study the effect of modulating ECM stiffness in a 3D context on tissue behavior. Accordingly, to study the effect of modulating ECM rigidity on epithelial behavior I generated type I collagen gels ranging from 1.2 to 3.2 mg/ml incorporating rBM (Col/rBM cultures; 2 mg/ml) as a polarity cue. I showed previously that these concentrations of collagen achieve gel stiffness that recapitulates the visco-elasticity typically found in a normal, pre malignant and early invasive tumorigenic human and mouse breast[12,20,71]. I then assayed for the effect of varying ECM stiffness in a 3D context on the growth and survival and morphogenesis of the nonmalignant human MEC line MCF10A, an immortalized human MEC line that undergoes multi-cellular epithelial morphogenesis in response to compliant 3D rBM cues[12].

Similar to what we and others observed previously, although the nonmalignant MECs incorporated into highly compliant Col/rBM gel (156 Pa ± 42 Pa) grew rapidly for the first six days, by day 10 they assembled growth-arrested acini as indicated by colonies with persistent diameters of 60.2 ± 5.4 μm, (Fig 1A; DIC image; Fig 1C). After 10 days of culture mammary acini in the compliant gels (1.2 mg/mL) also showed evidence of cleared lumens (see arrow figure 1A DIC, top and immunofluoresence, bottom) and achieved apical-basal polarity as demonstrated by basal deposition of laminin and apical-basal localization of β1 integrin (Fig 1A; lower left hand panel). By contrast, even moderate stiffening (2.2 mg/mL) of the Col/rBM (457 ± 67.3 Pa) significantly increased colony size suggestive of elevated cell proliferation (116.5 ± 24.2 μm; Fig 1A DIC top middle panel , Fig 1C). Yet, when gel stiffness approached that quantified in the stroma surrounding a pre-malignant breast epithelium[12], luminal clearing was compromised, indicative of enhanced cell survival (Fig 1B). Furthermore, a collagen stiffness approaching 800-1000 Pascals, similar to that measured in the ECM surrounding early invasive breast lesions, significantly disrupted apical-basal polarity, as revealed by diffuse localization of laminin V and relocalization of β1 integrin along the basal domain of the colony (Fig 1A, bottom middle panel). Intriguingly, not only did MECs embedded within Col/rBM gels with ECM stiffness approaching that measured in breast tumors (1411 ± 350.3 Pa) grow quite large (161.3 ± 21.1 μm; Fig 1C) and form highly disorganized, nonpolar colonies that lacked lumens (Fig 1A; lower panel right and Fig 1B) but these colonies also showed a propensity to form membrane protrusions that projected into the surrounding ECM, consistent with the notion that ECM stiffness promotes a tumor-like phenotype. Importantly however, despite these provocative findings, none of the nonmalignant MECs from the mammary colonies assembled within the rigid rBM/collagen I gels invaded into the gels (Fig 1A DIC top right).

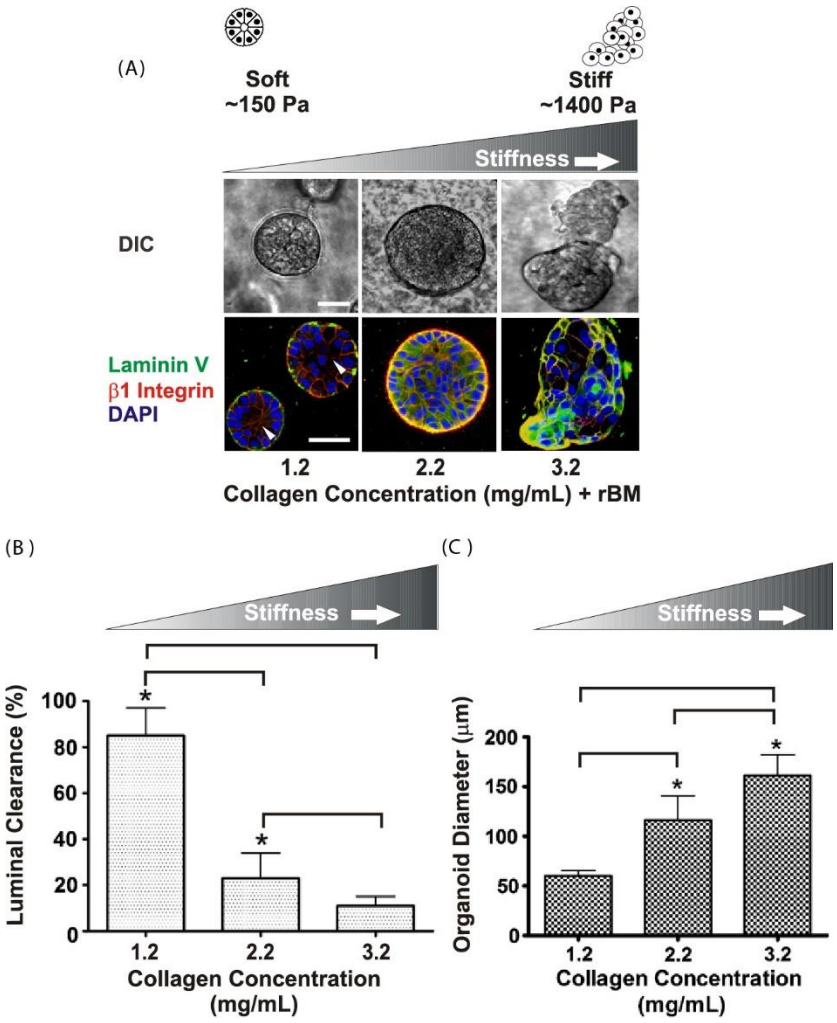

SAP Gels Figure 1. Increasing collagen concentration and rigidity stimulate epithelial growth and survival and compromise tissue morphogenesis and integrity.

(A) (Top) phase contrast images of multi-cellular MEC colonies embedded within type 1 collagen gels of increasing concentration (1.2–3.2 mg ml−1) and stiffness (150–1400 Pa) for 12 days. Bar equals 30 μm. (Bottom) laser confocal immunofluorescence images of multi-cellular MEC colonies as above, stained for β1 integrin (red), laminin V (green), and nuclei (DAPI; blue). Bar equals 40 μm. (B) Bar graphs showing quantification of luminal clearance measured in colonies shown in A. (C) Bar graph showing average colony diameter of colonies shown in A. ∗indicates $p < 0.001$. Values shown in (B) and (C) represent mean ± SEM of multiple measurements from at least three independent experiments.

Thus far my findings were consistent with the notion that ECM stiffness compromises epithelial morphogenesis and tissue integrity and induces a "tumor-like" phenotype even in nontransformed epithelial cells. Nevertheless, I noted that interpretation of data obtained with these gels was complicated by the fact that collagen ligand available to bind to cell surface receptors including integrins and discoidin receptors also significantly increased when the gel concentration was increased to stiffen the ECM. Moreover, SEM analysis revealed that the projected pore size and fiber thickness also changed dramatically as the concentration of the collagen gel was progressively increased (Fig 2A). Because ligand binding and pore size can significantly modify cell invasion, these findings indicate that studies aimed at assessing the interplay between ECM stiffness and cell invasion may be compromised using this approach. Furthermore, matrix topology per se can significantly modulate cellular phenotype further complicating the interpretation of experiments conducted using this gel system[56,72–75]. Thus, these results emphasize that it is still not clear if ECM stiffness per se can induce invasion of non-transformed epithelial tissues. Indeed, the data imply that although collagen gels offer an attractive model system with which to rapidly assess the effect of modulating ECM stiffness on cellular behavior in a 3D context, several confounding variables seriously compromise any ability to rigorously isolate and interpret the effect of matrix stiffness per se on cellular behavior using this hydrogel model.

Self Assembling Peptides (SAPs) are Flexible, Protein-absorbing, Synthetic Matrix that Mimic Collagen Architecture

There exist a number of readily-available materials whose elasticity can be modulated without changing ligand density. Materials such as hyaluronic acid, poly(ethylene) glycol, and

polyglycolic acid can be modified to provide rigorously controlled biochemical cues[56,76–82]. Unfortunately, the architecture of these materials is strikingly different from that of natural ECMs such as type I collagen, thereby compromising their utility as natural ECM substrates. By contrast, self assembling peptide hydrogels (SAPs) are biocompatible synthetic substrates that not only mimic the micro-architecture of natural collagen gels (Fig 2C) but lend themselves to chemical modification. SAPs are composed of 16 repeating amino acid residues (alternating hydrophilic and hydrophobic chains) that self-assemble to form nano fibers under physiological salt conditions due to hydrophobic (between alanines) and ionic bonding (between arginine and aspartic acid residues) between the amino acids[65]. Although SAPs can be mechanically tethered with ligand[69,83], these peptides are also protein-adsorbing[84]. Thus, although they do not contain integrin-binding sites, and therefore they cannot mediate ligand-dependent ECM receptor signaling, they can be readily conjugated, tethered, or adsorbed with quantifiable concentrations of ligand via direct peptide conjugation or through ECM protein adsorption. Moreover, by varying the concentration of the SAP, the stiffness of the gel can be modulated over a physiologically appropriate range to achieve a visco elasticity similar to soft tissues such as a healthy breast on the one hand and a cancerous breast on the other hand[12,20,85,86].

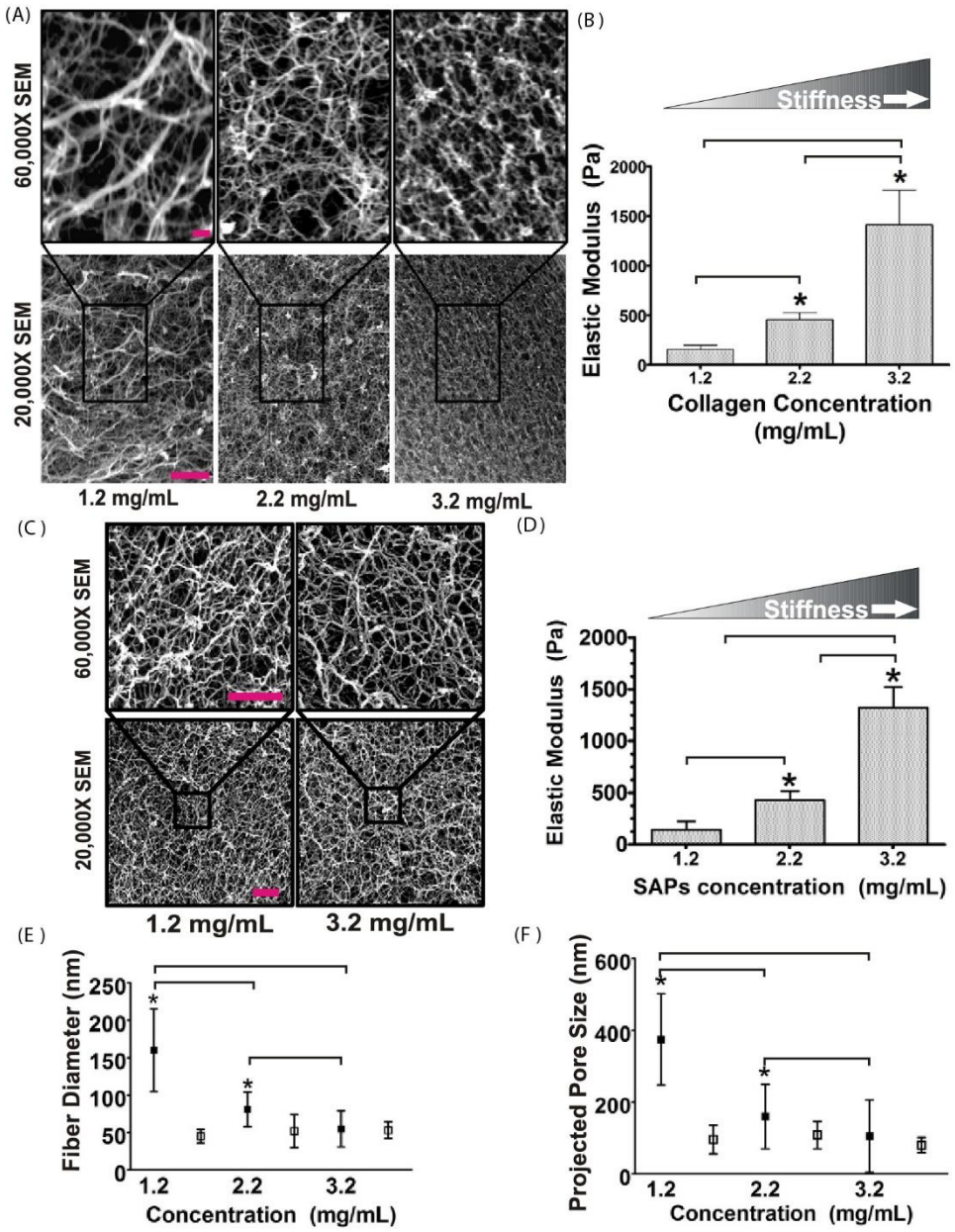

SAP Gels Figure 2. Self-assembling peptides (SAP): flexible, protein-absorbing, synthetic matrix that mimic collagen architecture.

(*A*) SEM microscopy images of collagen gels taken at high (top) and low (bottom) magnification illustrating the structural changes induced in collagen morphology, topology and pore size when collagen concentration is increased. Bar equals 5 μm. (*B*) Bar graph quantifying Young's modulus of collagen gels of varying concentration as measured by shear rheology. (*C*) SEM microscopy images of SAP gels taken at high (top) and low (bottom) magnification illustrating minimal structural changes in gel fiber morphology, topology and pore size when gel

concentration is increased. Bar equals 200 nm. SEM resolution is 3–5 nm (according to the manufacturer). (*D*) Bar graphs quantifying SAP gel stiffness as a function of gel concentration as measured by shear rheology. (*E*) Graphical depiction of fiber diameter quantified as a function of collagen (filled boxes) and SAP (open boxes) gel concentration. (*F*) Graphical depiction of pore size measured as projected pore size in collagen (filled boxes) and SAP (open boxes) gels as a function of gel concentration. ⋆indicates $p < 0.001$. Values shown in B and (*D*) and (*F*) represent mean with SEM of multiple measurements from at least three independent experiments.

To explore the utility of SAPs as biocompatible materials for exploring the effect of ECM stiffness on epithelial morphogenesis and homeostasis I characterized the physical topology and mechanical properties of one of these commercially available SAPs gels, PuraMatrix, over the range of visco elasticity deemed useful for the study of normal and transformed epithelial behavior. I found that varying SAP concentration from 1.2-3.2 mg/mL generated Young's moduli that ranged from 120-1,200 Pa, analogous to what I was able to achieve by varying collagen concentration from 1.2-3.2 mg/mL (Fig 2B and 2D). Importantly, SEM analysis revealed that unlike collagen I gels, SAPs gel micro-architecture did not substantially change within this stiffness range and gel concentration. Indeed, I noted that pore size only varied by approximately 10% and fibril topology remained within the range of 45-75 nm even when gel contraction was varied from 1.2-3.2 mg/mL (Fig 2E-F). By contrast the pore size of the collagen gels varied by over 30% and fibril topology ranged from 50 to 170 μm when collagen concentration was modified across this same range (Fig 2E-F). Curiously, although I detected no statistically-significant differences in the overall fiber organization and matrix topology as a function of SAPs gel concentration and stiffness, I did quantify a modest, but consistent increase in peptide mass per volume (data not shown). The fact that the observed difference was only a 10% increase in the fraction of soluble peptide at the highest gel concentration indicates that the elevated gel stiffness likely reflects a subtle increase in either the fiber diameter, length, or

absolute number. In this respect, I determined that the projected pore size and overall fiber mesh did not change drastically, suggesting that SAP gel stiffness was more than likely due to an increase in fiber diameter and/or enhanced fiber density. Indeed, there was a positive but-insignificant trend between SAP stiffness and decreased projected pore size and increased fiber thickness. The fact that I could not accurately document changes in these variables is more than likely due to the resolution limitation of our detection method which is unable to detect such subtle nano-scale differences in fiber diameter and pore size variability. The stiffness of a fibrous material can be largely attributed to the sum of the bending moments of all the fibers. Second moment of inertia is a shape property that can be used to predict deflections and stresses in the beams/fibers, which would be representative of its bulk stiffness. Assuming a circular cross-section of the fibers, the moment of inertia, I_o, would be proportional to the radius raised to the 4^{th} power ($I_o = \pi r^2/4$), such that incredibly small changes in the radius would be reflected by an increased capacity to dramatically alter the bendability or stiffness of the material. In these studies I observed an approximate six fold increase in gel stiffness between the soft and the stiff SAPs gels which can easily be accounted for by a mere 2 nm change in fiber thickness. As such, the theoretical differences between soft and stiff SAP gels are well beyond the 3-5 nm resolution capacity of SEM imaging. Moreover and importantly, despite the fact that it is obvious that SAP morphology must vary to some degree as a function of gel concentration/ stiffness, the magnitude of such a modest nanometer-scale variation would exert a negligible effect on cellular functions, such as migration and invasion, because cells operate on a length scale of 10-50 μm. Instead, variations in pore and fiber diameter within the tens to hundreds of nanometers, which is comparable to what I quantified for collagen gels of increasing concentration/ stiffness, are likely to significantly alter cellular invasion and migration. These findings suggested that SAP gels

could provide a viable alternative ECM for studying the effect of ECM rigidity on epithelial invasive phenotype in a 3D context.

SAP Gels Support Epithelial Morphogenesis and Direct Apical-Basal Tissue Polarity

To explore the utility of SAP gels as a tractable matrix system for studying the interplay between ECM stiffness and epithelial cell behavior in 3D, I grew MECs within un-conjugated, compliant, SAP gels in the absence of adsorbed ECM protein. I noted that MECs embedded within SAP gels survived and grew to assemble epithelial colonies. However, colony size was non-uniform and immuno-fluorescence analysis revealed that the colonies lacked polarity (data not shown). I therefore supplemented the SAP gels with laminin (100 μg/mL) or rBM (2 mg/mL; 10%) and assayed for effects on MEC growth, survival, and multi-cellular morphogenesis. Analogous to MECs embedded within rBM or a mixture of collagen I and rBM, MECs embedded within the laminin- or rBM-supplemented SAP gels proliferated rapidly for the first 5-6 days after which they growth-arrested, as revealed by loss of Ki-67 immuno-staining and the maintenance of a stable colony diameter, and initiated tissue morphogenesis, as indicated by elevated numbers of cells in the center of the colonies positive for activated caspase 3 (Fig 3B, Fig 4C and 4D). Consistently, MEC colonies generated in the laminin-supplemented SAPs gels assembled acini with cleared lumens that had similar diameters to those generated in rBM and collagen I/rBM gels (Fig 3A and 3C, quantified in 3B). Moreover, acini generated in the laminin-supplemented SAP gels achieved apical-basal polarity, as revealed by basally localized β4 integrin (Fig 3D, left panel, see arrow), basal-lateral β1 integrin, and cell-cell localized β-catenin (Fig 3D, middle and right panels, see arrows). These phenotypes are analogous to those observed in rBM or in 1.2 mg/mL collagen I gels supplemented with laminin or rBM (Fig 1A). Moreover, and

importantly, similar to what I and others have routinely observed using rBM gels, SAP gels were able to support stable acini development as revealed by uniform colony differentiation and repression of genes that compromise acini stability and differentiation, such as fibronectin (Fig 3D, right panel; Fig 4E-F). These findings indicated that compliant SAP gels, when supplemented with the appropriate biochemical ECM cues, can support normal MEC growth and viability and direct multi-cellular tissue morphogenesis.

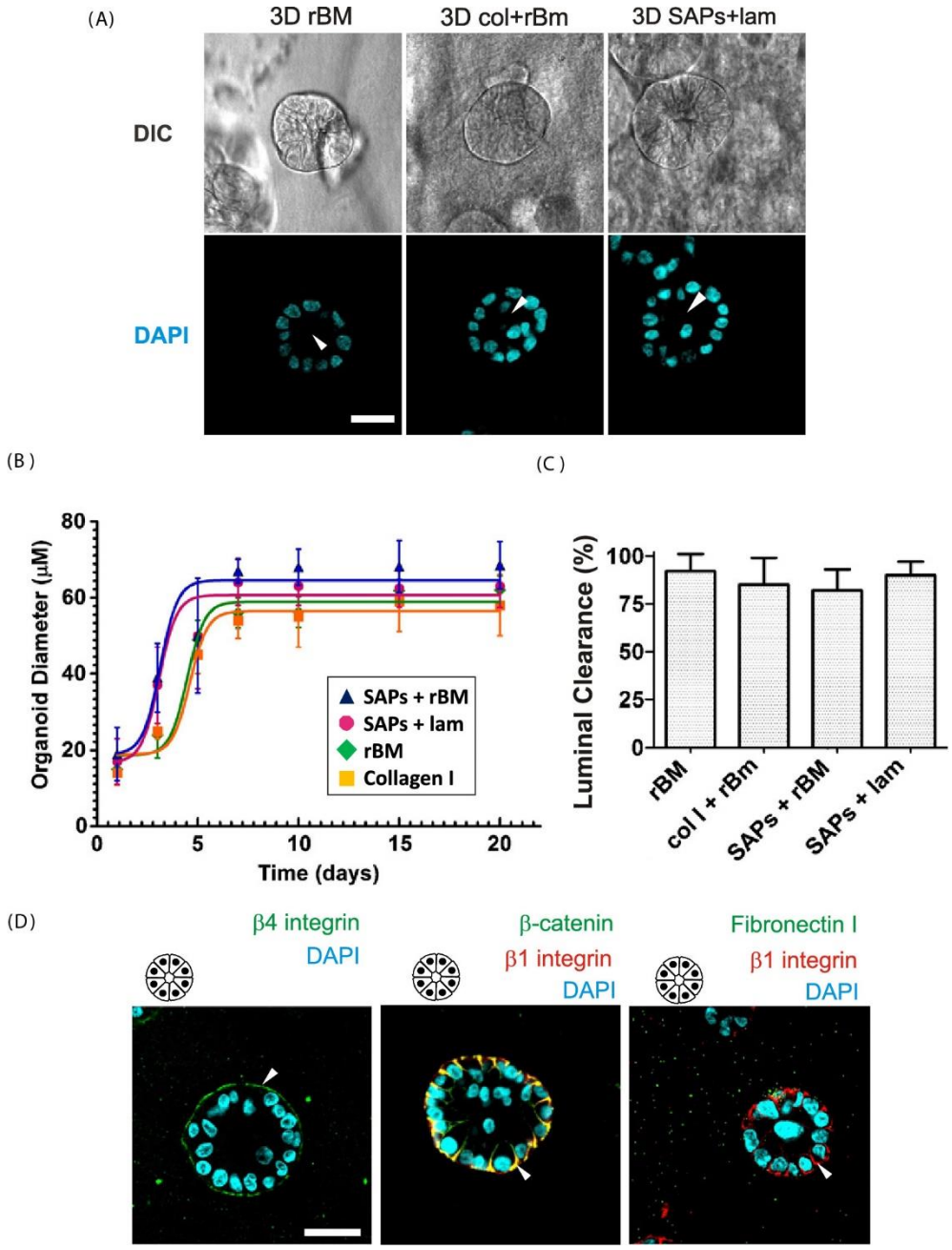

SAP Gels Figure 3. SAP gels support epithelial morphogenesis and direct apical–basal tissue polarity.

(A) (Top) phase contrast images of representative multi-cellular MEC acini following growth within reconstituted basement membrane (rBM, Matrigel), type I collagen gels mixed with 10% rBM, or SAPs containing 100 μg ml−1 laminin for 20 days. (Bottom) laser confocal immunofluorescence images of cryosections (10 μm) of multi-cellular MEC colonies stained with DAPI to reveal nuclei (blue) showing presence of cleared lumens in acini generated in

all gel conditions as described above. Bar equals 25 μm. (B) Line graphs showing growth curves for mammary colonies grown within rBM (green diamond), type 1 collagen gels mixed with 10% rBM (orange box) and SAPs supplemented either with laminin (red circle) or rBM (blue triangle). (C) Bar graphs showing quantification of cleared lumens in mammary acini grown in rBM, type 1 collagen gels mixed with 10% rBM and SAPs supplemented either with laminin or rBM (differences in the diameters were not statistically significant). (D) Laser confocal immunofluorescence images of cryosections (10 μm) of multi-cellular acini generated in SAPs supplemented with laminin stained with (left image) β4 integrin (green), (middle image) β-catenin (green) and β1 integrin (red) and (right image) fibronectin (green) and β1 integrin. All colonies were counter stained with DAPI (blue) to reveal nuclei. Bar equals 30 μm. Values shown in (B) and (C) represent mean ± SEM of multiple measurements from at least three independent experiments.

Modulating SAP Stiffness Perturbs Epithelial Morphogenesis, Disrupts Apical-Basal Tissue Polarity, and Induces Pro-tumor Gene Expression

I next asked whether increasing SAPs gel stiffness could perturb MEC morphogenesis and tissue integrity to induce a tumor-like phenotype. MECs were embedded within 1.2-3.2 mg/mL SAPs gels at concentrations that generated mechanical properties (Young's modulus) that recapitulated what the Weaver group had previously measured for normal and early stage breast tumor tissue, respectively[12] (Fig 2D). Similar to MECs within rBM gels, MEC colonies embedded within highly compliant laminin-supplemented SAPs assembled growth-arrested acini that showed negligible Ki-67 staining by day 10 of culture (Fig 4C and 4D). Mammary acini within soft SAPs also consistently cleared their lumens, likely through induction of apoptosis in the cells lacking contact with the protein-adsorbed SAPs gels, as revealed by elevated numbers of cells within the day 10-12 colony lumens with activated caspase 3 staining (Fig 4B). By contrast, MEC colonies embedded within rigid SAP gels continued to proliferate, as revealed by elevated Ki-67 staining throughout the colony (Fig 4D), showed negligible death of the cells within the

center of the colony, as revealed by reduced activated caspase 3 positive cells in the center of the colonies (Fig 4C), and consequently failed to clear their lumens (Fig 4A-B). The colonies assembled within the rigid SAPs also lacked apical-basal polarity, as revealed by highly diffuse β-catenin and β1 integrin (Fig 4E). Intriguingly, I noted that the MECs embedded within the stiff SAPs matrix also showed severely compromised colony integrity, as revealed by gross disorganization of the colony and individual MECs disseminating away from the colony and invading into the surrounding matrix (Fig 4E). These findings imply that matrix stiffness per se may in fact promote cell invasion given the appropriate matrix context and cell state. In this regard, by way of a plausible mechanism, I noted that SAP stiffness induced the expression of two genes implicated in tumor progression and invasion, fibronectin 1 and EGFR (Fig 4F), and additionally enhanced fibronectin 1 deposition by the MECs embedded within the gel (Fig 4E-F).

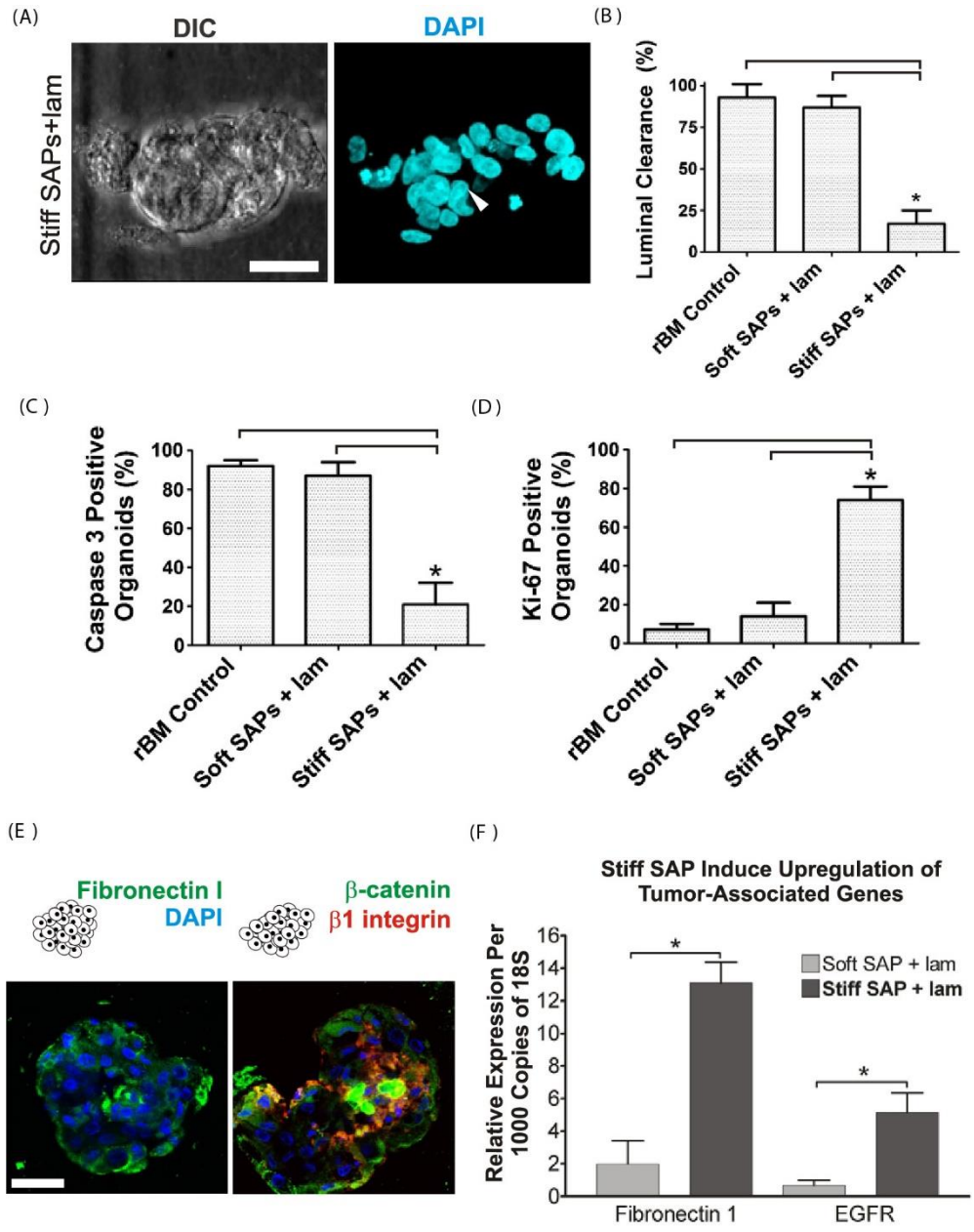

SAPs Gels Figure 4. Modulating SAP stiffness perturbs epithelial morphogenesis, disrupts apical–basal tissue polarity, and alters gene expression.

(*A*) (Left) phase contrast images of representative multi-cellular MEC acini following growth within rigid SAPs containing 100 μg ml^{-1} laminin for 20 days. (Right) laser confocal immunofluorescence image of a cryosection (10 μm) of a multi-cellular MEC colony, generated as described above, stained with DAPI to reveal nuclei (blue) showing absence of cleared lumen in colony generated in a rigid SAP. Note the arrow pointing to the cells migrating into the stiff SAP gel suggestive of invasive behavior. Bar equals 25 μm. (*B*) Bar graphs showing quantification of

cleared lumens in mammary acini grown in rBM as compared to MEC colonies assembled in the soft and stiff SAPs supplemented with laminin. Note the high percent of luminal clearance quantified in the acini assembled in either the rBM gels or the compliant SAP gels and a significant reduction of cleared lumens quantified in the colonies generated in the stiff SAP gels. (*C*) Bar graphs quantifying the number of caspase three positive lumens in colonies generated in rBM gels versus those assembled within compliant versus stiff SAP gels supplemented with laminin. Data indicate that SAP stiffness represses apoptosis in MECs. (*D*) Bar graphs quantifying the number of Ki67 positive colonies detected in rBM gels versus those assembled within compliant versus stiff SAP gels supplemented with laminin. Data show that SAP stiffness promotes MEC proliferation. (*E*) Laser confocal immunofluorescence showing representative image of cryosections (10 μm) of a multi-cellular MEC colony generated in a stiff SAP supplemented with laminin that was stained with (left) fibronectin (green) and (right) β-catenin (green) and β1 integrin (red) and counter stained with DAPI (blue) to reveal nuclei. Bar equals 30 μm. (*F*) Bar graphs showing the relative expression (by quantitative PCR) of fibronectin 1 and EGFR in acini isolated from soft and stiff laminin-supplemented SAP gels. Values shown in (*B*) and (*D*) and (*F*) represent mean with SEM of multiple measurements from at least three independent experiments.

Discussion

I exploited the unique properties of one SAP gel (PuraMatrix) to study the interplay between ECM stiffness and multi-cellular epithelial morphogenesis and transformation. SAPs gels provide a versatile model system with tunable mechanical properties and a native-like ECM fibril morphology. I was able to show that 3D laminin- or rBM- adsorbed compliant SAPs gels are able to recapitulate MEC morphogenesis and that a stiff SAPs gel disrupts tissue architecture, compromises tissue polarity and induces fibronectin and EGFR expression to promote an invasive, tumor-like phenotype without substantially altering ECM topology, pore size, and ligand density. Thus, I maintain that this matrix is a defined and tractable system that could be used to definitively study the effect of ECM tension on multi-cellular epithelial cell behavior in a 3D tissue-like context. The availability of such a versatile system could have profound clinical

implications by permitting the execution of experiments aimed at clarifying the biophysically-driven changes in tissue phenotype and molecular signature associated with tumor progression. One could imagine using this system for high throughput drug screening to identify novel therapeutics that would provide improved, personalized cancer therapeutics designed to not only target tumor cells but also to treat their phenotypic response to modifications in their surrounding ECM.

Unlike natural gels which exhibit striking changes in architecture, decreased pore size and altered ligand density as matrix stiffness is increased, SAP gels offer a tractable system with which to vary ECM stiffness over a dynamic range without significantly affecting any of these variables. In this regard, while other synthetic systems, including HA gels and PEG gels, have been adapted to study the effect of ECM rigidity on cell and tissue behavior these substrates fail to recapitulate the topology of natural matrices, cannot be remodeled without conjugation of collagenase digestible peptides, and often limit invasion due to minute pore size features (unpublished findings). Two major approaches for engineering in vitro systems with tunable mechanical properties have been the conjugation of cell-compatible adhesion peptides into synthetic matrices[58,87–89] or the application of biophysically-modified natural matrices (e.g. varying collagen gel concentration and/or cross-linking). Synthetic matrices allow for a robust control of ligand density as a function of stiffness however, they typically fail to recapitulate the appropriate topological cues programmed in the networks of natural materials. On the other hand, natural materials offer physiologically-relevant architectures, but introduce an array of confounding biophysical cues when concentration is varied or cross-linking status is changed (as means to vary stiffness). This includes profound effects on ligand density, fiber diameter, pore

size, and overall micro-architecture. These complicating variables are not insignificant in that cells are able to sense and respond to matrix topology and presentation[90–94]. For instance, tumors show elevated contractility and enhanced cross-talk with stromal fibroblasts in response to changes in matrix topology and this perturbed dialogue promotes tension-dependent remodeling and linearization of collagen fibers that promote an invasive tumor matrix that can foster metastasis[95,96]. Thus, due to a myriad of limitations endemic to current in vitro systems, the issue as to whether or not ECM compliance per se can modulate tissue morphology and transformation (as well as the identification of molecular mechanisms that drive these phenomena) remains unresolved. In this regard, the SAP system that I describe here has a multitude of positive features that might overcome many of these limitations, and while mechanical fragility remains one challenge when manipulating these gels, their net benefit at present far outweighs this minor experimental difficulty.

Prior studies using 3D collagen gels with increasing concentration and/or elevated collagen cross-links (and hence stiffness) indicate that ECM stiffness perturbs multi-cellular epithelial morphogenesis but fails to induce invasion unless combined with elevated growth factor or oncogenic signaling[12,14]. Such findings imply that ECM stiffness collaborates with oncogenes to drive tumor progression and argue that stiffness is a tumor promoter rather than initiator. I noted that elevating SAP stiffness was sufficient to drive epithelial invasion suggesting stiffness alone could promote cell invasion. One plausible explanation for why prior studies failed to demonstrate invasion causality through ECM stiffness is that stiffened collagen gels (mediated through elevated protein concentration or cross-linking) simultaneously decrease pore size and limit growth factor diffusion, thereby complicating data interpretation because these variables

would themselves impede and delay migration. Indeed, prior studies suggest that stiffer collagen or fibrin gels can in fact reduce the rate of cell migration and that migration within such gels relies critically on MMP-dependent matrix remodeling to permit tumor cell invasion[97–99]. Yet, ECM stiffness promotes invadopodia[3,99,100] and modulates integrin adhesion dynamics[34,72,101,102]. Furthermore, ECM rigidity enhances cell contractility to enhance cell motility and promotes invasion through ECM reorganization and alignment, suggesting ECM stiffness should promote and not impede invasion. These findings indicate that ECM stiffness could be both a tumor promoter and initiator; a possibility that now needs to be rigorously addressed. In this regard, SAP gels could prove instrumental in addressing this intriguing possibility.

In conclusion, tumor progression is associated with loss of tissue organization and disassembly of multi-cellular tissue structures. I observed that compliant laminin-supplemented SAPs gels are able to support MEC acini morphogenesis and that a stiff SAPs gel perturbs tissue polarity, destabilizes cell-cell adhesions and increases the expression of tumor promoting genes including fibronectin and the EGF receptor. These findings are consistent with the notion that ECM rigidity per se, in conjunction with appropriate architecture, could promote tumor progression through destabilization of tissue architecture; a findings that the Weaver group is currently applying to other investigations, such as understanding the effect of ECM stiffness on gene expression changes in epithelial cancers .

A 3D tension bioreactor platform to study the interplay between ECM stiffness and tumor phenotype

Given the profound effects of ECM structure, composition, and stiffness on tissue development and pathologies described in the above section we developed another 3D *in vitro* platform, a tension bioreactor system permitting precise mechanical tuning of collagen hydrogel stiffness, while maintaining consistent composition and pore size was developed and characterized (Fig. 1, [103]). This was achieved by mechanically loading collagen hydrogels covalently-conjugated to a polydimethylsiloxane (PDMS) membrane to induce hydrogel stiffening. Collaboratively with my colleague Luke Cassereau, we validated the biological application of this system with oncogenically transformed mammary epithelial cell organoids embedded in a 3D collagen I hydrogel, either uniformly stiffened or calibrated to create a gradient of ECM stiffening, to visually demonstrate the impact of ECM stiffening on transformation and tumor cell invasion[103]. As such, this bioreactor presents the first tunable 3D natural hydrogel system that is capable of independently assessing the role of ECM stiffness on tissue phenotype in a dynamic fashion.

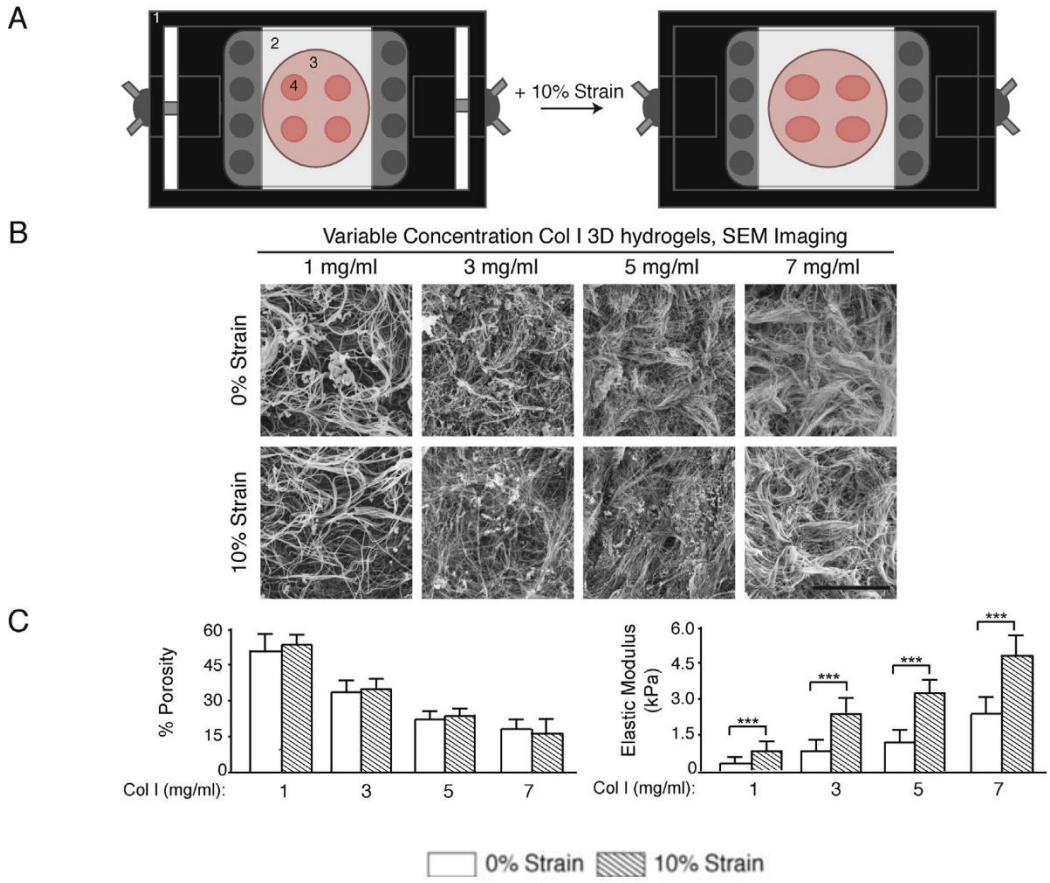

3D Tension Bioreactor Fig. 1. Characterization and biological application of tension bioreactor.

(A) Schematic of tension bioreactor system, consisting of (1) stretching frame, (2) PDMS stretchablemembrane, (3) media reservoir, (4) Col I hydrogels. (B) SEM images of Col I hydrogels of varying collagen concentration at 0 and 10% strain in the bioreactor system (scale bar = 2 μm). (C) Quantification of gel pore size and elastic modulus as a function of Col I concentration and the application of uniaxial strain (error bars represent standarddeviation, *** denotes $p < 0.05$ evaluated by t-test).

In vitro 3D Brain Compression Bioreactor System

Motivation: High interstitial fluid pressure (IFP) represents a major obstacle in solid cancers and a barrier for drug uptake[104]. Solid tumors are associated with increases in IFP due to vascular

leakiness and drainage resistance due to increased cell density, and stromal cell mediated synthesis and contraction of the interstitial matrix[104]. Such altered mechanical environment compresses tumor and surrounding normal tissue and promotes osmotic swelling of tumor cells. Although studies have clarified the role of tumor vasculature, it is still unclear how osmotic changes and mechanical stresses regulate tumor cell biology. To study if elevated compressive pressure regulates tumor biology I optimized a highly controlled *in vitro* bioreactor system (Fig 1 and 2) with which I could interrogate whether compressive forces can reprogram tumor cells towards a more aggressive behavior. Indeed, using this system I was able to show that compression induces tumor cell proliferation and activation of mechanically-active signaling cascades *in vitro* (Fig 3) which supports and validates the *in vivo* findings of our collaborator, Dr. Persson, indicating that IFP promotes tumor growth in xenograft mouse models of GBM (Fig 4). In addition, based on previous work by Dr. Anders Persson, we employed antisecretory factor (AF), an endogenous peptide known for its antisecretory properties and safe use in patients, to reduce IFP in xenografted human GBM. A specially produced (SPC) diet induces endogenous production of AF in animals and humans, reduced intracranial pressure in rodents, and lowered IFP in subcutaneous solid tumor models[105–107].We therefore have utilized this agent to reduce pressure and survey the effects on tumor cell biology *in vitro* and *in vivo* (Fig 3-4). We have confirmed reversion of tumor cell proliferation *in vitro* using the compressive bioreactor system (Fig 3b) and Dr. Anders Persson demonstrated that SPC diet induced AF levels in tumor tissue, lowering IFP in tumors and prolonging survival (Fig 4A-B). Intranasal delivery or SPC diet inhibited proliferation and induced apoptosis in tumor cells, data confirmed by MR imaging **(**Fig 4C-D). Importantly, SPC diet or intranasal delivery of AF induced uptake of doxorubicin, as well as other therapeutics, in tumors, confirming elevated IFP as a barrier for drug uptake

(data not shown). Further, microarray analysis of GBM neurospheres compressed using the developed bioreactor system with either physiological (0 mmHg) or pathological (50mmHg) pressure revealed substantial and profound shifts in the gene expression of micro RNA processing machineries with increased pressure and this phenomenon was completely normalized and reversed by AF treatment *in vitro* (data not shown); a findings that the Weaver and Persson groups will carry forward and interrogate further.

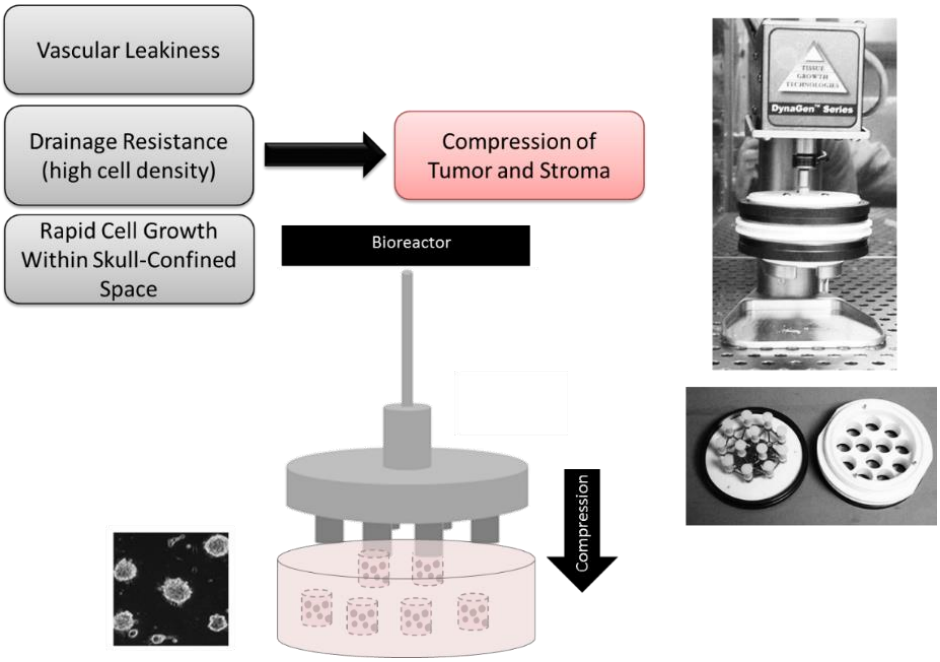

Compression Bioreactor Figure 1. In vitro compression model system

Bioreactor model system (right) utilized to recapitulate increased intracranial pressure observed in patients with glioblastoma multiforme (GBM), the most common and deadly form of adult brain cancer, due to buildup of fluids from vascular leakiness, peritumoral edema, and rapid cellular growth. Primary patient GBM cells were allowed to form neurospheres (bottom left), embedded into hyaluronic acid gels and compressed for 48 hours prior to sample isolation for RNA, DNA, protein, microarray, and immunohistochemical analyses. 65 KDa methacrylated HA with 30% methacrylation (generous gift by Dr. Jason Burdick) was photocrosslinked (365nm UV light; 1 inch away from

the surface of neurosphere-seeded constructs; 10 minutes) with 0.05% irgacure2959 photoinitiator to generate hyaluronic acid gels of approximately 3,000 Pa.

The long-term goal of these collaborative tool development efforts is to understand the biological impact of IFP-driven compressive forces on cancer aggression. In particular, our data will dissect how IFP components regulate tumor growth and drug uptake in human GBM. Importantly, Dr. Anders Persson is currently working with UCSF clinicians to introduce AF-induction as a novel therapy against solid cancers in children and adults. We believe that our work will fundamentally change how we view mechanical forces as potential therapeutic targets in disease.

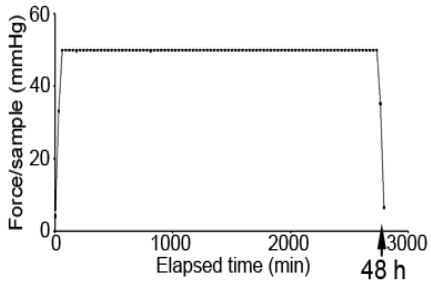

Compression Bioreactor Figure 2. Compression force profile

Typical force profile set to ramp from 0 to 50 mmHg rate at a rate of 0.005 N/sec and hold 50mm Hg for 48 hours.

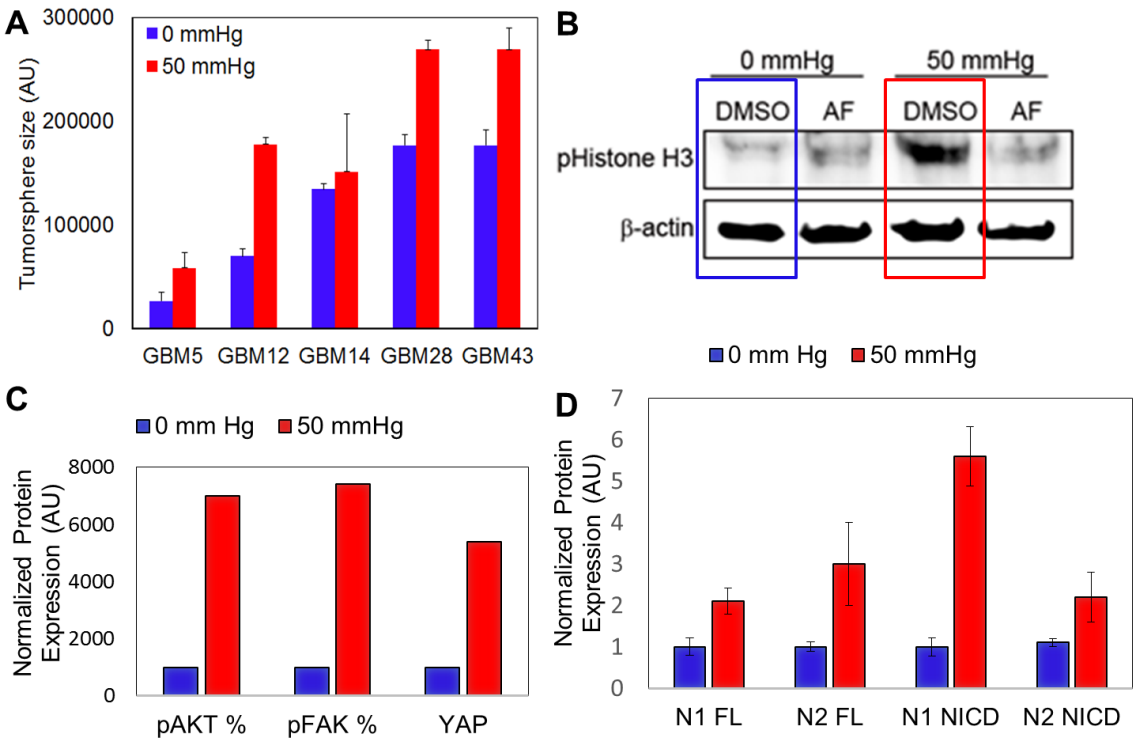

Compression Bioreactor Figure 3. Elevated pressure promotes tumor cell expansion and mechanosignaling.

Human primary GBM cell neurospheres were embedded a 3D hyaluronic acid matrix and were placed in a compression bioreactor for 48 hours either at 0 (blue) or 50(red) mmHg. Compression promoted tumor sphere expansion (A), proliferation (B) which was reverted with a treatment of pressure-reducing antisecretory factor (AF). Further compression resulted in elevation of mechanosignaling (C) and upregulation of mechano-sensitive notch pathway (D).

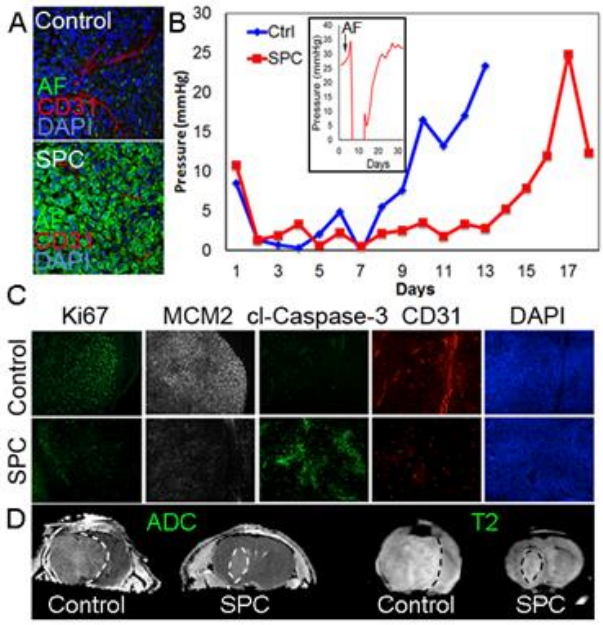

Compression Bioreactor Figure 4. Antisecretory factor reduces IFP and tumor growth in xenografted GBMs in vivo

SPC diet induces (A) expression of AF in tumors that (B) retain low IFP and extend survival in mice. Nasal delivery of AF16 peptide reduced IFP in tumors. (C) SPC diet resulted in reduced tumor proliferation, massive apoptosis, and caused vascular remodeling in GBMs. *Figure kindly provided by Dr. Anders Persson.

In vitro 3D Bead Invasion Assay

As was discussed previously, one of the many cellular facets that are highly sensitive to the biochemical and biophysical cues from the ECM is invasion. In order to be able to accurately quantify cellular speed and persistence in addition to assaying the effect environmental factors on 3D invasion of GBM cells, I established a 3D bead invasion assay (Fig. 1A) in which GBM cells are allowed to incubate with glass microbeads (sorted by size exclusion to be between 100-125 μm) at a density of 500 cells/bead for 8 hours at 37 degrees centigrade with occasional shaking, embedded into a 3D HA gels (described in previous section and supplemented with

10% matrigel for invasion studies), and then subjected either to live cell microscopy or fixed at desired timepoints for analysis.

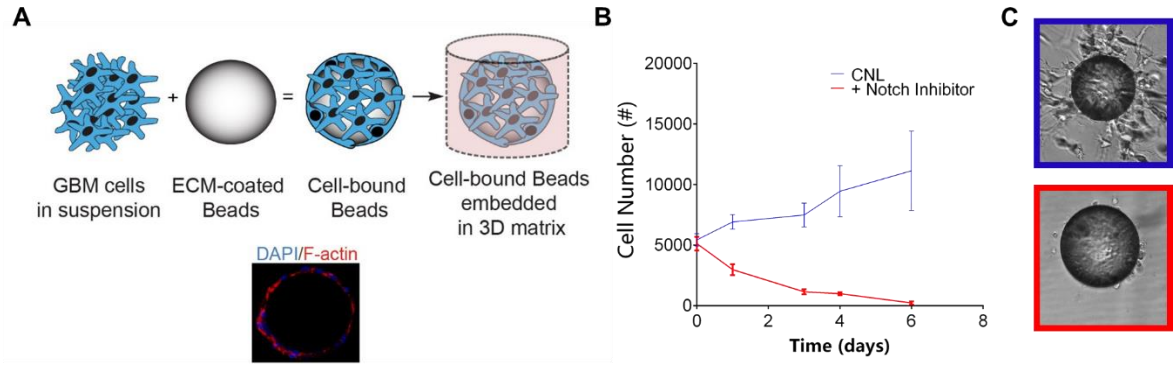

3D Bead Invasion Figure 1. Established 3D bead invasion assay and its validation using Notch inhibition

A) Schematic of the *in vitro* invasion assay setup for the studies. Non-specific notch inhibition with 5μM γ-secretase or 5μM *all trans* retinoic acid (ATRA; red) compromises primary GBM cell survival (B) and invasiveness (C). Cell number and viability for (B) were assessed using Guava PCA/Viacount reagents according to manufacturer's instruction (Millipore) – all experiments were performed in triplicates. Invasion studies in C) were setup using procedure demonstrated in (A) with equal numbers of control GBM cells adhering to beads as those surviving 48-hr pretreatment. Invasion studies were imaged with time-lapse microscopy and radial extension of cell processes from the beads was quantified with ImageJ software

Biological utility of the established 3D bead invasion system was first established by validating the previously described effect of γ-secretase and ATRA, both nonspecific inhibitors of notch signaling which is critical for GBM invasion[108,109] (Fig. 1B-C) as well as confirming the established role of ECM stiffness in promoting early stage tumor cell invasion (Fig. 2).

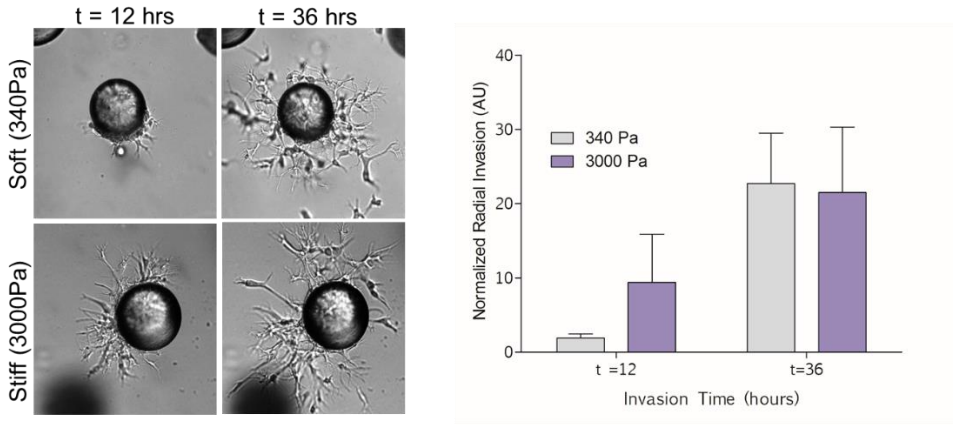

3D Bead Invasion Figure 2. Stiffness induces early-time invasion in primary human GBM cells

A) Bright field images of GBM cell-coated bead embedded either in soft (340Pa – normal-like brain ECM stiffness) or stiff (3000 Pa – GBM ECM stiffness) HA gels (polymerized as described in previous section and supplemented with 10% matrigel to facilitate matrix remodeling) and imaged at either 12 or 36 hours. B) Quantification of the extent of radial invasion (quantified in imageJ).

CHAPTER 3: BREAST CANCER STUDIES

Ligation of α5β1 integrin by the fibronectin synergy site is necessary and sufficient for tension-dependent malignant transformation

Summary. Tissue fibrosis and stiffening via increased collagen deposition and crosslinking promotes malignant transformation and metastasis. Yet, α2β1 integrin, the major collagen receptor in mammary cells, is tumor-suppressive. Fibronectin and its receptor α5β1 integrin, on the other hand, are frequently elevated in tumors, particularly within the collagen-rich invasive front, which is especially enriched for rigid collagen fibers. Our studies, employing mechanically tunable polyacrylamide gels, a 3D tension bioreactor, and transgenic and xenograft murine tumor models, revealed that fibronectin-α5β1 integrin binding is necessary and sufficient for collagen-mediated, stiffness-driven malignant transformation. Using Forster resonance energy transfer (FRET) microscopy, traction force microscopy, and a hydrodynamic cell adhesion strength assay, we observed that α5β1 ligation of the RGD and synergy binding sites of fibronectin is required to elevate cytoskeletal tension and induce the focal adhesion signaling necessary for perturbing tissue integrity and driving tumor cell invasion and persistent migration. Live optical tracking and gain of function/loss of function studies permitted us to causally link a stiffened fibronectin extracellular matrix (ECM) with activation of growth factor receptor signaling and YAP-dependent mechanosignaling and through these pathways, enhanced cell growth, invasion, and angiogenesis. Our findings thereby identify a molecular mechanism by which collagen-mediated ECM stiffening drives malignant progression of a tissue through engagement of α5β1 integrin via fibronectin bound to a cross-linked collagen network. We observed that collagen-

dependent ECM tension is transduced to tumor cells via force-dependent unfolding of fibronectin, which reveals the cryptic synergy binding site. The combined ligation of the fibronectin synergy site with the RGD site in turn induces mechano- and growth factor signaling to drive tumor cell invasion and promote malignancy. Our data thereby explain how a rigid collagen-rich ECM is able to induce malignant transformation and why α5β1 integrin and fibronectin are so consistently up-regulated in tumors and correlate so strongly with tumor aggression.

Introduction

Tumors are highly fibrotic [110–113]. Fibrotic tumors contain abundant quantities of extracellular matrix (ECM) proteins, such as type I collagen, fibronectin (FN), tenascin (TN), and assorted proteoglycans, and cancerous tissues typically exhibit altered levels and activities of ECM receptors like integrins [114–116]. Elevated β1 integrin expression and FAK activity correlate positively with high tumor grade and predict for poor patient prognosis [117]. Moreover, inhibiting β1 integrin ligand binding represses the malignant phenotype of tumor cells *in vitro* and *in vivo*, and transgenic ablation of β1 integrin or focal adhesion kinase (FAK) prevent oncogene-induced malignant transformation and metastasis [118,119]. These findings emphasize the importance of interplay between tissue fibrosis and integrin signaling in malignancy.

Tumors are mechanically corrupted and exhibit high interstitial pressure, elevated compression, extracellular matrix (ECM) stiffening, and increased cellular tension [12,20,71,113,120]. Tumors that are highly fibrotic are especially rigid and stiff tumors are associated with increased aggression and high mortality [121–123]. Consistently, elevating cell tension or stiffening the ECM via increased

deposition and crosslinking of ECM components like collagen promotes the malignant transformation of a tissue [12,20]. Conversely, reducing cell tension, interstitial pressure, or preventing matrix stiffening decreases tumor incidence and aggression and improves treatment efficacy [12,20,113]. Cell tension and ECM stiffness promote focal adhesion assembly, and integrin signaling is necessary for force-dependent malignant transformation [12,20,113]. Thus, tissue tension promotes tumor progression via integrin signaling. Nevertheless, the relationship between the high force environment of a tumor and selective expression of specific integrins and their ECM ligands has yet to be determined. Indeed, while deposition and crosslinking of collagen promotes ECM stiffening and tumor progression, its major receptor, α2β1 integrin, is tumor-suppressive rather than tumor promoting [124].

Fibronectin (FN) levels are frequently elevated at both the primary and metastatic tumor site and aggressive tumors express abundant FN [116,125–127]. Moreover, the major FN receptor, α5β1 integrin, is associated with increased tumor aggression and progression [116]. FN is assembled with type I collagen and cross-linked collagen increases FN unfolding to reveal cryptic binding sites for α5β1 integrin ligation. Indeed, on the ability of α5β1 to simultaneously engage both the RGD and synergy sites of FN may be a potential mechanism by which the tumor cells are able to sense and respond to the mechanical properties of their microenvironment. Such mechanosensing would be reinforced by the force-sensitive, FN-mediated FAK activation, which would in turn amplify tumor cell growth, survival and migration [128,129]. Indeed, cells with FN-bound α5β1 integrin exert higher forces on the surrounding ECM and cells with more FN-bound α5β1 exhibit an altered migratory behavior [130]. Further, ECM stiffness increases the expression of α5 integrin and FN, and the accessibility of the synergy site of FN is enhanced in a cross-linked,

stiffened ECM [131–134]. These findings are in accordance with data showing that FN and its integrin receptor, α5β1 integrin, are frequently up-regulated in primary and metastatic tumors, which are stiffer than normal tissue [116,135,136]. They are also consistent with evidence indicating that high expression of α5 integrin and FN and elevated tissue tension independently correlate with poor patient prognosis [6,20,116,135–138]. Here, we tested the idea that the stiffening of the tumor ECM, which has long been characterized by increased collagen deposition, is mediated via the selective up-regulation of FN and α5β1 integrin levels and activity. We explored the possibility that the ability of ECM stiffness to drive tumor cell invasion and cancer progression strictly depends upon tension-mediated exposure of FN-bound α5β1 integrin, engagement of tumor cell mechanosignaling, and activation of key growth, survival and angiogenic signaling.

Results

Mammary malignancy is associated with increased expression of integrins that ligate fibronectin

Malignant transformation in mammary tissue is associated with altered expression of integrins and ECM proteins, ECM stiffening, and elevated cell tension, all of which have been shown to promote tumor progression [12,13,115,132,139]. Here, we examined which integrins are functionally linked to force-dependent malignant transformation.

Consistent with previous studies functionally implicating a multitude of integrins in tumor progression, Second Harmonic Generation (SHG) and immunofluorescence analysis indicated increased fibronectin (green) deposition along collagen tracks (indicated in gray) in the invading fronts (sparse PI staining indicating cell strands protruding from tumor border) of

highly stiffened, late stage PyMT tumors (Figure 1A). Indeed, the collagen network is the main ECM component that undergoes remodeling and altered crosslinking, leading to elevated extracellular matrix stiffness in tumors. Paradoxically, α2β1 integrin, the main collagen receptor in mammary cells, is thought to be tumor suppressive, while the fibronectin receptor, α5β1 integrin, is highly upregulated in aggressive and metastatic tumors [20,124,140,141]. These findings intrigued us to investigate whether collagen-mediated ECM-stiffening promotes fibronectin secretion at stiff ECM sites, where it then engages α5β1 integrin in a tension-dependent manner. This would provide a rationale for selective expression of α5β1 integrin in the context of a stiffened ECM of a tumor. To determine whether tissue stiffness, malignant transformation, and α5β1 integrin expression are linked, we examined tissue harvested from a cohort of Her2/Neu and PyMT mice treated with and without either a function blocking antibody or a pharmacological inhibitor of lysyl oxidase (Lox) that prevents collagen cross-linking and ECM stiffening [20,71]. Confocal immunofluorescence imaging of mammary tumor tissue from these mice revealed strong ^{p397}FAK and elevated ^{p}MLC in the epithelium of the non-treated invasive Her2/Neu (Figure 1B) and PyMT (not shown) tumors, and low to non-detectable levels in tissue from mice that had been treated with Lox inhibitor (Figure 1B). Coincident with the elevated focal adhesion signaling and high cytoskeletal tension detected in untreated mammary tumors, we also observed a significant increase in FN deposition in these tissues and robust reduction in the Lox inhibited tissue (Figure 1B). We additionally observed high levels of α5, α2 integrin and αv integrin in the invasive tumors and determined that their expression appeared lower when ECM stiffening and tumor tension were inhibited, whereas no differences in levels of α2 integrin were detectable (Figure 1B). These findings established a positive and specific association

between collagen-mediated FN deposition, the expression of its integrin receptors α5β1 and αvβ3, and tissue tension and mammary malignancy *in vivo*.

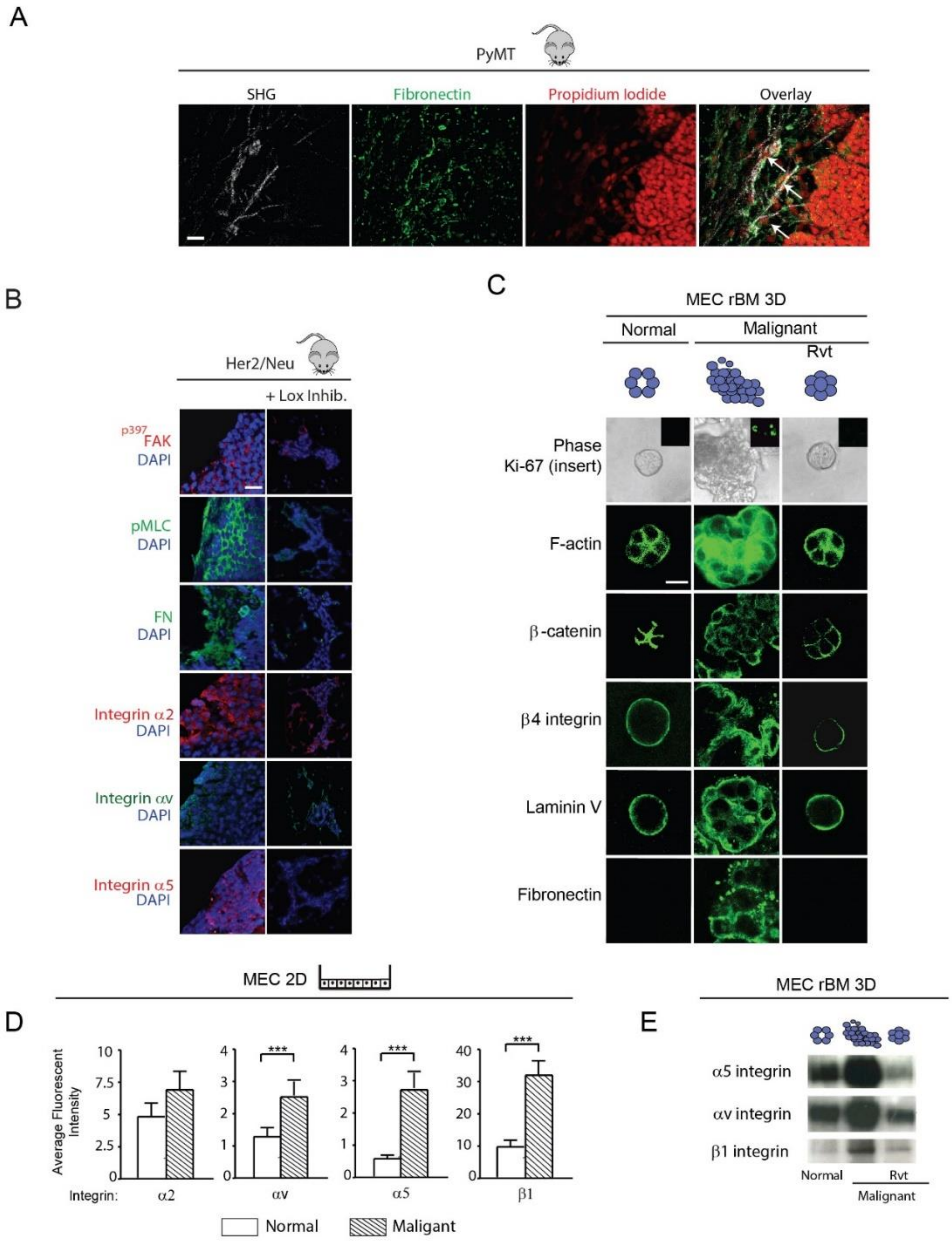

Breast Cancer Figure 1. Mammary malignancy is associated with increased expression of fibronectin-binding integrins.

A) Second Harmonic Generation (SHG) images of collagen (grey), fibronectin (green), and nuclei (red) in the 7 month old PyMT tumors at the invasive front. Scale Bar 20μm. Arrows indicate cells migrating along FN-coated

collagen fibers. B) Confocal immunofluorescence images of mammary tissue stained for ^{p}MLC, ^{p397}FAK, fibronectin (FN) and α5β1 integrin, α2 integrin and αv integrin in tissue excised from 7 month old control (Her2/Neu) or lysyl oxidase inhibitor treated (Lox inhibitor) Her2/Neu transgenic mice. Scale Bar 10μm C) Phase contrast and confocal immunofluorescence images of Ki-67 (insert), Phalloidin (F-actin), β-catenin, β4 integrin, laminin-5, and fibronectin stained colonies of nonmalignant (S-1), malignant (T4-2) and phenotypically-reverted (T4 Rvt) HMT-3522 human mammary epithelial cells (MECs) grown within a reconstituted basement membrane (rBM) for two weeks. Scale Bar 10 μm. C) Bar graphs of FACS analysis of membrane localized integrins in S-1 compared to T4-2 MECs. E) Representative immunoblot image of α5, αv and β1 integrin in lysates from S-1, T4-2 and T4 Rvt 3D rBM colonies shown in D. (n>50 acini). Results are the mean ± S.E.M. of 3 separate experiments (*p<0.05; **p<0.01;***p< 0.001).

To explore the impact of tissue tension, FN, and its integrin receptors α5β1 and αvβ3 on breast malignancy, we used the nonmalignant S1 and malignant T4-2 mammary epithelial cells (MECs) from the HMT3522 human breast cancer progression series [142]. The T4-2 MECs from this series exert significantly more traction force than their nonmalignant counterparts [12]. Moreover, as shown previously, upon embedment into a reconstituted basement membrane (rBM), the low force-exerting S1 MECs from this series formed polarized, growth-arrested acini-like structures demonstrated by lack of Ki-67 nuclear staining, robust β-catenin localization to cell-cell junctions, apical-lateral actin, basally localized β4 integrin, and basally deposited laminin V. By contrast, the highly contractile, malignant T4-2 derivative MECs formed continuously growing, disorganized, and invasive colonies, as illustrated by elevated nuclear Ki-67 and disrupted localization of β-catenin, α6β4 integrin, and laminin V. However, inhibition of β1 integrin, using a ligand function-blocking antibody, reverted the malignant phenotype of the contractile T4-2 colonies towards that of a growth-arrested, noninvasive, and more differentiated structure indicated by absence of detectable nuclear Ki-67, restoration of cell-cell

localized β-catenin, apical-lateral actin, and basally localized α6β4 integrin and laminin V [12,13] (Figure 1C). Consistent with an association between tumor tension and ligation of the FN integrins α5β1 and αvβ3 and malignancy, FACS analysis revealed that the highly contractile T4-2 tumor cells expressed high levels of αv, α5, and β1 but not α2 (Figure 1D) or β3, β5, β6, α1, α3 or α6 integrin at their surface (not shown). Further, immunoblot analysis showed that following phenotypic reversion via blocking β1 integrin, both α5 integrin and αv integrin levels were substantially reduced (Figure 1E). Moreover, immunostaining revealed that while the T4-2 MECs deposited abundant FN, expression of this ECM protein was lost in the reverted structures (Figure 1C). These findings establish an association between tissue tension, expression of FN and its integrin receptors α5β1 and αvβ3, and mammary malignancy.

FN-ligated α5β1 integrin is necessary and sufficient for expression of the malignant phenotype *in vitro* and *in vivo*

To directly explore the functional relationship among FN and its integrin receptors α5β1 and αvβ3, and mammary tissue transformation, we treated 3D rBM cultures of T4-2 mammary epithelial cells, which secrete copious amounts of FN (Figure 1C), with α5 or αv function-blocking antibodies and compared effects of the function blocking to malignant MECs treated with α2, α3, and β1 function blocking antibodies. Data revealed that although blocking ligand binding to α2 (Figure 2A), αv, or α3 integrin (not shown) had little to no effect on the behavior of the T4-2 MECs, inhibiting α5 integrin repressed their malignant phenotype, similar to that observed following inhibition of β1 integrin ligand binding (Figure 2A; 1C). Thus, while T4-2 MECs treated with either IgG isotype matched control, α2 or αv function blocking antibodies in

forming continuously growing, large, disorganized and invasive colonies in rBM, as indicated by aberrantly localized α6 integrin, β-catenin and actin, the tumor cells pre-treated with function blocking antibodies against α5 or β1 integrin assembled growth arrested, polarized structures reminiscent of differentiated mammary acini (Figure 2A) that were at least 60-70 percent smaller than the non-treated colonies (Figure 2B). Moreover, preventing α5 or β1 integrin ligand binding in the T4-2 tumor cells significantly impaired anchorage independent growth and survival in soft agar (Figure 2C). These data indicate that FN-ligated α5β1 integrin is necessary for expression of the malignant phenotype in cultured human mammary epithelial tissue-like structures.

We next determined whether FN-ligated α5β1 integrin was sufficient to promote mammary malignancy. We expressed a tetracycline (tet)-regulated eGFP-tagged α5 or α2 integrin in nonmalignant S1 MECs (which express negligible α5 integrin) and assayed their response to FN. Immunoblot and fluorescence-activated cell sorting (FACS) analysis confirmed a tet-modulated increase in α5 and α2 integrin (data not shown) and showed that neither ectopic expression of α5 nor α2 integrin significantly altered the cell surface expression of any of the other integrin receptors in HMT-3522 S1 MECs (not shown). Moreover, 10-14 days following their embedment within a three dimensional (3D) rBM, nonmalignant S1 MECs expressing either elevated cell surface α2 or α5 integrin assembled growth-arrested (Figure 2E-F), polarized mammary acini with cleared lumens, as indicated by cell-cell localized β-catenin, basally-localized α6β4 integrin, and basally deposited collagen IV (Figure 2D). However, following FN engagement, the S1 MECs expressing high α5 integrin not only continued growing (Figure 2E), but also failed to clear their lumens, showed diffuse cell-cell localized β-catenin and lacked basal

polarity (Figure 2D). Indeed, in the presence of exogenous FN, nonmalignant S1 MECs expressing elevated α5 integrin formed mammary colonies that were 30-40 percent larger than S1 MECs expressing elevated α2 integrin, despite the availability of abundant collagen (Figure 2E). These findings demonstrate that FN-ligated α5β1 integrin is both necessary and sufficient for expression of the malignant phenotype of MECs *in vitro.*

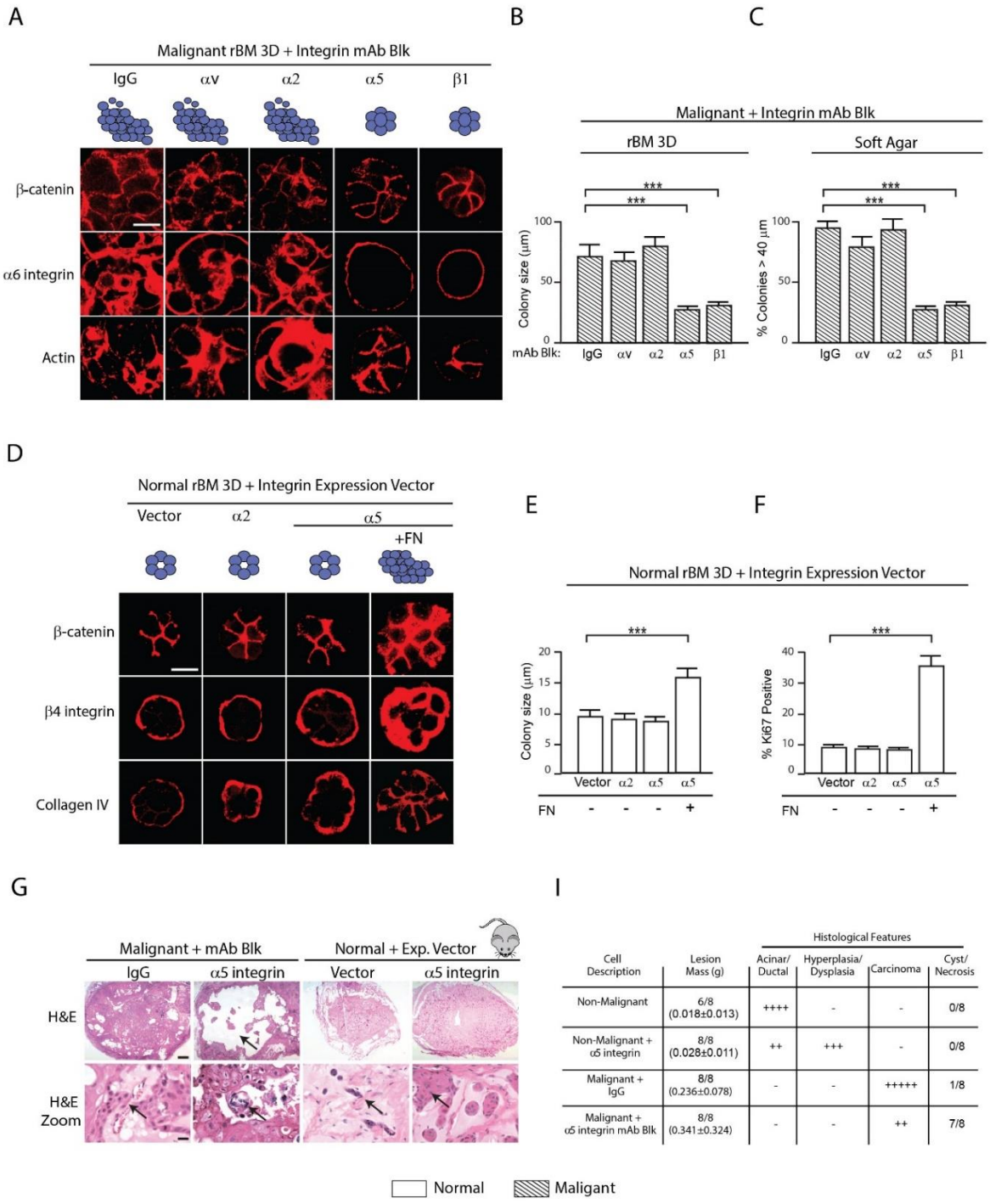

Breast Cancer Figure 2. Fibronectin-ligated α5β1 integrin is necessary and sufficient for expression of the malignant mammary epithelial cell phenotype *in vitro* and *in vivo*

A) Confocal immunofluorescence images of β-catenin, α6 integrin and actin (Phalloidin) staining of malignant (T4-2) MEC colonies grown for two weeks in rBM in the presence of a function-blocking antibody (mAb) to αv, α2,

α5 or β1 or an IgG isotype matched control mAb. Scale Bar 30 μm. **B)** Bar graph showing relative size of the T4-2 colonies shown in A. **C)** Bar graph showing percentage of tumor colonies formed in soft agar (40+ microns) following treatment with function-blocking mAbs to αv, α2, α5 or β1 integrin or an IgG isotype matched control mAbs. **D)** Confocal immunofluorescence images of β-catenin, β4 integrin and collagen IV staining of colonies of nonmalignant (S-1) vector (Ctrl) MECs and MECs expressing elevated α2 or α5 integrin grown in rBM with or without the addition of fibronectin (+FN) for two weeks. Scale Bar 10 μm. **E)** Bar graph showing relative size of S-1 MEC colonies shown in D. **F)** Bar graph showing percent Ki-67 positive S-1 MEC colonies shown in D. **G)** Phase contrast images of low (top panel) and high (second panel) magnification of H & E sections of tissue excised two months following injection of malignant T4-2 MECs with IgG or a function blocking antibody to α5 integrin and nonmalignant S-1 MECs expressing empty vector or an α5 integrin. Scale Bar 10 μm. **I)** Table summarizing tumor score and histological features. Scale Bar 10 μm. (*$p<0.05$; **$p<0.01$; ***$p< 0.001$).

To further implicate FN-ligation of α5β1 integrin in mammary malignancy, we manipulated α5 integrin expression and/or function in nonmalignant and malignant MECs and assayed for effects on tumorigenesis *in vivo*. We inoculated nonmalignant S1 MECs expressing eGFP (nonmalignant control) or high levels of α5 integrin (+ α5 integrin), as well as T4-2 tumorigenic MECs that had been treated with either an α5 integrin function blocking monoclonal antibody (α5 integrin inhibited) or an isotype IgG control antibody (tumor control), into the rear flanks of Balb/c nu/nu mice. Two months following MEC inoculation, the control tumors had formed large, actively growing, invasive, and highly angiogenic tumor masses, as indicated by elevated PCNA, negligible activated caspase 3, a clearly visible vasculature (confirmed by strong CD34 tissue staining), and histopathological analysis that showed invasive cell masses (Figures 2G-I, Supplemental Figure 1C-D). However, T4-2 cells treated with the α5 integrin function blocking antibody formed only small, non-proliferating tumor colonies that stained positively for the apoptosis marker activated caspase 3, lacked a vasculature, had no CD34 staining, and

showed histopathological evidence of cystic degeneration and necrosis (Figure 2G-I, Supplemental Figure 1C-D). As expected, the majority of the nonmalignant S1 MECs failed to survive, and those that did formed ductal-like differentiated tissue structures. By contrast, those S1 MECs expressing high levels of α5 integrin not only survived but grew to form hyperplastic/dysplastic cell masses that activated an angiogenic response, as indicated by a visible vasculature and positive CD34 tissue staining (Figure 2G-I, Supplemental Figure 1C-D). Indeed, a 3D *in vitro* co-culture angiogenesis assay (Supplemental Figure 1A) revealed that blocking α5 or β1 integrin binding activity in the T4-2 malignant MECs prevented endothelial network formation and showed that nonmalignant MECs expressing elevated FN-ligated α5 integrin, but not collagen-ligated α2 integrin, induced endothelial networks. Consistently, the FN-ligated α5β1 integrin MECs expressed abundant VEGF and inhibiting α5 or β1 integrin in the T4-2 malignant MECs reduced VEGF levels (Supplemental Figure 1B). These findings indicate that FN-ligated α5β1 integrin is both necessary and sufficient for expression of the malignant phenotype of MECs *in vitro* and *in vivo*.

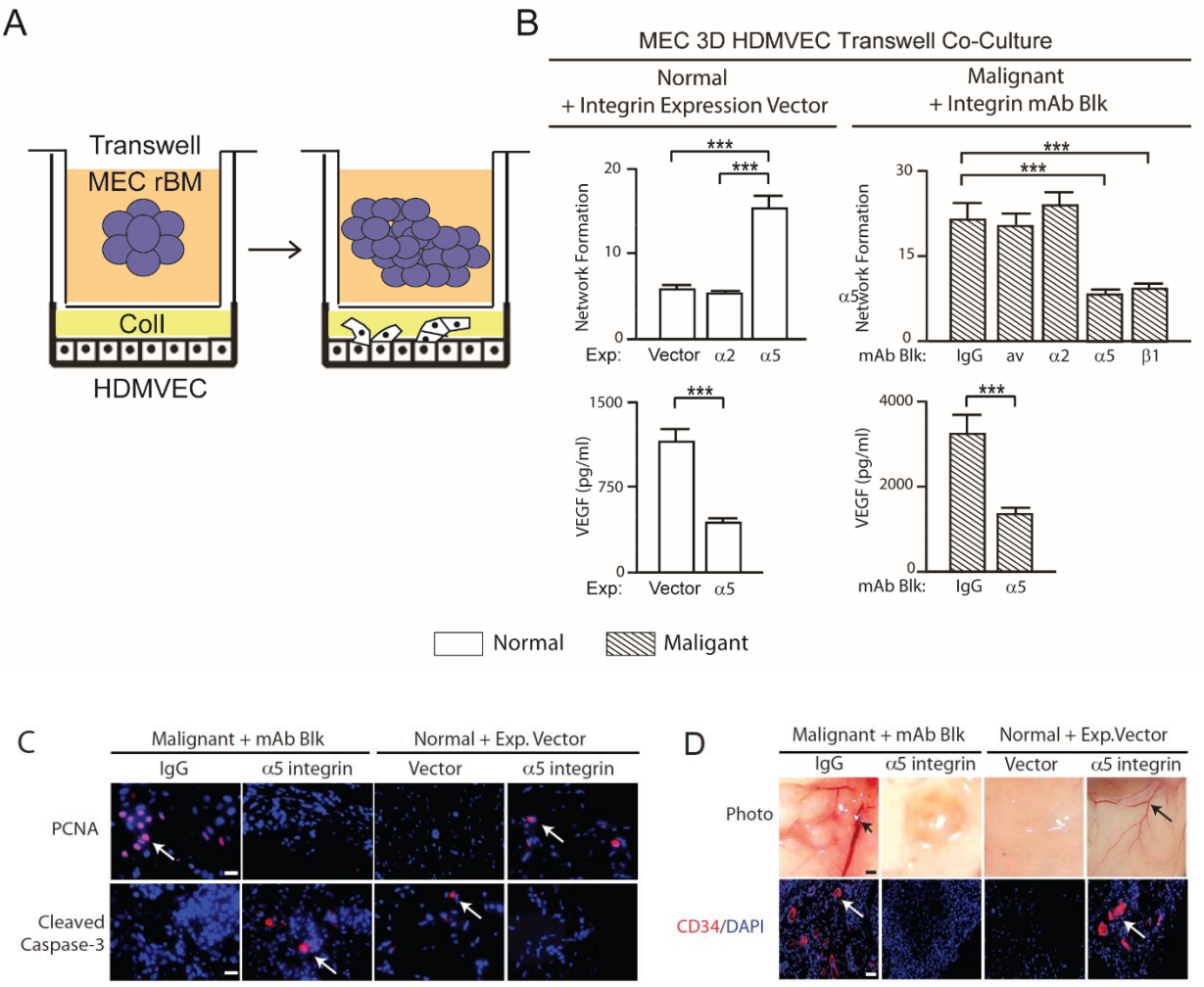

Breast Cancer Figure S1. Figure S1. α5β1 integrin expression promotes angiogenesis and VEGF secretion in vitro and in vivo.

A) Schematic of an *in vitro* endothelial network formation model system by human dermal microvascular endothelial cells (HDMVECs) co-cultured with MECs. B) *In vitro* network formation of HDMVECs is (top left) greatly increased in a co-culture setting with non-malignant MECs over-expressing α5 integrin and is (top right) highly reduced when either β1 or α5 integrins are functionally-blocked in the malignant MECs, but not α2 or αv; (bottom left) nonmalignant MECs overexpressing α5 integrin secrete higher levels of VEGF and (bottom right) function-blocking of α5 integrin in malignant MECs reduces their VEGF. **C)** Immunofluorescence images of xenograft mouse tissues stained for PCNA (top) and activated caspase 3 (lower). Scale Bar 10 μm. **D)** (upper panel) Photomicrographs of vasculature in tissue from injected malignant T4-2 MECs with and without α5 integrin

inhibition and nonmalignant S-1 MECs expressing empty vector or elevated α5 integrin. Scale Bar 10 mm. (lower panel) Immunofluorescence images of xenograft mouse tissue stained for the endothelial marker CD34. Results are the mean ± S.E.M. of 3 separate experiments (***p< 0.001).

Fibronectin-ligated α5β1 integrin increases cell tension to promote mammary malignancy

To directly test if FN-ligation of α5β1 integrin could promote mammary malignancy by increasing cell tension, we treated 3D collagen-FN cultures of MCF10A MECs expressing either elevated α5 or α2 integrin with either a ROCK inhibitor (Figure 3A) or myosin inhibitor (not shown).

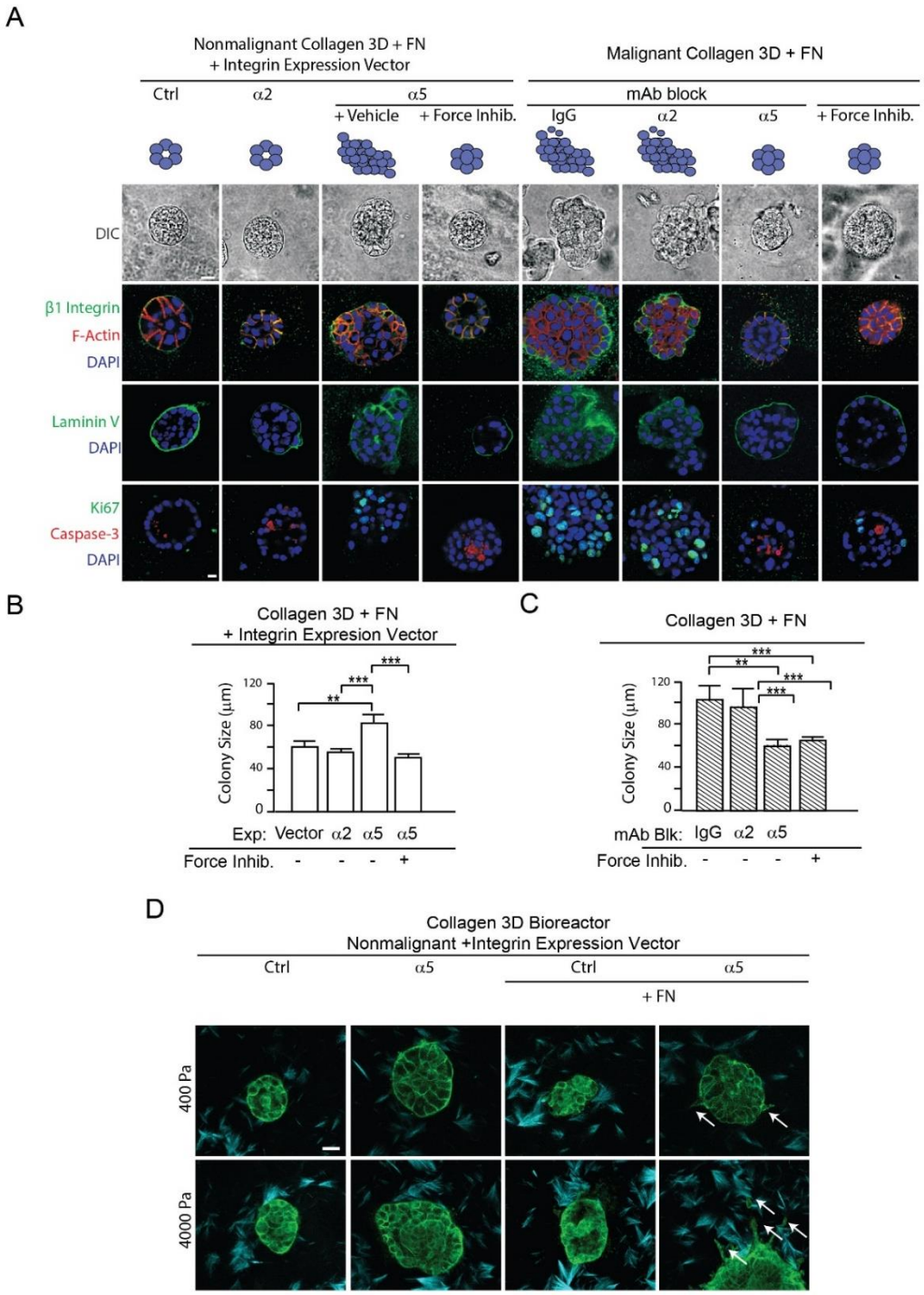

Breast Cancer Figure 3. Fibronectin-ligated α5β1 integrin increases cell tension to promote mammary malignancy

A) Phase contrast and confocal immunofluorescence images of β1 integrin, Phalloidin (F-actin), laminin V, Ki-67 and activated caspase 3 (Caspase-3) and DAPI (nuclei) stained colonies of nonmalignant (MCF10A) human

mammary epithelial cells (MECs) expressing empty vector or elevated α2 or α5 integrin treated with or without a ROCK inhibitor and malignant (HMT-3522 T4-2) incubated with nonspecific IgG or function blocking antibodies to α2 or α5 integrin or treated with or without a ROCK inhibitor grown within a collagen gel with added fibronectin (FN) for two weeks. Scale Bar 8 μm. **B)** Bar graph showing relative size of the non-malignant colonies shown in A. **C)** Bar graph showing relative size of the malignant colonies shown in A. **D)** Second Harmonic Generation images of nonmalignant (MCF10A) human mammary epithelial day 20 acini (green) expressing empty vector or elevated α5 integrin with or without FN embedded in collagen (blue) and installed into a 3D tension bioreactor system and subjected either to 0% (400Pa) or 10% (4000Pa) stretch, as described previously [103]. Arrows in D) indicate invasive cells. Results are the mean ± S.E.M. of 3-5 separate experiments. (**p<0.01; ***p<0.001). We next asked how FN-ligated α5β1 integrin promoted mammary tissue malignancy. Examination of the adhesions assembled by MECs plated on either FN or collagen coated glass slides revealed that nonmalignant MECs with FN-ligated α5β1 integrin had larger numbers of prominent, peripheral adhesions (Figures 4B) with more ^{p397}FAK (Figure 4A) and recruited greater quantities of the force-activated molecules vinculin and zyxin (Figure 4C-F) as compared to MECs expressing collagen-ligated α2β1 integrin (Figures 4A-F) or FN-ligated αvβ3 integrin (not shown). Importantly, we also determined that α5β1-expressing MECs contained higher levels of nuclear yes-associated protein (YAP), which reflects enhanced activity of the mechanoactivated Hippo pathway [143] (Figure 4G). These findings show that FN-ligation of α5β1 integrin in MECs increases their tension at matrix adhesions and elevates their mechano-signaling.

Examination of FN-doped 3D collagen cultures of nonmalignant MCF10A MECs expressing elevated α5 integrin showed that inhibition of ROCK activity or actomyosin contractility normalized their tissue structure to that assembled by control nonmalignant MECs or nonmalignant MECs expressing elevated α2 integrin (Figure 3A). While α5β1 integrin expressing nonmalignant MECs formed disorganized, invasive, proliferating large colonies, those cultures in which cell tension was reduced were growth-arrested and formed smaller colonies (Figure 3B) that exhibited apical-lateral actin networks and β1 integrin, basally-

localized laminin, and exhibited evidence of active luminal clearance as indicated by elevated activated caspase 3 (Figure 3A; left panel). Similarly, T4-2 mammary tumor cells treated with these force inhibitors also formed smaller (Figure 3C), growth-arrested, phenotypically-reverted tissue-like structures similar to those generated in the presence of a function blocking antibody to α5 integrin and in marked contrast to the significantly larger, highly proliferative, invading, and disorganized colonies observed in the IgG isotype-treated or vehicle-treated control cells or those in which α2 integrin was inhibited (Figure 3A; right panel). Furthermore, we directly implicated tension-dependent and α5β1-FN-mediated cellular invasion and disorganization of acini using a 3D tension bioreactor. To better recapitulate the evolving microenvironment of the tumor, we embedded acini in a soft, non-stretched collagen gels with or without fibronectin, then uniaxially stretched and stiffened the matrix as described previously [103]. Similarly to static growth culture 3D studies, acini only disorganized and invaded (indicated by arrows) in a context of a stiff environment upon high expression of α5 integrin and its ligation to fibronectin (Figure 3D). Interestingly, although they did not fully invade, α5 overexpressing acini began to form protrusions on the basal side in the context of exogenous FN even in a soft, non-stretched collagen (as indicated by arrows) (Figure 3D).

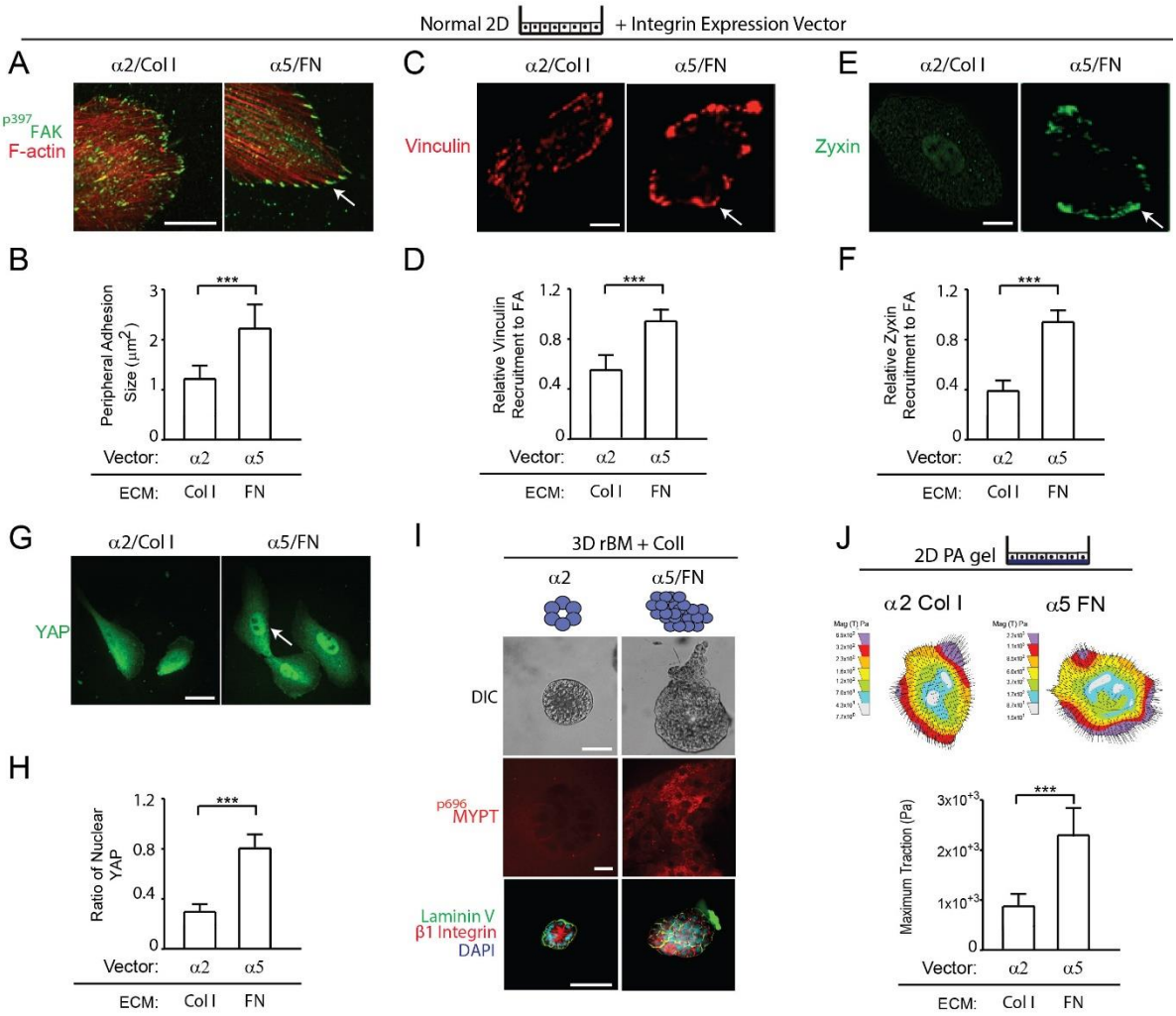

Breast Cancer Figure 4. Fibronectin-ligated α5β1 integrin, and not collagen-ligated α2β1 integrin, increases mammary epithelial cell tension

A) Immunofluorescence confocal images of nonmalignant mammary epithelial cells (MECs) expressing either exogenous α2 integrin plated on type 1 collagen (α2/Col 1) or exogenous α5 integrin plated on fibronectin (α5/FN) stained for ^{p397}FAK (^{p397}FAK; green) or with phalloidin (F-actin; red). Scale Bar 10 μm. **B)** Bar graph quantifying size of peripheral adhesions shown in A. **C)** Immunofluorescence confocal images of α2/Col 1 and α5/FN nonmalignant MECs stained for vinculin (Vinculin; red) Scale Bar 3 μm. **D)** Bar graphs showing quantification of relative amount of vinculin recruited to focal adhesions in MECs shown in C. **E)** Immunofluorescence confocal images of α2/Col 1 and α5/FN nonmalignant MECs stained for zyxin (Zyxin; green) Scale Bar 3 μm**. F)** Bar graphs showing quantification of relative zyxin recruited to focal adhesions in MECs shown in E. **G)** Immunofluorescence

images of α2/Col 1 and α5/FN nonmalignant MECs stained for YAP (arrow indicating nuclear localization of YAP). Scale Bar 15 μm **H)** Bar graphs quantifying percent nuclear YAP in MECs shown in H. **I)** Immunofluorescence confocal images (top and bottom panels) and phase contrast images (middle panel) of three dimensional cultures of α2/Col 1 and α5/FN nonmalignant MECs stained for the ROCK target ^{p696}MYPT (top) or β1 integrin (red) and laminin V (green) and DAPI (blue). Scale Bar 50 μm. **J)** Force maps of α2/Col 1 and α5/FN nonmalignant MECs and bar graphs showing maximum traction generated by MECs at the cell edge. Arrows in A), C), and E) indicate peripheral localization of adhesion molecules. Results are the mean ± S.E.M. of 3 separate experiments. (***$p<0.001$).

Consistent with the hypothesis that FN-ligated α5β1 integrin enhances tension in MECs, confocal immunofluorescence imaging revealed that the aberrant colonies assembled by the FN-ligated α5β1 integrin expressing nonmalignant MECs showed high levels of ROCK activity, as indicated by more activated ^{p1696}MYPT (myosin phosphatase binding protein), an observation that is consistent with high cell contractility and elevated actomyosin activity. By contrast, the nonmalignant MECs expressing collagen-ligated α2β1 integrin did not to stain positively for ^{p696}MYPT and formed small, polarized acini-like structures with apical-lateral β-catenin and basally-deposited the basement membrane (BM) protein laminin V (Figure 4I). Moreover, MECs expressing α5 integrin contracted 3D collagen gels to a greater extent (Supplemental Figure S2) than those expressing α2 integrin. Indeed, traction force microscopy demonstrated that MECs which had FN-ligated α5β1 integrin exhibited higher maximum cell traction force on their ECM as compared to α2 integrin-expressing MECs plated on collagen I-activated polyacrylamide gels (Figure 4J). These findings indicate that FN-ligated α5β1 integrin and not collagen-ligated α2β1 integrin specifically increases tension and mechano-signaling in MECs.

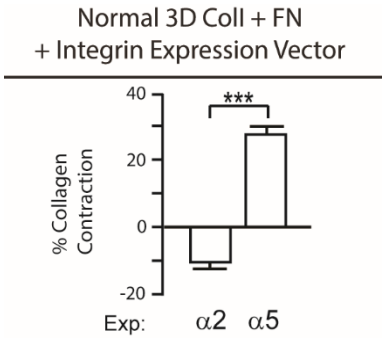

Breast Cancer Figure S2. MECs overexpressing α5β1 integrin are highly contractile.

Nonmalignant MECs overexpressing α5 integrin are able to contract 3-dimensional collagen gels to a much greater extent than those overexpressing α2 integrin. Results are the mean ± S.E.M. of 3 separate experiments (***p< 0.001).

The α5β1 integrin catch bond enhances mechanotransduction in MECs

Unlike αv integrin, α5 integrin binds to both the PHSRN synergy and RGD sites of fibronectin, and only FN bound α5β1, not αvβ3 integrin, exhibits a unique catch-bond phenotype in which ligand binding is strengthened in response to force [144] (Figure 5A). Consistently, shear force adhesion studies showed that α5β1 integrin expressing MECs attached to either full length (not shown) or a recombinant 9-10 domain FN bound with much greater strength compared to MECs plated on recombinant 9-10 domain FN in which the PHSRN domain was mutated (Figure 5A).

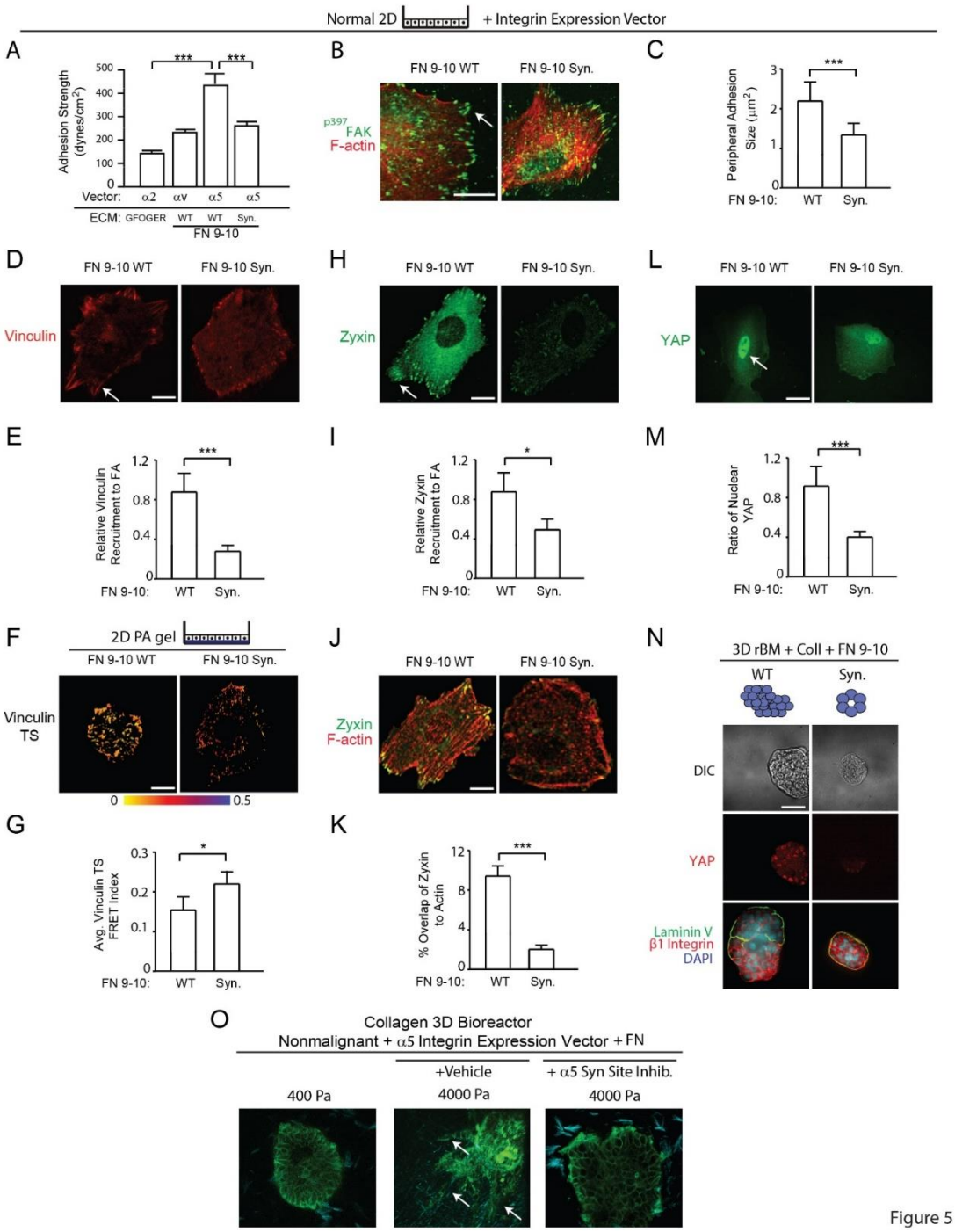

Figure 5

Breast Cancer Figure 5. The α5β1 integrin catch bond enhances mechanotransduction in MECs

A) Bar graphs showing adhesion strength of nonmalignant mammary epithelial cells (MECs) expressing integrins α2 plated on GFOGER, αv or α5 plated on recombinant fibronectin 9-10 (FN 9-10 WT), and α5 plated on

recombinant fibronectin 9-10 with the synergy site mutated (FN 9-10 Syn). **B)** Immunofluorescence confocal images of MECs expressing α5 integrin plated on FN 9-10 WT or FN 9-10 Syn stained for ^{p397}FAK (^{p397}FAK; green) and actin with phalloidin (F-actin; red). Scale Bar 10 μm. **C)** Bar graph quantifying size of peripheral adhesions shown in B. **D)** Immunofluorescence confocal images of MECs expressing α5 integrin plated on FN 9-10 WT or FN 9-10 Syn stained for vinculin. Scale Bar 3 μm**. E)** Bar graphs showing quantification of relative amount of vinculin recruited to focal adhesions in MECs shown in D. **F)** FRET images of MECs expressing α5 integrin and the vinculin force sensor plated on polyacrylamide gels conjugated with FN 9-10 WT or FN 9-10 Syn. Scale Bar 5 μm. **G)** Bar graphs showing quantification of FRET index at focal adhesions in MECs shown in F. **H)** Immunofluorescence confocal images of MECs expressing α5 integrin plated on FN 9-10 WT or FN 9-10 Syn stained for zyxin. Scale Bar 3 μm **I)** Bar graphs showing quantification of zyxin recruited to focal adhesions in MECs shown in H. **J)** Immunofluorescence confocal images of MECs expressing α5 integrin plated on FN 9-10 WT or FN 9-10 Syn double-stained for zyxin and F-actin (phalloidin). Scale Bar 3 μm. **K)** Bar graphs showing quantification of zyxin co-localization to actin in MECs shown in J. **L)** Immunofluorescence images of MECs expressing α5 integrin plated on FN 9-10 WT or FN 9-10 Syn stained for YAP. Scale Bar 15 μm. **M)** Bar graphs quantifying percent nuclear YAP in MECs shown in I. Results are the mean ± S.E.M. of 3 separate experiments. (***$p<0.001$). **N**) Immunofluorescence confocal images (middle and bottom panels) and phase contrast images (top panel) of three dimensional cultures of α5/FN9-10 WT and α5/FN9-10 Syn. Site Mutant nonmalignant MECs stained nuclear YAP (middle) or β1 integrin (red) and laminin V (green) and DAPI (blue) (bottom). **O)** Second Harmonic Generation images of nonmalignant (MCF10A) human mammary epithelial day 20 acini (green), expressing empty vector or elevated α5 integrin with FN and with or without FN synergy site inhibitor, embedded in collagen (blue) and installed into a 3D tension bioreactor system and subjected either to 0% (400Pa) or 10% (4000Pa) stretch. Arrows indicating invading cells. Scale Bar 50 μm.

Indeed, MECs expressing elevated α5 integrin bound with at least twice as much strength to recombinant 9-10 domain FN as compared to MECs expressing elevated αvβ3 integrin ligated to the same ECM or α2β1 integrin expressing MECs ligated to a GFOGER Col I substrate or

α5β1 integrin expressing MECs ligated to recombinant 9-10 FN in which the synergy site region was mutated (Figure 5A; Supplemental Figure 3A-B). The adhesions assembled by MECs with α5 integrin interacting with recombinant 9-10 FN also showed that in the absence of the synergy site the size of peripheral adhesions was greatly diminished (Figure 5C) as was the amount of ^{p397}FAK (Figure 5B) and the quantity of vinculin and zyxin at the integrin adhesions (Figure 5D-E, 5H-I). There was also a significant reduction in the amount of zyxin recruited to actin stress fibers at the α5β1 integrin adhesions in the MECs plated on the recombinant FN lacking the PHSRN synergy domain (Figure 5J-K) and less nuclear YAP, indicating that there was reduced mechano-signaling [143] (Figure 5L-M). Consistently, in the absence of the synergy site FN ligation of α5β1 integrin in MECs showed a significant reduction in vinculin-mediated FRET signaling indicative of reduced mechano-transduction (Figure 5F-G). Moreover, only the α5β1 integrin expressing MECs ligated a synergy site intact recombinant FN, and not α2β1 expressing MECs on collagen I or αvβ3 expressing MECs on fibronectin, demonstrated strong directional migration (durotaxis) in response to gradient ECM stiffness (Supplemental Figure 3C). Finally, while the α5β1 integrin expressing MECs formed continuously growing, large, and disorganized colonies with high levels of nuclear YAP when embedded in rBM doped with either recombinant 9-10 FN (Figure 5N) or a wild type full length FN (data not shown), in the absence of the synergy site the structures grew less, these same MECs barely activated YAP and they formed significantly smaller, polarized structures that showed evidence of active luminal clearance (Figure 5N). Furthermore, we directly tested the role of fibronectin's synergy site in the tension/α5β1-integrin-dependent cellular invasion and disorganization of acini using the 3D tension bioreactor described above [103]. Similarly to 2D findings and conventional 3D culture, acini disorganized and invaded in the context of a stiff environment only upon high expression

of α5 integrin and its ligation to full length fibronectin (indicated by arrows; Figure 5O). Colony invasiveness was abrogated with the inhibition of fibronectin's synergy site using a small molecule inhibitor ATN-161 (Figure 5O). These findings indicate that FN-ligated α5β1 integrin, by virtue of its unique ability to bind to the FN synergy site to enhance cell tension and mechano-signaling, promotes the force-dependent malignancy of MECs.

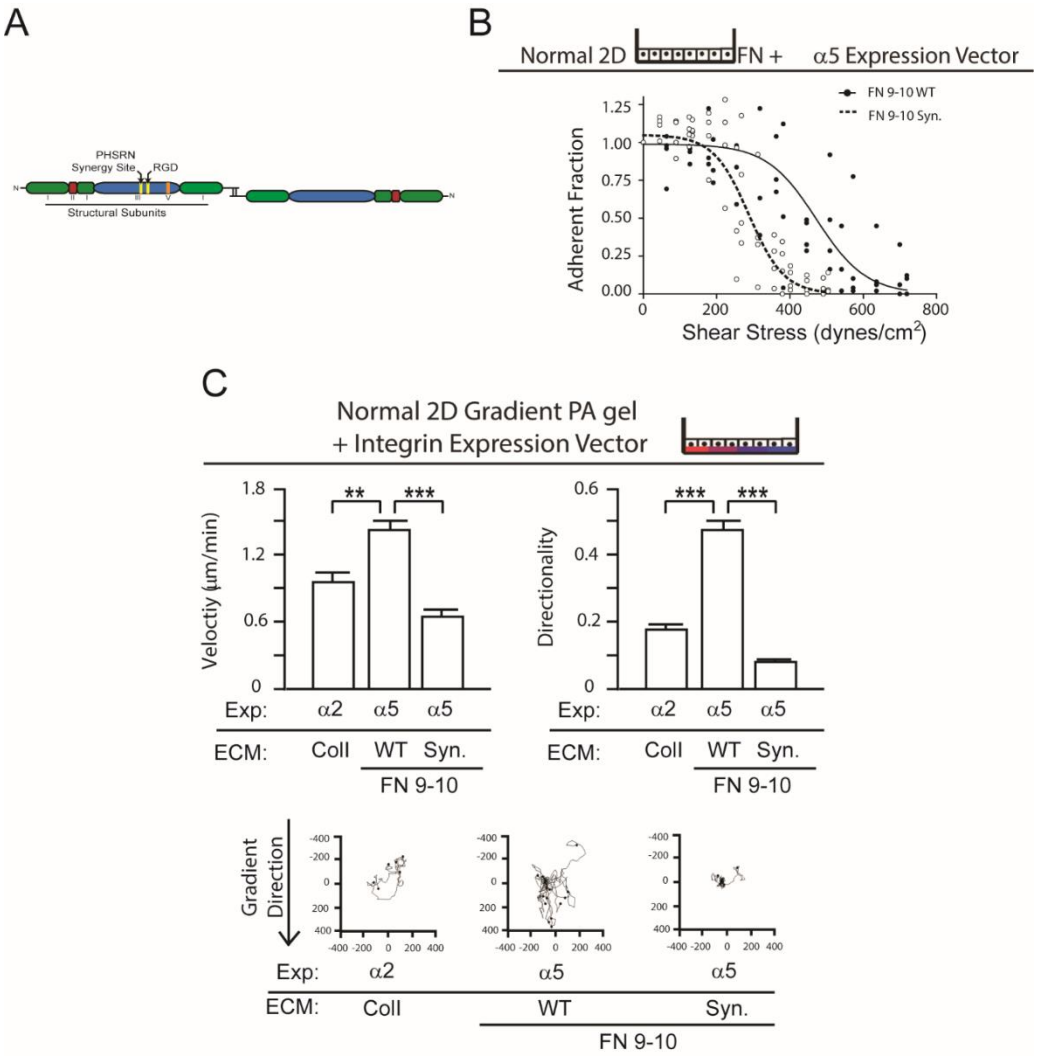

Breast Cancer Figure S3. α5β1 integrin's interaction with fibronectin is mechano-sensitive and mechano-responsive.

A) Schematic of FN domains relating RGD position to synergy site position. α5β1 integrin is able to switch between relaxed and tensioned states and the switch is controlled through the engagement of the synergy site on the

fibronectin under high tension environments. The schematic represents the relative positions of the RGD and the synergy sites on the fibronectin's type III domain. B) Higher fraction of MECs overexpressing α5 integrin remained adherent to WT versus synergy-site mutated FN9-10 with linearly increased applied hydrodynamic fluid shear force. C) Top: nonmalignant MECs overexpressing α5 integrin plated on wild type FN9-10 exhibit highly directional and fast migration towards the stiffer substrates when plated on polyacrylamide gels (PA) of gradient stiffness (140-60,000 Pa); this phenotype is abolished if the same cells are plated on FN9-10 with mutated synergy site. Bottom: images illustrate representative cell migration paths of MECs overexpressing α2 integrin migrating on collagen-coated PA gels of gradient stiffness as well as MECS overexpressing α5 integrin migrating on either WT or synergy-site-mutated FN9-10-coated PA gels of gradient stiffness.

The fibronectin synergy site-ligated α5β1 integrin increases MEC tension and promotes malignancy by amplifying PI3K signaling

We next examined how an increase in cell tension mediated by FN-ligation of α5β1 integrin could induce the malignant behavior of MECs. Growth factor receptor (GFR) signaling enhances MEC growth and survival by activating PI3K and ERK, and oncogenic transformation requires PI3K and ERK activity [145]. Consistently, we observed greatly reduced $^{p202/204}$ERK and ^{p473}Akt levels in the mammary epithelium of Her2/Neu mice in which collagen cross-linking and ECM stiffening had been prevented by inhibiting lysyl oxidase activity (Figure 6A), and this reduction in PI3K and ERK signaling correlated with lower ^{p397}FAK, ^{p}MLC, α5 integrin and FN expression *in vivo* (Figure 1B). We also observed that FN-ligation of α5β1 integrin increased the levels and duration of epidermal growth factor receptor (EGFR) stimulated ^{p473}Akt and $^{p202/204}$ERK activity in both nonmalignant and tumorigenic MECs in culture [20]. Thus, FN-ligated, nonmalignant HMT-3522 S1 MECs expressing α5β1 integrin showed a three hundred percent increase in ^{p473}Akt and a two hundred percent increase in $^{p202/204}$ERK ninety minutes following

EGF treatment, as compared to control cells expressing empty vector (Figure 6B left). Similarly, treating HMT-3522 T4-2 MECs plated on wildtype FN with a function-blocking antibody to α5 integrin significantly decreased ^{p473}Akt and $^{p202/204}$ERK activation in response to EGF stimulation (Figure 6B; right). Moreover, while S1 MECs cultured in 3D rBM gels doped with wildtype FN formed disorganized, invasive and non-polarized colonies, inhibition of PI3K, as well as EGFR or MEK (data now shown), activity reverted their phenotype to that exhibited by control nonmalignant MECs (Figure 6C; left panels and Supplemental S4) and significantly decreased colony size (Figure 6D; left).

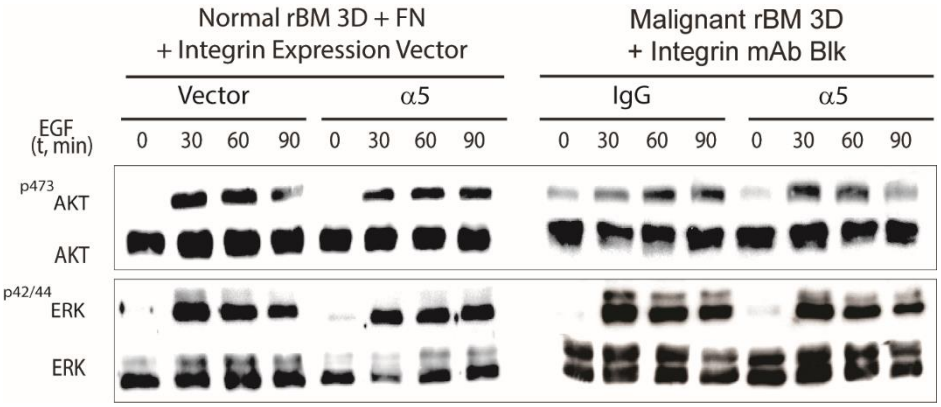

Breast Cancer Figure S4. α5β1 potentiates sustained Erk and Akt signaling.

Left: non-malignant MECs overexpressing α5 integrin exhibit sustained Erk and Akt signaling post EGF-stimulation after starvation. Right: function-blocking α5 integrin reduces the duration and potency of Erk and Akt signaling in malignant MECs.

Treatment of T4-2 MECs with these same inhibitors also reverted their phenotype to that exhibited by noninvasive, growth-arrested, polarized nonmalignant MECs (Figure 6C; right panels) and significantly decreased their colony size (Figure 6D; right). Importantly, the α5β1 integrin-mediated increase in ERK and PI3 kinase signaling required ligation of the synergy site of FN because nonmalignant α5β1 integrin expressing MCF10A MECs showed a profound and

sustained increase in EGF-stimulated ERK and Akt activation only when the cells were attached to recombinant FN that contained a synergy site (Figure 6E).

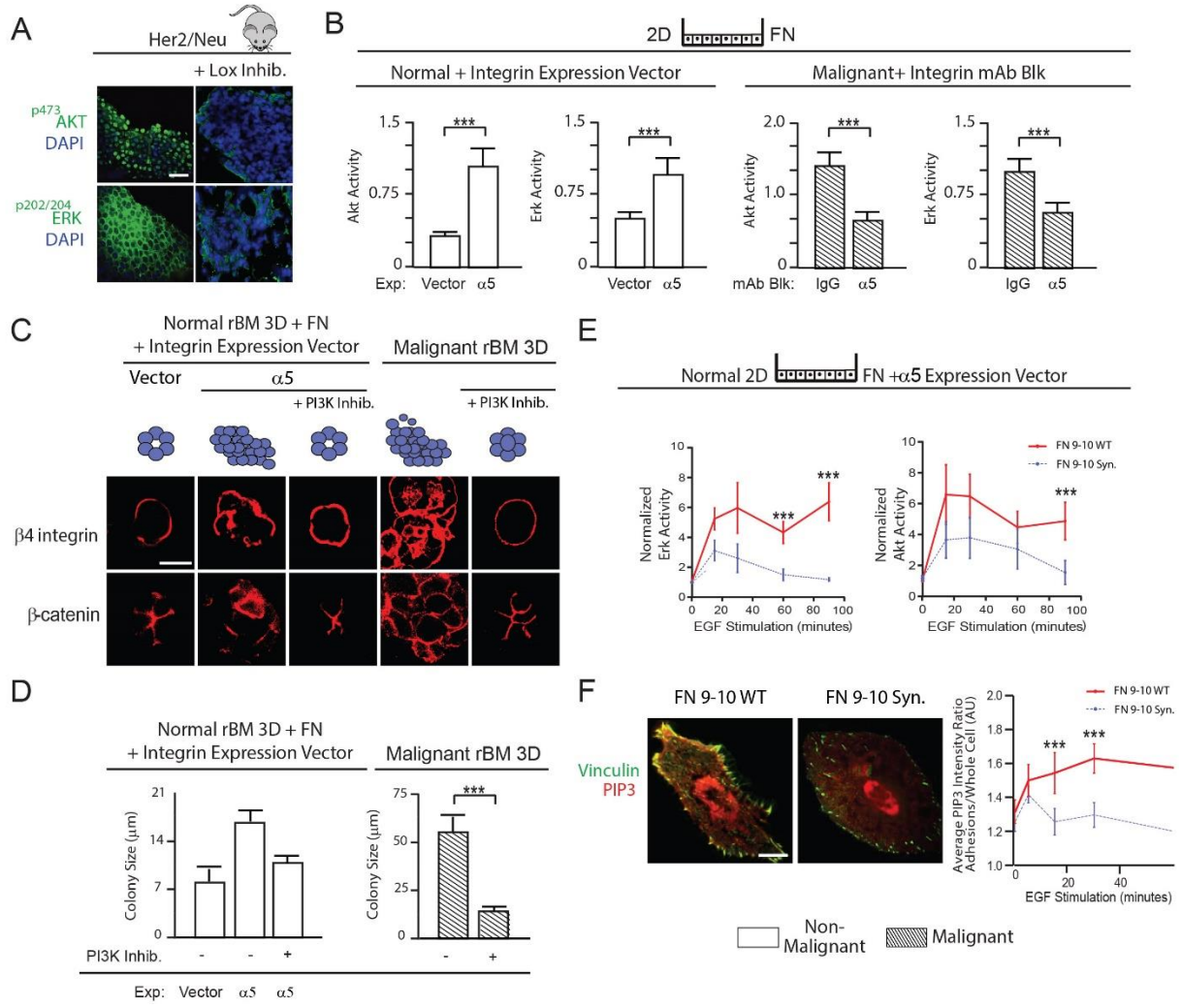

Breast Cancer Figure 6. The fibronectin synergy site-ligated α5β1 integrin increases MEC tension and promotes malignancy by amplifying PI3K signaling

A) Confocal immunofluorescence images of ^{p}Akt substrate, $^{pThr202/pTyr204}$ERK staining and DAPI stained nuclei of mammary tissue excised from 7 month old Her2/Neu transgenic mice treated with or without lysyl oxidase inhibitor (Lox inhibitor). Scale Bar 10μm. **B)** Bar graphs showing level of ^{p473}Akt and $^{pThr202/pTyr204}$ERK normalized to total cellular Akt and ERK in control or α5 integrin expressing non-malignant HMT-3522 S-1 mammary epithelial cells (MECs) and in T4-2 malignant MECs treated with either non-specific IgG or a function blocking antibody to α5

integrin 90 minutes following EGF treatment. **C)** Confocal immunofluorescence images of β4 integrin and β-catenin in colonies of control or α5 integrin expressing non-malignant HMT-3522 S-1 MECs and in T4-2 colonies treated with and without the PI3 kinase inhibitor LY294002. Scale Bar 10 μm. **D)** Bar graphs showing size of nonmalignant and malignant MEC colonies in C. **E)** Line graphs showing time course of EGF stimulated $^{pThr202/pTyr204}$ERK (top) and ^{p473}Akt (bottom) levels normalized to total ERK and Akt in nonmalignant MCF10A MECs expressing elevated α5 integrin plated on wildtype (WT) or synergy site mutated (Syn) fibronectin. **F)** Confocal images of non-malignant MEC cells expressing elevated α5 integrin, a probe for PIP3 activity (mKO2-PH-Grp1) and the focal adhesion protein vinculin, plated on recombinant 9-10 fibronectin with (WT) or without (Syn) site mutated. Scale Bar 3 μm. Line graphs showing time course of quantification of EGF-stimulated PIP3 recruited to focal adhesions in non-malignant MECs plated on wildtype (WT) or synergy site mutated (Syn) fibronectin. Measurements of all pixels in adhesions were averaged over whole cell. Results are the mean ± S.E.M. of 3 separate experiments. (**p<0.01; ***p<0.001).

We recently found that a force-stabilized vinculin-talin-actin-zyxin scaffolding complex facilitates PI3-kinase mediated conversion of phosphatidylinositol (3,4)-bisphosphate (PIP2) into phosphatidylinositol (3,4,5)-triphosphate (PIP3)[146]. We therefore asked whether the force-mediated stabilization of the vinculin-talin-actin-zyxin scaffolding complex by FN-ligation of α5β1 integrin led to enrichment of PIP3 at adhesions. Consistently, more mKO2-PH-Grp1 (a PIP3 localization reporter; [37]) was localized to the focal adhesions (indicated by vinculin mEmerald) in response to EGF in α5β1-overexpressing MCF10As, but only when they were ligated to a FN in which the synergy site was intact (Figure 6F). These findings demonstrate that the unique mechanical behavior of a FN-ligated α5β1 integrin increases cell tension to stabilize a vinculin-talin-actin-zyxin scaffolding complex that promotes mammary malignancy by amplifying GFR signaling through PI3 kinase.

Discussion

We determined that tumor tension selectively modulates levels of epithelial α5β1 integrin, which when bound to its ligand FN promotes force-dependent malignant transformation. Using 2D and 3D culture assays, a 3D tension bioreactor, and mouse models we showed that FN-ligated α5β1 integrin, by virtue of its ability to enhance cell tension, is both necessary and sufficient for expression of the malignant phenotype of MECs *in vitro* and *in vivo*. Our findings provide a plausible explanation for why α5β1 integrin and its ligand FN are so frequently elevated in many solid tumors where interstitial pressure and tension are also elevated, and in contractile primary and metastatic cancer cell lines and tumor cells which have high Rho and ROCK activity [11,23,24,38–40]. Our data are also consistent with prior results which showed that cancer cell lines expressing abundant FN, when sorted for high membrane α5 integrin levels, migrate faster and contract collagenous matrices to a greater extent [130] and studies showing that blocking the activity of RGD-binding receptors is critical for expression of the malignant phenotype of cultured breast cancer cells [41][116]. Here, we not only identified α5β1 integrin as the key the RGD receptor, but we also rigorously demonstrated that the ability of α5β1 integrin to promote the malignant phenotype of MECs requires binding to both the RGD and synergy site of FN (Figure 5). Importantly, α5β1 integrin exists in a relaxed state and requires tension to unfold the otherwise hidden synergy site on FN in order to full engage α5β1 and induce downstream signaling though FAK [128,129]. Our data imply that collagen-mediated ECM stiffening likely promotes malignancy by fostering α5β1 integrin binding to the FN synergy site along stiff collagen fibrils that allow for the force-dependent exposure of the synergy site on FN molecules[42–44].

Tumors contain abundant quantities of type I collagen, and crosslinked, remodeled type I collagen contributes critically to the tensile strength of a tissue [20,71]. Nevertheless, we failed to quantify differences in α2 integrin in either Her2/Neu mouse mammary tissue or in the 3D organotypic cultures of malignant MECs in which the tension had been reduced (Figure 1; Figure 6A). Instead, we established a relationship between cell tension and ECM stiffness and elevated expression of the FN receptor α5β1 integrin in mouse mammary tissue and mammary organoids. We determined that MECs with FN-ligated α5β1 integrin, but not collagen I-ligated α2β1, exerted higher traction forces and were able to contract collagen gels more (Figure 3J; Supplemental Figure 2S). Our data are consistent with prior studies suggesting that α2β1 integrin represses expression of the malignant phenotype of MECs in culture and is a tumor suppressor in the mammary gland *in vivo* [124] and recent data indicating that α2β1 integrin activates FAK by a force-independent mechanism [129]. Interestingly, FN and collagen are often secreted and processed in tandem [45], and a FN matrix can serve as a scaffold to guide collagen assembly [46]. Indeed, just as FN deposition and unfolding requires a collagen scaffold, collagen assembly and remodeling require FN [47–50], during which time FN can be crosslinked to collagen [51,52]. FN fibril assembly and collagen-remodeling form a feedback loop, with collagen-mediated ECM stiffness and cell contractility inducing conformational changes in FN that reveal hidden binding sites required for FN matrix assembly, which then further facilitate collagen remodeling [22,42]. Thus, our data are consistent with a paradigm where the highly crosslinked collagen form the scaffold upon which a FN meshwork is laid. This stiffened ECM, by virtue of its ability to modify FN, would then drive malignancy by permitting α5β1 integrin binding to enhance tension-dependent signaling in tumors. Nevertheless, it is also feasible that FN bound α5β1 integrin could collaborate with other transmembrane collagen receptors such as

the discoidin receptor (DDR) or syndecans to foster malignant progression, particularly since DDRs are also tension regulated [53–56].

PI3 kinase (PI3K) and ERK regulate cell growth, survival and invasion, and the levels and activity of these kinases are frequently elevated in tumors [57,58]. Accordingly, an assortment of pharmacological inhibitors has been developed to target these kinases and their associated signaling molecules to treat (and cure) various cancers with varying degrees of clinical success [59–61]. Here, we determined that while the Her2/Neu tumors, which are surrounded by a stiffened ECM, have elevated ERK and PI3K activity as expected, that merely preventing collagen crosslinking and stiffening by inhibiting Lox activity significantly reduced both ERK and Akt activity, and did so in tandem with a reduction in α5 integrin and FN. We also observed that that MECs with α5β1 integrin ligated by a wild-type, but not a synergy-site mutated FN, nucleated more vinculin-talin-actin-zyxin scaffolds and recruited more PIP3 to amplify EGF-dependent activation of Akt and ERK. Inhibiting PI3K or ERK repressed the malignant behavior of FN-ligated mammary MEC 3D tissue-like structures expressing elevated α5β1 integrin. Our findings thereby revealed how mechanical signals from stiffened tumor stroma or elevated cancer cell contractility can amplify oncogenic signaling by modifying GFR signaling via ligation of α5β1 integrin by the FN synergy site. The data thereby provide one plausible explanation for why in some instances targeted molecular therapies are less effective and suggest that combinatorial treatments that target both the mechanical properties of the cell or tissue and specific oncogenic signaling pathways might prove to be a better therapeutic option. Our findings are therefore clinically relevant, as they identify a tumor-specific mechanical signature, since the synergy site is only engaged in a high-force environment, such as that of a

tumor. Thus, inhibiting the ability of α5β1 integrin to ligate the synergy site of fibronectin could prove to be a potent cancer-specific therapy [42,62]. And since ECM mechanics and mechanotransduction are necessary for progression to malignancy but cannot be targeted directly in patients, targeting the pathways that are critical for mechanosensing and mechanotransduction, in addition to targeting relevant oncogenic pathways, might prove to be tractable therapeutic approaches with which to treat cancer. The data also suggest that strategies to detect the FN synergy site in tumor biopsies might be useful biomarkers to identify patients with potential kinase treatment resistance [154].

CHAPTER 4: PANCREATIC CANCER STUDIES

Genotype tunes PDAC tension to drive malignant matricellular-enriched fibrosis and tumor aggression

Summary: The fibrotic phenotype of pancreatic ductal carcinoma contributes to patient mortality. Nevertheless, anti-stromal therapies have had mixed results, suggesting there are multifaceted, anti and pro-tumorigenic role of fibrosis. We found that the genotype of pancreatic ductal carcinomas tunes the tension of the malignant epithelium to mechanically prime the stroma and promote tumor progression through epithelial pSTAT3 and YAP. Kras pancreatic tumors in mice lacking epithelial TGFβ signaling developed a highly stiff, matricellular-enriched fibrosis and exhibited increased epithelial myosin activity with elevated cytokine, Jak, Rock, Fak and Yap signaling, and Stat3-dependent inflammation. Increasing pancreatic epithelial mechanosignaling accelerated Kras-driven transformation that was accompanied by stromal stiffening and a matricellular-enriched fibrosis with high epithelial Yap and pStat3 activity. Elevating pStat3 increased tissue tension and matricellular-enriched fibrosis and activated Yap to accelerate Kras-dependent pancreatic transformation. By contrast, epithelial Stat3 ablation attenuated pancreatic malignancy and reduced the matricellular-enriched fibrosis, stromal stiffening, epithelial contractility and Yap activation induced by Kras/TGFβ knockout. Human biospecimens revealed that the least differentiated pancreatic tumors from patients with the shortest survival had matricellular-enriched fibrosis and a highly contractile, mesenchymal-like epithelium that lacked pSMAD and had elevated pSTAT3, YAP and SOX2. Our data underscore

the importance of tumor genotype in tuning stromal-epithelial interactions and illustrate how tissue tension can force malignancy, drive tumor aggression and compromise patient survival.

Introduction

Pancreatic ductal adenocarcinomas (PDACs) are profoundly fibrotic and PDAC patients have a high mortality rate[173]. PDAC fibrosis induces interstitial fluid pressure to disrupt blood vessel integrity and induce hypoxia that compromise drug delivery and promote disease aggression and therapy resistance[174–177]. Consequently, considerable resources have been expended to develop strategies to reduce PDAC fibrosis[178]. To this end, inhibition of stromal sonic hedgehog (SHH) signaling in a mouse model of PDAC significantly reduced fibrosis and increased intratumoral vascular density to increase drug update that, at least transiently, stabilized the disease[179]. Similarly, reducing mouse pancreatic tumor hyaluronan, using hyaluronidase, or treating xenografted human pancreatic tumors with an angiotensin inhibitor to reduce tissue tension, decreased interstitial fluid pressure and normalized the vasculature to facilitate chemotherapy response[180,181]. Yet, phase II clinical trials in PDAC patients treated with the SHH inhibitors IPI-926 or GDC-0449, or with a monoclonal antibody against the collagen cross-linking enzyme LOXL2, failed (NCT01472198)[182]. Experiments in mouse models of PDAC revealed that, while depletion of proliferating α-smooth muscle actin (αSMA) positive stromal cells reduced fibrosis, the vasculature remained abnormal and the tumor, while smaller, was hypoxic and less differentiated, with accelerated mortality[183]. Despite a frank reduction in fibrosis and enhancement of tissue vascularity, genetic ablation of SHH or treatment with a smoothened inhibitor induced mouse PDACs that were less differentiated and more, not less, aggressive[184]. These data imply that the stroma can both promote and restrain tumor progression, and suggest

stromal dependency may be context dependent. Whether such complexity could be explained by distinct tumor genotype - stromal interactions or by the natural evolution of PDACs remains unclear.

Malignant transformation of an epithelial tissue is universally accompanied by extracellular matrix (ECM) deposition and remodeling[3,185]. Nevertheless, the extent and nature of the fibrosis and the responsiveness of the transformed epithelium to the desmoplastic ECM can vary widely across cancers, amongst tumor subtypes and even within one tumor[186–189]. Indeed, the fibrotic response in patients with aggressive, treatment-resistant, quasi-mesenchymal PDACs (QM-PDA) is less prominent and tumor cells isolated from QM-PDA patients are only marginally anchorage-dependent for their growth and survival[190,191]. By contrast, patients with classical PDACs have a better prognosis and classical PDACs are more differentiated, and tumor cells isolated from these cancers retain Ras dependence and express higher levels of cell adhesion molecules[183,192]. Although the origins of the QM and classical histophenotypes have yet to be determined, PDAC development has been irrevocably linked to a handful of genetic modifications. Thus, pre-malignant pancreatic lesions (PanINs) frequently possess activating point mutations in the *Kras* proto-oncogene and PDAC progression correlates with either the genetic and/or epigenetic inactivation of the tumor suppressor genes *p16INK4a* (<90%), *p53* (<75%) and *SMAD4* (*DPC4*, <55%)[193]. Consistently, genetically-engineered mouse models (GEMMs) in which an activated Kras is expressed in the pancreatic ductal epithelium develop PanINS and when combined with deletion of a single allele of p53, p16INK4a, Smad4 or Tgfbr2 develop PDACs[194–197]. Of these genetic modifications, mice with combined Kras mutations and Tgfbr2 deletion are very aggressive and exhibit a mesenchymal-like phenotype following

stromal ablation[183,194]. Moreover, the human mesenchymal-like PDAC phenotype most frequently associates with aberrant TGFβ signaling in the epithelium[198]. These findings imply that distinct genotypes may dictate unique stromal-epithelial phenotypes. Importantly, as mouse PDACs develop they also increase expression of mesenchymal-like features, as do patients with recurrent PDACs, and ablation of proliferating alpha smooth muscle actin (αSMA) positive cells in Kras/p53 mouse PDAC permits the expansion of mesenchymal-like, aggressive tumors[199–201]. These observations suggest that the epithelium likely evolves over time towards a less stromally-dependent phenotype and imply that this evolution may be linked to the engagement of pathways that promote a mesenchymal-like transition.

High grade PDACs express more Sex-determining region Y (SRY)-Box2 (SOX2), a transcription factor that drives an epithelial-to-mesenchymal transition (EMT), with elevated Sox2 levels in PDACs linked to poor PDAC patient prognosis[202,203]. Poorly differentiated, mesenchymal-like PDACs (QM-PDACs) also express higher levels and activity of the Hippo transcription factor Yes-associated protein 1 (YAP), and YAP directly induces SOX2 and an EMT[191,204–208]. These findings suggest QM-PDACs may arise through elevated YAP and SOX2 activity. YAP is exquisitely sensitive to mechanical stimuli such that cells interacting with a stiff ECM activate more ROCK to increase nuclear YAP and induce YAP-dependent gene expression[143,209]. Importantly, PDACs are mechanically-activated tumors composed of a progressively stiffened ECM and high interstitial pressure[174,180,183]. Thus, the elevated tissue mechanics mediated by the stiffened tissue stroma and high interstitial pressure could eventually activate YAP to drive tumor aggression and induce an EMT. Moreover, many oncogenes also induce tissue tension by increasing Rock-dependent contractility. Indeed, the majority of PDACs

have activated Kras, and Kras activity, per se, increases ROCK to drive cell contractility which, in turn, induces ECM remodeling and stiffening to drive integrin-dependent mechanosignaling and malignant transformation[12,210211]. It is therefore equally plausible that the genotype of the pancreatic tumor epithelium additionally elevates tissue tension to drive tumor progression. Here, we examined human pancreatic tumor tissue of differing grades and survival, and exploited a series of PDAC GEMMs to explore the relationship between tumor genotype, stromal-epithelial interactions and tissue tension in PDAC progression and aggression.

Results

Human PDAC aggression is characterized by low epithelial TGFβ signaling and high myosin activity

PDACs are fibrotic, and contain abundant fibrillar collagen[173]. Yet, recent findings suggest collagen abundance may associate with better, not worse, patient prognosis and that high collagen content correlates with a more differentiated PDAC phenotype[212–214]. Nevertheless, high fibrillar collagen has repeatedly been implicated in PDAC aggression and treatment resistance[215]. To address this discrepancy, we constructed a gene list of major fibrillar collagens (Supplementary Table 1) and used this signature to interrogate a publically-available NCBI GEO agilent gene expression data set (GSE21501) consisting of 67 PDAC patients between the ages of 40 and 65. We could find no statistical differences in the combined expression levels of the major fibrillar collagens and patient survival. However, when we created a median centroid value representing an average high versus low Col1α2, Col2α1 and Col4α1 combined expression score for each patient and graphed each of the groups over time, a Cox-Mantel Log-rank analysis revealed that patients with high levels of these fibrillar collagens had a reduced overall survival,

as illustrated by Kaplan-Meier survival curves (log rank p≤0.04; Fig. 1a). These data suggest elevated expression of specific fibrillar and fibrillar associated collagens can predict poorer patient outcome.

Individual Genes Used for Survival Analysis of GSE21501
COL1A2
COL2A1
COL3A1
COL4A1
COL5A1
COL11A1
COL24A1
COL27A1

Pancreatic Cancer Supplementary Table 1

Collagens are subjected to a plethora of posttranslational modifications that can modify their organization and mechanical properties. Therefore, to more directly investigate the relationship between fibrillar collagens and PDAC tumor phenotype, we secured PDAC tissue arrays from US Biomax representing a total of 68 patients between the ages of 23 and 78 with well (n=19), moderately (n=23) and poorly differentiated (n=26) tumors. A UCSF pathologist confirmed tumor grade using H&E stained sections. Thereafter, serial sections were stained for total collagen using Massons Trichrome and assessed for fibrillar collagen levels, organization and diameter using polarized imaging of Picrosirius Red (PR) stained tissue and second-harmonic generation (SHG). A superficial analysis of the H&E and Trichrome stained images implied that the poorly differentiated PDACs contained reduced stroma and total collagen, consistent with the lower numbers of alpha smooth muscle actin (αSMA) positive cells we detected (Fig. 1b,b')[183,216]. Nevertheless, quantification of PR stained, polarized images revealed there was a modest, albeit non-significant, increase in total fibrillar collagen in the least differentiated tumors (Fig. 1 b, b'). Furthermore, quantitative analysis of SHG images revealed that the collagen fiber

diameter was significantly thicker in the poorly differentiated PDACs, suggesting higher localized tissue tension. Indeed, additional analysis revealed there was a significant and progressive increase in levels of pMLC2, reflecting higher mechanosignaling in the epithelium of the moderately and poorly differentiated tumors (Fig. 1b, b'). Interestingly, upon further examination, we established an inverse relationship between levels of nuclear pSmad and PDAC differentiation (Fig. 1b, b').

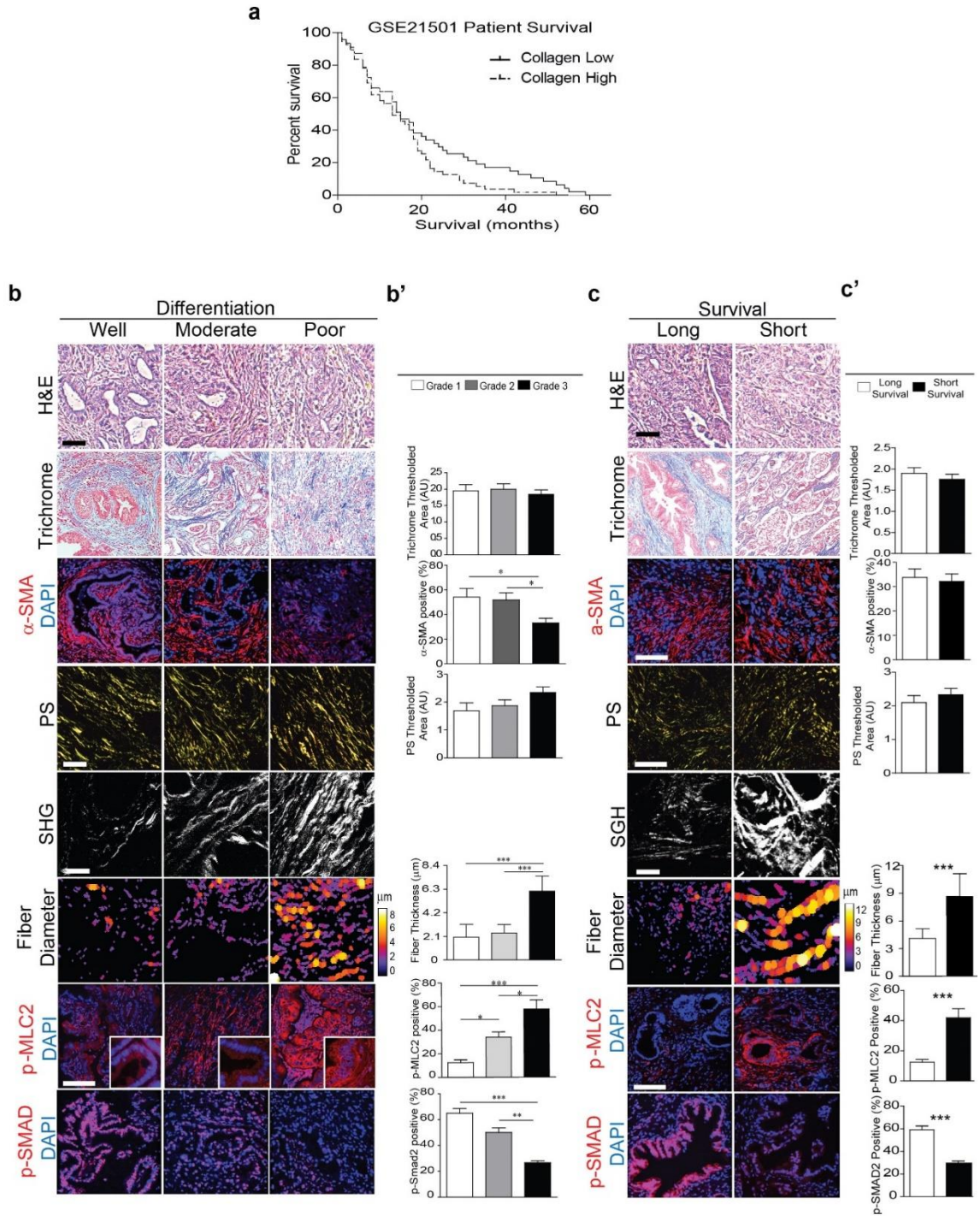

Pancreatic Cancer Figure 1: Human PDAC aggression is characterized by low epithelial TGFβ signaling and high myosin activity.

(a) Kaplan-Meier of overall survival of PDAC patients from GSE21501 with patients divided into those with high and low collagen expression by normalized microarray analysis of collagen gene expression, log rank p=0.04, n=67.

(b) Representative photomicrographs of H&E (top panel) and Masson's Trichrome (2nd panel) stained PDAC tissue arrays from patients with well (n=19), moderately (n=23) or poorly differentiated (n=26) tumors. Scale bar, 100µm. Representative immunofluorescence images of pancreatic tissue described above stained for SMA (red, 3rd, panel), pMLC2 (red, 7th panel), pSMAD2 (red, 8th panel) and DAPI (blue). Scale bar, 75µm. Representative polarized light images of picrosirius red (PR) stained pancreatic tissue (as described above) revealing collagen fiber structure, orientation and distribution within the tissue stroma (4th panel). Scale bar, 50µm. Representative second harmonic generation (SHG) images of extracellular collagen architecture in the pancreatic tissue around the epithelial ductal region described above (5th panel) and SHG color-coded images revealing collagen fiber diameter (6th panel). Scale bar, 75µm. (b') Bar graphs quantifying the tissue images shown in the panels in b. (c) Representative photomicrographs of H&E (top panel) and Masson's Trichrome (2nd panel) stained PDAC tissue arrays from PDAC patients cohort representing patients with a median short survival of 11-289 days (n=29) and median long survival of 1090-3298 days (n=28). Scale bar, 100µm. Representative immunofluorescence images of pancreatic tissue (as described above) stained for αSMA (red, 3rd, panel), pMLC2 (red, 7th panel), pSMAD2 (red, 8th panel) and DAPI (blue). Scale bar, 75µm. Representative polarized light images of PR stained pancreatic tissue as described above revealing collagen fiber structure, orientation and distribution within the tissue stroma (4th panel). Scale bar, 50µm. Representative SHG images of extracellular collagen architecture in the pancreatic tissue around the epithelial ductal region described above (5th panel) and SHG color-coded images revealing collagen fiber diameter (6th panel). Scale bar, 75µm. c'. Bar graphs quantifying the tissue images shown in the panels in c. (*p<0.05; **p<0.01, ***p<0.001, ****p<0.0001, "ns" denotes not significant).

To further interrogate the relationship between fibrillar collagen phenotype, mechanosignaling and patient survival, we evaluated 57 resected PDACs from a previously reported cohort, representing patients with a median short survival of less than 10 months (n=29) as compared to a median long-term survival of over 24 months (n=28)[217]. Consistent with prior findings, Massons Trichrome stained tissue and polarized imaging of PR stained sections indicated there was no consistent relationship between total and fibrillar collagen or αSMA positive stained cells in the tissues from patients with the short versus the longer survival (Fig. 1c, c'). However

and importantly, we again found that fiber diameter was significantly thicker in those patients with the shortest survival, as revealed by SGH. We also noted that the PDAC tissues from patients with the shortest survival contained the highest amount of epithelial pMLC2, suggesting they had elevated mechanosignaling and tissue tension (Fig. 1c, c'). Moreover, once again, the epithelium in the PDAC tissue excised from the patients with the shortest survival also had low to negligible detectable pSmad (Fig. 1c, c'). These findings indicate collagen organization and tissue tension, and not collagen abundance, are more robust indicators of PDAC aggression. The data also suggest reduced TGFβ signaling in the PDAC epithelium may alter stromal-epithelial interactions to drive tumor aggression.

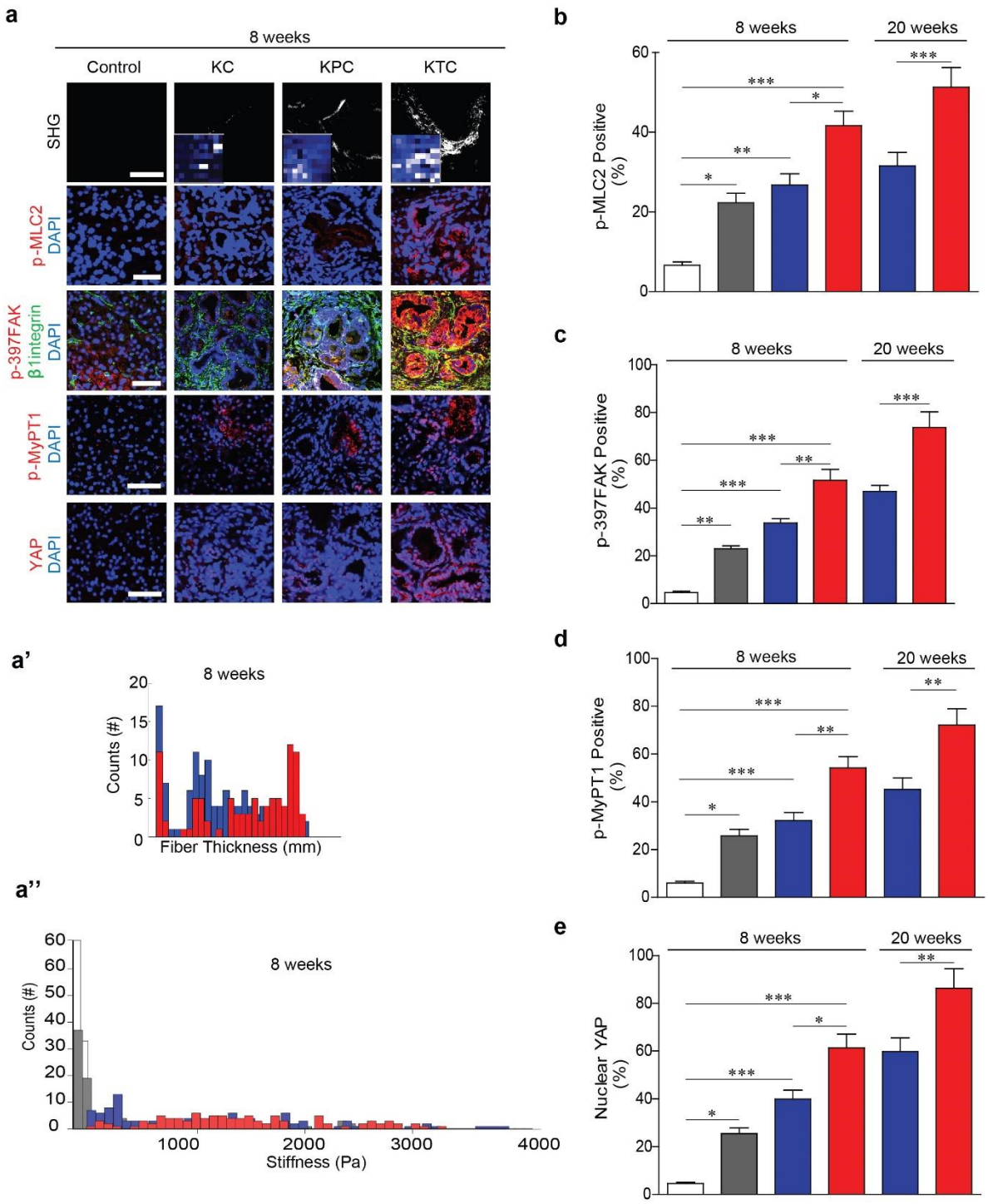

Pancreatic Cancer Figure S1.

(a) Representative second harmonic generation (SHG) images of extracellular collagen architecture and distribution in the pancreatic tissue from 8 week old pancreatic tissue excised from mice expressing Kras (KC), Kras with one mutant allele of P53 (KPC) or Kras with heterozygous loss of the Tgfbr2 receptor in the pancreatic epithelium

(KTC) (1st panel). Scale bar, 75μm. Representative force maps measured using atomic force microscopy (AFM) indentation of the stiffness of the extracellular matrix surrounding the pancreatic ductal lesions developing in the 8 week old animals (1st panel insert). Representative immunofluorescence images of pancreatic tissue described above stained for pMLC2 (red, 2nd panel), ß1integrin/^{p397}FAK (green/red, 3rd panel), pMyPT1 (red, 4th panel), YAP (red, 5th panel) and DAPI (blue). Scale bar, 50μm. **(a').** Bar graphs quantifying the fibril thickness and distribution imaged by SHG around the developing pancreatic ductal lesions of pancreatic tissue described above. **(a")** Bar graphs showing the distribution of the stiffness of the extracellular matrix surrounding the normal and developing lesions in tissue described above as measured by AFM indentation. **(b)** Bar graphs quantifying the tissue images shown in the panels in a and in Fig. 1a.

Tumor genotype tunes epithelial tension to regulate the fibrotic phenotype

To explore the relationship between TGFβ signaling and tissue mechanics, the fibrotic phenotype and tumor aggression we exploited available PDAC GEMMs. We used a GEMM in which mutant Kras was conditionally expressed in the pancreatic epithelial cells (Kras$^{LSL\text{-}G12D/+}$; Ptf1α-Cre; KC)[218] either alone or in combination with mice heterozygous for mutant P53 (Kras$^{LSL\text{-}G12D/+}$;TrP53$^{R172H/+}$; Pdx1-Cre; KPC), lacking one allele of P53 (Kras$^{LSL\text{-}G12D/+}$;TrP53$^{flox/wt}$; Ptf1α; KP-Ptf1α-C) or those lacking one allele of the TGFβ receptor II (Kras$^{LSL\text{-}G12D/+}$;Tgfbr2$^{flox/wt}$; Ptf1a-Cre; KTC). As has been previously reported, by 20 weeks Kras mice had progressed to PanIN lesions, whereas both the KPC and KTC mice developed frank PDACs[194,195]. Coincident with tumor formation, the pancreatic tissue of both the KPC and KTC mice was highly fibrotic, as indicated by abundant quantities of total and fibrillar collagen (not shown). Mass spectrometry based targeted proteomics confirmed that many of the fibrillar collagens in the KTC and KPC mice were present at similar levels (Supplementary Table 2) and immunofluorescence staining revealed that both mouse GEMM PDACs had similar levels collagen III and numbers of αSMA and FAP positive cells throughout their stroma

(Supplementary Fig. 2a). Gli-1, which regulates PDAC fibrosis, was also abundantly and uniformly expressed equally in the stroma in both PDAC models (Supplementary Fig. 2a).

Protein	Functional	Matrisome	MW	GENE	KPC/KC	p val	KTC/KC	p val	KTC/KPC	p val	Analytical CV(%)
Agrin(iso 2,3,4,5,&6)	Basement Membrane	Glycoprotein	208646	AGRN*	0.910	0.536	1.426	0.494	1.566	0.413	13%
Collagen alpha-1/5(IV) chain(Arresten/Core Protein)	Basement Membrane	Collagen	160613	COL4A1*	1.071	0.611	0.952	0.674	0.889	0.415	16%
Collagen alpha-1/5(IV) chain(Arresten/Core Protein)	Basement Membrane	Collagen	160613	COL4A1/5*	1.151	0.345	1.087	0.574	0.944	0.508	22%
Collagen alpha-2(IV) chain	Basement Membrane	Collagen	161386	COL4A2	1.047	0.735	1.065	0.669	1.017	0.844	14%
Collagen alpha-2(IV) chain(Canstatin/Core Protein)	Basement Membrane	Collagen	161386	COL4A2*	0.968	0.845	1.027	0.819	1.060	0.727	12%
Perlecan	Basement Membrane	Proteoglycan	375271	HSPG2	0.889	0.646	1.189	0.379	1.338	0.264	19%
Perlecan(Endorepellin)	Basement Membrane	Proteoglycan	375271	HSPG2*	0.908	0.712	0.958	0.827	1.055	0.860	7%
Laminin alpha-2	Basement Membrane	Glycoprotein	339982	LAMA2	1.108	ND	KC	ND	PC	ND	23%
Laminin alpha-5	Basement Membrane	Glycoprotein	404444	LAMA5	0.944	0.832	0.650	0.136	0.689	0.212	21%
Laminin Beta-1	Basement Membrane	Glycoprotein	197090	LAMB1	1.402	0.110	1.493	0.153	1.065	0.788	25%
Laminin Beta-2	Basement Membrane	Glycoprotein	196474	LAMB2	0.851	0.569	0.511	0.053	0.601	0.119	27%
Laminin Beta-3	Basement Membrane	Glycoprotein	128900	LAMB3	1.126	0.607	2.012	0.002	1.787	0.008	15%
Laminin Gamma-1	Basement Membrane	Glycoprotein	177387	LAMC1	0.881	0.389	1.054	0.775	1.197	0.361	ND
Laminin Gamma-2	Basement Membrane	Glycoprotein	130846	LAMC2	1.307	0.352	1.332	0.461	1.019	0.961	35%
Nidogen-1	Basement Membrane	Glycoprotein	137039	NID1	0.987	0.938	1.076	0.661	1.090	0.563	18%
Nidogen 1/2 (osteonidogen)(Nid1/2)	Basement Membrane	Glycoprotein	136538	NID1/2*	0.950	0.783	0.969	0.830	1.020	0.919	21%
Actin (All Isoforms)	Cytoskeletal	Cellular	42051	ACT	0.907	0.280	1.091	0.269	1.203	0.009	10%
Actin, cytoplasmic 1/2	Cytoskeletal	Cellular	41737	ACTB	1.139	0.300	1.271	0.128	1.116	0.497	10%
Desmin	Cytoskeletal	Cellular	53457	DES	0.515	0.373	0.257	0.163	0.499	0.338	12%
Spectrin alpha chain, non-erythrocytic 1	Cytoskeletal	Cellular	284637	SPTA2	1.143	0.400	0.984	0.928	0.861	0.280	20%
Tubulin beta-4B chain(4b & 5 chain)	Cytoskeletal	Cellular	49586	TUBB*	1.077	0.477	1.192	0.135	1.106	0.375	14%
Vimentin	Cytoskeletal	Cellular	53733	VIM	1.274	0.516	1.172	0.317	0.920	0.811	19%
Lysyl oxidase-like 1	ECM regulator	ECM regulator	66589	LOXL1	1.164	0.401	1.236	0.355	1.062	0.687	33%
Transglutaminase 2	ECM regulator	ECM regulator	77061	TGM2	1.017	0.829	0.669	0.013	0.657	0.001	11%
Collagen alpha-1(XII) chain	FACIT Collagen	Collagen	340214	COL12A1	0.782	0.421	1.724	0.171	2.203	0.097	13%
Collagen alpha-1(XIV) chain	FACIT Collagen	Collagen	191772	COL14A1	1.168	0.428	0.678	0.108	0.581	0.029	14%
Collagen alpha-1(I) chain	Fibrillar Collagen	Collagen	137953	COL1A1	0.911	0.250	0.916	0.529	1.005	0.969	10%
Collagen alpha-1(I) chain(C-term Propeptides (NC1 Domain))	Fibrillar Collagen	Collagen	137953	COL1A1*	1.002	0.979	1.365	0.133	1.363	0.128	12%
Collagen alpha-1(I) chain(fragment)	Fibrillar Collagen	Collagen	137953	COL1A1*	0.808	0.402	0.848	0.382	1.049	0.809	20%
Collagen alpha-2(I) chain	Fibrillar Collagen	Collagen	129564	COL1A2	0.931	0.393	1.036	0.801	1.112	0.465	14%
Collagen alpha-1(V) chain	Fibrillar Collagen	Collagen	183987	COL5A1	1.153	0.273	0.741	0.087	0.643	0.002	25%
Collagen alpha-2(V) chain	Fibrillar Collagen	Collagen	145018	COL5A2	0.997	0.987	0.759	0.295	0.762	0.125	11%
Collagen alpha-1(XVII) chain	Matricellular	Collagen	143568	COL17A1	1.009	0.968	1.594	0.173	1.580	0.114	26%
Collagen alpha-1(XVIII) chain	Matricellular	Collagen	182881	COL18A1	1.084	0.809	0.703	0.255	0.649	0.321	12%
Collagen alpha-1(VI) chain	Matricellular	Collagen	108806	COL6A1	0.980	0.938	0.574	0.081	0.586	0.117	15%
Collagen alpha-2(VI) chain	Matricellular	Collagen	108579	COL6A2	1.124	0.451	0.624	0.037	0.555	0.043	14%
Collagen alpha-3(VI) chain	Matricellular	Collagen	288133	COL6A3	0.730	0.314	0.391	0.002	0.536	0.244	16%
Collagen alpha-1(VII) chain(Fibronectin type-III 3 Domain)	Matricellular	Collagen	295092	COL7A1*	0.955	0.866	1.887	0.307	1.975	0.291	14%
Collagen alpha-1(VII) chain(Fibronectin type-III 1 Domain)	Matricellular	Collagen	295092	COL7A1*	1.001	0.972	1.882	0.318	1.879	0.176	25%
Dermatopontin	Matricellular	Glycoprotein	24203	DPT	1.281	0.176	0.757	0.101	0.591	0.025	11%
Fibulin 3	Matricellular	Glycoprotein	54596	EFEMP1	1.991	0.048	1.941	0.124	0.975	0.936	ND
Fibulin 4	Matricellular	Glycoprotein	44850	EFEMP2	0.754	0.366	1.423	0.031	1.887	0.063	14%
Emilin 1	Matricellular	Glycoprotein	106667	EMILIN1	1.042	0.658	0.889	0.265	0.853	0.156	17%
Fibulin 1	Matricellular	Glycoprotein	75381	FBLN1	1.349	0.183	2.678	0.052	1.985	0.093	34%
Fibronectin 1	Matricellular	Glycoprotein	272511	FN1	1.246	0.438	2.089	0.179	1.676	0.244	ND
Fibronectin 1(type-III 9 domain)	Matricellular	Glycoprotein	272511	FN1*	1.258	0.340	3.173	0.042	2.522	0.069	15%
Fibronectin 1(type-III 7 domain)	Matricellular	Glycoprotein	272511	FN1*	0.980	0.913	2.790	0.029	2.847	0.031	17%
Fibronectin 1(Anastellin/type-III 1 domain)	Matricellular	Glycoprotein	272511	FN1*	0.703	0.135	2.520	0.050	3.585	0.032	22%
Fibronectin 1(type-III 13 domain)	Matricellular	Glycoprotein	272511	FN1*	1.006	0.986	2.474	0.112	2.459	0.130	20%
Lumican	Matricellular	Proteoglycan	38279	LUM	1.092	0.106	0.983	0.888	0.900	0.393	9%
Periostin	Matricellular	Glycoprotein	93155	POSTN	0.831	0.086	1.300	0.369	1.563	0.191	15%
Prolargin	Matricellular	Proteoglycan	43179	PRELP	1.070	0.710	1.050	0.786	0.981	0.891	16%
Secreted protein, acidic, cysteine-rich (osteonectin)	Matricellular	Glycoprotein	34296	SPARC	1.280	0.513	1.366	0.109	1.068	0.827	15%
Osteopontin	Matricellular	Glycoprotein	34963	SPP1	0.794	0.360	1.193	0.451	1.503	0.174	14%
Thrombospondin 1	Matricellular	Glycoprotein	129647	THBS1	1.001	0.996	3.909	0.022	3.905	0.021	26%
tenascin C(Iso1,2,3,4,5)	Matricellular	Glycoprotein	221756	TNC*	1.052	0.927	4.324	0.033	4.112	0.036	14%
Versican	Matricellular	Proteoglycans	300008	VCAN	0.992	0.945	1.500	0.084	1.512	0.083	13%
Alpha/gamma-enolase	Other Cellular	Cellular	47128	ENO1/2	1.062	0.558	1.616	0.393	1.521	0.443	23%
Glyceraldehyde-3-phosphate dehydrogenase	Other Cellular	Cellular	35828	GAPDH	1.065	0.662	1.171	0.652	1.100	0.782	11%
Histone H1(H1.1,H1.2,H1.3,H1.4)	Other Cellular	Cellular	20863	H1*	1.178	0.433	0.780	0.133	0.662	0.080	9%
Histone 2A(H2A-A-K)	Other Cellular	Cellular	14077	H2A*	1.193	0.422	0.899	0.535	0.753	0.250	28%
Annexin A2	Other ECM	ECM-affiliated	38678	ANXA2	1.255	0.233	1.045	0.800	0.833	0.134	11%
Annexin A4	Other ECM	ECM-affiliated	35849	ANXA4	0.997	0.988	0.499	0.046	0.501	0.035	32%
Asporin	Other ECM	Proteoglycan	42573	ASPN	0.856	0.636	0.357	0.102	0.417	0.030	38%
Galectin-3	Other ECM	ECM-affiliated	27202	LGALS3	1.165	0.777	2.474	0.066	2.124	0.157	88%
Mimecan/Osteoglycin	Other ECM	Proteoglycan	34069	OGN	1.068	0.423	0.722	0.059	0.676	0.048	13%
Bone Marrow Proteoglycan(BMP & Eosinophil granule major basic protein)	Other ECM	Proteoglycan	25129	PRG2*	1.222	0.654	1.035	0.666	0.896	0.783	25%
Albumin	Secreted	Secreted	68731	ALB	0.945	0.671	1.093	0.604	1.156	0.442	13%
Transforming growth factor-beta-induced protein ig-h3	Secreted	Glycoprotein	74597	TGFBI	KC	ND	0.584	0.017	TC	ND	24%
Biglycan	Structural ECM	Proteoglycan	41706	BGN	1.175	0.285	1.682	0.021	1.431	0.079	10%
Decorin	Structural ECM	Proteoglycan	39805	DCN	1.345	0.007	0.764	0.017	0.568	0.000	19%
Fibrillin 1	Structural ECM	Glycoprotein	311952	FBN1	0.976	0.898	1.237	0.277	1.268	0.311	14%
Fibrillin 2	Structural ECM	Glycoprotein	313818	FBN2	1.059	0.694	1.129	0.778	1.066	0.881	21%
Fibromodulin	Structural ECM	Proteoglycan	43219	FMOD	0.813	0.500	1.601	0.008	1.970	0.036	21%
Latent transforming growth factor beta binding protein 1	Structural ECM	Glycoprotein	186599	LTBP1	0.897	0.647	1.917	0.138	2.137	0.127	ND
Microfibrillar-associated protein 2	Structural ECM	Glycoprotein	20578	MFAP2	1.024	0.822	1.033	0.791	1.009	0.950	13%

Pancreatic Cancer Supplementary Table 2

Nevertheless, and in agreement with our clinical findings, PR and SHG imaging revealed that the PDACs in the KTC mice had significantly thicker collagen bundles that were particularly evident in the region surrounding the tumor epithelium, which atomic force microscopy (AFM) indicated was significantly stiffer than the stroma surrounding the KPC tumor epithelium (Fig. 2a, a', a"). Upon further scrutiny, we noted that the altered fibrillar collagen phenotype and the elevated stromal stiffness in the KTC PDACs was accompanied by a significant increase in levels of matricellular proteins including tenascin C, fibronectin and collagen, type XII, alpha 1 (Fig. 2a, b). The epithelium of the KTC PDACs also had higher mechanosignaling, as revealed by more activated β1 integrin and ^{p397}FAK, with greater nuclear levels of the mechano-activated transcription factor YAP (Fig. 2a). These findings indicate that loss of pancreatic epithelial TGFβ signaling induces a mechanically-activated, matricellular-enriched fibrotic phenotype.

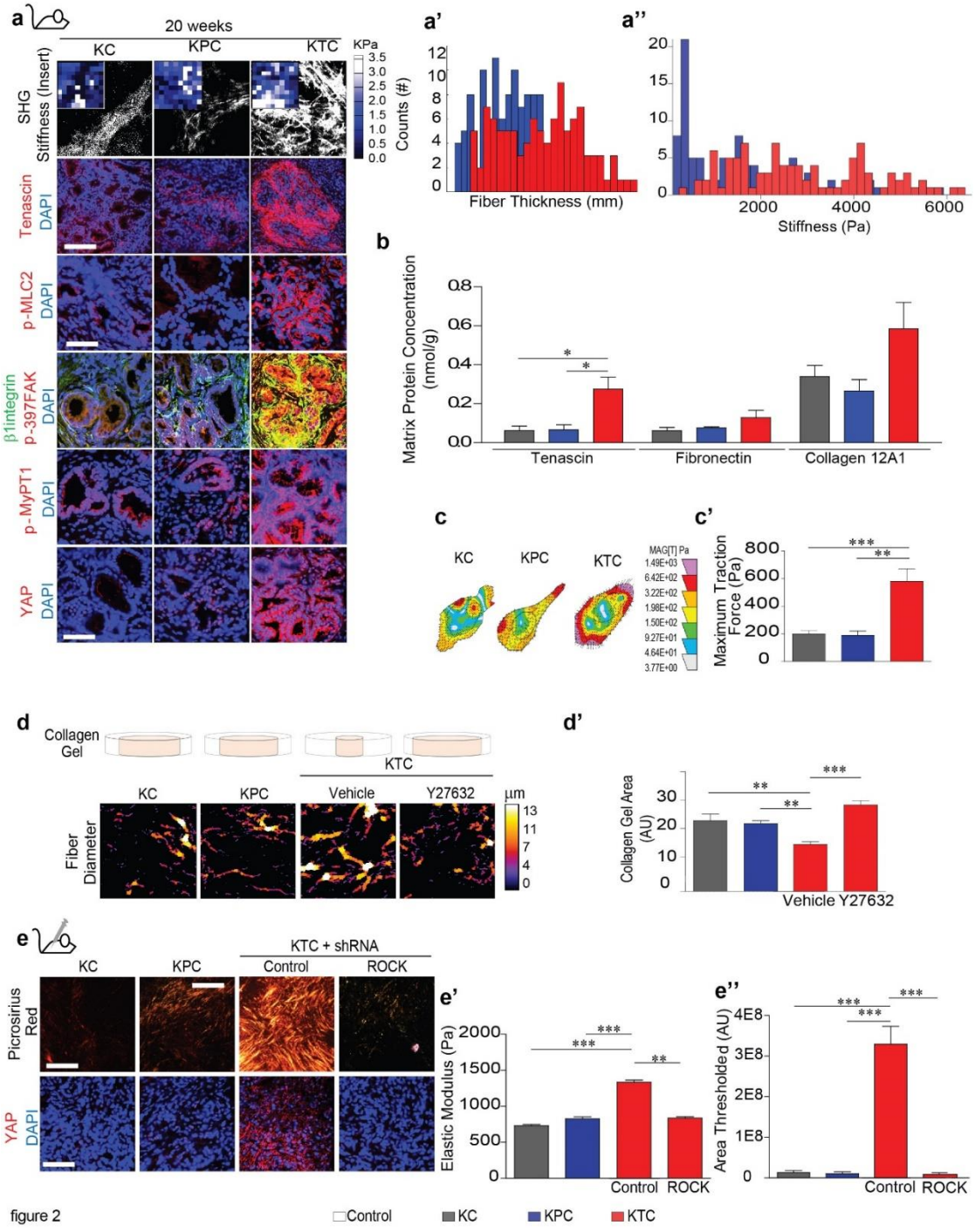

Pancreatic Cancer Figure 2: Tumor genotype tunes epithelial tension to regulate the fibrotic phenotype.

(a) Representative SHG images of extracellular collagen architecture and distribution in the pancreatic tissue from 20 weeks old pancreatic tissue excised from mice expressing Kras (KC), Kras with one mutant allele of P53 (KPC)

or Kras with heterozygous loss of Tgfr2 in the pancreatic epithelium (KTC) (1st panel). Scale bar, 75μm.Representative force maps measured using AFM indentation of the stiffness of the extracellular matrix surrounding the pancreatic ductal lesions developing in the 20 week old animals (1st panel insert). Representative immunofluorescence images of pancreatic tissue described above stained for Tenascin C (red, 2nd panel; scale bar, 75μm), pMLC2 (red, 3rd panel), β1integrin/pFAK (green/red, 4th panel), pMyPT1 (red, 5th panel), YAP (red, 6th panel) and DAPI (blue). Scale bar, 50μm. (a') Bar graphs quantifying the fibril thickness and distribution imaged by SHG around the developing pancreatic ductal lesions pf pancreatic tissue described above. (a") Bar graphs showing the distribution of the stiffness measurements of the extracellular matrix surrounding the normal and developing lesions (in tissue described above) as assessed by atomic force microscopy indentation. (b) Bar graphs quantifying the matrix protein concentration of Tenascin C, Fibronectin 1 and collagen, type XII, alpha1 in tissue described above as measured by mass spectrometry. (c) Representative traction force maps measured on polyacrylamide gels (2300 Pa) for isolated KC, KPC and KTC pancreatic epithelial tumor cells. (c') Corresponding quantification of c. (d) Polarized light images of color-coded PR stained collagen gels incubated with KC, KPC or KTC pancreatic epithelial tumor cells or with KTC cells treated with vehicle or the ROCK inhibitor Y27632. (d') Bar graphs quantifying three dimensional collagen gel contraction as indicated by collagen gel area. Cultures were assayed after 24 hours. (e) Representative polarized light images of PR stained pancreatic tissue excised from nude mice 3 weeks after injection with KC, KPC, and KTC pancreatic tumor cells expressing either a control shRNA or an shRNA to ROCK (top panel). Scale bar, 75μm. Representative immunofluorescence images of pancreatic tissue described above stained for YAP (red) and DAPI (blue). Scale bar, 50μm (bottom panel). (e') Bar graph quantifying the stiffness of the pancreatic tissue shown above in e using AFM indentation. (e") Graphs quantifying the total level of fibrillar collagen measured in the pancreatic tissue shown in e. For in vitro bar graphs, results are the mean +/- SEM of 3 independent experiments. For in vivo experiments, N=5 mice per group. (*$p<0.05$; **$p<0.01$, ***$p<0.001$, ****$p<0.0001$, "ns" denotes not significant).

Importantly and again consistent with our clinical findings, we quantified more pMLC2 and pMyPT1 in the epithelium of the KTC PDACs, implicating loss of TGFβ signaling in the elevated tissue mechanics (Fig. 2a). Indeed, traction force microscopy (TFM), which quantifies

the contractility phenotype of individual cells, revealed that freshly isolated pancreatic KTC tumor cells and cultured pancreatic Kras tumor cells lacking Tgfbr2 expression were significantly more contractile (Fig. 2c, c'). Further studies confirmed this observation and showed the KTC tumor cells were able to induce more ROCK-dependent collagen gel contraction than isolated cancer cells from KPC or KC mouse tumors (Fig. 2d, d' and Supplementary Fig. 3a, a'). The KTC pancreatic tumor cells also drove more ROCK-dependent collagen gel remodeling and stiffening (Fig. 2a, a' and Supplementary Fig. 3a, a', b, b'), more ROCK-dependent fibrosis and tissue stiffening when injected into the pancreas of immune-compromised mice, and activated more Yap, as indicated by higher nuclear levels and increased CTGF expression (Fig. 2e, e', e" and Supplementary Fig. 3c", c"').

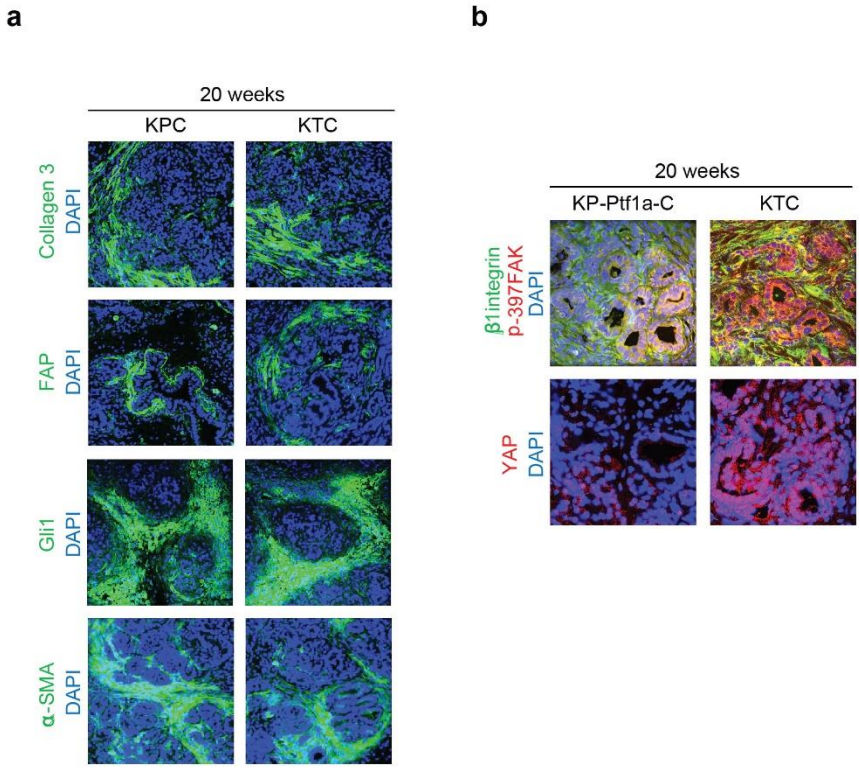

Pancreatic Cancer Figure S2.

(a) Representative immunofluorescence images of pancreatic tissues stained for Collagen 3 (green, 1st panel), FAP (green, 2nd panel), Gli1 (green, 3rd panel), αSMA (green, 4th panel) and DAPI (blue) from 20 weeks old tissue

excised from mice expressing Kras with one mutant allele of P53 (KPC) and Kras with heterozygous loss of the Tgfbr2 in the pancreatic epithelium (KTC). Scale bar, 75 μm. **(b)** Representative immunofluorescence images of pancreatic tissues stained for ß1integrin/^{p397}FAK (green/red, top panel), YAP (red, bottom panel) and DAPI (blue) from 20 weeks old tissue excised from mice expressing Kras with heterozygous loss of the P53 (KP-Ptf1a-C) and Kras with heterozygous loss of the Tgfbr2 in the pancreatic epithelium (KTC). Scale bar, 50 μm. For *in vivo* experiments, N=5 mice per group. *p<0.05; **p<0.01, ***p<0.001, ****p<0.0001, "ns" denotes not significant).

Not only were the pancreatic tumor cells able to directly promote ROCK-dependent tissue fibrosis, but the phenotype was independent of proliferation with the non-fibrotic KPC pancreatic tumor cells forming larger, not smaller, tumors than those generated by the control and ROCK-knockdown KTC tumor cells (Supplementary Fig. 3c, c').

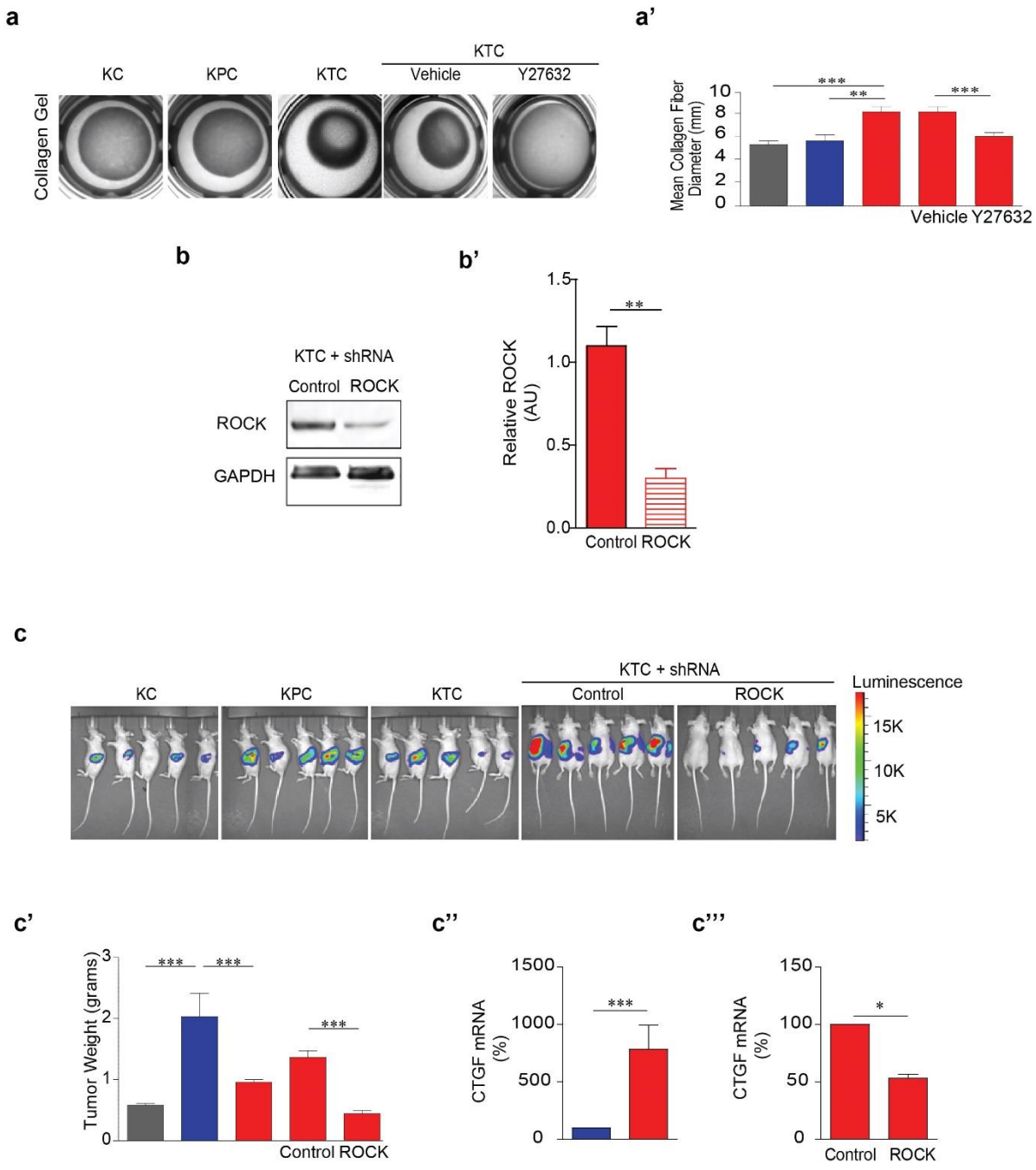

Pancreatic Cancer Figure S3.

(a) Representative images of collagen gels incubated with KC, KPC or KTC pancreatic epithelial tumor cells or with KTC cells treated with vehicle or the ROCK inhibitor Y27632. **(a')** Bar graphs quantifying the mean collagen fiber diameter in the three-dimensional collagen gels described in a. **(b)** Representative immunoblot showing ROCK protein levels in KTC tumor cells expressing either a control shRNA or an shRNA to ROCK. Results are normalized

to GAPDH. **(b')** Bar graph showing the quantification of b. **(c)** Representative bioluminescence images of tumor growth in nude mice 3 weeks after injection with KC, KPC, KTC and KTC pancreatic tumor cells expressing either a control shRNA or an shRNA to ROCK. **(c')** Bar graph showing the weight of the pancreatic tumors generated by the KC, KPC and KTC pancreatic epithelial cancer cells. **(c")** and **(c"')** Bar graphs quantifying CTGF mRNA expression for pancreatic tumors described in c. Results are normalized to β-actin. For *in vitro* bar graphs, results are the mean +/- SEM of 3 independent experiments. For *in vivo* experiments, N=5 mice per group. (*$p<0.05$; **$p<0.01$, ***$p<0.001$, ****$p<0.0001$, "ns" denotes not significant).

Thus, although pancreatic transformation is universally accompanied by a progressive fibrosis and stiffening of the ECM, the nature of the fibrotic response and the mechano-phenotype of the cancer can be modified by the genotype of the tumor. In particular, loss of TGFβ signaling in the epithelium can increase cancer cell contractility to "tune" the mechano-fibrotic phenotype of the malignant tissue.

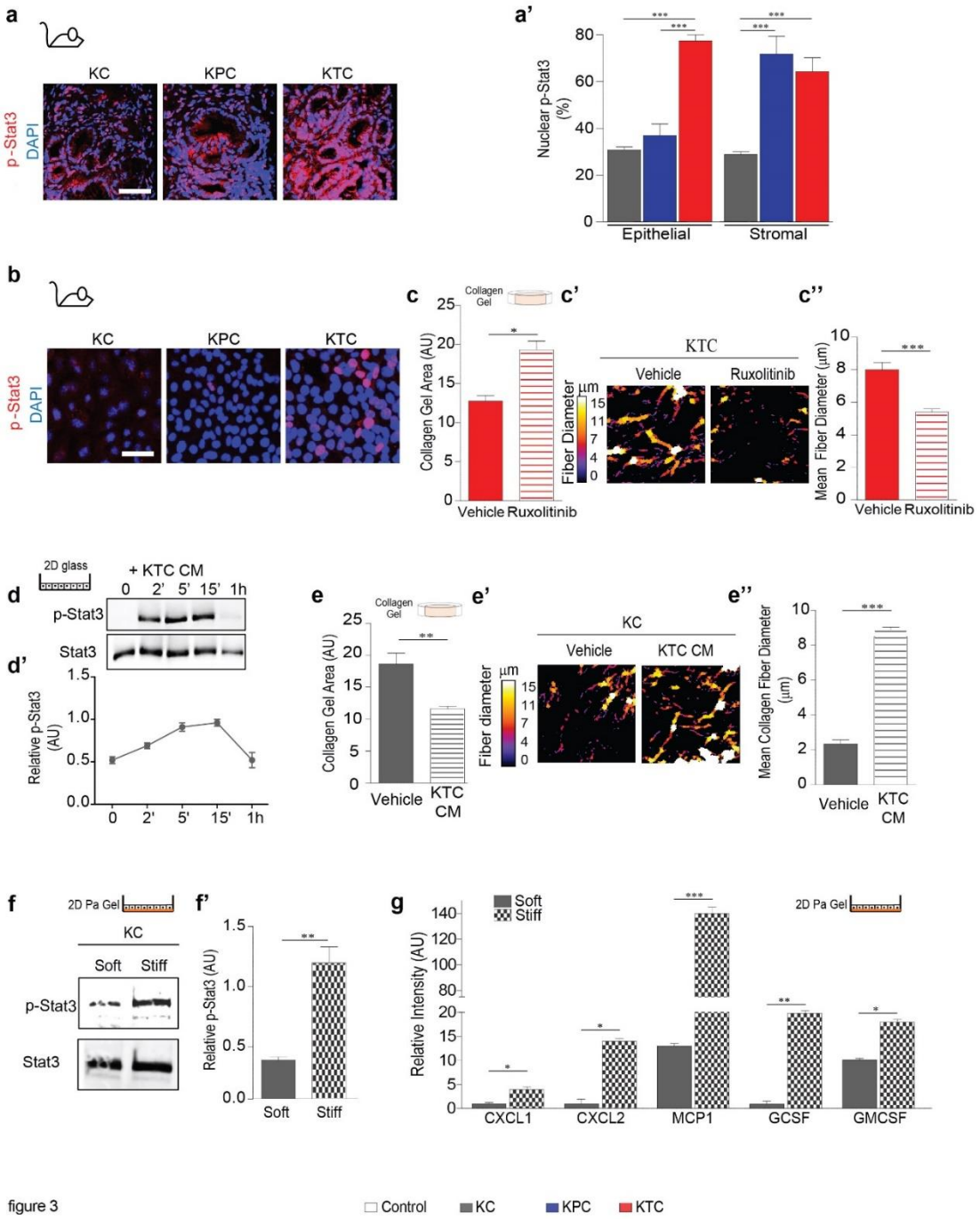

Pancreatic Cancer Figure 3: Loss of TGFβ signaling activates a JAK/Stat3 contractility feed forward circuit to induce ECM remodeling and tissue stiffening.

(a) Representative immunofluorescence images of pancreatic tissue excised from 20 week old KC, KPC and KTC mice stained for pStat3 (red) and DAPI (blue). Scale bar, 50μm. (a') Bar graphs quantifying the level of stromal

versus epithelial p-Stat3 in the tissues stained in a. (b) Representative immunofluorescence images of isolated KC, KPC and KTC tumor cells stained for pStat3 (red) and DAPI (blue). Scale bar, 25μm. (c) Representative polarized light images of PR stained color-coded fibrillar collagen in three dimensional collagen gels incubated with KTC tumor cells for 24 hours either with vehicle or the JAK inhibitor Ruxolitinib. (c') Bar graphs showing amount of collagen contraction as measured by total collagen gel area. (c") Bar graphs showing mean collagen fiber diameter measured in the three dimensional collagen gels shown in c. (d.) Representative immunoblot of Stat3 activation (pStat3) as a function of time following exposure to the conditioned media (CM) obtained from KTC tumor cells. (d') Line graph quantifying the relative level of pStat3 measured in the KC cells shown above in d. (e) Representative polarized light images of PR stained, color-coded fibrillar collagen in three-dimensional collagen gels incubated with KC tumor cells treated with vehicle or the conditioned media from 48 hour cultured KTC tumor cells. (e') Bar graphs showing amount of collagen contraction as measured by total collagen gel area in e'. (e") Bar graphs showing mean collagen fiber diameter measured in the three dimensional collagen gels shown in e. (f) Representative immunoblot of total (Stat3) and activated Stat3 (pStat3) levels in KC tumor cells cultured on soft or stiff polyacrylamide substrates. Results are normalized to total Stat3 and Gapdh. (f') bar graphs showing quantification of f. (g) Quantification of cytokine protein expression measured in the conditioned media of KC cells cultured on soft or soft polyacrylamide substrates. For in vitro bar graphs, results are the mean +/- SEM of 3 independent experiments. For in vivo experiments, N=5 mice per group. (*$p<0.05$; **$p<0.01$, ***$p<0.001$, ****$p<0.0001$, "ns" denotes not significant).

Loss of TGFβ signaling activates a JAK/Stat3 contractility feed forward circuit to induce ECM remodeling and tissue stiffening

G protein coupled receptor (GPCR)-mediated JAK activation not only stimulates Stat3 but activates ROCK and induces actomyosin-mediated cell contractility[219] and GPCR activation can activate Yap[209]. Stat3 activity is frequently elevated in pancreatic tumors[220,221] and KTC tumors express elevated cytokines. We therefore tested whether the matricellular-enriched fibrosis and elevated mechano-phenotype observed in the KTC mice could be mediated through elevated

pancreatic epithelial GPCR-JAK-ROCK-Stat3[222]. In keeping with this paradigm, we noted that pStat3 staining was, indeed, significantly higher in the pancreatic epithelium of the KTC mice (Fig. 3a, a'), even in the eight week old PanINs where the amount of infiltrating immune cells is quite low (Supplementary Fig. 4a, a').

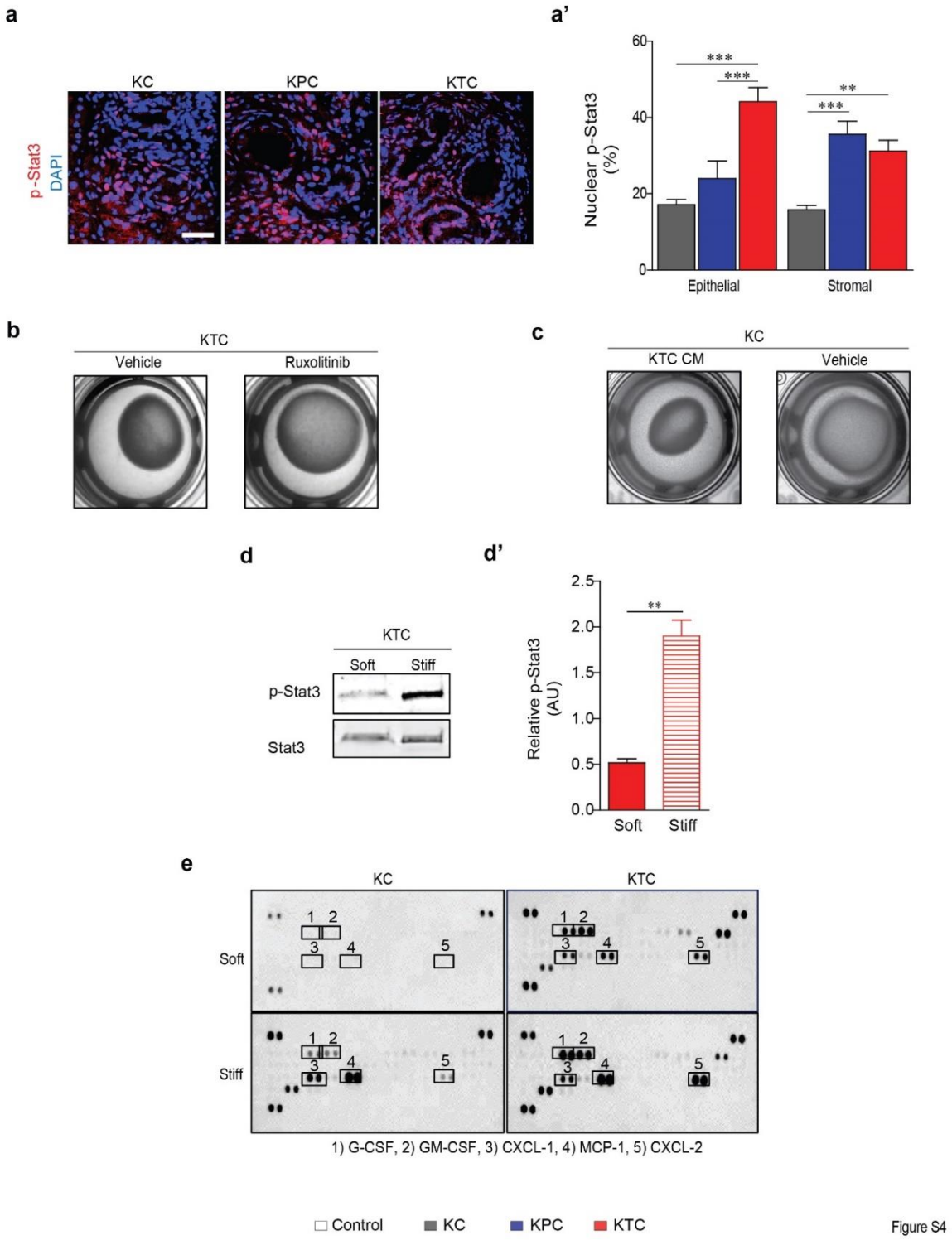

Pancreatic Cancer Figure S4.

(a) Representative immunofluorescence images of pancreatic tissue excised from 8 week old KC, KPC and KTC mice stained for pStat3 (red) and DAPI (blue). Scale bar, 50µm. **(a')** Bar graphs quantifying the level of stromal

versus epithelial pStat3 in the tissues stained in a. **(b)** Representative images of three-dimensional collagen gels incubated with KTC pancreatic epithelial tumor cells for 24 hours either with vehicle or the JAK inhibitor Ruxolitinib. **(c)** Representative images of three-dimensional collagen gels incubated with KC tumor cells treated with vehicle or the conditioned media from 48 hour cultured KTC tumor cells. **(d)** Representative immunoblot showing total (Stat3) and activated Stat3 (pStat3) levels in KTC tumor cells cultured on soft or stiff polyacrylamide substrates. **(d')** Bar graph showing the quantification of d. **(e)** Representative cytokines array images measured in the conditioned media of KC and KTC cells cultured on soft or soft polyacrylamide substrates. For *in vitro* bar graphs, results are the mean +/- SEM of 3 independent experiments. For *in vivo* experiments, N=5 mice per group. (*p<0.05; **p<0.01, ***p<0.001, ****p<0.0001, "ns" denotes not significant).

Indeed, while both the stroma and the PDACs in the KPC and KTC mice stained positively for pStat3, coincident with an abundant immune infiltrate[222], pStat3 was consistently higher in the KTC tumor pancreatic epithelium (Fig. 3a, a'). We also detected abundant pStat3 in non-stimulated, pancreatic epithelial cells isolated from KTC tumors, whereas no activity was detected in either the newly isolated KPC or the KC tumor cells (Fig. 3b). Moreover, the ability of the KTC tumor cells to contract collagen gels and to induce collagen remodeling was blocked by treatment with the JAK inhibitor Ruxolitinib (Fig. 3c, c", c"' and Supplementary Fig. 4b). We also noted that the 48 hour conditioned media from KTC tumor cells activated pStat3 in cultured KC cells (Fig. 3d, d'), and stimulated KC cell contraction and collagen remodeling, suggesting KTC cells secrete cytokines capable of inducing GPCR-JAK-ROCK-dependent contractility (Fig. 3e, e', e" and Supplementary Fig. 4c). Importantly, a stiff ECM can enhance GPCR-dependent Stat3 activation, and we observed higher steady state epithelial pStat3 and quantified higher levels of secreted cytokines in the media of Kras pancreatic tumor cells plated on a stiff ECM (Fig. 3f, f', g and Supplementary Fig. 4d, d', e). These findings not only identify epithelial JAK-ROCK-Stat3 signaling circuit as a candidate KTC tumor cell-specific

contractility mechanism that could drive ECM remodeling and drive a matricellular-enriched pancreatic fibrosis, they also imply that once stiffened, the rigid ECM will potentiate the activity of this pathway and would promote tumor aggression by activating mechano-activated pathways including Yap[191].

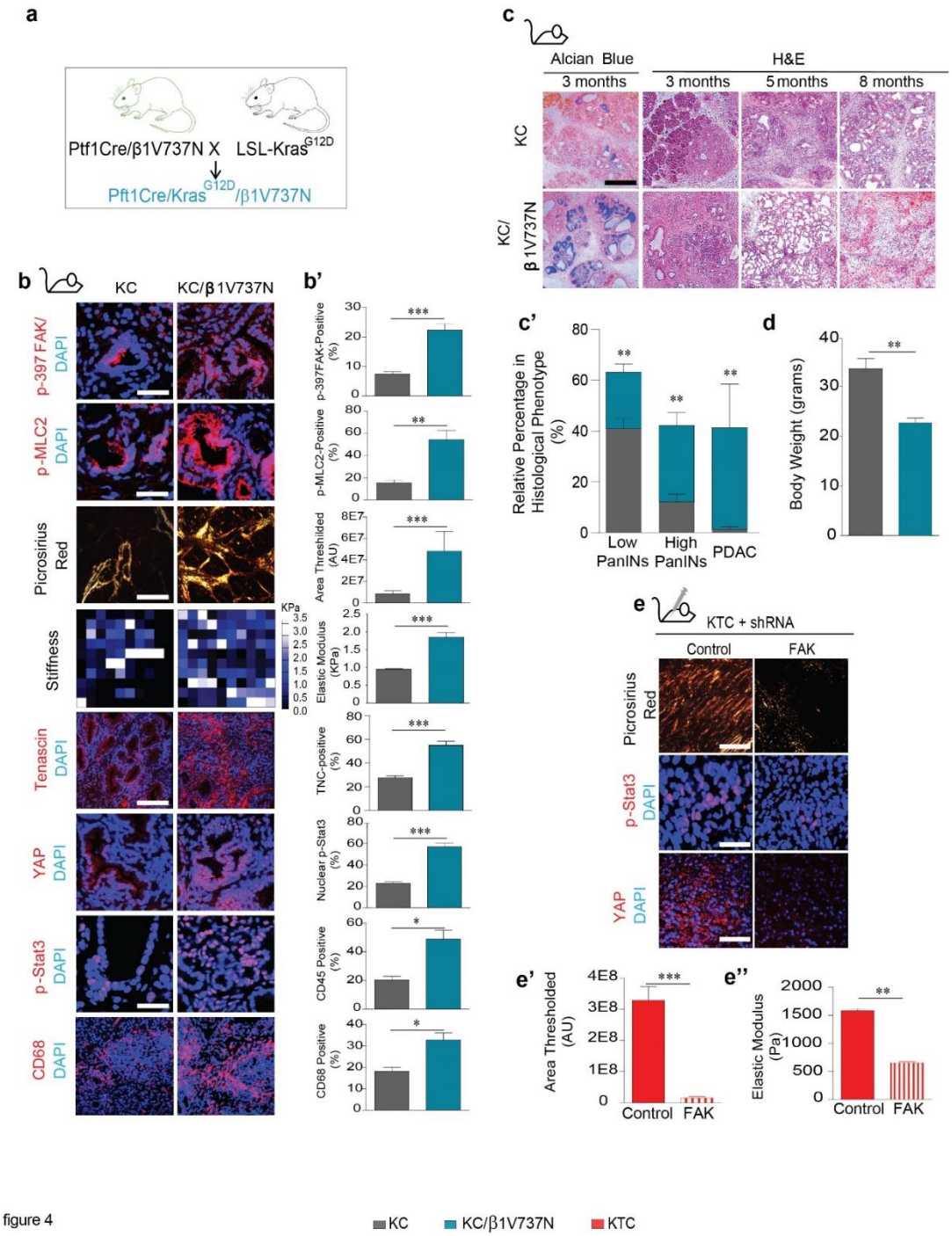

figure 4

Pancreatic Cancer Figure 4: Stat3 induces tissue fibrosis to accelerate Kras-induced PDAC.

(a) Cartoon of mouse manipulations used to study the impact of increasing pancreatic epithelial cell mechanosignaling using β1V737N on Kras-induced pancreatic malignancy. (b) Representative

immunofluorescence images of pancreatic tissues excised from 3 month old KC and KC/β1V737N mice stained for p397FAK (top panel; red) and p-MLC2 (2nd panel; red), Tenascin C (5th panel, red), YAP (6th panel, red), pStat3 (7th panel; red), scale bar, 50 μm, CD68 (8th panel; red), and DAPI (blue). Scale bar, 100μm. (3rd panel) Representative polarized light images of collagen fibers revealed by PR staining of pancreatic tissue described above. Scale bar, 75μm. b. (4th panel) Representative force maps of ECM stiffness measured using atomic force microscopy indentation in pancreatic tissue described above. (b') Bar graphs quantifying the tissue images shown in the panels in b. (c) Representative alcian blue images of transformed ducts and representative H&E images of pancreatic tissue and tumor morphology. Scale bar, 100μm. c' corresponding quantification of c. (d) Bar graphs showing mouse body weight at study termination. (e) (top) Representative polarized light images of collagen fibers revealed by PR staining of pancreatic tissues in nude mice injected with KTC tumor cells expressing either a control shRNA or a FAK shRNA. Scale bar, 75 μm (top panel). Representative immunofluorescence confocal images of pancreatic tissue described above in e stained for pStat3 (red, 2nd panel; scale bar, 25 μm), YAP (red 3rd panel; scale bar, 75 μm) and DAPI (blue). (e') Bar graphs quantifying total collagen fibril content of picrosirius stained tissue shown in e. (e") Bar graphs quantifying average elastic modulus (Pa) measured by atomic force microscopy of pancreatic tissue shown in e. For in vivo experiments, N=5 mice per group. (*$p<0.05$; **$p<0.01$, ***$p<0.001$, ****$p<0.0001$, "ns" denotes not significant).

Tumor cell tension induces JAK-Stat3 signaling and matricellular-enriched fibrosis to accelerate Kras PDAC

To directly test whether epithelial contractility, per se, could induce a matricellular-enriched fibrosis and PDAC progression we crossed transgenic mice expressing Ptf1α-Cre with mice expressing a conditional V737N β1 integrin, which recapitulates tension-dependent integrin clustering and promotes focal adhesion signaling to induce ROCK-dependent cell contractility in the pancreatic epithelium (Supplementary Fig. 5a) [12,223,224]. Immunofluorescence staining for ^{p397}FAK confirmed elevated focal adhesion kinase activity in the pancreatic epithelium in the β1V737N mice, and revealed higher epithelial contractility by increased pMLC2 and higher

mechano-signaling by elevated nuclear Yap targets such as CTGF (Supplementary Fig. 5b, c). Increased ductal collagen was indicated by intense PR staining around the epithelium (Supplementary Fig. 5b) while SHG revealed thicker, denser collagens (not shown), and AFM indentation quantified a stiffened ECM surrounding the ductal epithelium (Supplementary Fig. 4b). The presence of pStat3 positive pancreatic epithelial cells in the β1V737N mice, even in the absence of any activating oncogene or pre-existing inflammation, confirmed that epithelial tension can enhance p Stat3 (Supplementary Fig. 5b), a finding that we verified in a mouse cohort treated with a FAK inhibitor by the loss of pStat3 together with reduced ^{p397}FAK, pMLC2 and a matricellular-enriched fibrosis (Supplementary Fig. 6a, a'). Consistently, pancreatic orthotopic tumors formed by KTC cells lacking FAK were less fibrotic, and the tumors were softer and lacked epithelial pStat3 (Fig. 4e, e', e" and Supplementary Fig. 7a, a', b).

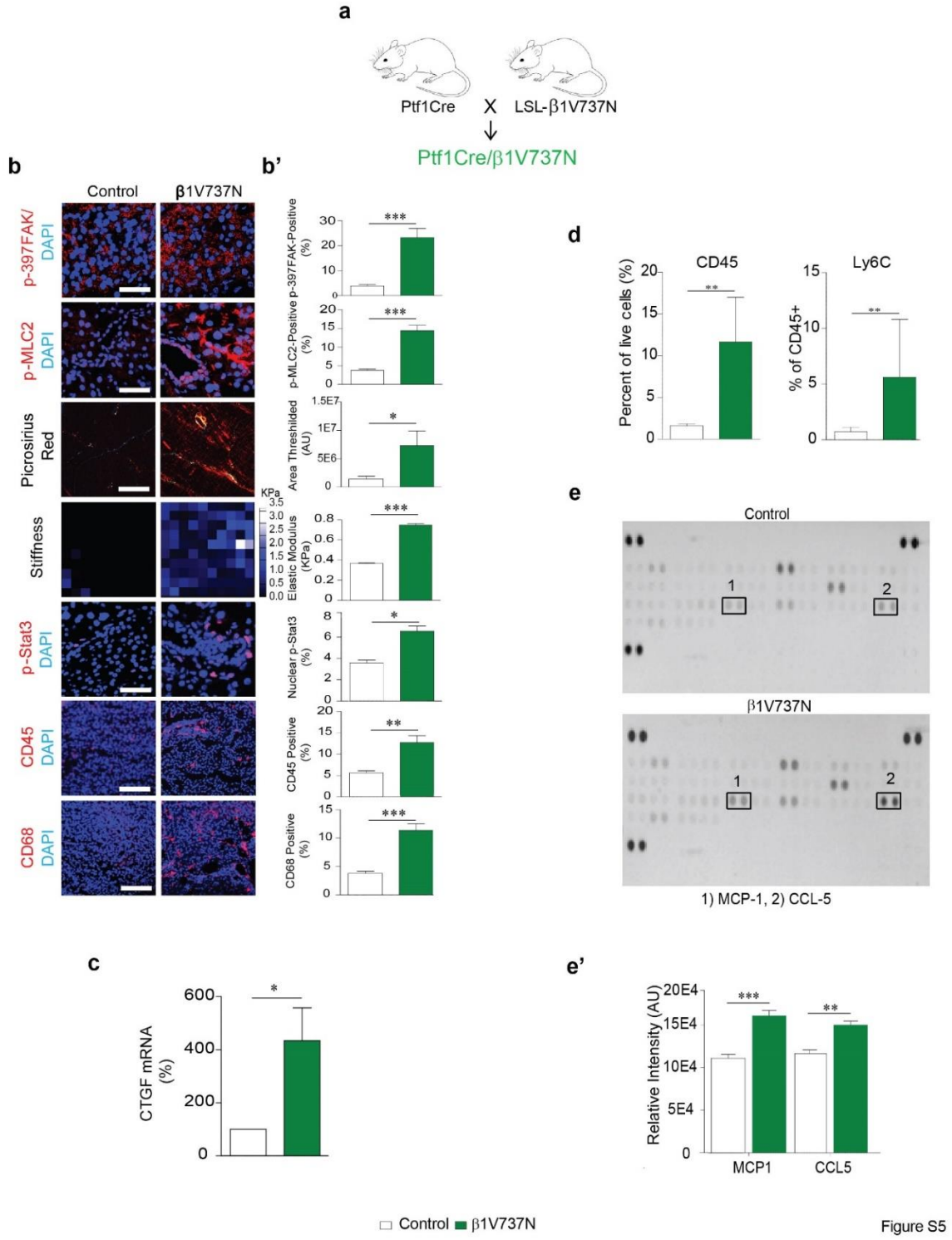

Figure S5

Pancreatic Cancer Figure S5.

(a) Graphic of mouse manipulations used to study the impact of β1V737N expression in the pancreatic epithelium on tissue fibrosis. **(b)** Representative immunofluorescence images of pancreatic tissues excised from 3 month old

control and β1V737N mice stained for ^{p397}FAK (top panel; red) and pMLC2 (2nd panel; red), pStat3 (5th panel; red), scale bar, 50 μm, CD45 (6th panel; red) and CD68 (7th panel; red), scale bar, 100μm, and DAPI (blue). **(b)** (3rd panel) Representative polarized light images of collagen fibers revealed by picrosirius red (PR) staining of pancreatic tissue described above. Scale bar, 75μm. **(b)** (4th panel) Representative force maps of ECM stiffness measured using AFM indentation in pancreatic tissue described above. **(b')** Bar graphs quantifying the tissue images shown in the panels in b. **(c)** Bar graphs quantifying CTGF mRNA expression for pancreatic tissue shown in b. Results are normalized to β-actin. **(d)** Bar graphs showing quantification of total pancreatic CD45+ and Ly6C immune cells as determined by flow cytometry. **(e)**. Representative cytokines array images measured in pancreatic tissue shown in b. **(e')** Bar graphs showing quantification of cytokine levels shown in e.

To directly assess the relationship between epithelial mechanosignaling and PDAC development, we bred Ptf1α-Cre V737N β1 integrin mice with KC mice and monitored the animals for development of a matricellular-enriched fibrosis, elevated tissue mechanics, pStat3 signaling and tumor formation (Fig. 4a). As early as 5 weeks of age, the pancreatic epithelium in the KC mice expressing the β1V737N transgene had high ^{p397}FAK and pMLC2 activity, and the amount and distribution of deposited collagen and ECM stiffening was highest around the ductal epithelium (Fig. 4b, 4b'), and markedly similar to what we documented in the developing KTC lesions (compare SHG in Fig. 2a to PR in Fig. 4b).

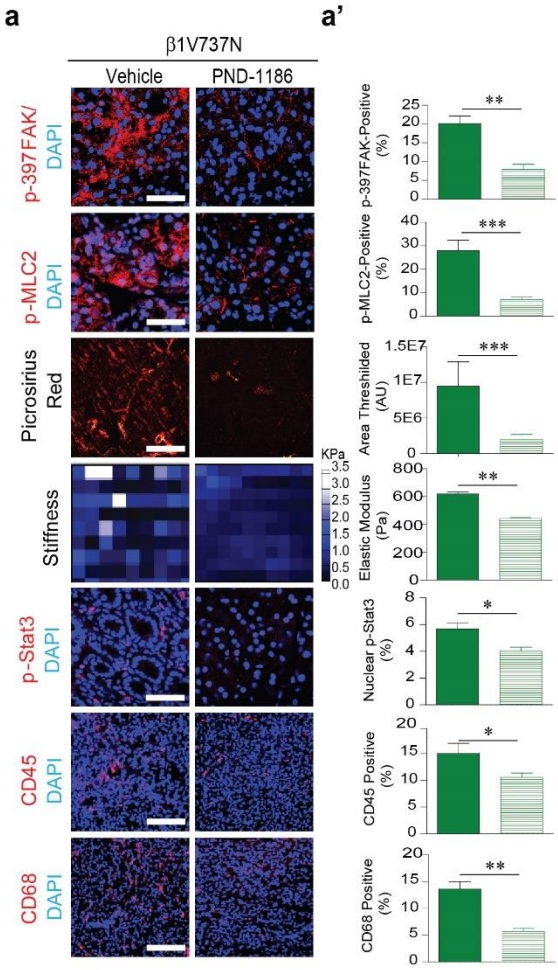

Pancreatic Cancer Figure S6.

(a) Representative immunofluorescence images of 6 week old pancreatic tissue excised from β1V737N mice treated with vehicle or the FAK inhibitor PND-1186 stained for ^{p397}FAK (top panel; red), pMLC2 (2nd panel; red), pStat3 (5th panel; red), scale bar, 50 µm, CD45 (6th panel), CD68 (7th panel; red) and DAPI (blue). Scale bar, 100µm. **(a)** (3rd panel) Representative polarized light images of collagen fibers revealed by PR staining of pancreatic tissue described above. Scale bar, 75µm. **(a)** (4th panel) Representative maps of ECM stiffness measured using AFM indentation in pancreatic tissue described above. **(a')** Bar graphs quantifying the tissue images shown in the panels in a.

Moreover, consistent with the matricellular-enriched fibrosis observed in the patient samples lacking pSmad and the KTC lesions, we also detected abundant tenascin and higher levels of

epithelial pStat3 in the KC/β1V737N mice (Fig. 4b, b'). This was accompanied by a significant increase in infiltrating CD45 immune cells (Supplementary Fig. 7c) and CD68 macrophages (Fig. 4b, b'), which FACS analysis suggested were tumor promoting (Supplementary Fig. 7c). Indeed, cytokine array analysis demonstrated that the KC/β1V737N mouse pancreas expressed significantly higher levels of pro-inflammatory factors C5α and IL1 (Supplementary Fig. 7d, d'). Finally and importantly, histological analysis confirmed that KC/β1V737N mice developed chronic pancreatitis as early as 3 months of age (Fig. 4c). Alcian blue staining of 3 month old KC/V737N mouse pancreatic tissue revealed that they had progressed to advanced, high grade PanINs that were evenly distributed throughout the tissue and H&E showed that 38% of the animals developed frank PDAC by 5-8 months of age, with accompanying physiological trauma, including loss of body weight (Fig. 4c, c', d). These results reveal that tumor cells with elevated mechano-signaling are more contractile and, by virtue of their ability to stiffen the ECM, induce a matricellular-enriched fibrosis, activate tension-regulated genes and stimulate an immune response, can promote pancreatic transformation.

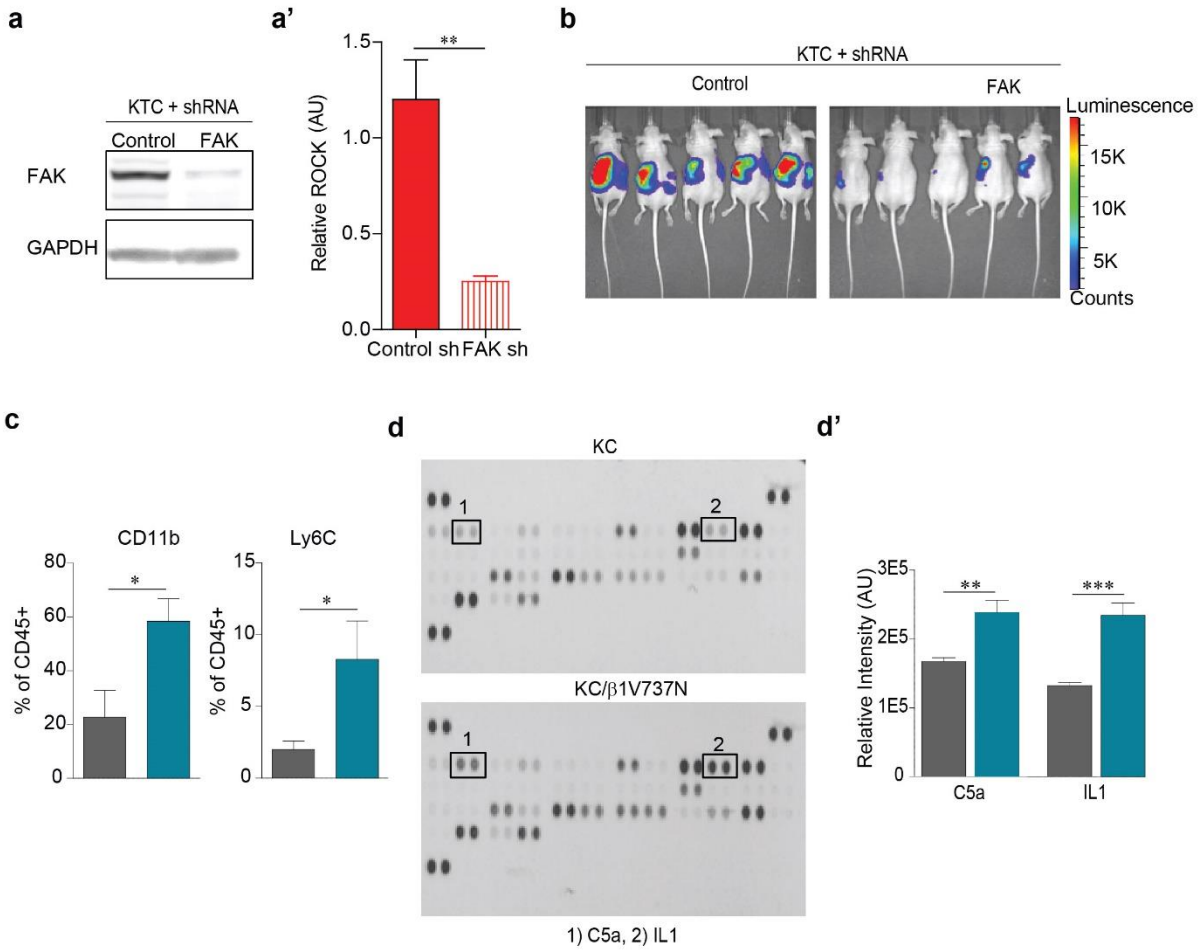

Pancreatic Cancer Figure S7.

(a) Representative immunoblot showing FAK level in KTC tumor cells expressing either a control shRNA or an shRNA to FAK. Results are normalized to GAPDH. **(a')**. Bar graph showing the quantification of a. **(b)** Representative bioluminescence images of tumor growth in nude mice 3 weeks after injection with KTC pancreatic tumor cells expressing either a control shRNA or an shRNA to FAK. **(c)** Bar graphs showing quantification of total pancreatic Ly6C and CD11b immune cells as determined by flow cytometry. **(d)** Representative cytokines array images measured in KC and KC/β1V737N pancreatic tissue. **(d')**. Bar graph showing the quantification of d.

Stat3 induces tissue fibrosis to accelerate Kras-induced PDAC

We next explored the relationship between activated Stat3, cell contractility and a pancreatic matricellular-enriched fibrosis in PDAC. KC mice were crossed into mice expressing one allele

of a constitutively active Stat3 (Stat3C, Fig. 5a)[225]. We first noted that Stat3C mice contained numerous cells within the pancreas that stained positively for activated Stat3 (Supplementary Fig. 9a, a') and that the level of pStat3 increased dramatically following expression of an activated Kras (Fig. 5b, b').

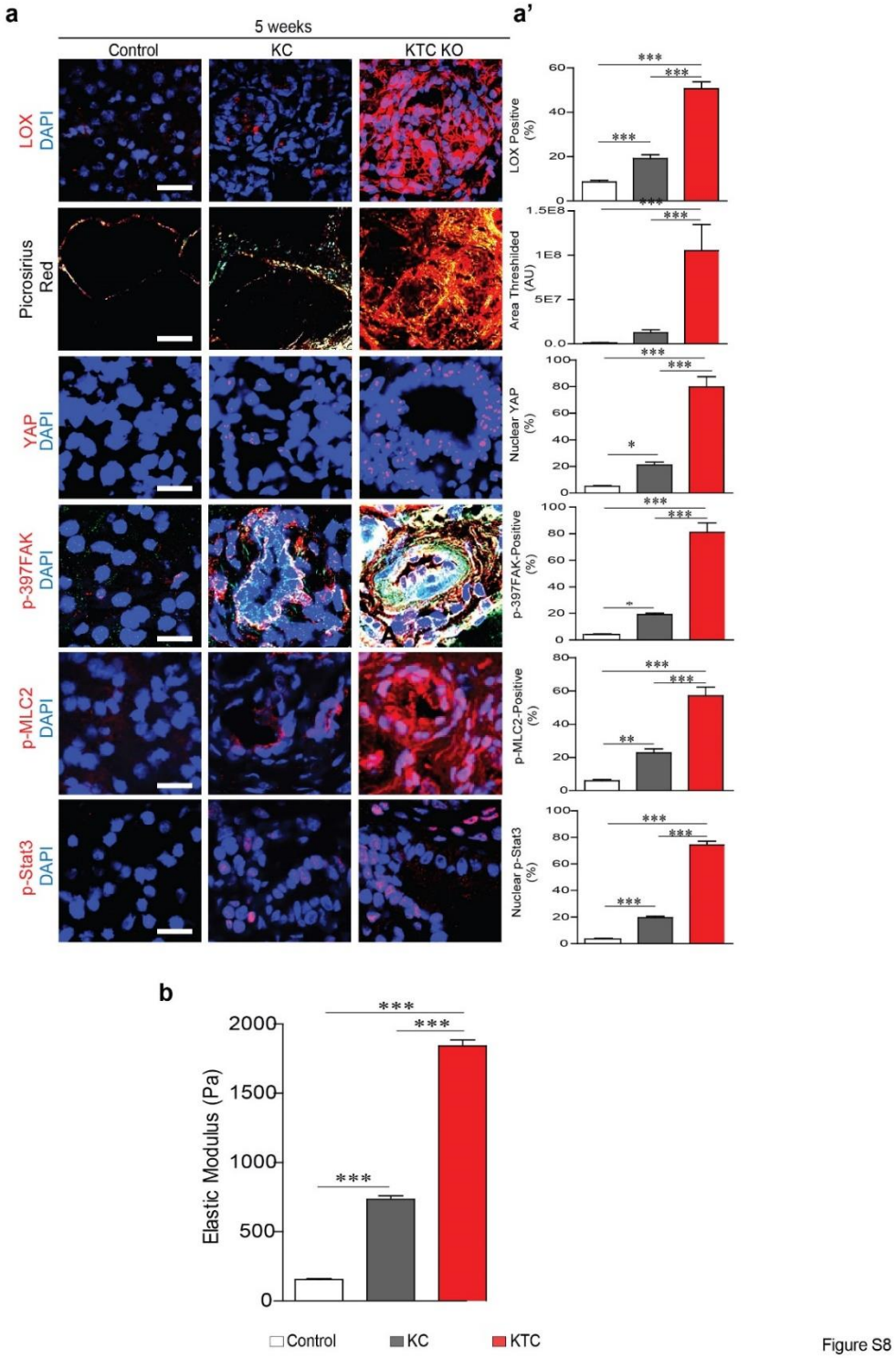

Figure S8

Pancreatic Cancer Figure S8.

(a) Representative immunofluorescence images of pancreatic tissues excised from 5 week old control, KC and homozygous KTC (KTC KO) mice stained for LOX (top panel; red), scale bar 50 µm, YAP (3rd panel, red), ^{p397}FAK

(4th panel, red) and p-MLC2 (5th anel, red) and pStat3 (6th panel, red) scale bar 20 µm, and DAPI (blue). **(a)** (2nd panel) Representative polarized light images of collagen fibers revealed by PR staining of pancreatic tissue described above. Scale bar, 75µm. a'. Bar graphs quantifying the tissue images shown in the panels in a. **(b)** Quantification of ECM stiffness measured by AFM in pancreatic tissue shown in a. For *in vivo* experiments, N=5 mice per group. (*p<0.05; **p<0.01, ***p<0.001, ****p<0.0001, "ns" denotes not significant).

We also quantified higher numbers of CD45 immune cells and CD68 macrophages within the Stat3C pancreatic tissues (Supplementary Fig. 9a, a') and found that these increased substantially with Kras activation, consistent with induction of a pro-inflammatory phenotype (Fig. 5b, b'). Indeed, the pancreatic tissues of the Stat3C/Kras mice showed marked pancreatitis that developed into frank PDAC, which compromised the survival of the mice (Fig. 5c). Consistent with a link between JAK/Stat3 activity and ROCK activity, immunofluorescence staining revealed that, while tumors were stiffer and pMLC2 was quite high in the KC/Stat3C mice, pMLC2 levels were already elevated in the pancreatic tissues of the Stat3C mice, even in the absence of Kras (Fig. 5b, b', d and Supplementary Fig. 9a, a').

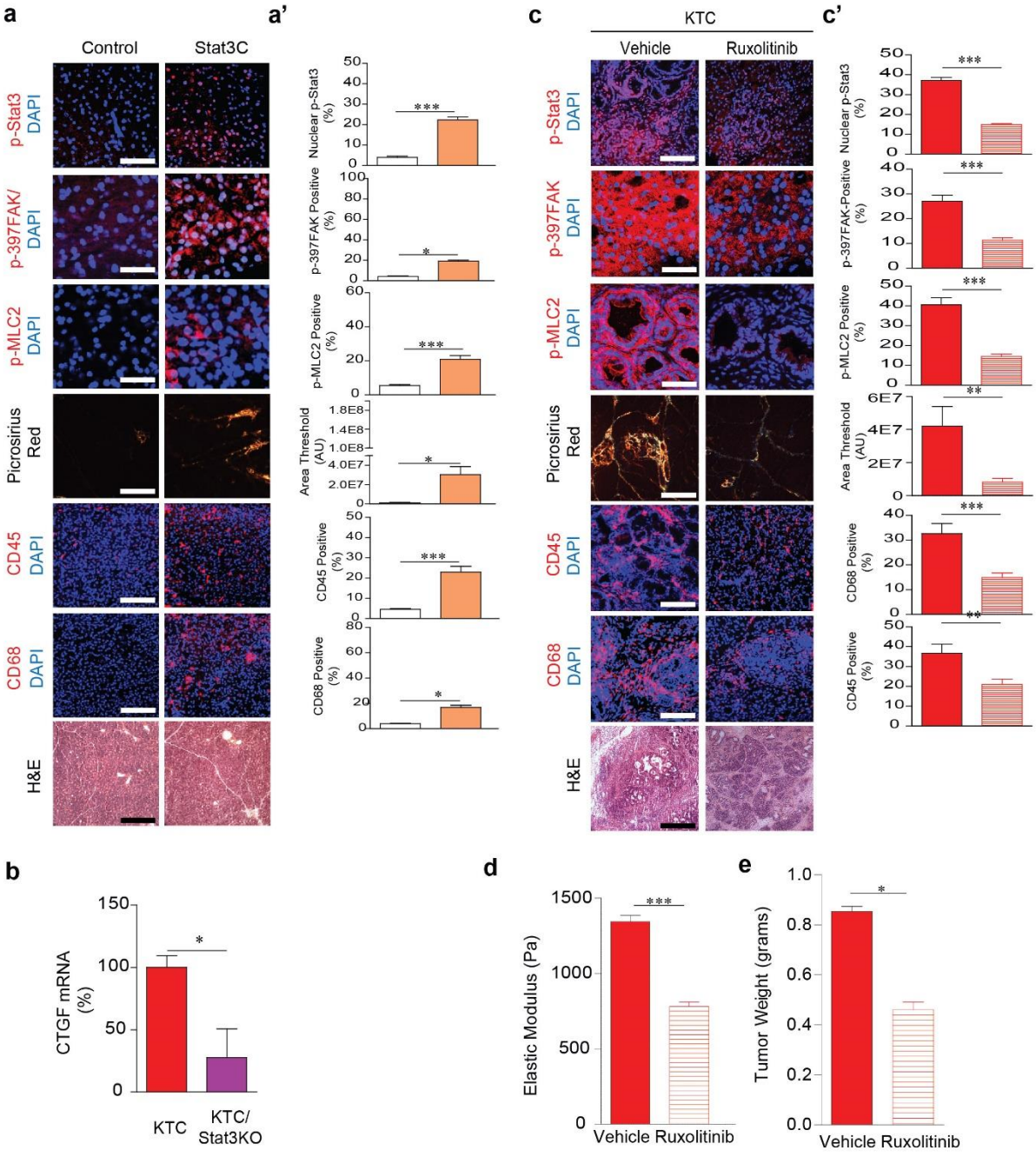

Pancreatic Cancer Figure S9.

(a) Representative immunofluorescence images of pancreatic tissues excised from 5 week old control and Stat3C mice stained for pStat3 (top panel; red), scale bar, 75 µm, ^{p397}FAK (2nd panel; red) and pMLC2 (3rd panel; red), Scale bar, 50 µm, CD45 (5th panel; red), CD68 (6th panel; red), and DAPI (blue). Scale bar, 100µm. **(a)**. (4th panel) Representative polarized light images of collagen fibers revealed by PR staining of pancreatic tissue described

above. Scale bar, 75µm. **(a)** (7th panel) Representative phase contrast images of H&E stained pancreatic tissue as described above. Scale bar, 100µm. **(a')** Bar graphs quantifying the tissue images shown in the panels in a. **(b)** Bar graphs quantifying CTGF mRNA expression for pancreatic tissue excised from 5 week old homozygous KTC (KTC KO) (Control) and KTC/Stat3 KO mice (Stat3 KO). Results are normalized to β-actin. **(c)** Immunofluorescence confocal images of pancreatic tissues from 6 week old KTC (het) mice treated with either vehicle or the JAK inhibitor Ruxolitinib stained for pStat3 (top panel; red), scale bar, 75 µm, ^{p397}FAK (2nd panel; red) and pMLC2 (3rd d panel; red), scale bar, 50 µm, CD45 (5th panel; red), CD68 (6th panel; red), scale bar, 100 µm, and DAPI (blue). **(c)** (4th panel) Representative polarized light images of collagen fibers revealed by PR staining of pancreatic tissue described above. Scale bar, 75µm. **(c)** (7th panel) Representative phase contrast images of H&E stained pancreatic tissue as described above. Scale bar, 100µm. **(c')**. Bar graphs quantifying the tissue images shown in the panels in c. **(d)** Quantification of ECM stiffness measured by AFM in pancreatic tissue shown in c. **(e)** bar graphs quantifying the weight of the pancreatic tumors shown in c. For *in vivo* experiments, N=5 mice per group. (*p<0.05; **p<0.01, ***p<0.001, ****p<0.0001, "ns" denotes not significant).

Polarized light imaging of PR stained tissue revealed that the pancreas of the Stat3C mice already contained abundant mature type I collagen (Supplementary Fig. 9a, a'). Indeed, we were able to detect elevated ^{p397}FAK throughout the pancreas of the Stat3C mice (Supplementary Fig. 9a, a'). These findings not only demonstrate that there are links between pStat3 and tissue inflammation, but they also suggest that pStat3 induces ROCK-dependent ECM remodeling and stiffening to drive fibrosis and mechanosignaling in PDAC.

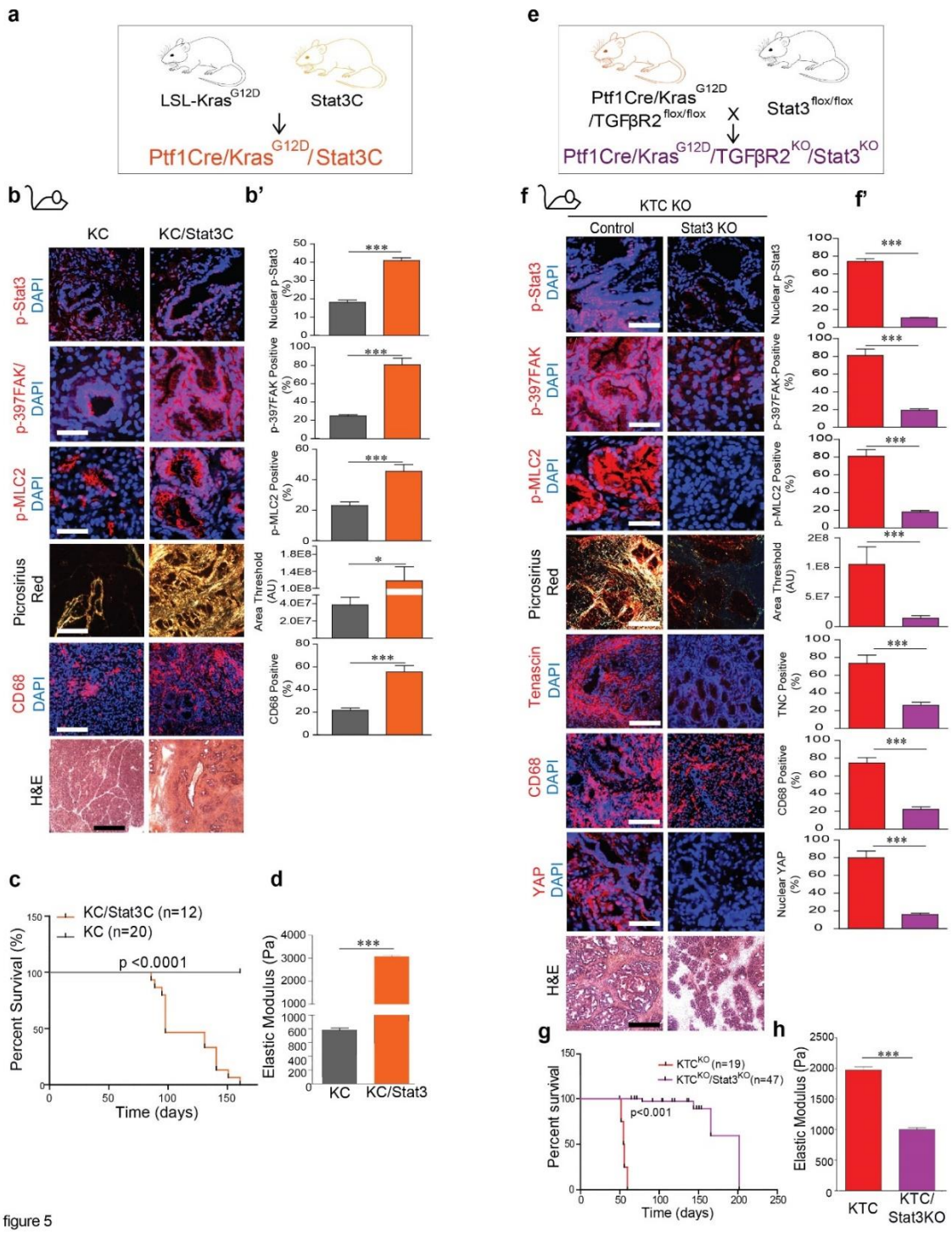

figure 5

Pancreatic Cancer Figure 5: Stat3 induces tissue fibrosis to accelerate Kras-induced PDAC.

(a) Cartoon depicting the mouse crosses used for the activated Stat3C manipulations. **(b)** Representative immunofluorescence images of pancreatic tissues excised from 5 week old KC and KC/Stat3C mice stained for

pStat3 (top panel; red), scale bar, 75 µm, p397FAK (2nd panel; red) and pMLC2 (3rd panel; red), Scale bar, 50 µm, CD68 (5th panel; red), and DAPI (blue). Scale bar, 100µm. b. (4th panel) Representative polarized light images of collagen fibers revealed by PR staining of pancreatic tissue described above. Scale bar, 75µm. b. (7th panel) Representative phase contrast images of H&E stained pancreatic tissue as described above. Scale bar, 100µm. b' Bar graphs quantifying the tissue images shown in the panels in b. **(c)** Kaplan-Meier graph showing survival of KC, Stat3C, and KC/Stat3C mice. **(d)** Quantification of ECM stiffness measured by atomic force microscopy in pancreatic tissue shown in b. **(e)** Cartoon depicting the mouse crosses used for the Stat3 knock studies. **(f)** Representative immunofluorescence images of pancreatic tissues excised from 5 week old 5 week old homozygous KTC (KTC KO) (Control) and KTC/Stat3 KO mice (Stat3 KO) stained for pStat3 (top panel; red), scale bar, 75 µm, p-397FAK (2nd panel; red) and p-MLC2 (3rd panel; red), scale bar, 50 µm, Tenascin (5th panel; red), CD68 (6th panel; red), scale bar, 100µm, YAP (7th panel; red) scale bar, 50µm, and DAPI (blue). (f) (4th panel) Representative polarized light images of collagen fibers revealed by PR staining of pancreatic tissue described above. Scale bar, 75µm. (f) (8th panel) Representative phase contrast images of H&E stained pancreatic tissue as described above. Scale bar, 100µm. f' Bar graphs quantifying the tissue images shown in the panels in f. **(g)** Kaplan-Meier graph showing survival of KTC and KTC/Stat3 KO mice. **(h)** Quantification of ECM stiffness measured by atomic force microscopy in pancreatic tissue shown in f. For *in vivo* experiments, N=5 mice per group. (*p<0.05; **p<0.01, ***p<0.001, ****p<0.0001, "ns" denotes not significant).

Stat3 enhances epithelial contractility to induce PDAC matricellular fibrosis and tumor aggression to compromise patient survival

To establish a causal relationship between pStat3, tissue mechanics and a matricellular-enriched fibrosis and PDAC development, we crossed mice expressing Kras (Kras$^{LSL\text{-}G12D/+}$) with mice homozygous for loss of both of the TGF β receptor 2 alleles (Tgfbr2$^{flox/flox}$, which exhibit an accelerated matricellular-enriched fibrotic phenotype and PDAC development, Supplementary Fig. 8a, b) and Stat3 both in the pancreatic epithelium (Stat3$^{flox/flox}$, Ptf1a-Cre) to create KTC

KO/Stat3 KO mice (Fig. 5e)[194,226]. Immunostaining confirmed efficient deletion of Stat3 in the pancreatic epithelium (Fig. 5f, f') and showed that this was accompanied by reduced CD68 tissue infiltration, consistent with decreased inflammation (Fig. 5f, f'). Loss of epithelial pStat3 was also accompanied by a significant reduction in epithelial ^{p397}FAK, pMLC2 and nuclear Yap levels and Yapactivity as indicated by lower CTGF expression (Fig. 5f, f' and Supplementary Fig. 9b). Also, pancreatic tissues with deleted epithelial Stat3 presented with a striking reduction in a matricellular-rich fibrosis and ECM stiffness, along with increased survival (Fig. 5f, f', g, h). Direct links between a matricellular-rich fibrotic phenotype, mechanics and pStat3 were confirmed in a cohort of mice treated with the JAK inhibitor Ruxolitinib, which not only inhibited pStat3 activity but also reduced ^{p397}FAK, pMLC2, collagen fibrillogenesis and ECM stiffening (Supplementary Fig. 9c, c', d) as well as Yap activation (not shown). Moreover, in the absence of a JAK-driven matricellular-rich fibrosis - mechanosignaling, Stat3-dependent inflammation and PDAC development were reduced (Supplementary Fig. 9c, c', e). Thus, tumor cell pStat3 not only stimulates inflammation, but increases epithelial cell tension and activates mechanosignaling to drive a matricellular-rich fibrosis and promote PDAC development and tumor aggression. Importantly and of clinical relevance, we detected elevated levels of tenascin and high nuclear YAP, SOX2 and pStat3 in the mesenchynmal-like, vimentin positive PDAC biopsies that we detected lower pSMAD2 in, that were excised from the patients with the shorter medium survival (Fig. 6a, a'). These findings imply that patients with genetic/epigenetic alterations that compromise TGFβ signaling are uniquely mechanically-activated and develop a unique, matricellular-enriched stroma that contributes to their aggression through YAP and SOX2 activation (Fig. 6b). Patients lacking TGFβ signaling may represent a unique cohort of PDACs towards which anti-stromal therapies should only be judiciously applied.

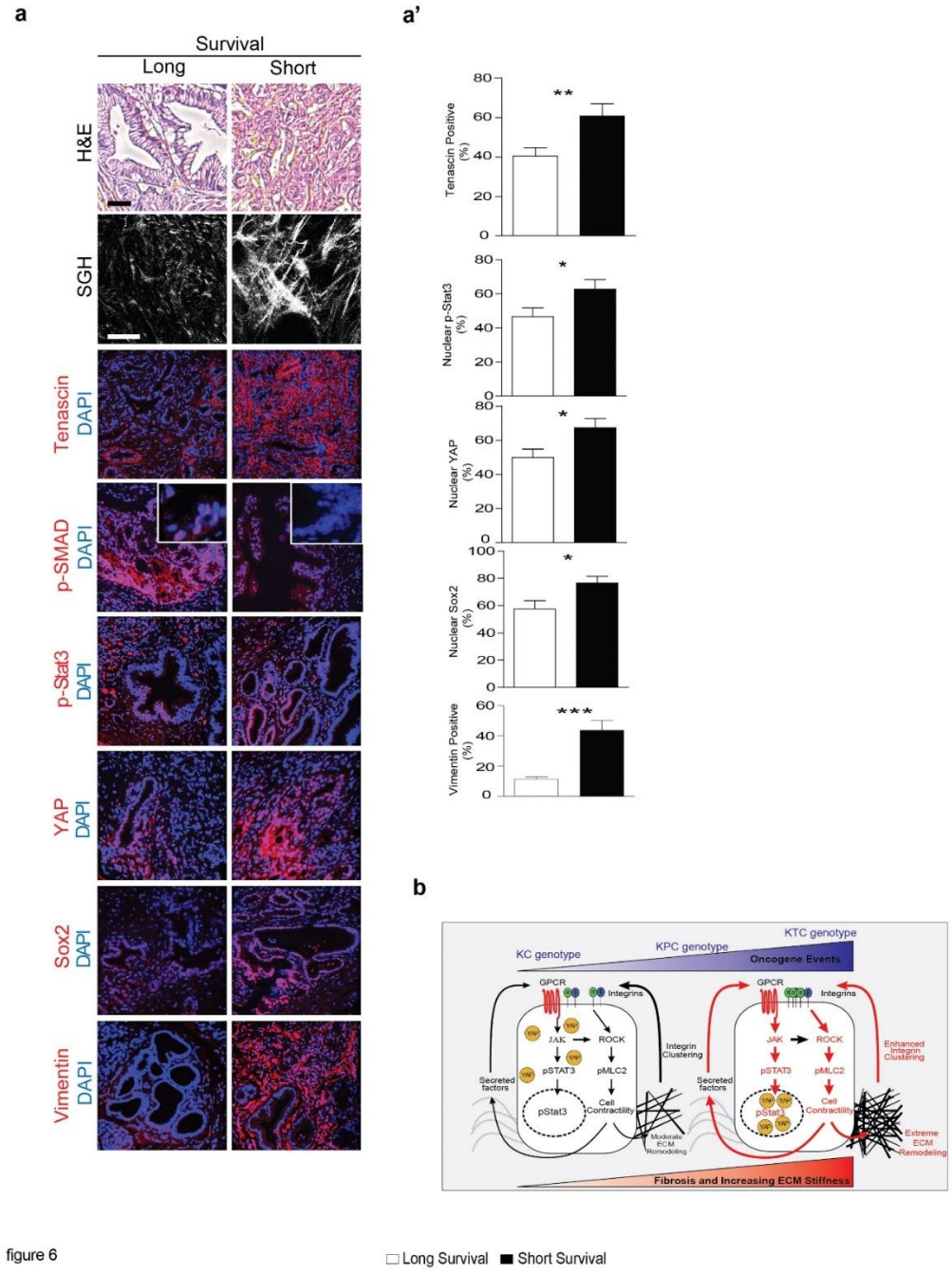

figure 6

Pancreatic Cancer Figure 6: Stat3 enhances epithelial contractility to induce PDAC matricellular fibrosis and tumor aggression to compromise patient survival.

(a) Representative photomicrographs of H&E from PDAC patients cohort representing patients with a median short survival of 11-289 days (n=29) and median long survival of 1090-3298 days (n=28) (top panel). Scale bar, 100µm.

Representative SHG images of extracellular collagen architecture in the pancreatic tissue around the epithelial ductal region in tissue described above (2nd panel). Scale bar, 75μm. Representative immunofluorescence images of pancreatic tissue described above stained for Tenascin C (red, 3rd panel), pSMAD2 (red, 4th, panel), pStat3 (red, 5th panel), YAP (red, 6th panel), Sox2 (red, 7th panel), Vimentin (red, 8th panel) and DAPI (blue). Scale bar, 75μm. **(a')** Bar graphs quantifying the tissue images shown in the panels in a. **(b)** Cartoon depicting the epithelial JAK-ROCK-Stat3-YAP feed forward circuit and its potentiation by a stiff extracellular matrix microenvironment.

Discussion

While PDACs present with inarguably elevated stromal fibrosis, recent findings suggest that collagen abundance may associate with better patient prognosis, with high collagen content correlating with a well-differentiated PDAC phenotype[213,227]. Nevertheless, elevated fibrillar collagen has repeatedly been implicated in both PDAC aggression and treatment resistance[212]. To address these contradictory perspectives, we examined the relationship between tumor genotype, tissue tension, and fibrosis composition and architecture in PDAC progression and aggression. Using a series of well-characterized GEMMs, we identified a unique matricellular-stromal signature that associates with PDAC genotypes that elevate pancreatic cell contractility and tumor aggression. This coordination of genetically-induced tumor cell contractility and a matricellular-enriched fibrosis "tunes" PDAC tissue tension and ultimately activates Yap to promote tumor aggression. This interplay suggests that bulk collagen content is a poor surrogate for the multi-facted contributions of PDAC fibrosis to cancer aggression. Specifically, genetically-elevated epithelial tension promoted Yap activation and tumor aggression by stimulating Stat3-mediated ECM remodeling and stiffening of the stroma surrounding the developing pancreatic lesions. Consistently, ectopically-increasing epithelial mechanosignaling induced a matricellular-rich fibrosis and stiffened the stroma adjacent to the pancreatic

epithelium, and activated Yap and Stat3 to induce inflammation and accelerate pancreatic transformation and induce aggression. Mechanistically, genetically-increasing epithelial Stat3 activity amplified epithelial tension to drive a matricellular-enriched stiffened phenotype and accelerate malignancy, whereas genetic-ablation of epithelial Stat3 reduced epithelial tension, diminished fibrosis and tempered tumor aggression. Our findings provide the first direct evidence that PDAC genotype calibrates tumor cell contractility to modulate the fibrotic phenotype of the tissue and by so doing modifies the pathology of the resultant cancer.

By exploiting a series of GEMMs, we were able to elucidate that the matricellular-enriched fibrotic phenotype we clinically-linked to the increased tumor cell contractility and loss of TGFβ signaling was driven by a highly conserved JAK/Stat3 cytokine feed forward circuit[219]. We demonstrated, for the first time, that in the absence of TGFβ signaling the Kras transformed tumor epithelium exhibits a significantly elevated actomyosin-mediated tension that is stimulated by an autocrine, cytokine-induced JAK-ROCK-Stat3 mechanosignaling circuit which conditions, remodels and stiffens the ECM adjacent to the developing pancreatic lesions to further amplify pStat3 signaling and drive tumor progression. Our data showed that this feed forward circuit potentiates a Stat3-mediated epithelial pro-inflammatory phenotype and promotes FAK-dependent Yap activation to drive tumor progression and aggression. Indeed, while inflammation and fibrosis can both independently promote pancreatic transformation and aggression, our findings describe a novel mechanism whereby Stat3-mediated tumor aggression is able to directly induce epithelial contractility to drive ECM stiffening and modify the fibrotic response[220,221]. Of clinical relevance, we demonstrated that nuclear YAP and YAP targets are progressively increased as a function of PDAC transformation and tissue fibrosis, and we showed

that this phenotype is significantly accelerated by Stat3-driven, contractility-mediated tissue stiffening (compare Fig. 2a to Fig. 5f). Our clinical findings revealed that the least differentiated PDACs and the PDACs developing in patients with the shortest survival that lacked TGFβ signaling also had the highest epithelial contractility and expressed elevated pSTAT3, YAP and the YAP target SOX2; all transcriptional regulators that have been implicated in tumor aggression and epithelial-to-mesenchymal transition[202–205]. Indeed, these same YAP and SOX2 expressing tumors also stained strongly for markers of a mesenchymal-like phenotype including vimentin and tenascin C (Fig. 6a, a')[228–230]. Given that YAP signaling can drive Kras-independent PDAC growth and survival, these findings imply that fibrotic PDAC tumors may naturally evolve towards Kras independence and that this phenotype will be potentiated by specific tumor genotypes including loss of TGFβ signaling. Accordingly, these findings may need to be taken into consideration when designing treatment strategies to treat pancreatic cancer patients with drugs such as next generation Ras inhibitors or anti stromal therapies[191,204]. Such results may also provide a rationale for the failures of classic anti-stromal therapies which do not target epithelial-driven fibrosis (NCT01472198)[182–184]. In this regard, our data present one plausible explanation for the mixed response of PDAC cancer patients to anti-stromal therapies, and suggest that FAK and JAK inhibitors, which target both stromal and epithelial-driven fibrosis, and both of which reduced YAP and tenascin induction, may comprise more efficacious therapeutic options.

While the magnitude of the fibrotic response derived from each distinct PDAC genotype initially varied, all of the PDAC models used in our studies eventually trended towards the development of fibrosis, albeit with different end stage fibrotic phenotypes. Thus, although the

KPC model demonstrated muted epithelial contractility and initial lower levels of tissue tension compared to the highly fibrotic KTC model, KPC tumor progression was eventually accompanied by an activated stroma that developed into a robust fibrotic response, a progressive stiffening of the ECM and accumulation of high nuclear Yap, in at least a subset of pancreatic tumor cells. The data suggest a primary tumor evolution towards the mesenchymal-like features often observed in patients presenting with recurrent PDAC. In fact, mesenchymal-like PDACs express higher levels and activity of YAP which, in turn, feeds back to further promote a pro-fibrotic, mesenchymal-like tumor phenotype both directly and via stimulation of SOX2. Our results thereby suggest that patients presenting with high grade PDAC will exhibit a highly mechanoresponsive epithelial phenotype early in PDAC progression while patients presenting with low grade disease will exhibit a gradual elevation of tissue fibrosis leading to eventual mechano-mediated YAP activation in the epithelial and stromal compartments by end state PDAC, as well as in recurring tumors. Given that YAP drives an EMT and mesenchymal-like tumor cells exhibit stromally-independent survival and growth, stromal ablation in PDAC patients with pre-existing disease or aggressive genotypes would predictably fail. Thus, our results may explain why ablation of fibrosis does not always block PDAC progression and, in some instances, actually promotes tumor aggression and why recent clinical trials using anti-stromal fibrotic agents failed to provide benefit to patients. Indeed, given that Kras-dependency is strongly linked to epithelial status[231] which diminishes with EMT and that YAP drives PDAC aggression independently of Kras by activating an EMT-like program[204], most PDAC patients may similarly exhibit resistance to targeted therapies including receptor tyrosine kinases and their downstream effectors and new generation Ras therapies. Importantly, our studies suggest that novel treatment modalities holistically targeting both epithelial and stromal-driven fibrosis,

cellular contractility and YAP activity, such as combinatory FAK/JAK inhibitor cocktails, will likely prove to be more efficacious therapeutic strategy with which to treat PDAC patients. These observations are consistent with previous implications of YAP in mechanotrasduction[143] and provide a mechanistic rationale with which to design future therapeutic interventions for patients since the highly contractile cell phenotype driven by Stat3 signaling exhibits high YAP activity which is reminiscent of the quasi-mesenchymal-like and recurrent patient PDAC phenotype. Taken together with previous findings, our work would then suggest that the use of FAK inhibitors may provide therapeutic benefit for the quasi-mesenchymal and Kras-independent PDAC subtypes with elevated YAP, block progression and recurrence of low grade PDAC, and slow the progression of high grade PDAC.

CHAPTER 5: BRAIN CANCER STUDIES

Introduction to Gliomas

Gliomas are the most common primary intracranial tumors in adults, accounting for more than 50% of all primary adult brain cancers [232]. These tumors have distinct cellular origins and are typically genetically heterogeneous[233,234]. Consequently, gliomas display a range of proliferative, survival and invasion phenotypes and exhibit distinct abilities to engage the vasculature in the highly invasive tumors[233,235]. Accordingly, patient outcome varies drastically as a function of tumor grade and histophenotype.The most aggressive of these tumors are glioblastoma multiforme (GBM - grade 4) with mean patient survival of 14.6 month; patients with anaplastic high grade glioma (AS3 - grade 3) tend to live 3-5 years post diagnosis and those with low grade glioma (AS2 - grade 2) tend to survive 7-10 years post diagnosis[233,235,236]. Moreover, recent microarray analyses of the most aggressive GBMs further emphasized the inherent within-tumor heterogeneity as it pertains to disease phenotype and patient mortality by uncovering four distinct subclasses within GBMs based on genomic abnormalities: from the least aggressive neural and proneural subclasses to classical, and the most aggressive mesenchymal subclass[237]. All aggressive GBMs exhibit rapid growth and as the result, the four FDA-approved post-operative GBM treatment modalities have been designed to target cell replication[238,239]. Yet, many GBMs demonstrate profound resistance to therapy, which is partly due to the fact that over 50% of GBM patients contain a mutation in a gene (MGMT) that encodes an enzyme able to repair DNA damage induced by chemo and radiation therapies[238]. In addition, the GBM phenotype most tightly associated with patient fatality is diffuse invasion into healthy brain

tissue, which not only prevents complete surgical resection of the tumor but also contributes to a high rate of tumor recurrence. In this regard, replication and migration appear to be mutually-exclusive cellular fates, so that the most invasive GBM cells are likely to be inherently resistant to traditional anti-proliferative treatments[240]. Clearly, a better understanding of the pathophysiology of GBM invasiveness should provide insight into the treatment resistance of this disease and help to identify novel treatment targets.

Intriguingly, presence of gain of function somatic mutations in a metabolic enzyme isocitrate dehydrogenous 1 (IDH1), which are highly common in low grade gliomas, is one of the most prominent single positive prognostic factors to GBM survival, on average providing one year improved survival to patients post correcting for age and other variables[241–243]. Fascinatingly, IDH1 mutations are only prevalent in two of the previously mentioned GBM subclasses (neural and proneural but not in classical or mesenchymal GBMs) and removal of IDH1 mutants from these two subclasses abrogates all differences in patient survival between the four subclasses[244]. The beneficial effect of IDH1 mutation to patient survival has been mostly attributed to production of an oncometabolite, (R)-2-hydroxyglutarate, which leads to genome-wide DNA and histone methylation alterations and/or altered cellular redox state to promote cellular transformation, however the exact mechanism is still an area of intense debate and interest [245,246]. This led us to investigate the biophysical landscape of the ECM in a context of IDH1 mutant versus IDH1 WT GBMs.

Reciprocal Interplay between Tissue Mechanics and IDH1-dependnet GBM Aggression

Summary: Glioblastoma multiforme (GBM) brain tumors develop within a mechanically-challenged microenvironment[137,175] that is characterized by high intracranial pressure, elevated solid stress and a dense, extracellular matrix (ECM) that compromise vascular integrity to induce hypoxia and activate HIF1α[247,248]. Presence of an R132H mutation in the metabolic regulator isocitrate dehydrogenous 1 (IDH1) improves patient prognosis in aggressive GBMs brain tumors[241]. IDH1 mutant GBMs may be less aggressive due to reduced HIF1α levels driven by elevated hypoxia-dependent proteosomal targeting of HIF1α[249–251]. Here, we show that a stiff ECM enhances the aggressiveness of IDH1 mutant GBMs by inducing HIF1α-dependent tenascin C expression. We found that GBM aggression and HIF1α expression associate with a stiffer, tenascin C-enriched ECM and elevated mechanosignaling that reflect a poor prognosis signature in patients. We determined that IDH1 mutational status and improved patient prognosis reflect low to absent HIF1α and negligible tenascin C expressions, and a softer ECM. Indeed, reducing tenascin C in GBMs not only prevented ECM stiffening, decreased mechanosignaling and repressed GBM aggression, but also lowered HIF1α, linking tenascin C-induced tissue mechanics to HIF1α. Conversely, elevating mechanosignaling in IDH1 mutant GBMs induced HIF1α-dependent tenascin C expression to stiffen the ECM and promoted tumor aggression. Importantly, ECM stiffness directly induced HIF1α and tenascin C in IDH1 mutant cells *in vitro*. These data are consistent with our analyses of patient biopsies demonstrating that recurrent IDH1 mutant GBMs not only expressed higher levels of tenascin C but were more mechanically-activated and stiffer than their primary GBM counterparts. Thus, our work suggests that elevated

matrix mechanics can induce HIF1α and HIF1α-dependent gene expression to bypass the protective activity of IDH1 mutational status and foster tumor aggression.

To establish whether there is any association between glioma aggression and tissue mechanics, we utilized atomic force microscopy (AFM) to quantify the stiffness of the ECM in a cohort of fresh-frozen human brain biopsies representing non-tumor gliosis, WHO grade III IDH1 wild type (WT) anaplastic astrocytoma and primary IDH1 WT WHO grade IV glioblastomas (GBMs) resected at the UCSF Medical Center. Findings revealed that gliotic tissue had the lowest ECM stiffness (Young's Modulus, E[71]; 10-180 Pa) while the anaplastic astrocytomas (50-1,400 Pa) and primary GBMs (70-13,500 Pa) were progressively stiffer (Fig. 1a). Consistent with the elevated ECM stiffness, mechanosignaling also increased in the anaplastic astrocytomas and was more evident in the stiffer GBMs, as indicated by higher phosphorylated focal adhesion kinase (pFAK; residues Tyr397 and Ser19, respectively) and myosin light chain 2 (pMLC2; Fig. 1b). Although vascular ablation somewhat reduced ECM stiffness, the effect was not significant, as was the contribution of cellular processes and tumor cell density (Supplementary Figure 1b-c). Importantly, NanoString nCounter gene expression analysis[252] of an outcome-predictive gene cluster[253] (aggressiveness measured on a scale of 1-10, 10 indicating best prognosis) of human GBM tissue biopsies indicated a significant correlation between the proportion of highly stiff areas within a GBM tissue ($E > 1,400$ Pa) and worst patient prognosis score (Fig. 1c, red). By contrast, those tissues that contained a high proportion of soft ECM ($E < 200$ Pa) had the best patient prognosis score (Fig. 1c, blue). Immunohistochemistry revealed that the elevated ECM stiffness in the patients with poorer prognosis was accompanied by a substantial increase in hyaluronic acid (HA) expression as well as increased levels of several of its cross-linkers

including, tenascin C (TNC), and the lecticans aggrecan and versican, and indicated that these levels increased progressively from grade 3 astrocytomas to the GBMs (Fig. 1d-e)[254]. Importantly, ECM stiffness did not correlate with levels or distribution of type I collagen (Supplementary Information 1d-e). Importantly, we excluded the vasculature as a critical contributor to the ECM mechanics, as percent vascularity did not correlate with ECM stiffness; normalization of vasculature with an anti-angiogenic treatment (B20) did not significantly alter ECM stiffness (Supplementary Figure 1f-g). Furthermore, mechanical AFM analysis of differentially vascularized oligodendroglioma tumors (less vascularized grade 2, OD2 versus highly vascularize grade 3, OD3) demonstrated no correlation with ECM stiffness (Supplementary Figure 1h-i).

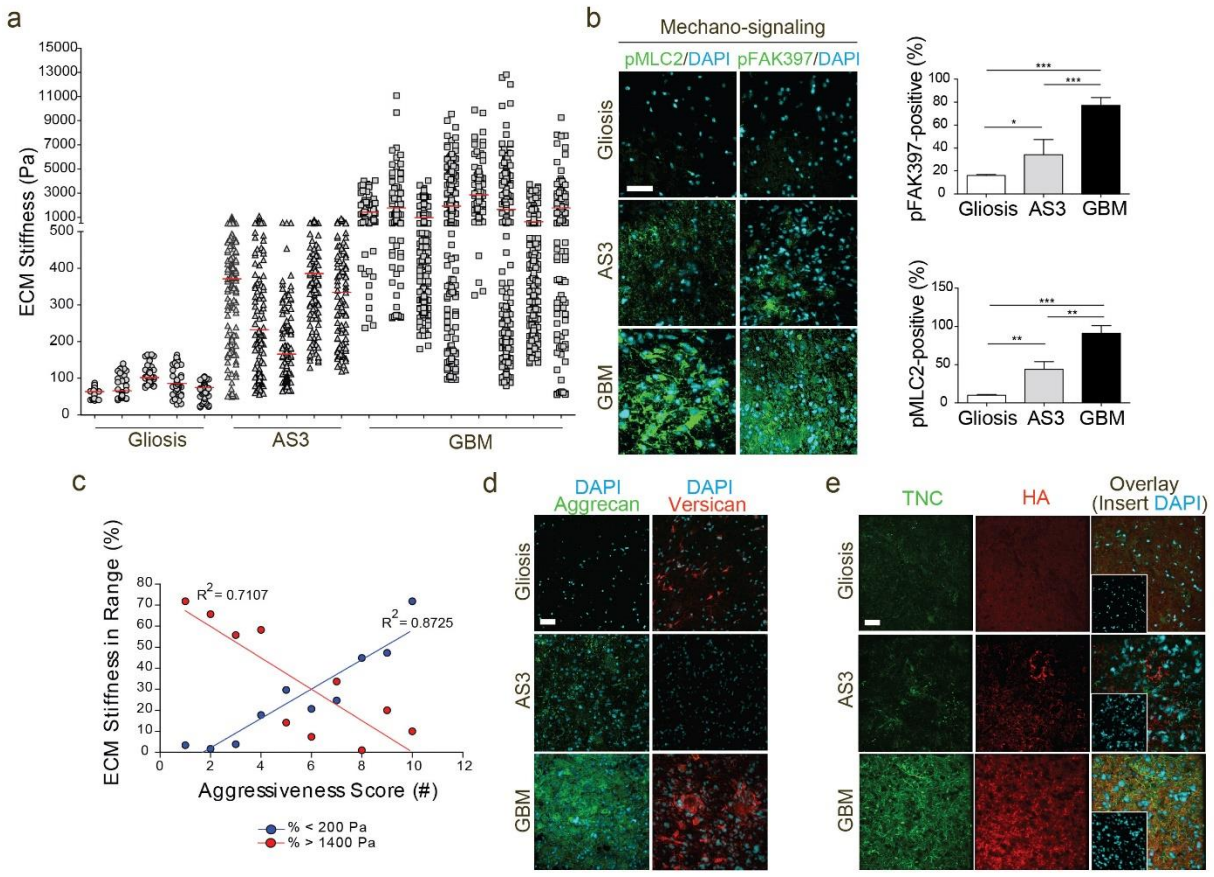

Brain Cancer (IDH1 & Mechanics) Figure 1. Elevated ECM stiffness correlates with worse GBM patient prognosis.

a, Distribution of ECM stiffness measured by atomic force microscopy (AFM) in gliotic non-tumor (Gliosis, n=5 patient samples, 10 regions/patient), IDH WT WHO grade III anaplastic astrocytoma (AS3, n=5 patient samples, 10 regions/patient) and IDH WT WHO grade IV GBMx (GBM, n=8 patient samples, 10 regions/patient) human patient samples. Means indicated with red lines; Kolmogorov-Smirnov test (two-sided) yielded 1.1e-04 (AS3 versus Gliosis) and 3.23e-05 (GBM versus Gliosis). **b**, Representative immunofluorescence images of patient tissues from (a) immunostained and quantified for pMLC2 (green, left) and pFAK397 (green, right). **c**, NanoString nCounter gene expression analysis score (scale:1-10 from most to least aggressive) plotted against proportion of highly stiff (E>1400 Pa, red) or soft (E <200 Pa, blue) ECM areas. **d**, Representative immunofluorescence images of patient tissue (a) stained for aggrecan (green, left) and versican (red, right) with DAPI (blue). **e**, Representative immunofluorescence images of patient tissues immunostained for TNC (green, left) and hyaluronic acid (red,

middle) with DAPI (blue, right). Scale bars, 50μm. (*p<0.05, **p<0.01 ***p<0.001 utilizing one way ANOVA followed by Tukey's post-hoc analysis unless otherwise indicated).

To further examine the relationship between GBM aggression and ECM stiffness, we studied a cohort of GBM patient biopsies that harbored the R132H gain of function mutation in IDH1 known to confer improved prognosis as compared to those with wild type IDH1[255]. Provocatively, we noted that the stiffness of the ECM in the tumors expressing the mutant IDH1 mutation was significantly more compliant than the ECM measured in the tumors expressing the WT IDHl gene (Fig. 2a). IDH mutant patient biopsies also had lower pFAK and pMLC2 levels, reflecting reduced mechanosignaling (Fig. 2b). To directly test the relationship between expression of the R132H IDH1 mutation, ECM stiffness and mechanosignaling and GBM aggression, we utilized an established U87 mouse xenograft model of GBM expressing either a WT or a mutant IDH1[256] (Supplementary Figure 2a). Importantly, not only did expression of the IDH1 mutation significantly improve the survival of nude mice injected intracranially with the GBM cells (Fig. 2c), but the resultant tumors were significantly softer and exhibited reduced mechanosignaling, as revealed by significantly decreased pMLC2 and pFAK (Fig. 2d-e). These findings were substantiated in a second set of *in vivo* injection studies conducted using a primary model of GBMs expressing the WT and mutant IDH1 (Fig. 2f-g). These data link ECM stiffness to GBM aggression. Further, in both the U87 and the primary xenograft models, as well as in patient samples, we noted that the softer IDH1 mutant expressing GBM tumors had low to negligible TNC expression (Fig. 2g-i). Indeed, a survey of the ECM status of the softer ECMs in the IDH1 mutant human GBM biopsies revealed that, although lectican expression was highly variable, a consistent and significant reduction in the levels of the HA cross-linker TNC was observed in all samples (Supplementary Figure 2b). Moreover, publically-available TCGA

mRNA expression array data[237] confirmed a significant correlation between IDH1 mutational status and TNC expression (Supplementary Figure 3a). Therefore, to investigate whether there is indeed a functional link between ECM stiffness, GBM aggression and TNC expression, we knocked-down TNC in primary IDH1 WT human GBMs using a lentivirally-expressed shRNA and assessed the resulting effects on ECM stiffness and tumor aggression (Supplementary Figure 3, b-c). Notably, the nude mice injected with GBM cells expressing reduced TNC not only survived longer (Fig. 3a) but the ECM associated with these tumors was softer and the cells had lower mechanosignaling, as revealed by reduced pFAK and pMLC2 (Fig. 3b-c). These findings imply that GBM aggression and ECM stiffness are linked to TNC expression and that TNC expression is regulated by IDH1 mutational status.

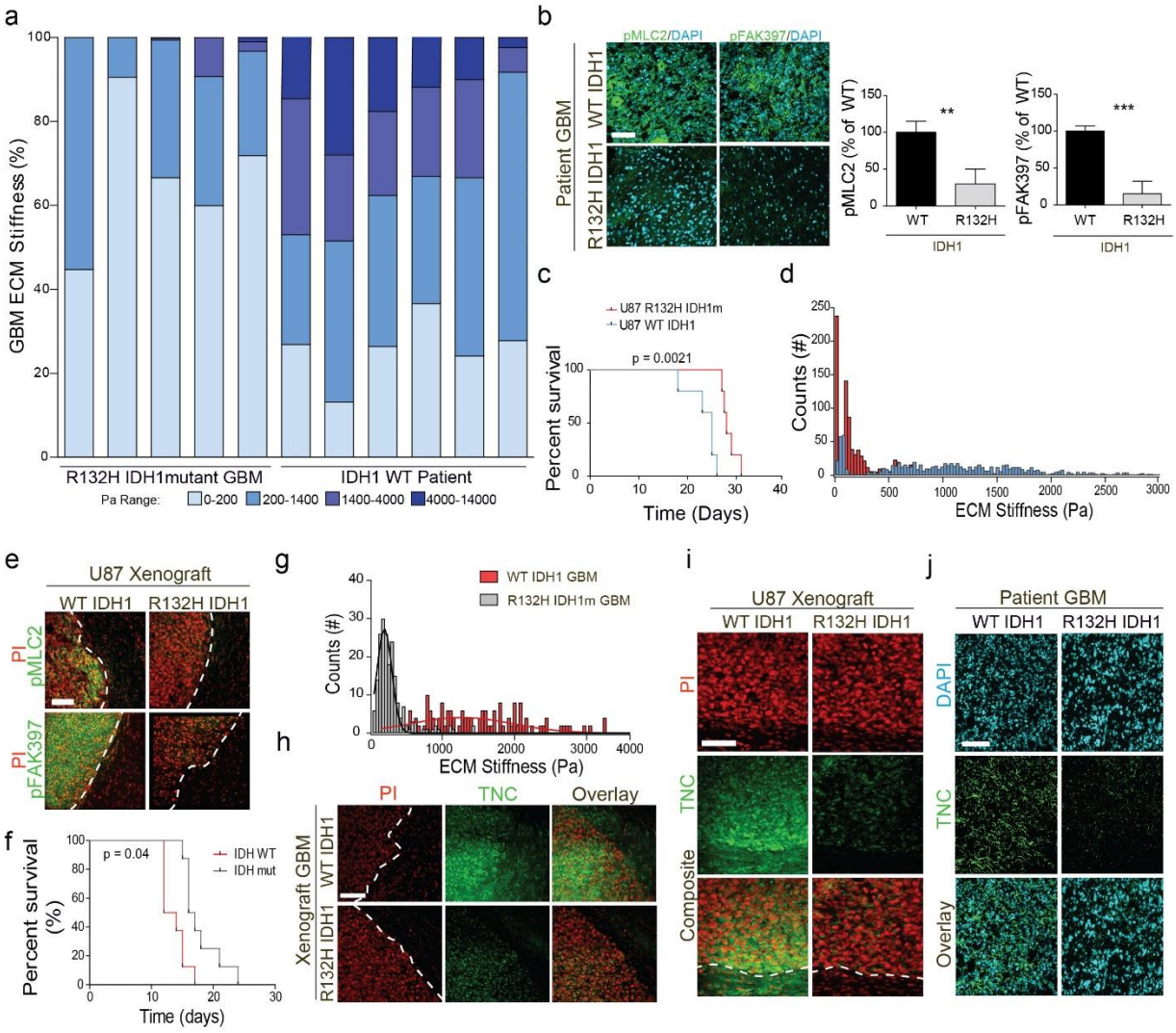

Brain Cancer (IDH1 & Mechanics) Figure 2. R132H IDH1 mutation abrogates ECM stiffness & mechanosignaling in GBMs

a, Distribution of ECM stiffness measured by AFM in R132H IDH1 mutant (n=5 patient samples, 10 regions/patient) and IDH1 WT (n=6 patient samples, 10 regions/patient) GBM human patient samples (two-sided Kolmogorov-Smirnov test yielded 4e-05). **b**, Representative immunofluorescence images of patient tumors (a) stained and quantified for pMLC2 (green, left) and pFAK397 (green, right) with DAPI (blue). **c**, Kaplan-Meier graph showing survival of xenograft mice injected orthotopically with either U87 WT IDH1 (blue, n=7 mice) or U87 R132H IDH1 mutant (red, n=7 mice) human GBM cells. **d**, Histogram showing the distribution of ECM stiffness measured by AFM in xenograft tumors derived from U87 WT (blue) or R132H mutant (red) IDH1 cells (n=5 mice/group, 5 regions/mouse, two-sided Kolmogorov-Smirnov test yielded p=0.97e-3). **e**, Representative

immunofluorescence images of U87 IDH1 WT and R132H mutant xenograft tumors immunostained for pMLC2 (green, top) and pFAK397 (green, bottom) with propidium iodide (PI, red). **f**, Kaplan-Meier graph showing survival of xenograft mice injected with either primary human WT IDH1 (red, n=8 mice) or R132H IDH1 mutant (grey, n=8 mice) GBM cells. **g**, Histogram showing the distribution of ECM stiffness measured by AFM in xenograft tumors derived from primary human GBM cells infected with either WT (red) or R132H mutant (grey) IDH1 cells (n=4/group, 5 regions/mouse, two-sided Kolmogorov-Smirnov test yielded p=1.3e-3). **h**, Representative immunofluorescence images of TNC (red) with DAPI (green) in xenograft tumors derived from either WT or R132H mutant IDH1 human primary cells. **i**, Representative immunofluorescence images of TNC (green) with PI (red) in xenograft tumors derived from either WT or R132H mutant IDH1 U87 cells. **j**, Representative immunofluorescence images of patient tissues from (a) immunostained for TNC (green) with DAPI (blue). Scale bars, 50μm. (**p<0.01, ***p<0.001 utilizing two-tailed Student's t-test, unless otherwise indicated).

The presence of the IDH1 mutation may enhance GBM patient survival by increasing the production of an oncometabolite, (R)-2-hydroxyglutarate, which can induce genome-wide DNA and histone methylation alterations and/or alter cellular redox state to promote cellular transformation[245,246]. However, IDH1 is also a metabolic enzyme that may influence tumor phenotype by regulating HIF1α, a subunit of a heterodimeric transcription factor complex that mediates cellular response to hypoxia[257]. Consistently, immunohistochemical analysis of a cohort of WT and R132H IDH1 mutant patient tumors revealed significantly higher numbers of tumor cells staining positive for carbonic anhydrase 9 (CA9, n=4 patients per condition), a downstream target of stabilized HIF1α[258] in WT GBMs (Supplementary Figure 3e). Importantly, HIF1α has also been implicated in TNC expression[259,260]. Accordingly, we explored the relationship between GBM aggression, IDH1 mutation and HIF1 α-induced TNC expression. Immunohistochemical analysis of primary WT and R132H IDH1 mutant expressing GBM brain xenografts revealed that, with the exception of a few sparse regions, IDH1 mutant GBMs had low to barely detectable nuclear HIF1α (Fig. 3d), despite evident necrosis (Fig. 3d,

asterisk) and marked tumor hypoxia (Fig. 4c). Consistently, immunoblot analysis confirmed that the IDH1 mutant GBMs had significantly reduced total tissue HIF1α protein (Fig 3e) suggesting a profound dysregulation of the hypoxic response in xenografted tumors expressing the R132H IDH1 mutation. Moreover, chromatin immunoprecipitation (ChIP) using HIF1α as the bait confirmed that HIF1α binds directly to the TNC promoter as indicated by co-precipitation of HIF1α with the TNC promoter (Fig. 3f). These observations imply that IDH1 mutational status in GBMs regulates tumor aggression by altering ECM stiffness through modulation of hypoxia-induced, HIF1α-dependent TNC expression.

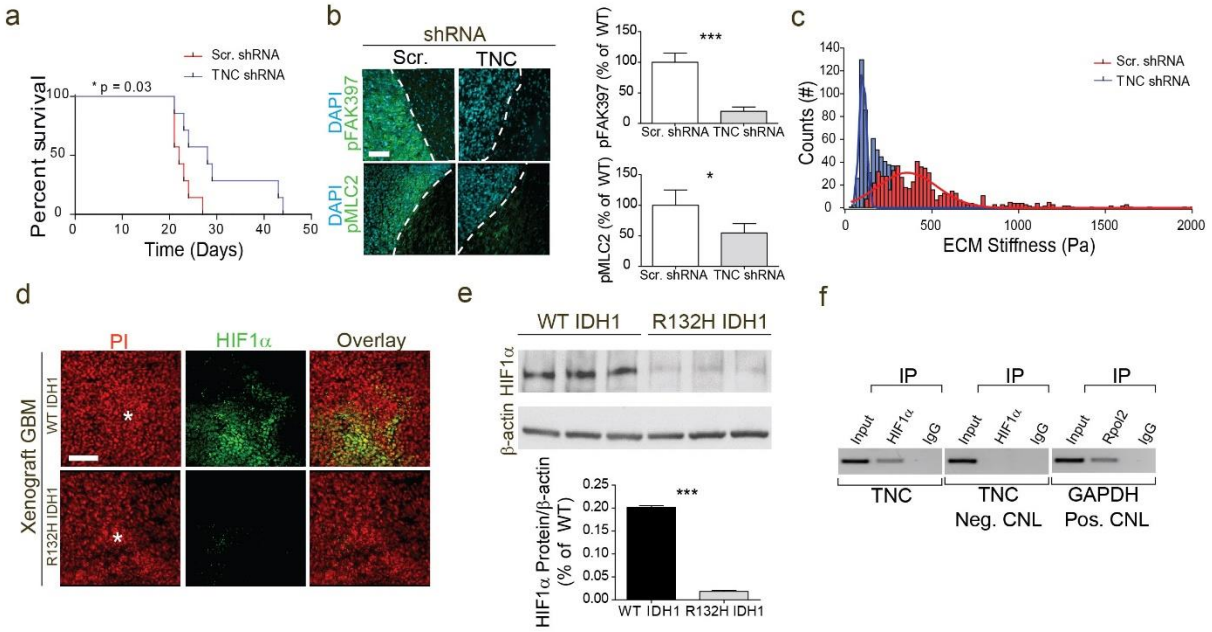

Brain Cancer (IDH1 & Mechanics) Figure 3. R132H IDH1 mutation modifies HIF1α-depednent hypoxia-sensing and TNC expression in GBMs

a, Kaplan-Meier graph showing survival of xenograft mice injected with GBM cells expressing either a control scramble shRNA (red, n=8 mice) or an shRNA for TNC (blue, n=8 mice). **b**, Representative immunofluorescence images of xenograft tumors expressing control scramble shRNA or shRNA for TNC that have been immunostained

and quantified for pFAK397 (green, top) and pMLC2 (green, bottom) with DAPI (blue)(n=4 mice, 5 images/mouse). **c**, Histogram showing the distribution of ECM stiffness measured by AFM in xenograft tumors derived from cells expressing either a control scramble shRNA (red) or an shRNA to TNC (blue)(n=6, 5 regions/mouse, two-sided Kolmogorov-Smirnov test yielded p=1.73e-2). **d**, Representative immunofluorescence images of xenograft tumors derived from either IDH1 WT or R132H mutant IDH1 human primary cells immunostained for HIF1α (green) with PI (red); asterisks indicate areas of necrosis. **e**, Representative immunoblot analysis of xenograft tumors derived from either WT or R132H mutant IDH1 human primary cells (n=3/group). Results were normalized to β-actin and quantified. **f**, Representative gel of chromatin immunoprecipitation (ChIP) studies in R132H mutant IDH1 primary human cells demonstrating the immunoprecipitation of HIF1α with the TNC promoter (neg. cnl denotes negative control and pos. cnl denotes positive control). Scale bars, 50μm. (**p<0.01 ***p<0.001 utilizing two-tailed Student's t-test, unless otherwise indicated).

To directly implicate tissue mechanics in GBM aggression, we expressed a V737N β1 integrin mutant, that recapitulates stiffness-dependent integrin clustering and elevates FAK signaling[12], in GBMs expressing a mutant IDH1 (Fig. 4a). Our objective was to determine whether enhancing cellular mechanosignaling in GBMs expressing a mutant IDH1 could restore tumor aggression and, if so, whether this would be associated with elevated HIF1α and TNC expression. Consistent with this prediction, we observed that R132H IDH mutant tumors expressing the V737N β1 integrin mutant not only had significantly elevated mechanosignaling as revealed by elevated pFAK and pMLC2 (Fig. 4a-b), but they also expressed HIF1α to levels that were comparable to those measured in IDH1 WT GBM tumors (Fig. 4c, blue). These IDH1 mutant GBMs expressing β1 V737N were also stiffer (Fig. 4d, blue) and the mice injected with these tumor cells had compromised survival (Fig. 4e, blue). In marked contrast, GBMs expressing the mutant IDH1 and a WT β1 integrin were comparatively softer, had low to non-detectable HIF1α and TNC, despite pronounced hypoxia (Fig. 4c-d, orange) and the mice injected with these tumor

cells lived significantly longer (Fig. 4e, orange line). These findings not only link GBM aggression to tissue mechanics but they also imply that elevated mechanosignaling can override the protective effect of mutant IDH1 by restoring levels of HIF1α expression. Indeed, upon further scrutiny, mechanical analysis of serial sections of brain xenografted mouse GBMs expressing the IDH1 mutation established a significant correlation between positive HIF1α expression and discrete regions of elevated ECM stiffness (Fig. 4g). Interestingly, we also noted that the more compliant ECM regions associated with tumors in which TNC expression was reduced (Fig 3c-e) and had much lower HIF1α staining (Fig. 4h). Accordingly, the data suggest that tissue mechanics and HIF1α may modify GBM aggression via positive feedback.

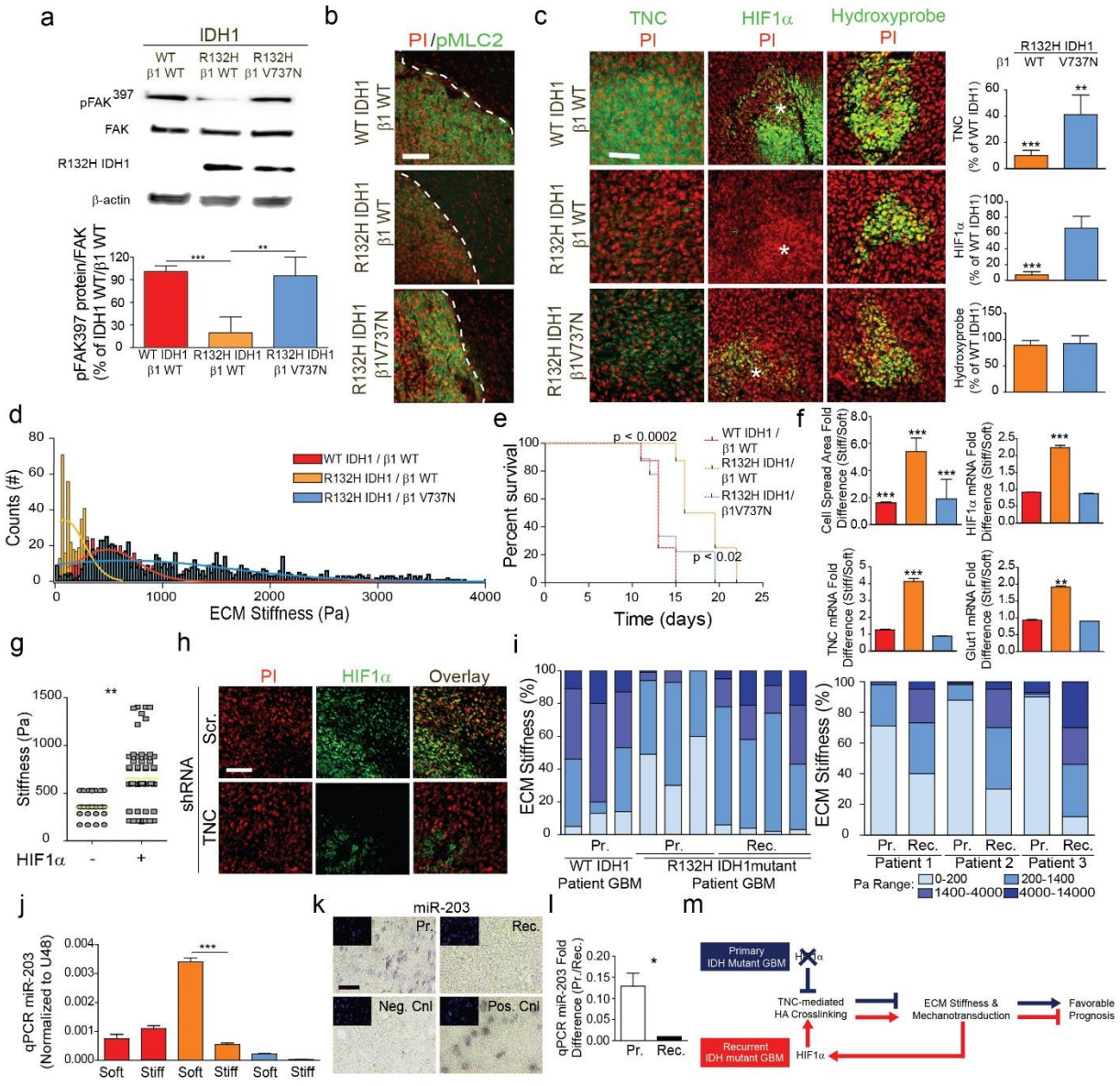

Brain Cancer (IDH1 & Mechanics) Figure 4. Upregulation of mechanosignaling in R132H IDH1m GBMs restores HIF1α and TNC expression and promotes tumor aggression.

a, Representative immunoblot of FAK activity downstream of integrin clustering, as measured by phosphorylation at Tyr397 (pFAK^{397}) in primary human GBM cells infected with WT IDH1/WT β1 (red), R132H IDH1/WT β1 (orange), R132H IDH1/β1V737N (blue) constructs; results were normalized to total FAK (FAK) and quantified. **b**, Representative immunofluorescence images of xenograft tumors derived from primary human GBM cells

expressing either WT IDH1/WT β1, R132H IDH1/WT β1 or R132H IDH1/β1V737N, and immunostained for pMLC (green) with PI (red). **c**, Representative immunofluorescence images of xenograft tumors derived from primary human GBM cells expressing either WT IDH1/WT β1, R132H IDH1/WT β1 or R132H IDH1/β1V737N, and immunostained for TNC (green, left), HIF1α (green, middle), and hypoxyprobe (green, right) with PI (red); asterisks indicate areas of necrosis. Immunofluorescence is quantified as percent of WT IDH1/WT β1 integrin. **d**, Histogram showing the distribution of ECM stiffness measured by AFM in xenograft tumors derived from either WT IDH1/WT β1 (red), R132H IDH1/WT β1 (orange) or R132H IDH1/β1V737N (blue) as indicated (n=8 mice/group, 5 regions/mouse, two-sided Kolmogorov-Smirnov Test yielded 2.87e-4 for WT IDH1/WT β1 vs R132H IDH1/WT β1). **e**, Kaplan-Meier graph showing survival of xenograft mice injected with either WT IDH1/WT β1 (red), R132H IDH1/WT β1 (orange) or R132H IDH1/β1V737N (blue) cells as indicated (n=8/group). **f**, Analysis of cell spreading area (top left), HIF1α mRNA expression (top right), as well as mRNA expression of HIF1α targets TNC (bottom left) and Glut1 (bottom right) on stiff (6000Pa) as compared to soft polyacrylamide substrates (140Pa) in WT IDH1/WT β1 (red), R132H IDH1/WT β1 (orange) or R132H IDH1/β1V737N (blue) cells *in vitro*. mRNA expression was normalized to ribosomal RNA RPL20, which itself was not changed by ECM stiffness. **g**, Distribution of ECM stiffness measured by AFM in xenograft tumors arising from primary R132H IDH1 cells in either HIF1α-positive or –negative regions surrounding areas of necrosis (n=4 mice, 3 regions/mouse, Kolmogorov-Smirnov test (two-sided) yielded 0.37e-1). **h**, Representative immunofluorescence images of xenograft tumors derived from cells expressing a control scramble shRNA or an shRNA for TNC shRNA immunostained for HIF1α with PI (red). **i**, Left**:** Distribution of ECM stiffness measured by AFM in newly diagnosed/non-treated WT IDH1 (n=3), newly-diagnosed/non-treated R132H IDH1 mutant (n=3), and recurrent R132H IDH1 mutant GBM (treated with temozolomide chemotherapy and radiation; n=4) patient samples (10 regions/patient; Kolmogorov-Smirnov test (two-sided) between newly diagnosed and recurrent R132H IDH1 mutant patient tumors yielded 0.21e-1); Right: Distribution of ECM stiffness measured by AFM in matched pairs of R132H IDH1 mutant newly-diagnosed/non-treated (n=3) and post-treatment recurrent GBM (10 regions/patient; Kolmogorov-Smirnov test yielded 2.11e-3). **j**, miR-203 mRNA expression as a function of stiffness in WT IDH1/WT β1 (red), R132H IDH1/WT β1 (orange), and R132H IDH1/β1V737N (blue) *in vitro*. Results were normalized to U6 small nuclear RNA. **k**, Representative brightfield images (insert: DAPI) of miR-203 *in situ*

hybridization with corresponding U6-positive control and scramble negative control of tissues from i (right) **l**, qPCR validation of miR-203 expression levels in patient samples form i (right) normalized by U48. **m**, Graphic depicting a model of reciprocal regulation of R132H IDH mutant GBM aggression by HIF1α and ECM mechanics-dependent TNC expression.

To further explore a plausible reciprocal link between tissue mechanics and HIF1α regulation, we assessed the mechano-responsiveness of GBM cells expressing WT β1 integrin and either R132H mutant or WT IDH1 (Fig. 4a-f). To implicate integrin-dependent mechanotransduction in the mechanophenotype of the GBMs, in parallel, we assessed the behavior of GBM cells expressing the IDH1 mutation together with the V737N β1 integrin[12,20,223], to enhance mechanosignaling and cell spreading, even in the absence of a stiff ECM (Fig. 4a-b). We plated the IDH1 mutant GBM cells on 2-dimensional polyacrylamide (PA) gels with a calibrated stiffness ranging from very soft (140 Pa, normal brain) to the stiffness we measured in human GBMs expressing a WT IDH1 (6000 Pa) and compared their spreading behavior, adhesion size and composition, and gene expression levels to those exhibited by GBM cells expressing a WT IDH1 or the mutant IDH1 plus the V737N β1 integrin. Intriguingly, although both the GBMs expressing a WT and mutant IDH1 spread more in response to the stiff PA gels, the GBM cells expressing the mutant IDH1 were markedly hypersensitive to substrate stiffness, exhibiting an increase in cell spread area that was 4 fold higher than that demonstrated by the GBM cells expressing the WT IDH1 (Fig. 4f, top left). This elevated mechano-responsiveness to ECM stiffness was echoed by a similarly significant fold increase in HIF1α mRNA expression and its transcriptional targets TNC and Glut1 (Fig. 4f, top right and bottom panels). Not only do these *in vitro* studies indicate that ECM stiffness can induce HIF1α levels, but they imply that expression of the IDH1 mutation sensitizes GBM cells to exogenous mechanical cues.

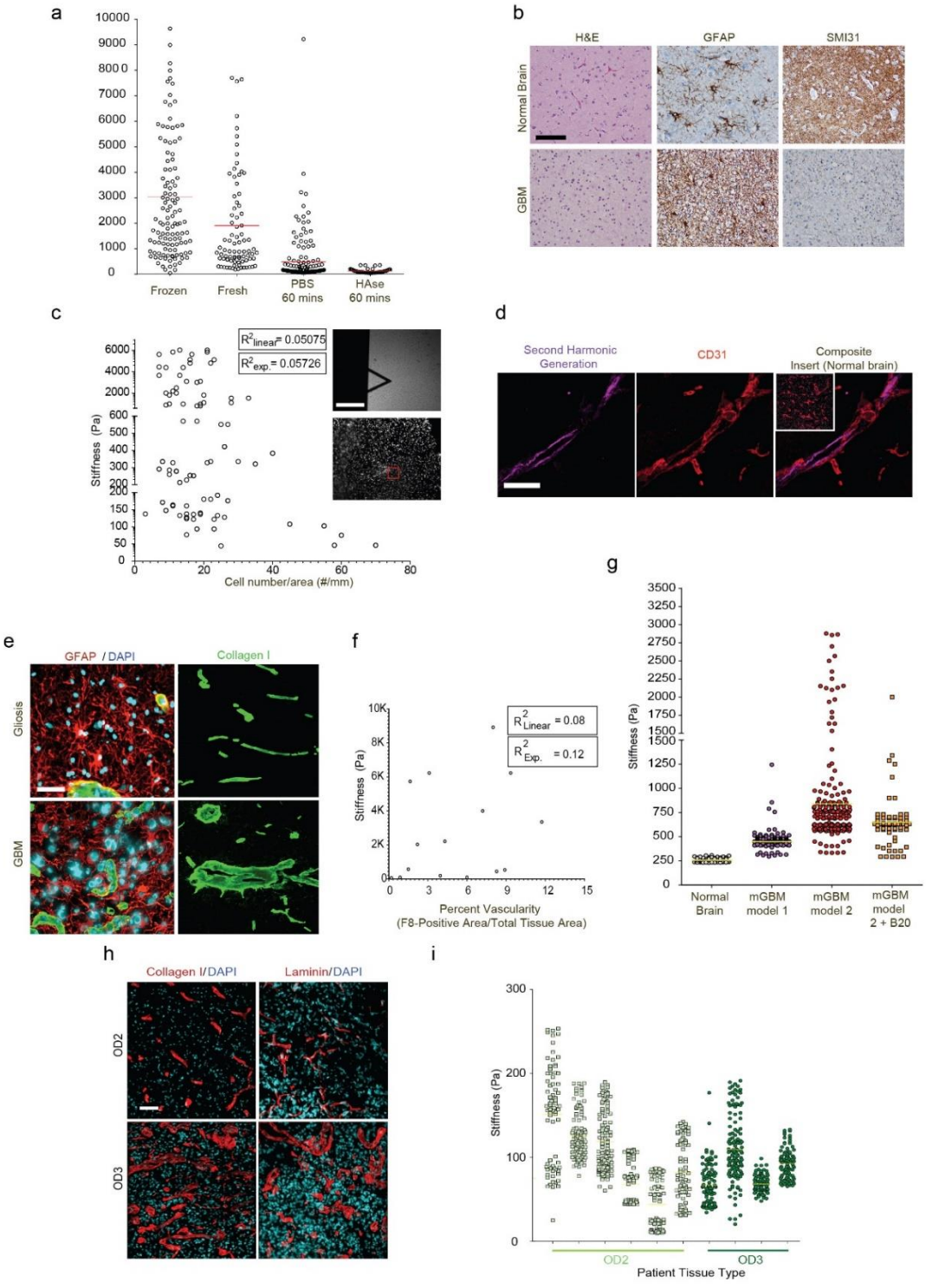

Brain Cancer (IDH1 & Mechanics) Supplementary Figure 1.

a, Representative scatter plots of ECM stiffness measured by atomic force microscopy (AFM) in a human patient sample analyzed immediately post resection from the operating room (Fresh), post snap freezing and analyzed either

within 30 minutes of being thawed in a cocktail of protein inhibitors (Frozen) or treated with either PBS (PBS) or hyaluronidase (HAse) for 60 minutes. **b**, Representative immunohistochemistry images of patient tissue immunostained for neuronal (SMI31) or astrocytic (GFAP) processes indicating a switch in the type but not density of the cellular processes in normal versus GBM brains. **c**, Correlation between measured ECM stiffness and cell number in the analyzed area revealing no relationship between the two variables (insert: representative image of the AFM method for tissue analysis). **d**, Representative second harmonic generation (SHG) image of fibrillary collagen (purple) and CD31-immunostained vasculature (red) in human GBMs (insert: composite image of SHG and CD31 in a normal human brain). **e**, Representative immunofluorescence images of astrocytic processes (GFAP, red) and vasculature (Collagen 1, green) in human gliotic (top) and GBM (bottom) biopsies. **f**, Correlation between measured ECM stiffness and percent vascularity of the tissue (percent area positive for FVIII stain) revealing no relationship between the two variables. **g**, Distribution of ECM stiffness measured by AFM in two (labelled as mGBM model 1 and mGBM model 2) mouse xenograft models of GBM (n=4, 5 regions/mouse), normal mouse brain (n=3, 5 regions/mouse), as well as mGBM model 2 treated with an antiangiogenic agent, avastin (labelled as mGBM model 2 + B20; n=5, 5 regions/mouse) revealing a slight but non-significant reduction in ECM stiffness upon B20-mediated normalization of GBM vasculature in mouse models of GBM. **h**, Representative immunofluorescence images of human non-astrocytic infiltrating glioma (oligodendroglioma) exhibiting profoundly altered vascular phenotype in WHO grade II versus III tumors as indicated by Collagen 1 (left, red) and laminin (right, red) with DAPI. **i**, Distribution of ECM stiffness measured by AFM in grade II oligodendrogliomas (OD2s, light green, n=6) and grade III oligodendrogliomas (OD3, dark green, n=4) exhibiting no statistically significant difference in ECM stiffness with grade, despite the severely different vascular phenotypes between grades.

Tissue levels of HIF1α can be altered at the mRNA level by Akt signaling, however it is primarily regulated at the protein level by redox regulatory pathways modified by the level of tissue oxygenation[261]. Yet, surprisingly, we found that GBM tumors expressing the mutant IDH1 failed to increase HIF1α mRNA or protein even when exposed to hypoxia (1% O_2 tension) whereas both mRNA and protein levels were significantly increased in response to ECM stiffness and elevated integrin-dependent signaling (Fig. 4c and 4f, Supplementary Figure 3d).

These results suggest that tissue mechanics can independently regulate cell and tissue levels of HIF1α. We then explored the potential mechanisms by which ECM stiffness may induce HIF1α in GBMs. Our prior array data showed that ECM stiffness alters the expression of a myriad of microRNAs (miRNAs) implicated in malignancy[223]. Loss of miR-203 has been implicated as a tumor suppressive miRNA in both GBM aggression and recurrence, and data suggest that maintenance of high miR-203 expression in GBMs associates with a significantly improved patient prognosis[167]. Intriguingly, we noted that while GBMs expressing the mutant IDH1 expressed very high levels of miR-203 on soft PA gels, these levels were significantly repressed in response to elevated ECM stiffness, and were essentially non-detectable in GBMs expressing the V737N β1 integrin with elevated integrin-dependent mechanosignaling (Fig. 4j). Furthermore, we identified several consensus sites in the 3' UTR of the HIF1α mRNA consistent with the notion that tissue mechanics may induce HIF1α in GBMs expressing the mutant IDH1 by reducing levels of miR-203 (Supplementary Figure 4a).

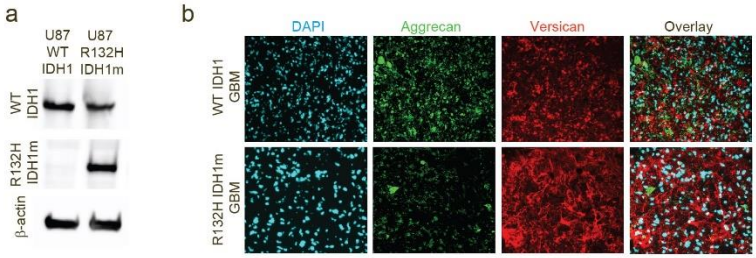

Brain Cancer (IDH1 & Mechanics) Supplementary Figure 2.

a, Representative immunoblot analysis confirming the R132H and WT IDH1 status in U87 GBM line. **b**, Representative immunofluorescence images of patient tissues immunostained for the lecticans, aggrecan (green) and versican (red).

Standard of care for GBM patients involves high dose radiation treatment and application of chemotherapy. Radiation and chemotherapy can each induce dramatic changes in the tissue microenvironment that include stimulation of ECM secretion, deposition and remodeling which we and others showed is associated with stromal stiffening[262]. Accordingly, we asked whether recurrent IDH1 mutant GBMs were stiffer than a set of molecularly matched primary GBMs. AFM analysis of a cohort of recurrent IDH1 mutant patient GBMs revealed highly stiff ECMs that were significantly stiffer than those measured in primary IDH1 mutant GBMs and were as stiff, if not stiffer, than those measured in primary poor prognosis WT IDH1 GBMs (Fig. 4i, left). Indeed, mechanical analysis of matched pairs of IDH1 mutant GBM patient tissues at primary diagnosis and at recurrence, after standard of care treatment with gamma radiation and temozolomide chemotherapy, revealed a remarkable increase in the stiffness of the associated ECMs in the recurrent IDH1 mutant GBMs (Fig. 4i, right).

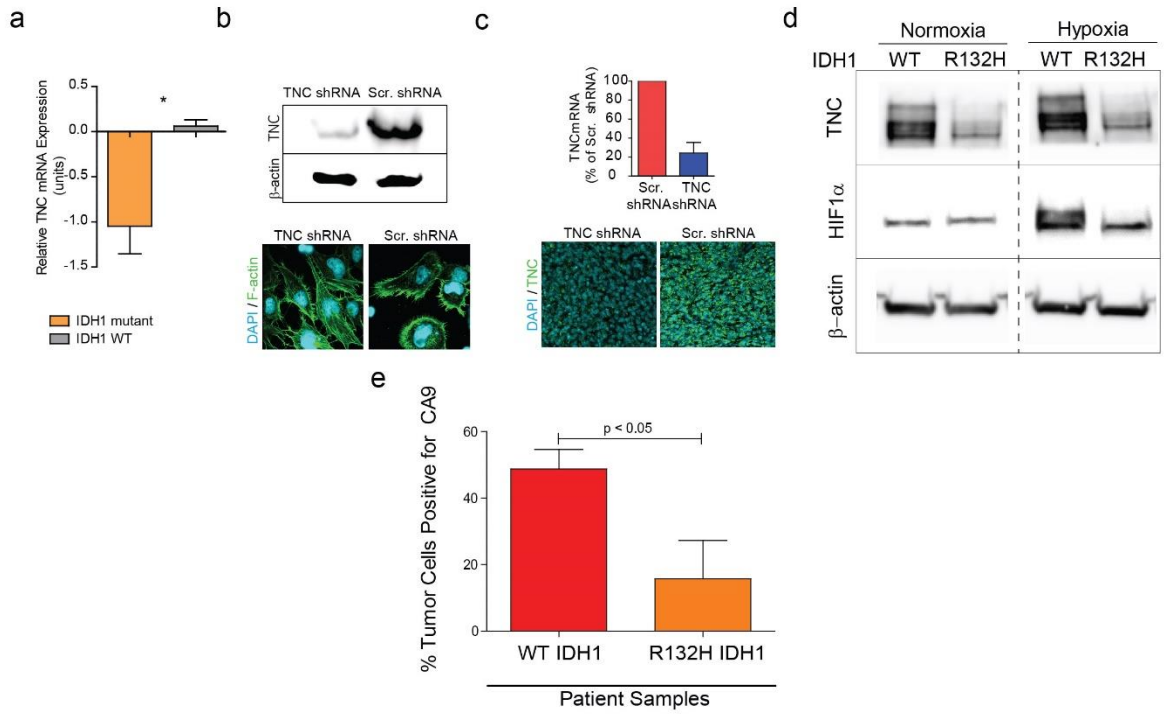

Brain Cancer (IDH1 & Mechanics) Supplementary Figure 3.

a, Bar graph analysis of publically available TCGA data analyzed for TNC expression in WT (n=199) and IDH1 mutant (n=12) human tumors (Wilcox/Mann Whitney U-test yielded p = 4.e-4 with the normal approximation assumption for the U score). **b**, Representative immunoblot analysis confirming lentiviral shRNA construct targeting of TNC (top). Representative images of cellular morphology (F-actin in green and DAPI in blue) of scramble shRNA and TNC shRNA cells (bottom). **c**, Confirmation of TNC knockdown in mouse xenograft tumors by mRNA (top) and immunofluorescence (bottom) in scramble and TNC shRNA constructs (mRNA samples: n=5 mice; immunofluorescence: n=5 mice, 3 regions/mouse). **d,** Representative immunoblot of WT and R132H IDH1 primary GBM cells plated on laminin-coated tissue culture plates under normoxic and hypoxic (1% oxygen) conditions probed for TNC and HIF1α. **e**, Bar graph analysis of percent CA9-positive tumor cells in WT vs IDH1 R132H mutant patient biopsies (n=4 patient tissues; quantified 5 fields/patients).

Intriguingly, *in situ* hybridization analysis of these matched pairs of IDH1 mutant GBM patient tissues for miR-203 expression (Fig. 4k), which we confirmed by qPCR analysis (Fig. 4l), revealed a prominent suppression of miR-203 expression upon recurrence. These striking

findings are consistent with our prediction that tumor treatment may contribute to the development of more aggressive IDH1 mutant GBMs, in part, by modifying ECM stiffness, particularly given our observation that GBM tumor cells expressing the IDH1 mutation are hyper-sensitive to mechanical cues (Fig. 4a-h). Taken together, our findings predict that recurrent IDH1 mutant tumors exhibit treatment-induced remodeling and stiffening of the ECM that induces HIF1α and HIF1α-dependent gene expression (Fig. 4m) to increase tumor aggression and override some of the protective activity of IDH1 mutational status.

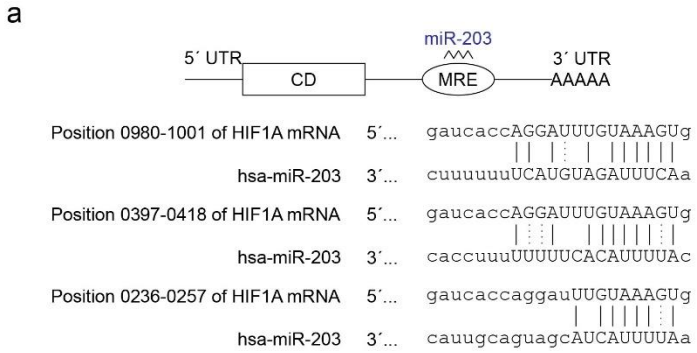

Brain Cancer (IDH1 & Mechanics) Supplementary Figure 4.

Diagram of miR-203 targeting seed sequences located in 3'-untranslated regions (3' UTRs) of human HIF1α mRNAs.

Collectively, our results highlight the significance of TNC-mediated tissue mechanics to IDH1 mutant GBM aggression and implicate HIF1α-dependent hypoxia sensing and stiffness-sensitive gene expression to IDH1 mutant GBM recurrence.

STAT3 blockade inhibits a radiation-induced proneural-to-mesenchymal transition in glioma

Malignant gliomas are associated with dismal prognoses in part due to the invasive nature of glioma cells which enables them to migrate through the narrow extracellular spaces in the brain across relatively long distances which makes them elusive targets for effective surgical management within the vital organ of the body[263]. Additionally, after surgical resection and adjuvant treatment of malignant gliomas, the residual cancer cells peripheral to the excised lesion give rise to a recurrent tumor that in more than 90% of cases develops immediately adjacent to the resection margin[264–266]. Clinical and experimental data have also demonstrated that invasive malignant glioma cells show a decrease in proliferation rate and a relative resistance to apoptosis compared to the highly dense cellular center of the tumor, and this may contribute to their resistance to conventional pro-apoptotic chemotherapy and radiotherapy[266]. Indeed, glioblastomas present a catastrophic prognosis due to a local recurrence despite surgery, radiotherapy and chemotherapy. In that respect, although ionizing radiation extends survival in patients with malignant glioma, tumors unescapably relapse and may exhibit elevated aggression and treatment resistance[267]. Radiation has been shown to stimulate GBM cell aggression by promoting proneural to mesenchymal transition *in vitro* [268–270]. Our colleagues Dr. Jasmine Lau et al., in collaboration with us, have recently demonstrated that that radiation does indeed drive a cell-intrinsic proneural to mesenchymal transition (PMT) both *in vitro* and *in vivo* and that this transition is dependent on signal transducer and activator of transcription 3 (STAT3), which has been previously implicated in maintenance of mesenchymal features[271–273]. Dr. Jasmine Lau showed that pretreatment with inhibitors of JAK2, a kinase that regulates STAT3, blocked

activation of STAT3, and abrogated this mesenchymal transition (Lau et al., accepted for publication in Cancer Research, August 2015). Given that radiation induces sustained mesenchymal phenotype which leads to radioresistance, blocking this transition may prevent patient relapse or decrease therapy-resistance in relapsed tumors. In that respect this work suggested that therapeutic blockade of JAK2-STAT3 signaling in patients undergoing radiation therapy for high grade glioma may prevent acquired treatment-resistance and mesenchymal phenotype at recurrence.

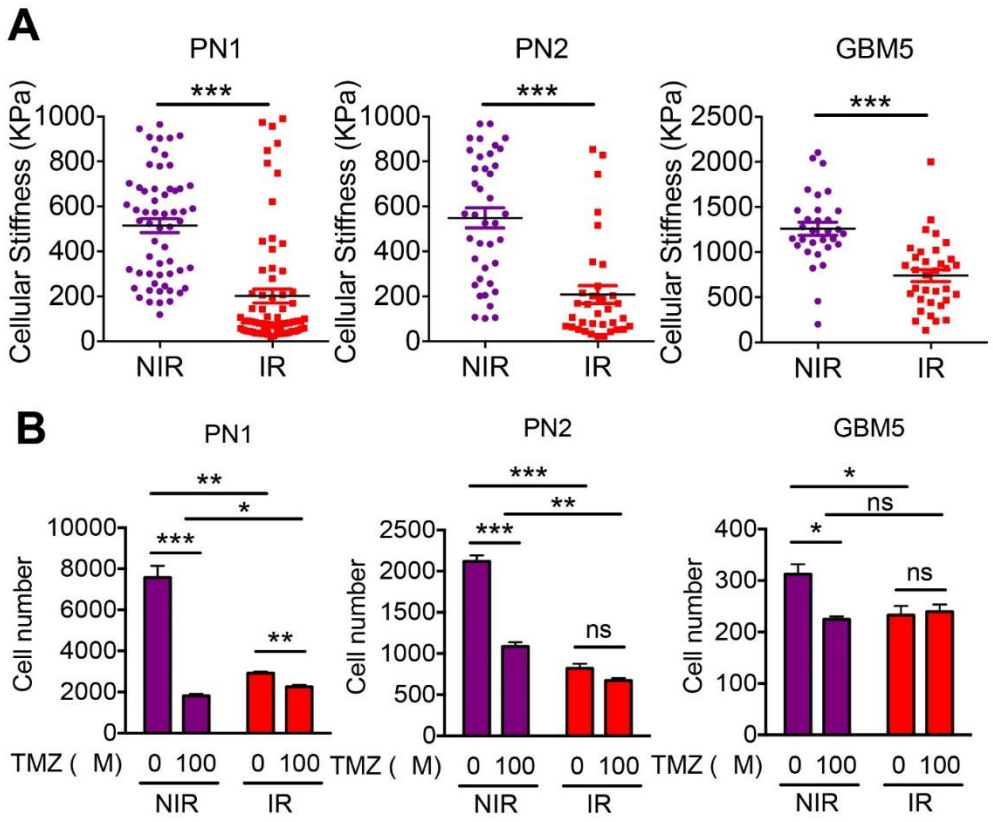

STAT3 Radiation Figure 1. Murine and human proneural high grade glioma (HGG) cells exposed to irradiation (IR) in vitro display reduced cell stiffness, reduced proliferation and increased TMZ resistance.

(A) Atomic force microscopy results show cellular stiffness of murine (PN1-PN2) and human (GBM5) proneural HGG cells four days following radiation, compared to non-irradiated control cultures. (B) CyQuant DNA

proliferation assay results show proliferation and TMZ resistance in TMZ- (100μM) versus DMSO-treated murine (PN1-PN2) and human (GBM5) proneural HGG cultures, following a single dose of IR (10 Gy). * $P < 0.05$, ** $P < 0.01$, *** $P < 0.001$.

We have complemented the work of Dr. Jasmine Lau with analysis of cell-intrinsic biophysical and invasive properties induced by radiation to implicate the role of radiation therapy to recurrence in a context of invasiveness. We first noted profound changes in the actin cytoskeleton of irradiated cells in 2D and hypothesized that these changes will manifest in altered cellular rheology which may mediate cell motility. To answer this question, cells were seeded sparsely on laminin-coated glass coverslips and subjected either to irradiation (IR) or control treatment (NIR) and were analyzed four days following irradiation by atomic force microscopy by nano-indenting single cells with low force (below 2nN). Indeed radiation induced cellular compliance (Fig. 1A) which was consistent with our F-actin immunostaining observations and predicted enhanced invasiveness by enabling cells to better navigate the confines of the ECM. These alterations in cell-intrinsic biophysical properties paralleled Dr. Jasmine Lau's findings indicating that radiation reduced proliferation and increased resistance to a standard of care GBM chemotherapeutic temozolomide, TMZ (Fig 1B).

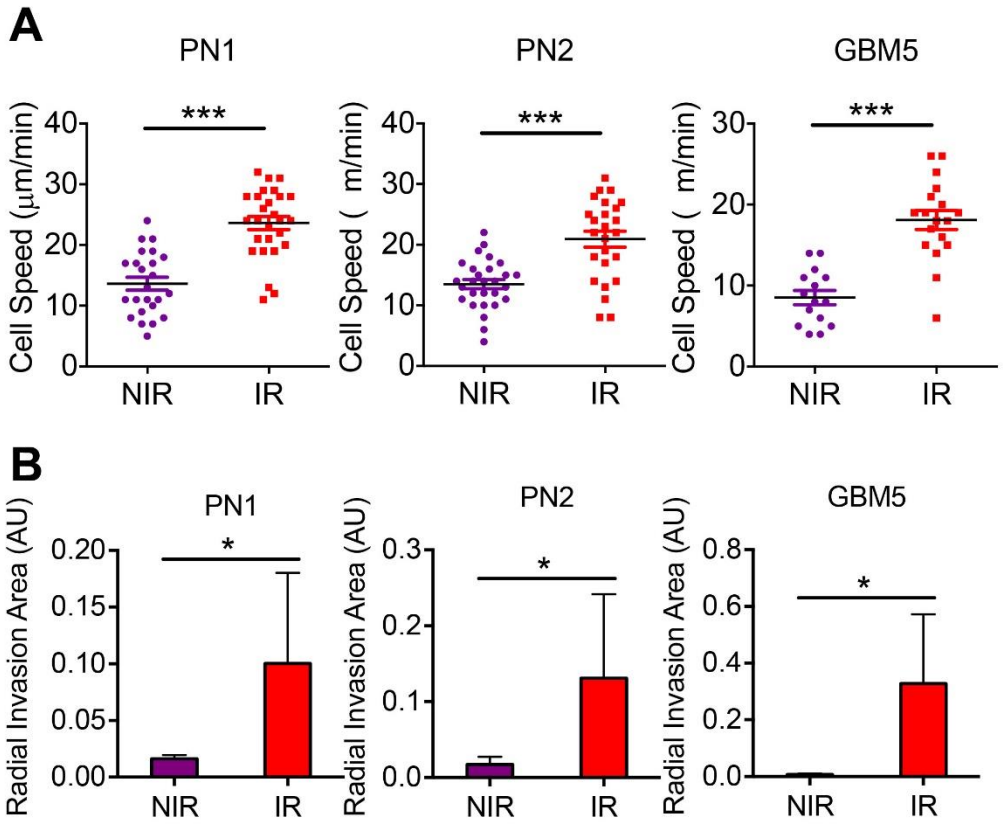

STAT3 Radiation Figure 2. Radiation-induced increased motility and invasiveness in murine and human HGG

(A) Average cell speed (µm/min) by time-lapse imaging show 2D cell motility of murine (PN1-PN2) and human (GBM5) proneural HGG cultures four days following radiation, compared to non-irradiated control cultures. (B) Relative radial invasion area (arbitrary units: AU) of murine (PN1-PN2) and human 3 (GBM5) proneural HGG tumorspheres embedded in 3D Matrigel conditions four days following radiation, compared to non-irradiated tumorspheres.

To confirm the effect of irradiation (IR) on the invasive properties of glioma cells we first performed 2D motility studies of GBM cells plated on laminin-coated glass coverslips that were subjected to irradiation (IR) or control conditions (NIR) and analyzed these samples four days post treatment. Coverslips were mounted in microscope-compatible chambers and subjected to life cell imaging for 8 hours; migration capacity, as measured by cellular speed, was quantified

using ImageJ (Fig 2A). We then followed up with a 3D tumorsphere invasion studies which were performed on cells that were irradiated in non-adherent plate conditions; cells were allowed to form tumorspheres in non-adherent plates for 4 days at which point they were embedded into 3D matrigel and imaged for 24 hours. Invasion area was quantified using ImageJ and defined as the area covered by protrusive extensions radiating from the tumor spheres and normalized to initial tumor sphere size (Fig 2B). Importantly, upon inhibiting STAT3 with a JAK2 inhibitor AZD1480 (AZD), we were able revert radiation-induced invasiveness (Fig 3C) which corresponded well with Dr. Jasmine Lau's data not only directly implicating STAT3 in driving radiation-driven mesenchymal transition (Fig 3A-B), but also functionally linking STAT3 signaling in a context of radiation therapy to modifying survival *in vivo* (Fig 3D).

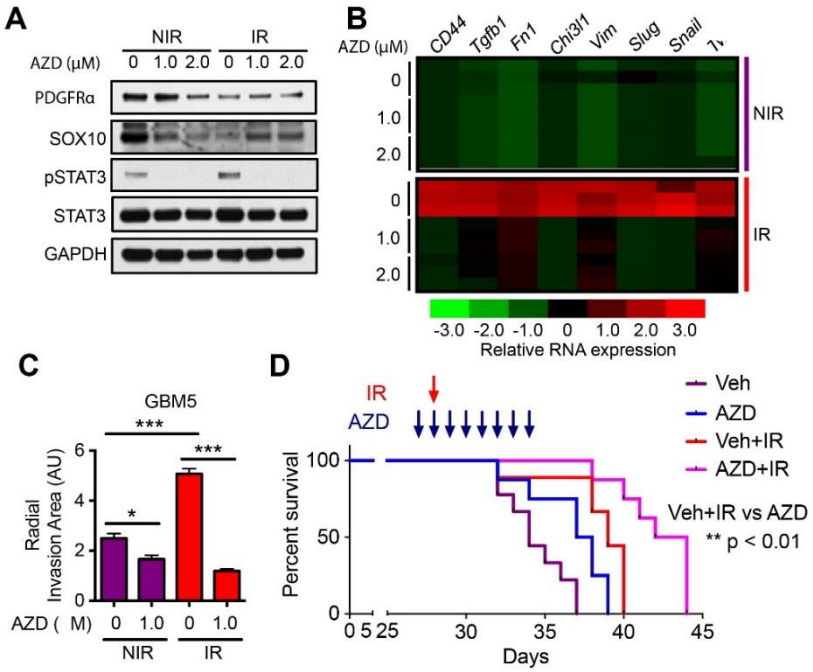

STAT3 Radiation Figure 3. Pharmacological inhibition of JAK2-STAT3 signaling inhibits radiation (IR) induced PMT in proneural HGG cells and confers survival benefit *in vivo*.

(A) Immunoblotting for phosphorylated and total STAT3, and proneural markers (PDGFRα, SOX10) in irradiated (10 Gy) and control cultured murine proneural HGG cells, treated in combination with JAK inhibitor AZD (1.0-2.0

μM). Inhibitor was added two hours prior to IR and cells were harvested five days following irradiation. (B) Heatmap showing relative mRNA expression of a panel of mesenchymal genes in irradiated and control murine proneural HGG cells treated in combination with JAK2 inhibitor AZD (1.0-2.0 μM) harvested at five days following irradiation. AZD was added two hours prior to IR and cells were harvested five days following IR. (C) Relative radial invasion area (arbitrary units: AU) of human (GBM5) proneural HGG tumorspheres embedded in 3D Matrigel conditions four days following combination treatment with radiation and JAK inhibition with AZD (1.0 μM), compared to non-irradiated tumorspheres. (D) Kaplan-Meier survival curves of mice injected with freshly sorted PDGFRα+ proneural HGG cells, treated with AZD1480 (30 mg/kg) or vehicle, and IR (10 Gy). * $P < 0.05$, ** $P < 0.01$, *** $P < 0.001$.

Cell-intrinsic biophysical properties of primary human GBM cells

We have established that ECM mechanics, specifically ECM stiffness, actively regulates tissue homeostasis and is consistently modified with tumor progression in many tissues types[12,20,223]. One of the myriad of mechanisms by which tissue mechanics drives malignant behavior is by fostering integrin and growth factor receptor clustering to enhance ERK activation and increase actomyosin-dependent cell contractility and focal adhesion formation[12]. These concepts however have never been clarified in primary human GBM cells. To test the idea that ECM mechanics is an active mediator of cell aggression, we examined the effect of ECM stiffness on cell morphology, YAP mechanotransduction, and gene expression in human GBM cells found that ECM stiffness indeed enhances the expression of genes and proteins that are associated with increased survival and invasion, such as CD44, fibronectin, hyaluronic acid, mushashi-1, and CTGF (Fig 1). As predicted, ECM stiffness drove integrin clustering, potentially resulting from the HA-rich micro-domains within the membrane that kinetically trapped integrins into HA-free regions thereby facilitating their activation (Fig 1C).

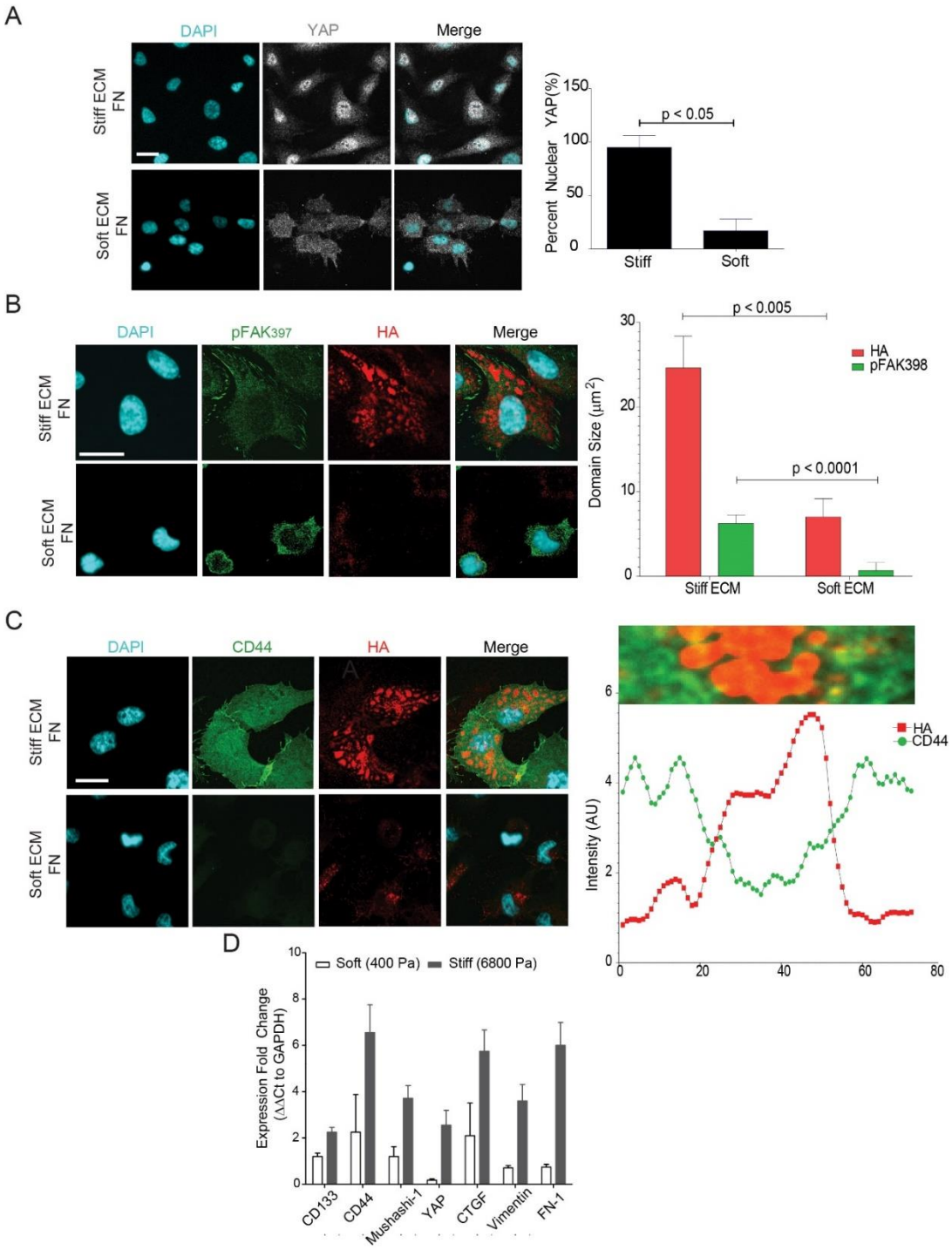

Cell-Intrinsic GBM Characterization Figure 1: ECM stiffness per se promotes GBM cell aggression

A) Primary human GBM cells plated on stiff (3000Pa; top) or soft (140Pa; bottom) fibronectin-conjugated polyacrylamide gels stained for DAPI (blue) and YAP (grey). Percentage nuclear YAP is quantified on right **B)**

Primary human GBM cells plated on stiff (3000Pa; top) or soft (140Pa; bottom) fibronectin-conjugated polyacrylamide gels stained for DAPI (blue), pFAK397 (green), and hyaluronic acid/HA (red). pFAK397 and HA domain size is quantified on right. **C)** Immunofluorescence analysis of primary human GBM cells plated on stiff (3000Pa; top) or soft (140Pa; bottom) fibronectin-conjugated polyacrylamide gels stained for DAPI (blue), CD44 (green), and hyaluronic acid/HA (red). Representative plot of CD44 and HA intensity is plotted on right demonstrated domain exclusivity. **D)**.GAPDH normalized mRNA expression fold change (stiff/soft fibronectin-coated polyacrylamide substrates) for CD133, CD44, mushashi-1, YAP and one of its mechanically-active targets CTGF, vimentin, and FN-1. Scale bar is 50 μm.

It is important to point out that these striking ECM stiffness-driven changes were only observed when cells were conjugated to a fibronectin matrix and not collagen I or laminin which do not engage mechanotransductive cellular machineries (Fig 2A-C). Consistently, primary human GBM cells plated on matrigel-conjugated polyacrylamide gels of increasing stiffness did not exhibit stiffness-induced increase in cell spread area observed when cells were plated on fibronectin-coated polyacrylamide gels. These findings argue that GBM aggression may be an adaptive response to a high force microenvironment which is only activated in a context of both abundant mechanical cues and the expression of mechanically-sensitive machineries.

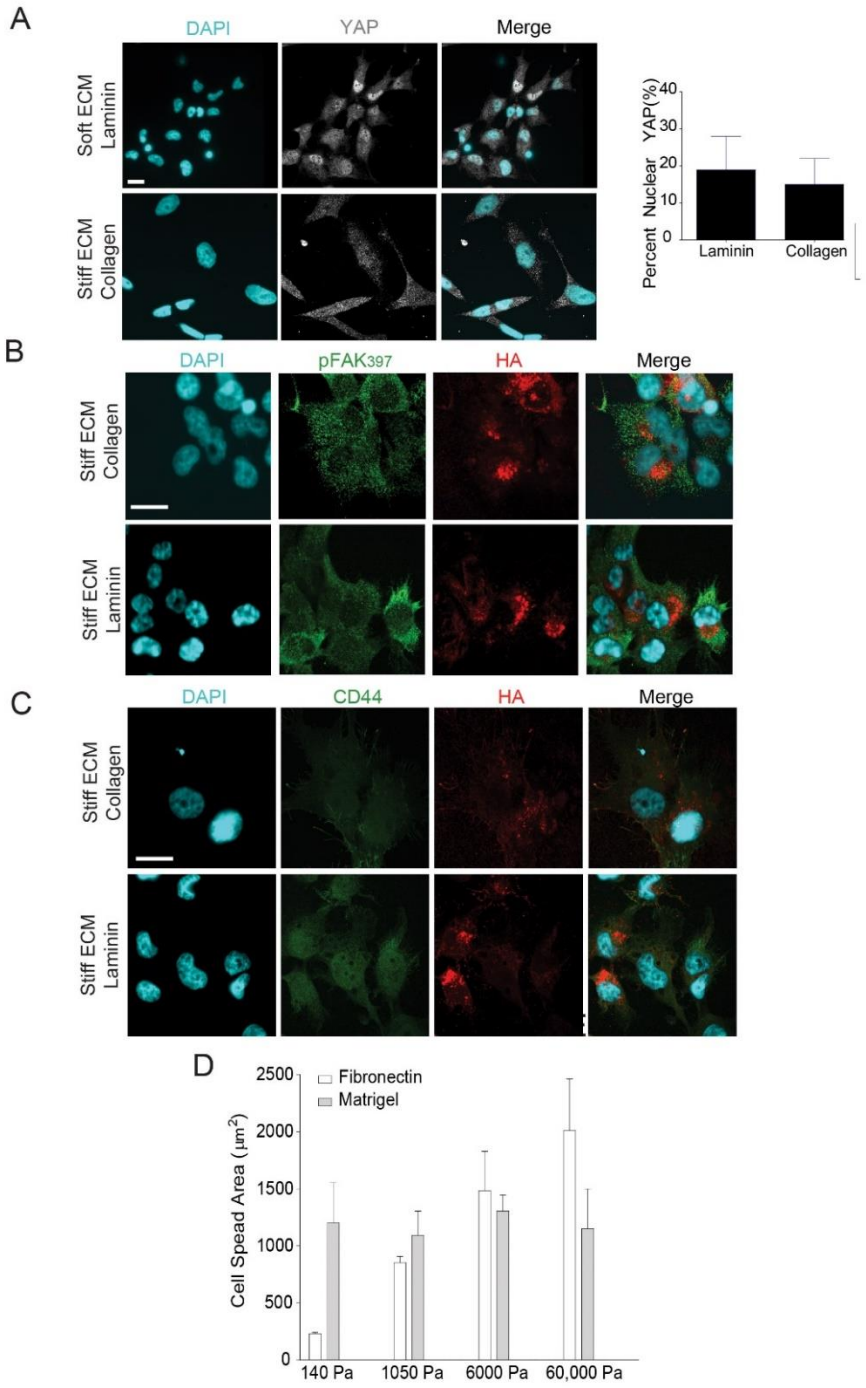

Cell-Intrinsic GBM Characterization Figure 2: Elevated ECM stiffness does not elicit morphological changes in GBM cell behavior when ligated to lamin 111 or collagen 1.

Primary human GBM cells plated on stiff polyacrylamide gels conjugated with either collagen I (top) or laminin (bottom) do not exhibit nuclear YAP **(A)** quantified on right, focal adhesion assembly as indicated by pFAK397

immunofluorescence (**B**), high CD44 and organized HA domains by immunofluorescence (**C)**. (D) Quantification of cell spread area of primary human GBM cells plated on fibronectin (white bars) or matrigel (grey bars) conjugated polyacrylamide gels. Scale bar is 50 μm.

Cell-extrinsic ECM forces are not the sole biophysical drivers of transmembrane receptor membrane organization and clustering. The biophysical properties of the cell-associated carbohydrate layer, the glycocalyx, has been recently shown to engage integrins and promote both their clustering by funneling active integrins into adhesion signaling complexes as well as their activation by applying tensional forces to matrix-bound integrins, independent of actomyosin-dependent contractility[274,275].

These data were consistent with the clinical findings indicating abundant over-expression of bulky glycoproteins on circulating tumor cells from patients with advanced disease fostering their metastasis via mechanically priming integrin activity and downstream function[275]. As a matter of fact the glycocalyx is frequently altered in tandem with changes in cell fate during development, differentiation, and cancer[276–278] and in the brain it has been implicated in migration, survival, invasion, tumor core detachment, ECM-attachment, treatment resistance, adaptability to hypoxia, and the maintenance of stemness[279–287]. For instance, GBMs are notorious for secreting excess hyaluronc acid (HA) to condition the ECM, but 12-15% of that HA is thought to remain associated with the cell and contribute to the glycocalyx[284,286,288]. Additionally, the extent of HA expression is increased with tumor grade. In that respect, a multitude of glycocalyx members have been implicated with tumor grade, such as neural cell adhesion molecule (NCAM), heparin sulfate (HS), podoplanin (PDPN), CD-133, etc[20,274,279–284,286–289]. The majority of the studies focused on the biochemical role of the glycocalyx in driving motility, such as charge interactions, direct growth factor receptor-glycoprotein binding, and

ligand affinity[288–293]. These findings underscore the importance of the glycocalyx to tumor cell biology but fail to provide a unifying theme with which to explore their role in the cancer phenotype. Recently, Dr. Matthew Paszek et al. determined that the biophysical properties of the glycocalyx per se can foster integrin clustering to drive focal adhesion formation *in silico*[274] and further went on to demonstrate this mechanism *in vitro* in a context of epithelial carcinomas[275]. Gliomas depend on integrin and growth factor receptor signaling, such as EGFR, PDGF, and PI3K, for motility and survival[233–237,294–297]. Indeed, in light of the evidence that the glycocalyx can promote integrin and growth factor receptor activity to enhance cell growth, survival and motility through its biophysical properties[274,275], we have performed preliminary characterization of this layer in primary human GBM lines with the goal of exploring the role of this alternative mechanism of the glycocalyx in the enhanced motility and invasiveness of aggressive GBMs.

First, we established a signature in our primary human GBM cell lines that associated with higher aggressiveness and was also modulated by ECM stiffness (measured by faster proliferation and more persistent and prominent invasion *in vitro* which also translated into 4X shortened survival in mouse xenograft tumors – data not shown) by mRNA analysis for high expression of PDPN and CD44 (Fig 3A). We then plated the less aggressive proneural GBMs on stiff fibronectin-conjugated polyacrylamide gels, allowed to attach and spread for 24 hours, then FACs sorted for high (hi) and low (lo) dual expression of CD44 and PDPN (Fig 3B). Paradoxically, we found that GBM cells that were high for both PDPN and CD44 were less contractile (Fig 3C), exhibited lower cellular rheology (Fig 3D), and exhibited lowered orthogonal extent of the glycocalyx (Fig 3F). These findings were quite surprising, especially the decreased thickness of the glycocalyx layer, since abundant members of the glycocalyx family appear to be associated with the cells

by immunofluorescence analysis (Fig 3G), and their biophysical role to GBM cell aggression needs to investigated further; howerver, we postulate that perhaps sensitivity to ECM stiffness is an early event in cellular transformation towards aggressiveness and once this state is acquired, the cells may yet again modify their physical properties, suggesting an exceedingly dynamic and plastic cellular state that is highly sensitive to the local microenvironment as well as cellular neighbors. Importantly, cells of varying aggressiveness, at least as defined by high versus low PDPN/CD44 cell surface expression do indeed exhibit strikingly and robustly different biophysical features under identical conditions and the implications of these findings needs to be investigated further.

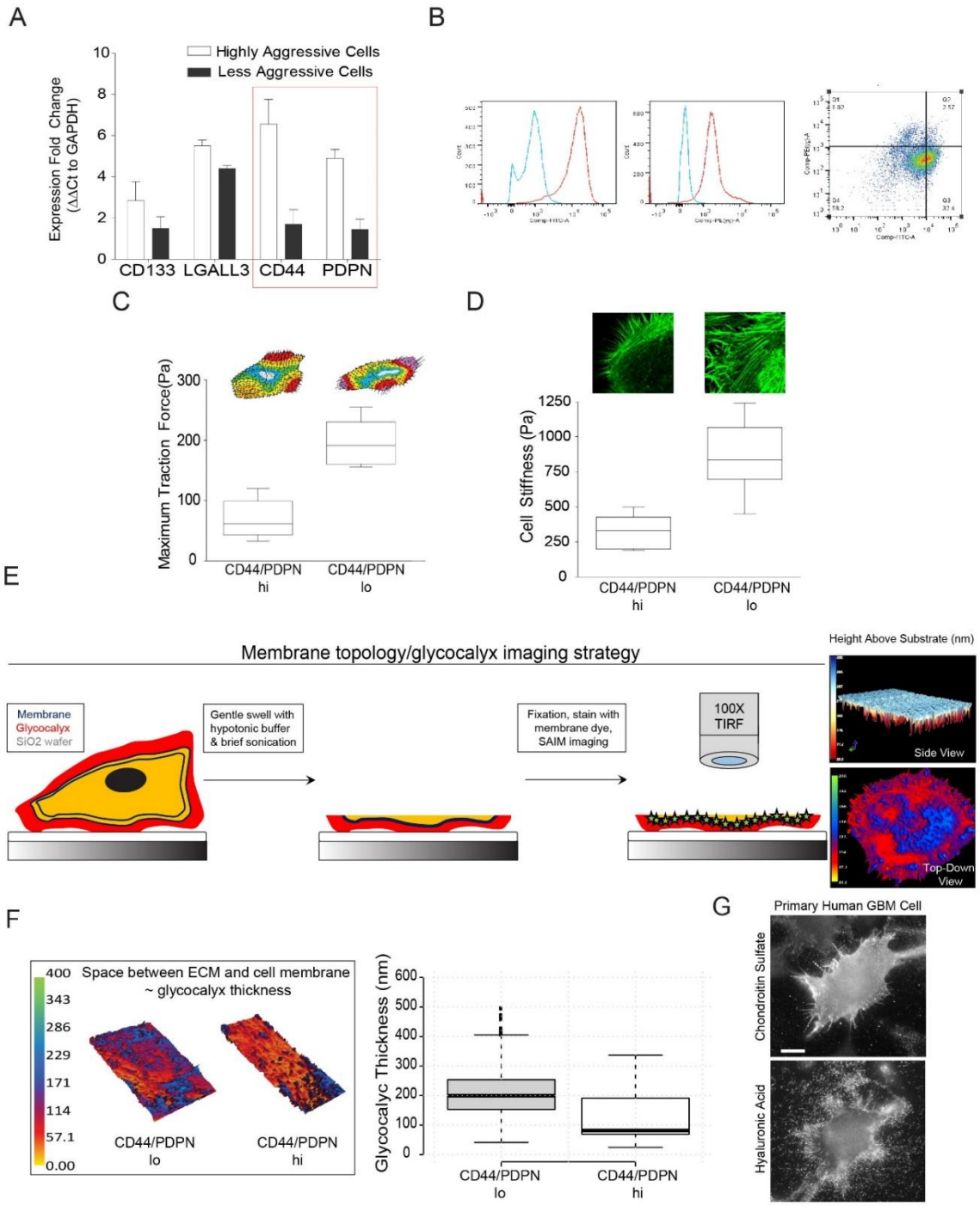

Cell-Intrinsic GBM Characterization Figure 3: Highly aggressive GBMs exhibit altered cell-intrinsic biophysical properties

A) mRNA expression fold change, normalized to GAPDH, of highly aggressive primary human GBMs of mesenchymal origin over the less aggressive proneural origin B) Fluorescence activated cells sorting strategy to

select stiffness-induced highly aggressive podoplanin(PDPN)/CD44 high (hi) cells and less aggressive PDPN/CD44 low (lo) cells. C). Traction force microscopy performed on PDPN/CD44 hi (n=22) and lo (n=18) cells. D) Atomic force microscopy measurements performed on PDPN/CD44 hi (n=30) and lo (n=21) cells; F-actin morphology (green) indicated in immunofluorescent micrographs(top). E) Schematic demonstrating sample preparation for scanning angle interference microscopy (FLIC) analysis of the glycocalyx/ventral membrane topology (left); typical post-analysis output images (right; side view – top; top down view – bottom); adopted from 298. F) FLIC analysis (n=15; each condition) of PDPN/CD44 lo and hi GBM cells. G) Representative immunofluorescence micrographs depicting high abundance of cell-associated bulky glycocalyx members, chondroitin sulfate and HA, in primary human GBM cells. Scale bar is 50 μm.

The unexpected glycocalyx thickness measurements were confirmed in two other models of differential aggression. First, we utilized a set of primary human GBM cells with knocked down galectin 1 (GAL KO) and focal adhesion kinase (FAK KO) – both lines established by Dr. James Barnes and were both shown to prolong mouse xenograft survival and were therefore expected to exhibit lowered glycocalyx. However, the inverse was observed as compared to control (CNL) cells (Fig 4A; quantified on bottom). Even more surprisingly, inhibition of hyaluronic acid (HA) synthesis via the knockdown of hyaluronic acid synthase 2 (HAS KO) did not result in decrease in the orthogonal extent of the glycocalyx (Fig 4A; quantified on bottom) – these findings were not predicted because we expected that HA would be the most prominent contributor to the thickness of the glycocalyx since GBM cells are known to secrete copious HA, however its association with the membrane has actually never been shown directly. Likewise, we originally expected that the less aggressive R132H IDH1 mutant (IDH mut) cells discussed earlier would exhibit lowered glycocalyx but instead these cells showcased not only elevated thickness of this layer but also a much larger domain size and highly patterned membrane topology as compared to the WT IDH1 (IDH WT) cells (Fig 4B). Intriguingly however, elevation of mechanosignaling

via forced expression of β1 cluster mutant (IDH mut/β1V737N) resulted in abrogation of highly patterned membrane topology and decrease the extent of the glycocalyx (Fig 4B). These findings are indeed contradictory to initial hypothesis but the fact that we see consistent and robust links between GBM aggression and lowered glycocalyx thickness (versus the expected elevation) in three different models of variable GBM aggression does point to a functional implication (or consequential result of modified aggression) of the biophysical properties of this layer to GBM biology and need to be interrogated further.

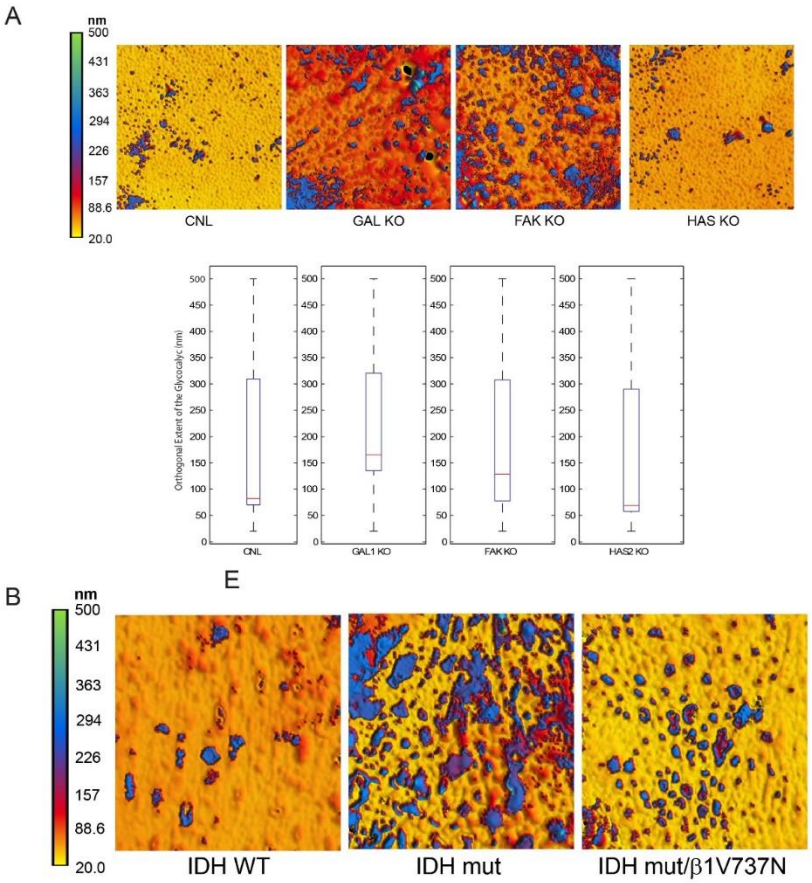

Cell-Intrinsic GBM Characterization Figure 4: The orthogonal extent of the glycocalyx is modified with cell aggression.

A) SAIM analysis (n=12 – CNL, n= 10 GAL KO, n=11 FAK KO, n= 10 HAS KO) in control mesenchymal stem cells and those with shRNA knocked-down (knockdown performed by Dr. James Barnes) galectin 1 (GAL KO),

focal adhesion kinase (FAK KO), and hyaluronan synthase 2 (HAS2); quantified on bottom. **B**). SAIM analysis (n= 15 each condition) of primary human GBM cells with WT IDH1 (IDH WT), R132H IDH mutant (IDH mut), and R132H IDH mutant GBM cells with β1V737N cluster mutant (IDH mut/β1V737N).

One of the fascinating aspects of GBM cell aggression is the diversity of their migration modes under highly compressed and mechanically-challenged environment that is associated with GBM progression. We were therefore interested in understanding the role of cellular stiffness and F-actin organization as it pertained to GBM invasion. To answer with question we utilized a number of pharmacological inhibitors of various pathways previously implicated in GBM aggression that either induced cell-softening which tracked with loss of F-actin stress fiber or promoted prominent stress-fiber formation and cellular stiffening (Fig 5A-B). Every single compound that stiffened cells via inducing F-actin stress fiber formation hindered cell invasion (Fig 5B compounds graphed in red; raw 3D invasion data not shown) while those that abrogated F-actin stress fibers and increased cellular compliance resulted in robust enhancement of 3D invasion (Fig 5A-B – compounds graphed in green; raw 3D invasion data not shown). We further analyzed the relationship between differentiation status of GBM cells and cellular rheology utilized a spectrum of previously utilized differentiation agents implicated in abrogating GBM stemness and we were able show, utilizing human neural stem cells and non-differentiated primary human GBM cells as controls, that cellular stiffness was robustly upregulated in all differentiated GBM cells (Fig 5C). Consistent with these findings, GBM cells of mesenchymal origin, which are more aggressive and are hypothesized to be more stem-like, were significantly softer than the less aggressive proneural GBM cells (Fig 5D). Finally, we set out to link the degree and the mode of invasiveness with cellular rheology and observed that the softest control GBM cells (Fig 5E left panel) invading within stiff hyaluronic acid gels preferentially migrated

using amoeboid migration mode by pushing their cell bodies through the dense pores of the surrounding matrix (red arrows) and sending out long protrusions to sense the matrix (blue arrows) while the stiffest, and presumably most differentiated, cells (Fig 5E right panel) completely lacked the ability to invade their surrounding matrix; cells with intermediate cellular stiffness appeared to exhibit quiasi-ameboid or mesenchymal invasion style (Fig 5E middle panels).

Taken together our analyses point to intimate links between the state of the glycocalyx and F-actin-mediated cellular rheology to GBM aggression and indicate that mechanical perturbations in these cellular components play an active and causal role in mediating tumor development and progression, especially as it pertains invasion, proliferation, and survival.

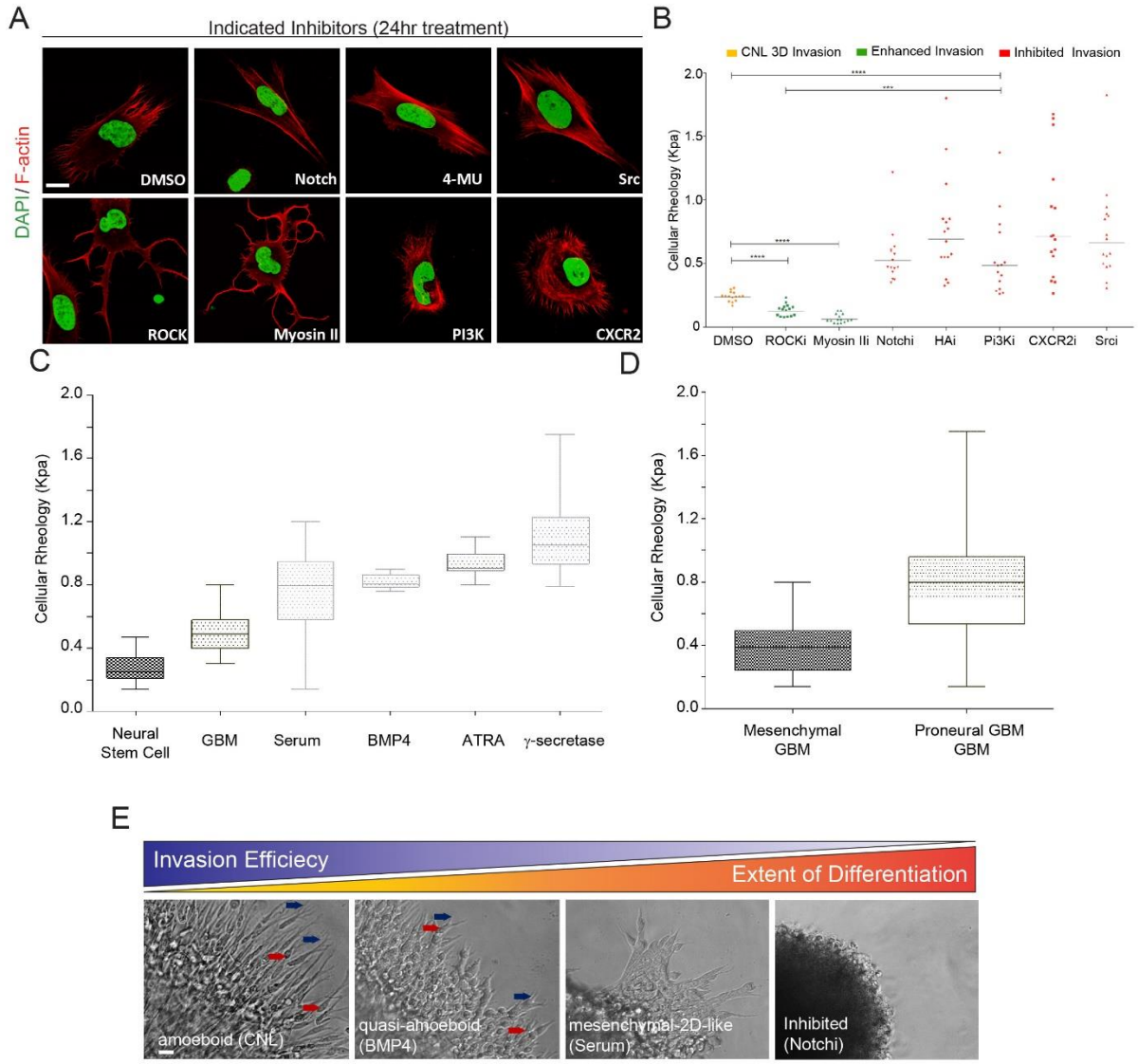

Cell-Intrinsic GBM Characterization Figure 5: Cellular rheology tracks with cellular invasion capacity.

A) Representative immunofluorescence micrographs of primary human GBM cellular morphology treated with indicated inhibitors stained for DAPI (green) and F-actin (red). **B**) Atomic force microscopy analysis of cellular rheology of primary human GBMs treated with indicated inhibitors. **C**) Atomic force microscopy analysis of cellular rheology of primary human GBMs treated with indicated differentiation factors. **D**) Atomic force microscopy analysis of cellular rheology of primary human GBMs of mesenchymal versus proneural origin. **A**) Representative immunofluorescence micrographs of primary

human GBM tumor spheres embedded in stiff (3000 Pa) 3D hyaluronic acid gels treated with indicated differentiation inhibitors. Red arrows point to squeezing nuclei; blue arrows point to protrusions. Scale bar is 50 μm.

CHAPTER 6: IMPACT, CONCLUSIONS & FINAL REMARKS

Impact

The work presented in this dissertation aimed to 1) develop 3-dimensinal model systems capable of controlling various aspects of biophysical forces relevant to solid cancer aggression and progression, 2) address the uniformity of the mechanophenotype and its downstream effectors across distinct tissue types in disease, and 3) establish clinical relevance of tissue mechanics with respect to development of novel treatment modalities for specific types of breast, pancreatic, and brain cancers, as well as shedding light on the potential harmful long-term side effects of current standard of care treatment strategies that modify tissue mechanophenotype and foster tumor recurrence and patient relapse via biophysically-driven pathways.

In that respect, the established bioreactor model systems and the various *in vitro* assays described in this thesis are currently being utilized for a number of parallel studies in the Weaver lab, such as the interrogation of gene expression changes induced by elevated ECM stiffness, dimensionality, and multicellularity. Further, the Persson laboratory, in collaboration with myself and Dr. Valerie Weaver, are in the process of utilizing gene expression microarray data, which resulted directly from the work described in this thesis, to screen for micro RNA targets regulating GBM cell proliferation in response to compressive forces. Additionally and importantly, and in complement to Dr. Persson's laboratory's *in vivo* data, our *in vitro* bioreactor studies strongly suggest that the addition of pressure-reducing AF peptide to the standard of care and under-development GBM therapeutics may significantly improve drug uptake and thereby treatment efficacy; if robust, this finding alone could fundamentally change the ideology and the

methodology with which GBM treatment modalities will be screened and administered to patients; addition of AF to other treatment regimens could also potentially apply to any solid state tumor.

The work described in this thesis also addressed both the universality and the uniqueness of the pathological mechanoresponse in breast, pancreatic, and brain cancers. We found that in the context of breast cancer, the stiff ECM engages a unique pathway through the ligation of $\alpha5\beta1$ integrin by fibronectin's synergy; by contrast, in the context of PDAC pancreatic cancer we disclosed the utilization of the STAT3, TNC, and various aspects of the inflammatory response to mediating stiffness-induced tumor epithelial response. Therefore, despite the common epithelial origin, these tumor types exhibited uniform but non-identical mechanical corruption and utilized distinct downstream mechanosignaling pathways to elicit altered tumor biology. In the context of GBM brain cancer, we uncovered TNC-mediated crosslinking of hyaluronic acid as the mechanism for increased ECM stiffening which was fostered by HIF1α-hypoxia sensing with GBM onset; we further implicated the positively-prognostic IDH1 mutational status in inhibiting this mechanophenotype. In summary, despite many commonalities, mechanical corruption elicited differential responses in breast (through engaging a mechanically-active integrin), pancreatic (through mechanical fostering of STAT3 inflammation), and brain (through mechanical fostering of HIF1α hypoxia sensing) cancers but was unequivocally involved in modifying tumor behavior. With respect to clinical application and therapeutic development, the work presented in this thesis collectively argues that there is a great need for improved stratification of patients based on therapeutically-relevant elements of tissue mechanics and

strategically-designed personalized treatment regimes for the different patient subtypes exhibiting differentially-stiffened ECM.

Scientific Conclusions

We have shown that mechanical and topological cues from the microenvironment are critical regulators of tumor progression and aggression in breast and pancreatic cancers of epithelial origin, as well as in glioblastoma multiforme brain cancer of glial origin. In the context of breast cancer we have elucidated the apparent discrepancy between the tumor-promoting deposition and remodeling of fibrillary collagen I and a tumor-suppressive functionality of its major receptor, $\alpha 2\beta 1$ integrin, and described a novel role for fibronectin-ligating $\alpha 5\beta 1$ integrin in transducing collagen-mediated stiffness-driven malignant transformation, especially at the exceedingly rigid tumor fronts with high degree of association between fibronectin and collagen. Since the functional end of $\alpha 5\beta 1$, its synergy site, is only engaged in a high-force environment of a tumor and, despite being necessary for malignancy, ECM mechanics itself cannot be targeted directly in patients, the synergy site may prove to be a relevant therapeutic target in breast cancer.

Our pancreatic work shed light on the conflicting data in support of both the tumor-promoting and tumor-suppressive functions of the anti-fibrotic therapies in pancreatic cancer by clarifying two distinct routes for tumor fibrosis either through the canonical stromal remodeling or via the stromally-independent epithelium-driven fibrotic phenotype, dictated by tumor cell genotype. We thereby clarified that stromal dependency is highly context-dependent and that in order to design therapeutic modalities that maximally benefit pancreatic cancer patients, stromal therapies must be matched appropriately to patient's tumor genotypes or they may otherwise fail

to provide benefit. Importantly and more specifically, our findings suggested that innovative treatment modalities holistically targeting both epithelial- and stromal-driven fibrosis, cellular contractility, and YAP activity, such as combinatory FAK/JAK inhibitor cocktails, will likely prove to be more efficacious therapeutic strategy with which to treat PDAC patients, especially for the quasi-mesenchymal and Kras-independent PDAC subtypes with elevated YAP.

Our biophysics work in GBM malignancy is the first to directly implicate ECM mechanics to GBM aggression and reveal the critical role for the tenascin C-mediated tissue stiffening in a context of positively prognostic IDH1 mutation to drive tumor aggression by restoring HIF1α-dependent hypoxia sensing and stiffness-sensitive gene expression. Further, our work not only demonstrated that forced elevation of mechanosignaling in IDH1 mutant GBMs induced HIF1α-dependent tenascin C expression to stiffen the ECM and promoted tumor aggression, thereby bypassing the protective activity of IDH1 mutational status, but also indicated that standard of care radiation treatment-induced tissue stiffening may be a key contributor to IDH1 mutant GBM recurrence. These data are also in accordance with a separate set of collaborative studies pointing to radiation-induced mesenchymal transition and elevation of mechanosignaling and cell invasion upon cell and tumor irradiation *in vitro* and *in vivo*, respectively. Moreover, biophysical characterization studies revealed a robust relationship between cell-intrinsic biophysical properties, which are much better therapeutic targets than ECM mechanics itself, and both the changes in the mechanical state of cell-extrinsic environment and cellular aggression and invasion.

Altogether, our studies demonstrate that cell-extrinsic context is a critical regulator of cellular behavior, largely due to cellular plasticity, and perhaps this plastic phenotype can be utilized as means with which to design rational therapeutic modalities to benefit cancer patients.

Final Remarks

Major scientific breakthroughs and clinically-relevant advances in cancer research over the past decades have emerged by challenging accepted dogmas and integrating concepts from apparently unrelated fields in order to provide holistic understanding of carcinogenesis. This suggests that the key to finding effective cancer treatment modalities has a higher probability of emerging from the integration of data acquired using novel, transdisciplinary, and orthogonal approaches to cancer biology. Much of the work in this dissertation challenges the paradigm that cancer aggression arises primarily due to irreversible changes in the cellular genome and proposes the notion that physiological and pathological states of tissues are mediated via the dynamic and reciprocal balance of cell-intrinsic and cell-extrinsic forces that are capable to epigenetically control cellular fate in ways that are parallel to cellular genetic milieu.

There exist tremendous unmet clinical needs in breast, pancreatic, and brain cancers and our work suggests that a successful route to a cure for these pathologies is likely one that considers not only the canonical biochemical pathways targeting oncogenes and tumor suppressors, but one that takes into the consideration biophysical mechanisms of tumor aggression. The fundamental goal of the work presented in this thesis is to add to the field's understanding of the alternative, biophysically-driven mechanisms of cancer survival, invasiveness, and treatment resistance in order to make a contribution to the revelation of more effective cancer treatment

modalities, extend patient survival, prevent relapse, and improve quality of life for cancer patients.

CHAPTER 7: REFERENCES

1. DuFort, C. C., Paszek, M. J. & Weaver, V. M. Balancing forces: architectural control of mechanotransduction. *Nat. Rev. Mol. Cell Biol.* **12,** 308–319 (2011).

2. Kumar, S. & Weaver, V. M. Mechanics, malignancy, and metastasis: the force journey of a tumor cell. *Cancer Metastasis Rev.* **28,** 113–27 (2009).

3. Butcher, D. T., Alliston, T. & Weaver, V. M. A tense situation: forcing tumour progression. *Nat. Rev. Cancer* **9,** 108–122 (2009).

4. Jaalouk, D. E. & Lammerding, J. Mechanotransduction gone awry. *Nat. Rev. Mol. Cell Biol.* **10,** 63–73 (2009).

5. Yin, M. *et al.* Assessment of hepatic fibrosis with magnetic resonance elastography. *Clin. Gastroenterol. Hepatol.* **5,** 1207–1213.e2 (2007).

6. Venkatesh, S. K. *et al.* MR elastography of liver tumors: preliminary results. *AJR. Am. J. Roentgenol.* **190,** 1534–40 (2008).

7. Feier, D., Lupsor Platon, M., Stefanescu, H. & Badea, R. Transient elastography for the detection of hepatocellular carcinoma in viral C liver cirrhosis. Is there something else than increased liver stiffness? *J. Gastrointestin. Liver Dis.* **22,** 283–9 (2013).

8. De Angelis, C., Manfrè, S. F. & Pellicano, R. Endoscopic ultrasonography for diagnosis and staging of pancreatic adenocarcinoma: key messages for clinicians. *Minerva Med.* **105,** 121–8 (2014).

9. Berg, W. A. *et al.* Diagnostic Accuracy of Mammography, Clinical Examination, US, and MR Imaging in Preoperative Assessment of Breast Cancer1. *Radiology* **233,** 830–849 (2004).

10. Moffat, B. A. *et al.* Functional diffusion map: a noninvasive MRI biomarker for early stratification of clinical brain tumor response. *Proc. Natl. Acad. Sci. U. S. A.* **102,** 5524–9 (2005).

11. Hove, J. R. *et al.* Intracardiac fluid forces are an essential epigenetic factor for embryonic cardiogenesis. *Nature* **421,** 172–177 (2003).

12. Paszek, M. J. *et al.* Tensional homeostasis and the malignant phenotype. *Cancer Cell* **8,** 241–54 (2005).

13. Weaver, V. M. *et al.* Reversion of the malignant phenotype of human breast cells in three-dimensional culture and in vivo by integrin blocking antibodies. *J. Cell Biol.* **137,** 231–45 (1997).

14. Engler, A. J., Sen, S., Sweeney, H. L. & Discher, D. E. Matrix Elasticity Directs Stem Cell Lineage Specification. *Cell* **126,** 677–689 (2006).

15. Ingber, D. E. Mechanical control of tissue morphogenesis during embryological development. *Int. J. Dev. Biol.* **50,** 255–266 (2006).

16. Yu, H., Mouw, J. K. & Weaver, V. M. Forcing form and function: Biomechanical regulation of tumor evolution. *Trends Cell Biol.* **21,** 47–56 (2011).

17. Engler, A. J. *et al.* Embryonic cardiomyocytes beat best on a matrix with heart-like elasticity: scar-like rigidity inhibits beating. *J. Cell Sci.* **121,** 3794–3802 (2008).

18. Klocke, R., Cockcroft, J. R., Taylor, G. J., Hall, I. R. & Blake, D. R. Arterial stiffness and central blood pressure, as determined by pulse wave analysis, in rheumatoid arthritis. *Ann. Rheum. Dis.* **62,** 414–418 (2003).

19. Flanagan, L. A., Ju, Y.-E., Marg, B., Osterfield, M. & Janmey, P. A. Neurite branching on deformable substrates. *Neuroreport* **13,** 2411–2415 (2002).

20. Levental, K. R. *et al.* Matrix crosslinking forces tumor progression by enhancing integrin signaling. *Cell* **139,** 891–906 (2009).

21. Paszek, M. J. & Weaver, V. M. The tension mounts: Mechanics meets morphogenesis and malignancy. *J. Mammary Gland Biol. Neoplasia* **9,** 325–342 (2004).

22. Pelham, R. J. & Wang, Y. L. Cell locomotion and focal adhesions are regulated by the mechanical properties of the substrate. in *Biol. Bull.* **194,** 348–350 (1998).

23. Yeung, T. *et al.* Effects of substrate stiffness on cell morphology, cytoskeletal structure, and adhesion. *Cell Motil. Cytoskeleton* **60,** 24–34 (2005).

24. Wong, J. Y., Velasco, A., Rajagopalan, P. & Pham, Q. Directed movement of vascular smooth muscle cells on gradient-compliant hydrogels. *Langmuir* **19,** 1908–1913 (2003).

25. Gaudet, C. *et al.* Influence of type I collagen surface density on fibroblast spreading, motility, and contractility. *Biophys. J.* **85,** 3329–3335 (2003).

26. Heidemann, S. R. & Wirtz, D. Towards a regional approach to cell mechanics. *Trends Cell Biol.* **14,** 160–166 (2004).

27. Discher, D. E., Janmey, P. & Wang, Y.-L. Tissue cells feel and respond to the stiffness of their substrate. *Science* **310,** 1139–1143 (2005).

28. Engler, A. J. *et al.* Myotubes differentiate optimally on substrates with tissue-like stiffness: Pathological implications for soft or stiff microenvironments. *J. Cell Biol.* **166,** 877–887 (2004).

29. Reinhart-King, C. A., Dembo, M. & Hammer, D. A. Cell-cell mechanical communication through compliant substrates. *Biophys. J.* **95,** 6044–6051 (2008).

30. Califano, J. P. & Reinhart-King, C. A. The effects of substrate elasticity on endothelial cell network formation and traction force generation. in *Proc. 31st Annu. Int. Conf. IEEE Eng. Med. Biol. Soc. Eng. Futur. Biomed. EMBC 2009* 3343–3345 (2009). doi:10.1109/IEMBS.2009.5333194

31. Khatiwala, C. B., Kim, P. D., Peyton, S. R. & Putnam, A. J. ECM compliance regulates osteogenesis by influencing MAPK signaling downstream of RhoA and ROCK. *J. Bone Miner. Res.* **24,** 886–898 (2009).

32. Gardel, M. L. *et al.* Traction stress in focal adhesions correlates biphasically with actin retrograde fl ow speed. *J. Cell Biol.* **183,** 999–1005 (2008).

33. Pasapera, A. M., Schneider, I. C., Rericha, E., Schlaepfer, D. D. & Waterman, C. M. Myosin II activity regulates vinculin recruitment to focal adhesions through FAK-mediated paxillin phosphorylation. *J. Cell Biol.* **188,** 877–890 (2010).

34. Gardel, M. L., Schneider, I. C., Aratyn-Schaus, Y. & Waterman, C. M. Mechanical integration of actin and adhesion dynamics in cell migration. *Annu. Rev. Cell Dev. Biol.* **26,** 315–333 (2010).

35. Lee, J. S. H. *et al.* Ballistic intracellular nanorheology reveals ROCK-hard cytoplasmic stiffening response to fluid flow. *J. Cell Sci.* **119,** 1760–1768 (2006).

36. Khatau, S. B. *et al.* A perinuclear actin cap regulates nuclear shape. *Proc. Natl. Acad. Sci. U. S. A.* **106,** 19017–19022 (2009).

37. Lee, J. S. H. *et al.* Nuclear lamin A/C deficiency induces defects in cell mechanics, polarization, and migration. *Biophys. J.* **93,** 2542–2552 (2007).

38. Spencer, V. A., Xu, R. & Bissell, M. J. Gene expression in the third dimension: The ECM-nucleus connection. *J. Mammary Gland Biol. Neoplasia* **15,** 65–71 (2010).

39. Boudreau, N., Werb, Z. & Bissell, M. J. Suppression of apoptosis by basement membrane requires three-dimensional tissue organization and withdrawal from the cell cycle. *Proc. Natl. Acad. Sci. U. S. A.* **93,** 3509–3513 (1996).

40. Wang, F. *et al.* Phenotypic reversion or death of cancer cells by altering signaling pathways in three-dimensional contexts. *J. Natl. Cancer Inst.* **94,** 1494–1503 (2002).

41. Weaver, V. M., Fischer, A. H., Peterson, O. W. & Bissell, M. J. The importance of the microenvironment in breast cancer progression: recapitulation of mammary tumorigenesis using a unique human mammary epithelial cell model and a three-dimensional culture assay. *Biochem. Cell Biol.* **74,** 833–51 (1996).

42. Pedersen, J. A. & Swartz, M. A. Mechanobiology in the third dimension. *Ann. Biomed. Eng.* **33,** 1469–1490 (2005).

43. Pampaloni, F., Reynaud, E. G. & Stelzer, E. H. K. The third dimension bridges the gap between cell culture and live tissue. *Nat. Rev. Mol. Cell Biol.* **8,** 839–845 (2007).

44. Weaver, V. M. *et al.* β4 integrin-dependent formation of polarized three-dimensional architecture confers resistance to apoptosis in normal and malignant mammary epithelium. *Cancer Cell* **2,** 205–216 (2002).

45. Zahir, N. & Weaver, V. M. Death in the third dimension: Apoptosis regulation and tissue architecture. *Curr. Opin. Genet. Dev.* **14,** 71–80 (2004).

46. Jacks, T. & Weinberg, R. A. Taking the study of cancer cell survival to a new dimension. *Cell* **111,** 923–925 (2002).

47. Tse, J. R. & Engler, A. J. Stiffness gradients mimicking in vivo tissue variation regulate mesenchymal stem cell fate. *PLoS One* **6,** (2011).

48. Provenzano, P. P. *et al.* Collagen density promotes mammary tumor initiation and progression. *BMC Med.* **6,** 11 (2008).

49. Barcellos-Hoff, M. H., Aggeler, J., Ram, T. G. & Bissell, M. J. Functional differentiation and alveolar morphogenesis of primary mammary cultures on reconstituted basement membrane. *Development* **105,** 223–235 (1989).

50. Foster, C. S., Smith, C. A., Dinsdale, E. A., Monaghan, P. & Neville, A. M. Human mammary gland morphogenesis in vitro: The growth and differentiation of normal breast epithelium in collagen gel cultures defined by electron microscopy, monoclonal antibodies, and autoradiography. *Dev. Biol.* **96,** 197–216 (1983).

51. Richards, J. *et al.* Response of end bud cells from immature rat mammary gland to hormones when cultured in collagen gel. *Exp. Cell Res.* **147,** 95–109 (1983).

52. Emerman, J. T., Burwen, S. J. & Pitelka, D. R. Substrate properties influencing ultrastructural differentiation of mammary epithelial cells in culture. *Tissue Cell* **11,** 109–119 (1979).

53. Chalupowicz, D. G., Chowdhury, Z. A., Bach, T. L., Barsigian, C. & Martinez, J. Fibrin II induces endothelial cell capillary tube formation. *J.Cell Biol.* **130,** 207–215 (1995).

54. Ghajar, C. M. *et al.* The effect of matrix density on the regulation of 3-D capillary morphogenesis. *Biophys. J.* **94,** 1930–1941 (2008).

55. Roeder, B. A., Kokini, K., Sturgis, J. E., Robinson, J. P. & Voytik-Harbin, S. L. Tensile mechanical properties of three-dimensional type I collagen extracellular matrices with varied microstructure. *J. Biomech. Eng.* **124,** 214–222 (2002).

56. Ulrich, T. A., Jain, A., Tanner, K., MacKay, J. L. & Kumar, S. Probing cellular mechanobiology in three-dimensional culture with collagen-agarose matrices. *Biomaterials* **31,** 1875–1884 (2010).

57. Lutolf, M. P. *et al.* Synthetic matrix metalloproteinase-sensitive hydrogels for the conduction of tissue regeneration: engineering cell-invasion characteristics. *Proc. Natl. Acad. Sci. U. S. A.* **100,** 5413–5418 (2003).

58. Seliktar, D., Zisch, A. H., Lutolf, M. P., Wrana, J. L. & Hubbell, J. A. MMP-2 sensitive, VEGF-bearing bioactive hydrogels for promotion of vascular healing. *J. Biomed. Mater. Res. A* **68,** 704–716 (2004).

59. Schmedlen, R. H., Masters, K. S. & West, J. L. Photocrosslinkable polyvinyl alcohol hydrogels that can be modified with cell adhesion peptides for use in tissue engineering. *Biomaterials* **23,** 4325–4332 (2002).

60. Mann, B. K. & West, J. L. Cell adhesion peptides alter smooth muscle cell adhesion, proliferation, migration, and matrix protein synthesis on modified surfaces and in polymer scaffolds. *J. Biomed. Mater. Res.* **60,** 86–93 (2002).

61. Kloxin, A. M., Kasko, A. M., Salinas, C. N. & Anseth, K. S. Photodegradable hydrogels for dynamic tuning of physical and chemical properties. *Science* **324,** 59–63 (2009).

62. DeForest, C. A., Polizzotti, B. D. & Anseth, K. S. Sequential click reactions for synthesizing and patterning three-dimensional cell microenvironments. *Nat. Mater.* **8,** 659–664 (2009).

63. Caplan, M. R., Schwartzfarb, E. M., Zhang, S., Kamm, R. D. & Lauffenburger, D. A. Control of self-assembling oligopeptide matrix formation through systematic variation of amino acid sequence. *Biomaterials* **23,** 219–227 (2002).

64. Zhang, S. *et al.* Self-complementary oligopeptide matrices support mammalian cell attachment. *Biomaterials* **16,** 1385–1393 (1995).

65. Sieminski, A. L., Was, A. S., Kim, G., Gong, H. & Kamm, R. D. The stiffness of three-dimensional ionic self-assembling peptide gels affects the extent of capillary-like network formation. *Cell Biochem. Biophys.* **49,** 73–83 (2007).

66. Gelain, F., Bottai, D., Vescovi, A. & Zhang, S. Designer self-assembling peptide nanofiber scaffolds for adult mouse neural stem cell 3-dimensional cultures. *PLoS One* **1,** (2006).

67. Horii, A., Wang, X., Gelain, F. & Zhang, S. Biological designer self-assembling peptide nanofiber scaffolds significantly enhance osteoblast proliferation, differentiation and 3-D migration. *PLoS One* **2,** (2007).

68. Wang, S., Nagrath, D., Chen, P. C., Berthiaume, F. & Yarmush, M. L. Three-dimensional primary hepatocyte culture in synthetic self-assembling peptide hydrogel. *Tissue Eng. Part A* **14,** 227–236 (2008).

69. Genové, E. *et al.* Functionalized self-assembling peptide hydrogel enhance maintenance of hepatocyte activity in vitro. *J. Cell. Mol. Med.* **13,** 3387–3397 (2009).

70. Gudjonsson, T. *et al.* Normal and tumor-derived myoepithelial cells differ in their ability to interact with luminal breast epithelial cells for polarity and basement membrane deposition. *J. Cell Sci.* **115,** 39–50 (2002).

71. Lopez, J. I., Kang, I., You, W.-K., McDonald, D. M. & Weaver, V. M. In situ force mapping of mammary gland transformation. *Integr. Biol. (Camb).* **3,** 910–21 (2011).

72. Fischer, R. S., Gardel, M., Ma, X., Adelstein, R. S. & Waterman, C. M. Local Cortical Tension by Myosin II Guides 3D Endothelial Cell Branching. *Curr. Biol.* **19,** 260–265 (2009).

73. Zaman, M. H., Matsudaira, P. & Lauffenburger, D. A. Understanding effects of matrix protease and matrix organization on directional persistence and translational speed in three-dimensional cell migration. *Ann. Biomed. Eng.* **35,** 91–100 (2007).

74. Kim, H.-D. *et al.* Epidermal growth factor-induced enhancement of glioblastoma cell migration in 3D arises from an intrinsic increase in speed but an extrinsic matrix- and proteolysis-dependent increase in persistence. *Mol. Biol. Cell* **19,** 4249–4259 (2008).

75. Provenzano, P. P., Inman, D. R., Eliceiri, K. W., Trier, S. M. & Keely, P. J. Contact guidance mediated three-dimensional cell migration is regulated by Rho/ROCK-dependent matrix reorganization. *Biophys. J.* **95,** 5374–5384 (2008).

76. Cima, L. G., Ingber, D. E., Vacanti, J. P. & Langer, R. Hepatocyte culture on biodegradable polymeric substrates. *Biotechnol. Bioeng.* **38,** 145–158 (1991).

77. Cima, L. G. *et al.* Tissue engineering by cell transplantation using degradable polymer substrates. *J. Biomech. Eng.* **113,** 143–151 (1991).

78. Domansky, K. *et al.* Perfused multiwell plate for 3D liver tissue engineering. *Lab Chip* **10,** 51–58 (2010).

79. Burdick, J. A. & Anseth, K. S. Photoencapsulation of osteoblasts in injectable RGD-modified PEG hydrogels for bone tissue engineering. *Biomaterials* **23,** 4315–4323 (2002).

80. Hoque, M. E. *et al.* Fabrication using a rapid prototyping system and in vitro characterization of PEG-PCL-PLA scaffolds for tissue engineering. *J. Biomater. Sci. Polym. Ed.* **16,** 1595–1610 (2005).

81. Brigham, M. D. *et al.* Mechanically robust and bioadhesive collagen and photocrosslinkable hyaluronic acid semi-interpenetrating networks. *Tissue Eng. Part A* **15,** 1645–1653 (2009).

82. Chung, C., Beecham, M., Mauck, R. L. & Burdick, J. A. The influence of degradation characteristics of hyaluronic acid hydrogels on in vitro neocartilage formation by mesenchymal stem cells. *Biomaterials* **30,** 4287–96 (2009).

83. Genové, E., Shen, C., Zhang, S. & Semino, C. E. The effect of functionalized self-assembling peptide scaffolds on human aortic endothelial cell function. *Biomaterials* **26,** 3341–3351 (2005).

84. Sieminski, A. L., Semino, C. E., Gong, H. & Kamm, R. D. Primary sequence of ionic self-assembling peptide gels affects endothelial cell adhesion and capillary morphogenesis. *J. Biomed. Mater. Res. - Part A* **87,** 494–504 (2008).

85. Beil, M. *et al.* Sphingosylphosphorylcholine regulates keratin network architecture and visco-elastic properties of human cancer cells. *Nat. Cell Biol.* **5,** 803–811 (2003).

86. Colpaert, C., Vermeulen, P., Van Marck, E. & Dirix, L. The presence of a fibrotic focus is an independent predictor of early metastasis in lymph node-negative breast cancer patients. *Am. J. Surg. Pathol.* **25,** 1557–8 (2001).

87. Peyton, S. R., Raub, C. B., Keschrumrus, V. P. & Putnam, A. J. The use of poly(ethylene glycol) hydrogels to investigate the impact of ECM chemistry and mechanics on smooth muscle cells. *Biomaterials* **27,** 4881–4893 (2006).

88. Peyton, S. R., Kim, P. D., Ghajar, C. M., Seliktar, D. & Putnam, A. J. The effects of matrix stiffness and RhoA on the phenotypic plasticity of smooth muscle cells in a 3-D biosynthetic hydrogel system. *Biomaterials* **29,** 2597–607 (2008).

89. Patterson, J. & Hubbell, J. A. Enhanced proteolytic degradation of molecularly engineered PEG hydrogels in response to MMP-1 and MMP-2. *Biomaterials* **31,** 7836–45 (2010).

90. Ayala, P., Lopez, J. I. & Desai, T. A. Microtopographical cues in 3D attenuate fibrotic phenotype and extracellular matrix deposition: implications for tissue regeneration. *Tissue Eng. Part A* **16,** 2519–2527 (2010).

91. Collins, J. M., Ayala, P., Desai, T. A. & Russell, B. Three-dimensional culture with stiff microstructures increases proliferation and slows osteogenic differentiation of human mesenchymal stem cells. *Small* **6,** 355–60 (2010).

92. Bernards, D. A. & Desai, T. A. Nanotemplating of biodegradable polymer membranes for constant-rate drug delivery. *Adv. Mater.* **22,** 2358–62 (2010).

93. Choquet, D., Felsenfeld, D. P. & Sheetz, M. P. Extracellular matrix rigidity causes strengthening of integrin-cytoskeleton linkages. *Cell* **88,** 39–48 (1997).

94. Chen, C. S., Mrksich, M., Huang, S., Whitesides, G. M. & Ingber, D. E. Geometric control of cell life and death. *Science* **276,** 1425–1428 (1997).

95. Provenzano, P. P. *et al.* Collagen reorganization at the tumor-stromal interface facilitates local invasion. *BMC Med.* **4,** 38 (2006).

96. Rhee, S. & Grinnell, F. Fibroblast mechanics in 3D collagen matrices. *Adv. Drug Deliv. Rev.* **59,** 1299–1305 (2007).

97. Harley, B. A. C. *et al.* Microarchitecture of three-dimensional scaffolds influences cell migration behavior via junction interactions. *Biophys. J.* **95,** 4013–4024 (2008).

98. Zaman, M. H., Kamm, R. D., Matsudaira, P. & Lauffenburger, D. A. Computational model for cell migration in three-dimensional matrices. *Biophys. J.* **89,** 1389–1397 (2005).

99. Zaman, M. H. *et al.* Migration of tumor cells in 3D matrices is governed by matrix stiffness along with cell-matrix adhesion and proteolysis. *Proc. Natl. Acad. Sci. U. S. A.* **103,** 10889–10894 (2006).

100. Albiges-Rizo, C., Destaing, O., Fourcade, B., Planus, E. & Block, M. R. Actin machinery and mechanosensitivity in invadopodia, podosomes and focal adhesions. *J. Cell Sci.* **122,** 3037–3049 (2009).

101. Stricker, J., Falzone, T. & Gardel, M. L. Mechanics of the F-actin cytoskeleton. *J. Biomech.* **43,** 9–14 (2010).

102. Borghi, N., Lowndes, M., Maruthamuthu, V., Gardel, M. L. & Nelson, W. J. Regulation of cell motile behavior by crosstalk between cadherin- and integrin-mediated adhesions. *Proc. Natl. Acad. Sci. U. S. A.* **107,** 13324–13329 (2010).

103. Cassereau, L., Miroshnikova, Y., Ou, G., Lakins, J. & Weaver, V. M. A 3D tension bioreactor platform to study the interplay between ECM stiffness and tumor phenotype. *J. Biotechnol.* **193,** 66–69 (2014).

104. Heldin, C.-H., Rubin, K., Pietras, K. & Ostman, A. High interstitial fluid pressure - an obstacle in cancer therapy. *Nat. Rev. Cancer* **4,** 806–813 (2004).

105. Al-Olama, M. *et al.* The peptide AF-16 decreases high interstitial fluid pressure in solid tumors. *Acta Oncol.* **50,** 1098–1104 (2011).

106. Jennische, E. *et al.* The peptide AF-16 abolishes sickness and death at experimental encephalitis by reducing increase of intracranial pressure. *Brain Res.* **1227,** 189–197 (2008).

107. Johansson, E., Al-Olama, M., Hansson, H.-A., Lange, S. & Jennische, E. Diet-induced antisecretory factor prevents intracranial hypertension in a dosage-dependent manner. *Br. J. Nutr.* **109,** 2247–52 (2013).

108. Lino, M. M., Merlo, A. & Boulay, J.-L. Notch signaling in glioblastoma: a developmental drug target? *BMC Med.* **8,** 72 (2010).

109. Sahlgren, C., Gustafsson, M. V, Jin, S., Poellinger, L. & Lendahl, U. Notch signaling mediates hypoxia-induced tumor cell migration and invasion. *Proc. Natl. Acad. Sci. U. S. A.* **105,** 6392–6397 (2008).

110. Ewald, A. J., Werb, Z. & Egeblad, M. Dynamic, long-term in vivo imaging of tumor-stroma interactions in mouse models of breast cancer using spinning-disk confocal microscopy. *Cold Spring Harb. Protoc.* **2011,** pdb.top97 (2011).

111. Nakagawa, H. *et al.* Loss of liver E-cadherin induces sclerosing cholangitis and promotes carcinogenesis. *Proc. Natl. Acad. Sci. U. S. A.* 2–7 (2014). doi:10.1073/pnas.1322731111

112. López-Novoa, J. M. & Nieto, M. A. Inflammation and EMT: an alliance towards organ fibrosis and cancer progression. *EMBO Mol. Med.* **1,** 303–14 (2009).

113. Samuel, M. S. *et al.* Actomyosin-mediated cellular tension drives increased tissue stiffness and β-catenin activation to induce epidermal hyperplasia and tumor growth. *Cancer Cell* **19,** 776–91 (2011).

114. Ioachim, E. *et al.* Immunohistochemical expression of extracellular matrix components tenascin, fibronectin, collagen type IV and laminin in breast cancer: their prognostic value and role in tumour invasion and progression. *Eur. J. Cancer* **38,** 2362–2370 (2002).

115. Desgrosellier, J. S. & Cheresh, D. a. Integrins in cancer: biological implications and therapeutic opportunities. *Nat. Rev. Cancer* **10,** 9–22 (2010).

116. Nam, J.-M., Onodera, Y., Bissell, M. J. & Park, C. C. Breast cancer cells in three-dimensional culture display an enhanced radioresponse after coordinate targeting of integrin alpha5beta1 and fibronectin. *Cancer Res.* **70,** 5238–48 (2010).

117. Recher, C. *et al.* Expression of Focal Adhesion Kinase in Acute Myeloid Leukemia Is Associated with Enhanced Blast Migration , Increased Cellularity , and Poor Prognosis Expression of Focal Adhesion Kinase in Acute Myeloid Leukemia Is Associated with Enhanced Blast Migratio. 3191–3197 (2004).

118. Stoeltzing, O. *et al.* Inhibition of integrin alpha5beta1 function with a small peptide (ATN-161) plus continuous 5-FU infusion reduces colorectal liver metastases and improves survival in mice. *Int. J. Cancer* **104,** 496–503 (2003).

119. Nimwegen, M. J. Van, Verkoeijen, S., Buren, L. Van, Burg, D. & Water, B. Van De. Requirement for Focal Adhesion Kinase in the Early Phase of Mammary Adenocarcinoma Lung Metastasis Formation Mammary Adenocarcinoma Lung Metastasis Formation. 4698–4706 (2005).

120. Heldin, C.-H., Rubin, K., Pietras, K. & Ostman, A. High interstitial fluid pressure - an obstacle in cancer therapy. *Nat. Rev. Cancer* **4,** 806–13 (2004).

121. Shimosato, Y. *et al. Prognostic implications of fibrotic focus (scar) in small peripheral lung cancers. Am. J. Surg. Pathol.* **4,** 365–373 (1980).

122. Maeshima, A. M. *et al.* Modified scar grade: A prognostic indicator in small peripheral lung adenocarcinoma. *Cancer* **95,** 2546–2554 (2002).

123. Willis, B. C. & Borok, Z. TGF-beta-induced EMT: mechanisms and implications for fibrotic lung disease. *Am. J. Physiol. Lung Cell. Mol. Physiol.* **293,** L525–L534 (2007).

124. Zutrer, M. M., Santoro, S. A., Staatz, W. D. & Tsung, Y. L. Re-expression of the 02131 integrin abrogates the malignant phenotype of breast carcinoma cells. **92,** 7411–7415 (1995).

125. Kaplan, R. N. *et al.* VEGFR1-positive haematopoietic bone marrow progenitors initiate the pre-metastatic niche. *Nature* **438,** 820–7 (2005).

126. Quail, D. F. & Joyce, J. A. Microenvironmental regulation of tumor progression and metastasis. *Nat. Med.* **19,** 1423–37 (2013).

127. Liu, D., Aguirre Ghiso, J., Estrada, Y. & Ossowski, L. EGFR is a transducer of the urokinase receptor initiated signal that is required for in vivo growth of a human carcinoma. *Cancer Cell* **1,** 445–57 (2002).

128. Friedland, J. C., Lee, M. H. & Boettiger, D. Mechanically activated integrin switch controls alpha5beta1 function. *Science* **323,** 642–4 (2009).

129. Seong, J. *et al.* Distinct biophysical mechanisms of focal adhesion kinase mechanoactivation by different extracellular matrix proteins. *Proc Natl Acad Sci U S A* **110,** 19372–19377 (2013).

130. Mierke, C. T., Frey, B., Fellner, M., Herrmann, M. & Fabry, B. Integrin α5β1 facilitates cancer cell invasion through enhanced contractile forces. *J. Cell Sci.* **124,** 369–83 (2011).

131. Miroshnikova, Y. a *et al.* Engineering strategies to recapitulate epithelial morphogenesis within synthetic three-dimensional extracellular matrix with tunable mechanical properties. *Phys. Biol.* **8,** 026013 (2011).

132. Yeung, T. *et al.* Effects of substrate stiffness on cell morphology, cytoskeletal structure, and adhesion. *Cell Motil. Cytoskeleton* **60,** 24–34 (2005).

133. García, A. J., Schwarzbauer, J. E. & Boettiger, D. Distinct activation states of alpha5beta1 integrin show differential binding to RGD and synergy domains of fibronectin. *Biochemistry* **41,** 9063–9 (2002).

134. Li, F., Redick, S. D., Erickson, H. P. & Moy, V. T. Force measurements of the alpha5beta1 integrin-fibronectin interaction. *Biophys. J.* **84,** 1252–62 (2003).

135. Yao, E. S. *et al.* Increased beta1 integrin is associated with decreased survival in invasive breast cancer. *Cancer Res.* **67,** 659–64 (2007).

136. Dingemans, A.-M. C. *et al.* Integrin expression profiling identifies integrin alpha5 and beta1 as prognostic factors in early stage non-small cell lung cancer. *Mol. Cancer* **9,** 152 (2010).

137. Ulrich, T. a, de Juan Pardo, E. M. & Kumar, S. The mechanical rigidity of the extracellular matrix regulates the structure, motility, and proliferation of glioma cells. *Cancer Res.* **69,** 4167–74 (2009).

138. Huang, S. & Ingber, D. E. Cell tension, matrix mechanics, and cancer development. *Cancer Cell* **8,** 175–6 (2005).

139. Guo, W. & Giancotti, F. G. Integrin signalling during tumour progression. *Nat. Rev. Mol. Cell Biol.* **5,** 816–26 (2004).

140. Samani, A., Zubovits, J. & Plewes, D. Elastic moduli of normal and pathological human breast tissues: an inversion-technique-based investigation of 169 samples. *Phys. Med. Biol.* **52,** 1565–76 (2007).

141. Plodinec, M. *et al.* The nanomechanical signature of breast cancer. *Nat. Nanotechnol.* **7,** 757–65 (2012).

142. Briand, P., Petersen, O. W. & Deurs, B. A new diploid nontumorigenic human breast epithelial cell line isolated and propagated in chemically defined medium. *Vitr. Cell. Dev. Biol.* **23,** 181–188 (1987).

143. Dupont, S. *et al.* Role of YAP/TAZ in mechanotransduction. *Nature* **474,** 179–183 (2011).

144. Kong, F., García, A. J., Mould, a P., Humphries, M. J. & Zhu, C. Demonstration of catch bonds between an integrin and its ligand. *J. Cell Biol.* **185,** 1275–84 (2009).

145. Weber, G. *et al.* Roles of the RAF/MEK/ERK and PI3K/PTEN/AKT pathways in malignant transformation and drug resistance. *Adv. Enzyme Regul.* **46,** 249–279 (2006).

146. Rubashkin, M. G. *et al.* Force engages vinculin and promotes tumor progression by enhancing PI3K activation of phosphatidylinositol (3,4,5)-triphosphate. *Cancer Res.* **74,** 4597–611 (2014).

147. Martin-Belmonte, F. *et al.* PTEN-mediated apical segregation of phosphoinositides controls epithelial morphogenesis through Cdc42. *Cell* **128,** 383–97 (2007).

148. Yu, M. *et al.* RNA sequencing of pancreatic circulating tumour cells implicates WNT signalling in metastasis. *Nature* **487,** 510–3 (2012).

149. Maschler, S. *et al.* Tumor cell invasiveness correlates with changes in integrin expression and localization. *Oncogene* **24,** 2032–41 (2005).

150. Valastyan, S. *et al.* A pleiotropically acting microRNA, miR-31, inhibits breast cancer metastasis. *Cell* **137,** 1032–46 (2009).

151. Park, C. C. *et al.* Beta1 integrin inhibitory antibody induces apoptosis of breast cancer cells, inhibits growth, and distinguishes malignant from normal phenotype in three dimensional cultures and in vivo. *Cancer Res.* **66,** 1526–35 (2006).

152. Baneyx, G., Baugh, L. & Vogel, V. Fibronectin extension and unfolding within cell matrix fibrils controlled by cytoskeletal tension. **2002,** (2002).

153. Martino, M. M. *et al.* Controlling integrin specificity and stem cell differentiation in 2-D and 3-D environments through regulation of fibronectin domain stability. **30,** 1089–1097 (2010).

154. Barker, T. H. *et al.* SPARC regulates extracellular matrix organization through its modulation of integrin-linked kinase activity. *J. Biol. Chem.* **280,** 36483–93 (2005).

155. Ledger, P. W., Uchida, N. & Tanzer, M. L. Immunocytochemical localization of procollagen and fibronectin in human fibroblasts: effects of the monovalent ionophore, monensin. *J. Cell Biol.* **87,** 663–71 (1980).

156. Singh, P., Carraher, C. & Schwarzbauer, J. E. Assembly of fibronectin extracellular matrix. *Annu. Rev. Cell Dev. Biol.* **26,** 397–419 (2010).

157. Dallas, S. L. *et al.* Fibronectin regulates latent transforming growth factor-beta (TGF beta) by controlling matrix assembly of latent TGF beta-binding protein-1. *J. Biol. Chem.* **280,** 18871–80 (2005).

158. Dallas, S. L., Chen, Q. & Sivakumar, P. Dynamics of Assembly and Reorganization of Extracellular Matrix Proteins. *Curr. Top. Dev. Biol.* **75,** 1–24 (2006).

159. Mcdonald, J. A. EXTRACELLULAR MATRIX ASSEMBLY. *Proc Natl Acad Sci U S A* **88,** 183–207 (1988).

160. Kadler, K. E., Hill, A. & Canty-Laird, E. G. Collagen fibrillogenesis: fibronectin, integrins, and minor collagens as organizers and nucleators. *Curr. Opin. Cell Biol.* **20,** 495–501 (2008).

161. Eyre, D. R., Paz, M. a & Gallop, P. M. Cross-linking in collagen and elastin. *Annu. Rev. Biochem.* **53,** 717–48 (1984).

162. Mosher, D. F. Cross-linking of fibronectin to collagenous proteins. *Mol. Cell. Biochem.* **58,** 63–68 (1984).

163. Shintani, Y. *et al.* Collagen I-mediated up-regulation of N-cadherin requires cooperative signals from integrins and discoidin domain receptor 1. *J. Cell Biol.* **180,** 1277–89 (2008).

164. Vuoriluoto, K. *et al.* Syndecan-1 supports integrin alpha2beta1-mediated adhesion to collagen. *Exp. Cell Res.* **314,** 3369–81 (2008).

165. Liebersbach, B. F. & Sanderson, R. D. Expression of syndecan-1 inhibits cell invasion into type I collagen. *J. Biol. Chem.* **269,** 20013–9 (1994).

166. Shyu, K.-G., Chao, Y.-M., Wang, B.-W. & Kuan, P. Regulation of discoidin domain receptor 2 by cyclic mechanical stretch in cultured rat vascular smooth muscle cells. *Hypertension* **46,** 614–21 (2005).

167. Chappell, W. H. *et al.* Ras/Raf/MEK/ERK and PI3K/PTEN/Akt/mTOR inhibitors: rationale and importance to inhibiting these pathways in human health. *Oncotarget* **2,** 135–64 (2011).

168. McCubrey, J. A. *et al.* Roles of the Raf/MEK/ERK pathway in cell growth, malignant transformation and drug resistance. *Biochim. Biophys. Acta* **1773,** 1263–84 (2007).

169. Engelman, J. A. Targeting PI3K signalling in cancer: opportunities, challenges and limitations. *Nat. Rev. Cancer* **9,** 550–62 (2009).

170. McCubrey, J. A. *et al.* Targeting survival cascades induced by activation of Ras/Raf/MEK/ERK, PI3K/PTEN/Akt/mTOR and Jak/STAT pathways for effective leukemia therapy. *Leukemia* **22,** 708–22 (2008).

171. Wong, K.-K., Engelman, J. A. & Cantley, L. C. Targeting the PI3K signaling pathway in cancer. *Curr. Opin. Genet. Dev.* **20,** 87–90 (2010).

172. García, A. J., Huber, F. & Boettiger, D. Force required to break alpha5beta1 integrin-fibronectin bonds in intact adherent cells is sensitive to integrin activation state. *J. Biol. Chem.* **273,** 10988–93 (1998).

173. Ryan, D. P., Hong, T. S. & Bardeesy, N. Pancreatic Adenocarcinoma. *N. Engl. J. Med.* **371,** 1039–1049 (2014).

174. Chauhan, V. P. *et al.* Compression of pancreatic tumor blood vessels by hyaluronan is caused by solid stress and not interstitial fluid pressure. *Cancer Cell* **26,** 14–5 (2014).

175. Swartz, M. A. & Lund, A. W. Lymphatic and interstitial flow in the tumour microenvironment: linking mechanobiology with immunity. *Nat. Rev. Cancer* **12,** 210–219 (2012).

176. Yu, M. & Tannock, I. F. Targeting Tumor Architecture to Favor Drug Penetration: A New Weapon to Combat Chemoresistance in Pancreatic Cancer? *Cancer Cell* **21,** 327–329 (2012).

177. Provenzano, P. P. & Hingorani, S. R. Hyaluronan, fluid pressure, and stromal resistance in pancreas cancer. *Br. J. Cancer* **108,** 1–8 (2013).

178. Neesse, A., Krug, S., Gress, T. M., Tuveson, D. A. & Michl, P. Emerging concepts in pancreatic cancer medicine: Targeting the tumor stroma. *Onco. Targets. Ther.* **7,** 33–43 (2013).

179. Olive, K. P. *et al.* Inhibition of Hedgehog signaling enhances delivery of chemotherapy in a mouse model of pancreatic cancer. *Science* **324,** 1457–1461 (2009).

180. Provenzano, P. P. *et al.* Enzymatic targeting of the stroma ablates physical barriers to treatment of pancreatic ductal adenocarcinoma. *Cancer Cell* **21,** 418–29 (2012).

181. Chauhan, V. P. *et al.* Angiotensin inhibition enhances drug delivery and potentiates chemotherapy by decompressing tumour blood vessels. *Nat. Commun.* **4,** 2516 (2013).

182. Rosow, D. E. *et al.* Sonic Hedgehog in pancreatic cancer: from bench to bedside, then back to the bench. *Surgery* **152,** S19–32 (2012).

183. Pentcheva-hoang, T. *et al.* Article Depletion of Carcinoma-Associated Fibroblasts and Fibrosis Induces Immunosuppression and Accelerates Pancreas Cancer with Reduced Survival. 1–16 (2014).

184. Rhim, A. D. *et al.* Stromal elements act to restrain, rather than support, pancreatic ductal adenocarcinoma. *Cancer Cell* **25,** 735–747 (2014).

185. Pickup, M. W., Mouw, J. K. & Weaver, V. M. The extracellular matrix modulates the hallmarks of cancer. *EMBO Rep.* **15,** 1243–1253 (2014).

186. Cheung, K. J., Gabrielson, E., Werb, Z. & Ewald, A. J. Collective invasion in breast cancer requires a conserved basal epithelial program. *Cell* **155,** 1639–1651 (2013).

187. Hoadley, K. A. *et al.* Multiplatform Analysis of 12 Cancer Types Reveals Molecular Classification within and across Tissues of Origin. *Cell* (2013). doi:10.1016/j.cell.2014.06.049

188. Thiery, J. P., Acloque, H., Huang, R. Y. J. & Nieto, M. A. Epithelial-Mesenchymal Transitions in Development and Disease. *Cell* **139,** 871–890 (2009).

189. Collisson, E. a. *et al.* Comprehensive molecular profiling of lung adenocarcinoma. *Nature* **511,** 543–50 (2014).

190. Collisson, E. A. *et al.* Subtypes of pancreatic ductal adenocarcinoma and their differing responses to therapy. *Nat. Med.* **17,** 500–503 (2011).

191. Kapoor, A. *et al.* Yap1 activation enables bypass of oncogenic kras addiction in pancreatic cancer. *Cell* **158,** 185–97 (2014).

192. Deer, E. L. *et al.* Phenotype and genotype of pancreatic cancer cell lines. *Pancreas* **39,** 425–435 (2010).

193. Pérez-Mancera, P. A., Guerra, C., Barbacid, M. & Tuveson, D. A. What we have learned about pancreatic cancer from mouse models. *Gastroenterology* **142,** 1079–1092 (2012).

194. Ijichi, H. *et al.* Aggressive pancreatic ductal adenocarcinoma in mice caused by pancreas-specific blockade of transforming growth factor-β signaling in cooperation with active Kras expression. *Genes Dev.* **20,** 3147–3160 (2006).

195. Hingorani, S. R. *et al.* Trp53R172H and KrasG12D cooperate to promote chromosomal instability and widely metastatic pancreatic ductal adenocarcinoma in mice. *Cancer Cell* **7,** 469–483 (2005).

196. Aguirre, A. J. *et al.* Activated Kras and Ink4a/Arf deficiency cooperate to produce metastatic pancreatic ductal adenocarcinoma. *Genes Dev.* **17,** 3112–3126 (2003).

197. Bardeesy, N. *et al.* Smad4 is dispensable for normal pancreas development yet critical in progression and tumor biology of pancreas cancer. *Genes Dev.* **20,** 3130–3146 (2006).

198. Kabashima, A. *et al.* Side population of pancreatic cancer cells predominates in TGF-beta-mediated epithelial to mesenchymal transition and invasion. *Int. J. Cancer* **124,** 2771–2779 (2009).

199. Izeradjene, K. *et al.* KrasG12D and Smad4/Dpc4 Haploinsufficiency Cooperate to Induce Mucinous Cystic Neoplasms and Invasive Adenocarcinoma of the Pancreas. *Cancer Cell* **11,** 229–243 (2007).

200. Izumchenko, E. *et al.* The TGFβ-miR200-MIG6 pathway orchestrates the EMT-associated kinase switch that induces resistance to EGFR inhibitors. *Cancer Res.* **74,** 3995–4005 (2014).

201. Rhim, A. D. *et al.* EMT and dissemination precede pancreatic tumor formation. *Cell* **148,** 349–361 (2012).

202. Herreros-Villanueva, M. *et al.* SOX2 promotes dedifferentiation and imparts stem cell-like features to pancreatic cancer cells. *Oncogenesis* **2,** e61 (2013).

203. Jiang, J. *et al.* MiR-1181 inhibits stem cell-like phenotypes and suppresses SOX2 and STAT3 in human pancreatic cancer. *Cancer Lett.* **356,** 962–970 (2015).

204. Shao, D. D. *et al.* KRAS and YAP1 converge to regulate EMT and tumor survival. *Cell* **158,** 171–184 (2014).

205. Yimlamai, D. *et al.* Hippo pathway activity influences liver cell fate. *Cell* **157,** 1324–1338 (2014).

206. Zhang, J. *et al.* YAP-dependent induction of amphiregulin identifies a non-cell-autonomous component of the Hippo pathway. *Nat. Cell Biol.* **11,** 1444–1450 (2009).

207. Seo, E. *et al.* SOX2 Regulates YAP1 to Maintain Stemness and Determine Cell Fate in the Osteo-Adipo Lineage. *Cell Rep.* **3,** 2075–2087 (2013).

208. Basu-roy, U. *et al.* Sox2 antagonizes the Hippo pathway to maintain stemness in cancer cells. *Nat. Commun.* **6,** 1–14 (2015).

209. Yu, F. X. *et al.* Regulation of the Hippo-YAP pathway by G-protein-coupled receptor signaling. *Cell* **150,** 780–791 (2012).

210. Calvo, F. *et al.* Mechanotransduction and YAP-dependent matrix remodelling is required for the generation and maintenance of cancer-associated fibroblasts. *Nat Cell Biol* **15,** 637–646 (2013).

211. Samuel, M. S. *et al.* Actomyosin-mediated cellular tension drives increased tissue stiffness and β-catenin activation to induce epidermal hyperplasia and tumor growth. *Cancer Cell* **19,** 776–91 (2011).

212. Erkan, M. *et al.* The Activated Stroma Index Is a Novel and Independent Prognostic Marker in Pancreatic Ductal Adenocarcinoma. *Clin. Gastroenterol. Hepatol.* **6,** 1155–1161 (2008).

213. Sinn, M. *et al.* α-Smooth muscle actin expression and desmoplastic stromal reaction in pancreatic cancer: results from the CONKO-001 study. *Br. J. Cancer* **111,** 1917–1923 (2014).

214. Bever, K. M. *et al.* The prognostic value of stroma in pancreatic cancer in patients receiving adjuvant therapy. *Hpb* n/a–n/a (2014). doi:10.1111/hpb.12334

215. Dangi-Garimella, S. *et al.* Three-dimensional collagen I promotes gemcitabine resistance in pancreatic cancer through MT1-MMP-mediated expression of HMGA2. *Cancer Res.* **71,** 1019–1028 (2011).

216. Wang, W. Q. *et al.* Intratumoral α-SMA Enhances the Prognostic Potency of CD34 Associated with Maintenance of Microvessel Integrity in Hepatocellular Carcinoma and Pancreatic Cancer. *PLoS One* **8,** (2013).

217. Schultz, N. a *et al.* MicroRNA expression profiles associated with pancreatic adenocarcinoma and ampullary adenocarcinoma. *Mod. Pathol.* 1609–1622 (2012). doi:10.1038/modpathol.2012.122

218. Hingorani, S. R. *et al.* Preinvasive and invasive ductal pancreatic cancer and its early detection in the mouse. *Cancer Cell* **4,** 437–450 (2003).

219. Sanz-Moreno, V. *et al.* ROCK and JAK1 Signaling Cooperate to Control Actomyosin Contractility in Tumor Cells and Stroma. *Cancer Cell* **20,** 229–245 (2011).

220. Fukuda, A. *et al.* Stat3 and MMP7 Contribute to Pancreatic Ductal Adenocarcinoma Initiation and Progression. *Cancer Cell* **19,** 441–455 (2011).

221. Lesina, M. *et al.* Stat3/Socs3 Activation by IL-6 Transsignaling Promotes Progression of Pancreatic Intraepithelial Neoplasia and Development of Pancreatic Cancer. *Cancer Cell* **19,** 456–469 (2011).

222. Ijichi, H. *et al.* Inhibiting Cxcr2 disrupts tumor-stromal interactions and improves survival in a mouse model of pancreatic ductal adenocarcinoma. *J. Clin. Invest.* **121,** 4106–4117 (2011).

223. Mouw, J. K. *et al.* Tissue mechanics modulate microRNA-dependent PTEN expression to regulate malignant progression. *Nat. Med.* **20,** 360–7 (2014).

224. Li, R. *et al.* Activation of integrin alphaIIbbeta3 by modulation of transmembrane helix associations. *Science* **300,** 795–798 (2003).

225. Barbieri, I. *et al.* Constitutively active Stat3 enhances neu-mediated migration and metastasis in mammary tumors via upregulation of Cten. *Cancer Res.* **70,** 2558–2567 (2010).

226. Alonzi, T. *et al.* Essential Role of STAT3 in the Control of the Acute-Phase Response as Revealed by Inducible Gene Activation in the Liver Essential Role of STAT3 in the Control of the Acute-Phase Response as Revealed by Inducible Gene Activation in the Liver. **21,** 1621–1632 (2001).

227. Whatcott, C. J. *et al.* Desmoplasia in primary tumors and metastatic lesions of pancreatic cancer. *Clin. Cancer Res.* (2015). doi:10.1158/1078-0432.CCR-14-1051

228. Kohler, I. *et al.* Detailed analysis of epithelial-mesenchymal transition and tumor budding identifies predictors of long-term survival in pancreatic ductal adenocarcinoma. *J. Gastroenterol. Hepatol.* **30,** 78–84 (2015).

229. Paron, I. *et al.* Tenascin-c enhances pancreatic cancer cell growth and motility and affects cell adhesion through activation of the integrin pathway. *PLoS One* **6,** (2011).

230. Esposito, I. *et al.* Tenascin C and annexin II expression in the process of pancreatic carcinogenesis. *J. Pathol.* **208,** 673–685 (2006).

231. Singh, A. *et al.* A Gene Expression Signature Associated with 'K-Ras Addiction' Reveals Regulators of EMT and Tumor Cell Survival. *Cancer Cell* **15,** 489–500 (2009).

232. Furnari, F. B. *et al.* Malignant astrocytic glioma: Genetics, biology, and paths to treatment. *Genes Dev.* **21,** 2683–2710 (2007).

233. Westphal, M. & Lamszus, K. The neurobiology of gliomas: from cell biology to the development of therapeutic approaches. *Nat. Rev. Neurosci.* **12,** 495–508 (2011).

234. Hoelzinger, D. B., Demuth, T. & Berens, M. E. Autocrine factors that sustain glioma invasion and paracrine biology in the brain microenvironment. *J. Natl. Cancer Inst.* **99,** 1583–1593 (2007).

235. Bergers, G. & Hanahan, D. Mode of resistance to anti-angiogenic therapy. *Nat. Rev. Cancer* **8,** 592–603 (2008).

236. Zohrabian, V. M., Forzani, B., Chau, Z., Murali, R. & Jhanwar-Uniyal, M. Rho/ROCK and MAPK signaling pathways are involved in glioblastoma cell migration and proliferation. *Anticancer Res.* **29,** 119–123 (2009).

237. Verhaak, R. G. W. *et al.* Integrated Genomic Analysis Identifies Clinically Relevant Subtypes of Glioblastoma Characterized by Abnormalities in PDGFRA, IDH1, EGFR, and NF1. *Cancer Cell* **17,** 98–110 (2010).

238. Ahmed, R., Oborski, M. J., Hwang, M., Lieberman, F. S. & Mountz, J. M. Malignant gliomas: Current perspectives in diagnosis, treatment, and early response assessment using advanced quantitative imaging methods. *Cancer Manag. Res.* **6,** 149–170 (2014).

239. Norden, A. D., Drappatz, J. & Wen, P. Y. Malignant gliomas in adults. *Blue Books Neurol.* **36,** 99–120 (2010).

240. Noberini, R. & Pasquale, E. B. Proliferation and Tumor Suppression: Not Mutually Exclusive for Eph Receptors. *Cancer Cell* **16,** 452–454 (2009).

241. Parsons, D. W. *et al.* An integrated genomic analysis of human glioblastoma multiforme. *Science* **321,** 1807–1812 (2008).

242. Bleeker, F. E. *et al.* The prognostic IDH1(R132) mutation is associated with reduced NADP+-dependent IDH activity in glioblastoma. *Acta Neuropathol.* **119,** 487–94 (2010).

243. Songtao, Q. *et al.* IDH mutations predict longer survival and response to temozolomide in secondary glioblastoma. *Cancer Sci.* **103,** 269–273 (2012).

244. Guan, X. *et al.* Molecular subtypes of glioblastoma are relevant to lower grade glioma. *PLoS One* **9,** (2014).

245. Turcan, S. *et al.* IDH1 mutation is sufficient to establish the glioma hypermethylator phenotype. *Nature* **483,** 479–483 (2012).

246. Losman, J. A. & Kaelin, W. G. What a difference a hydroxyl makes: Mutant IDH, (R)-2-hydroxyglutarate, and cancer. *Genes Dev.* **27,** 836–852 (2013).

247. Louis, D. N. Molecular pathology of malignant gliomas. *Annu. Rev. Pathol.* **1,** 97–117 (2006).

248. Jain, R. K. Normalization of tumor vasculature: an emerging concept in antiangiogenic therapy. *Science* **307,** 58–62 (2005).

249. Zhao, S. *et al.* Glioma-derived mutations in IDH1 dominantly inhibit IDH1 catalytic activity and induce HIF-1alpha. *Science* **324,** 261–265 (2009).

250. Koivunen, P. *et al.* Transformation by the (R)-enantiomer of 2-hydroxyglutarate linked to EGLN activation. *Nature* **483,** 484–488 (2012).

251. Metellus, P. *et al.* IDH mutation status impact on in vivo hypoxia biomarkers expression: New insights from a clinical, nuclear imaging and immunohistochemical study in 33 glioma patients. *J. Neurooncol.* **105,** 591–600 (2011).

252. Geiss, G. K. *et al.* Direct multiplexed measurement of gene expression with color-coded probe pairs. **26,** 317–326 (2008).

253. Colman, H. *et al.* N E U RO - O N CO LO GY A multigene predictor of outcome in glioblastoma. **77401,** (2009).

254. Zimmermann, D. R. & Dours-Zimmermann, M. T. Extracellular matrix of the central nervous system: From neglect to challenge. *Histochem. Cell Biol.* **130,** 635–653 (2008).

255. Parsons, D., Jones, S., Zhang, X. & Lin, J. An integrated genomic analysis of human glioblastoma multiforme. *Science (80-.).* **321,** 1807–12 (2008).

256. Chaumeil, M. M. *et al.* Non-invasive in vivo assessment of IDH1 mutational status in glioma. *Nat. Commun.* **4,** 2429 (2013).

257. Masson, N. & Ratcliffe, P. J. Hypoxia signaling pathways in cancer metabolism : the importance of co-selecting interconnected physiological pathways. **2,** 1–17 (2014).

258. Ivan, M. *et al.* HIFalpha targeted for VHL-mediated destruction by proline hydroxylation: implications for O2 sensing. *Science* **292,** 464–468 (2001).

259. Koperek, O., Akin, E., Asari, R., Niederle, B. & Neuhold, N. Expression of hypoxia-inducible factor 1 alpha in papillary thyroid carcinoma is associated with desmoplastic stromal reaction and lymph node metastasis. *Virchows Arch.* **463,** 795–802 (2013).

260. Midwood, K. S. & Orend, G. The role of tenascin-C in tissue injury and tumorigenesis. *J. Cell Commun. Signal.* **3,** 287–310 (2009).

261. Stroka, D. M. *et al.* HIF-1 is expressed in normoxic tissue and displays an organ-specific regulation under systemic hypoxia. *FASEB J.* **15,** 2445–2453 (2001).

262. Barcellos-Hoff, M. H. & Ravani, S. A. Irradiated mammary gland stroma promotes the expression of tumorigenic potential by unirradiated epithelial cells. *Cancer Res.* **60,** 1254–1260 (2000).

263. Bellail, A. C., Hunter, S. B., Brat, D. J., Tan, C. & Van Meir, E. G. Microregional extracellular matrix heterogeneity in brain modulates glioma cell invasion. *Int. J. Biochem. Cell Biol.* **36,** 1046–1069 (2004).

264. Hatanpaa, K. J., Burma, S., Zhao, D. & Habib, A. A. Epidermal growth factor receptor in glioma: signal transduction, neuropathology, imaging, and radioresistance. *Neoplasia* **12,** 675–684 (2010).

265. Gilbert, C. A. & Ross, A. H. Cancer stem cells: Cell culture, markers, and targets for new therapies. *J. Cell. Biochem.* **108,** 1031–1038 (2009).

266. Krakstad, C. & Chekenya, M. Survival signalling and apoptosis resistance in glioblastomas: opportunities for targeted therapeutics. *Mol. Cancer* **9,** 135 (2010).

267. Lomonaco, S. L. *et al.* The induction of autophagy by gamma-radiation contributes to the radioresistance of glioma stem cells. *Int. J. Cancer* **125,** 717–22 (2009).

268. Mao, P. *et al.* Mesenchymal glioma stem cells are maintained by activated glycolytic metabolism involving aldehyde dehydrogenase 1A3. *Proc. Natl. Acad. Sci. U. S. A.* **110,** 8644–9 (2013).

269. Halliday, J. *et al.* In vivo radiation response of proneural glioma characterized by protective p53 transcriptional program and proneural-mesenchymal shift. *Proc. Natl. Acad. Sci. U. S. A.* **111,** 5248–53 (2014).

270. Mahabir, R. *et al.* Sustained elevation of Snail promotes glial-mesenchymal transition after irradiation in malignant glioma. *Neuro. Oncol.* **16,** 671–685 (2014).

271. Puget, S. *et al.* Mesenchymal transition and PDGFRA amplification/mutation are key distinct oncogenic events in pediatric diffuse intrinsic pontine gliomas. *PLoS One* **7,** e30313 (2012).

272. Colomiere, M. *et al.* Cross talk of signals between EGFR and IL-6R through JAK2/STAT3 mediate epithelial-mesenchymal transition in ovarian carcinomas. *Br. J. Cancer* **100,** 134–44 (2009).

273. Carro, M. S. *et al.* The transcriptional network for mesenchymal transformation of brain tumours. *Nature* **463,** 318–325 (2010).

274. Paszek, M. J., Boettiger, D., Weaver, V. M. & Hammer, D. A. Integrin clustering is driven by mechanical resistance from the glycocalyx and the substrate. *PLoS Comput. Biol.* **5,** (2009).

275. Paszek, M. J. *et al.* The cancer glycocalyx mechanically primes integrin-mediated growth and survival. *Nature* **511,** 319–25 (2014).

276. Lanctot, P. M., Gage, F. H. & Varki, A. P. The glycans of stem cells. *Curr. Opin. Chem. Biol.* **11,** 373–380 (2007).

277. Haltiwanger, R. S. & Lowe, J. B. Role of glycosylation in development. *Annu. Rev. Biochem.* **73,** 491–537 (2004).

278. Varki, A., Kannagi, R. & Toole, B. P. *Chapter 44 Glycosylation Changes in Cancer*. *Cancer* (2009).

279. Spicer, A. P., Joo, A. & Bowling, R. A. A hyaluronan binding link protein gene family whose members are physically linked adjacent to chrondroitin sulfate proteoglycan core protein genes. The missing links. *J. Biol. Chem.* **278,** 21083–21091 (2003).

280. Bernfield, M. *et al.* Functions of cell surface heparan sulfate proteoglycans. *Annu.Rev.Biochem.* **68:729-77.,** 729–777 (1999).

281. Steck, P. A. *et al.* Altered expression and distribution of heparan sulfate proteoglycans in human gliomas. *Cancer Res.* **49,** 2096–2103 (1989).

282. Sarrazin, S., Lamanna, W. C. & Esko, J. D. Heparan sulfate proteoglycans. *Cold Spring Harb. Perspect. Biol.* **3,** 1–33 (2011).

283. Sieg, D. J. *et al.* FAK integrates growth-factor and integrin signals to promote cell migration. *Nat. Cell Biol.* **2,** 249–256 (2000).

284. Twarock, S., Tammi, M. I., Savani, R. C. & Fischer, J. W. Hyaluronan stabilizes focal adhesions, filopodia, and the proliferative phenotype in esophageal squamous carcinoma cells. *J. Biol. Chem.* **285,** 23276–23284 (2010).

285. Isaji, T., Sato, Y., Fukuda, T. & Gu, J. N-Glycosylation of the I-like Domain of Î²1 Integrin Is Essential for Î²1 Integrin Expression and Biological Function. *J. Biol. Chem.* **284,** 12207–12216 (2009).

286. Wicki, A. & Christofori, G. The potential role of podoplanin in tumour invasion. *Br. J. Cancer* **96,** 1–5 (2007).

287. Drake, P. M. *et al.* Sweetening the pot: Adding glycosylation to the biomarker discovery equation. *Clin. Chem.* **56,** 223–236 (2010).

288. Duenisch, P. *et al.* Neural cell adhesion molecule isoform 140 declines with rise of WHO grade in human gliomas and serves as indicator for the invasion zone of multiform glioblastomas and brain metastases. *J. Cancer Res. Clin. Oncol.* **137,** 399–414 (2011).

289. Lagana, A. *et al.* Galectin binding to Mgat5-modified N-glycans regulates fibronectin matrix remodeling in tumor cells. *Mol. Cell. Biol.* **26,** 3181–3193 (2006).

290. Clark, K. *et al.* A specific alpha5beta1-integrin conformation promotes directional integrin translocation and fibronectin matrix formation. *J. Cell Sci.* **118,** 291–300 (2005).

291. Leone, D. P. *et al.* Regulation of neural progenitor proliferation and survival by beta1 integrins. *J. Cell Sci.* **118,** 2589–2599 (2005).

292. Bertozzi, C. R. & Kiessling, L. L. Chemical glycobiology. *Science* **291,** 2357–2364 (2001).

293. Wiranowska, M. *et al.* Modulation of hyaluronan production by CD44 positive glioma cells. *Int. J. Cancer* **127,** 532–542 (2010).

294. Tate, M. C. & Aghi, M. K. Biology of Angiogenesis and Invasion in Glioma. *Neurotherapeutics* **6,** 447–457 (2009).

295. Maher, E. A. *et al.* Malignant glioma: genetics and biology of a grave matter. *Genes Dev.* **15,** 1311–33 (2001).

296. Zheng, P.-P., Severijnen, L.-A., van der Weiden, M., Willemsen, R. & Kros, J. M. Cell proliferation and migration are mutually exclusive cellular phenomena in vivo: implications for cancer therapeutic strategies. *Cell Cycle* **8,** 950–1 (2009).

297. Dell'Albani, P. Stem cell markers in gliomas. *Neurochem. Res.* **33,** 2407–2415 (2008).

298. Paszek, M. J. *et al.* Scanning angle interference microscopy reveals cell dynamics at the nanoscale. *Nat. Methods* **9,** 825–827 (2012).

Publishing Agreement

It is the policy of the University to encourage the distribution of all theses, dissertations, and manuscripts. Copies of all UCSF theses, dissertations, and manuscripts will be routed to the library via the Graduate Division. The library will make all theses, dissertations, and manuscripts accessible to the public and will preserve these to the best of their abilities, in perpetuity.

Please sign the following statement:

I hereby grant permission to the Graduate Division of the University of California, San Francisco to release copies of my thesis, dissertation, or manuscript to the Campus Library to provide access and preservation, in whole or in part, in perpetuity.

Author Signature

Date